VOLCANIC GEOLOGY AND GEOMORPHOLOGY OF THE KAIMAI RHYOLITE DOME COMPLEX, TAURANGA VOLCANIC CENTRE, NEW ZEALAND

A thesis

submitted in partial fulfilment

of the requirements for the degree

of

Master of Science (Research) in **Earth Science**

at

The University of Waikato

by

Morgan Peter Clark

THE UNIVERSITY OF
WAIKATO
Te Whare Wānanga o Waikato

2026

Abstract

The Kaimai Rhyolite Dome Complex (KRDC) is an extinct rhyolite dome complex on the Waikato-Bay of Plenty border which forms a prominent feature at the southern end of the Kaimai Range. Published $^{40}Ar/^{39}Ar$ and U-Pb zircon ages place dome emplacement between approximately 2.87 and 2.2 Ma, placing the KRDC within the Tauranga Volcanic Centre (TgVC) spatially, temporally, and within the transitionary phase of subduction-related volcanism within the North Island from the Coromandel Volcanic Zone to the Taupo Volcanic Zone. It is contemporaneous with the Alexandra Volcanic Group and Okete Volcanics of the western North Island, the wider Minden Rhyolite Subgroup of the TgVC, and predates the ~2.1 Ma Waitearikiki Supereruption of the Omanawa Caldera. Despite its prominence on the Tauranga skyline and regional significance the KRDC has never been the primary subject of a dedicated study. This study applies modern volcanological techniques to define the complex and its place within the TgVC, incorporating field mapping, LiDAR-derived geomorphological analysis, petrography, SEM-EDS, XRD, whole-rock major and trace element geochemical analysis (XRF and LA-ICP-MS), and zircon saturation thermometry.

The KRDC is recognised in this study for the first time and its six discrete dome centres, Te Weraiti, Kaimai, Kakahu, Hiwiroa, the Eastern Dome, and the Southeastern Dome, all previously mapped as Minden Rhyolite Group on Rotorua QMAP with undefined internal unit contacts and margins. Hiwiroa, the Eastern Dome, and the Southeastern Dome are recognised for the first time on the basis of geomorphology and morphometric analysis. The complex forms a coalesced composite dome ridge spanning 25.8 km along a N-S corridor with a total post erosional volume of 5.67 km^3. Field and geomorphological evidence confirm that dome emplacement predates the Waitearikiki supereruption. A three-tier framework was developed describing the structural control on emplacement of the dome centres derived from elongation ratios and spatial context, fault-controlled fissure emplacement (Te Weraiti, Kakahu; ER 2.81–3.16), intermediate point-source emplacement within a fault corridor (Kaimai; ER 1.44), and minimal direct fault control (Hiwiroa, Eastern, Southeastern; ER 1.47–1.85). The bimodal distribution of elongation ratios indicating two distinct emplacement modes of both fissure derived

and point source rather than a continuous spectrum. Phenocryst assemblages at Te Weraiti and Kaimai are plagioclase + quartz ± biotite ± sanidine ± pyroxene. The KRDC lavas are hornblende absent distinguishing it from the hornblende bearing Waitearikі Ignimbrite. Devitrification groundmass textures are pervasive across all KRDC lavas displaying large spherulites of cristobalite + sanidine, an assemblage consistent across CVZ–TgVC Minden Rhyolites from ~7.8 Ma (Hahei) to ~2.2 Ma (KRDC). KRDC lavas are high-silica 74–78 wt.% SiO_2 high-K calc-alkaline to shoshonitic, peraluminous rhyolites that underwent plagioclase-dominated fractionation. Single-stage fractional crystallisation modelling could not produce these lavas from either Waitearikі Ignimbrite or the potential parental basaltic-andesite basement, requiring assimilation-fractional crystallisation. Zircon saturation thermometry produces mean KRDC melt temperatures ~40 °C cooler than the comparable Mount Misery rhyolite series within the TgVC, indicating the KRDC lavas represent a cooler, more evolved magma batch through a similar petrogenetic process but from a separate plumbing system.

Acknowledgements

I would like to thank my supervisor, Adrian Pittari, for his guidance, patience, and feedback throughout this project. His breadth of knowledge across this field and his commitment to both my study and personal issues has been more than I could've asked for. He has been both a mentor and a source of personal support throughout. Thank you for our hour-long conversations and guidance throughout my undergrad and postgrad work.

I am also grateful to Marlena Prentice for her thoughts and conversations throughout this project as a second opinion and advice, joining me in the field, and her sharing of data and ideas. Her input has strengthened my knowledge.

I am especially grateful to Kirsty Vincent who provided guidance, support, and patience throughout the laboratory component of this project, assisting with sample preparation and analytical work at every stage. Sophia Rodrigues and Stella Raynova are thanked for their assistance with scanning electron microscopy and EDS analyses, and Danielle Blackwell for my LA-ICP-MS data. Their help made the analytical components of this thesis possible.

Fieldwork across the Kaimai Range was made possible by the Department of Conservation, who granted access to large parts of the study area, and by JSWAP, who provided access to the Kaimai farm and Matamata Metal Supplies quarry.

To my fellow postgraduates at the University of Waikato, thank you for the discussions, banter, and companionship throughout this experience.

Finally, to my family and friends, thank you for your continuous support, encouragement, patience, and for putting up with me talking about geology for hours and hours. Without you this thesis would not be possible.

Table of Contents

List of Figures

List of Tables

Chapter One: Introduction

1.1 Introduction

Silicic lava dome complexes are common features of silicic volcanic systems in tectonically active settings worldwide, including subduction zones, continental rifts, and caldera-related volcanism. The morphology of individual domes preserves a record of magma rheology, conduit geometry, and the structural setting in which emplacement occurred. Where dome complexes occur in tectonically active settings, the spatial distribution and orientation of individual domes can reveal the influence of regional fault architecture on magma ascent and vent location. At the same time, the geochemical and petrographic variation preserved within a single dome complex records the evolution of the underlying magma reservoir, including processes such as fractionation, magma mixing, and crustal assimilation. Dome complexes therefore offer an opportunity to investigate both the structural and magmatic controls on silicic volcanism within a complex and within a regional volcanic centre.

The Kaimai Rhyolite Dome Complex (KRDC) is a substantial silicic dome complex situated within the southern Kaimai Range on the western margin of the Tauranga Volcanic Centre, North Island, New Zealand. It comprises an undifferentiated rhyolite unit of three peaks, Te Weraiti, Kaimai, and Kakahu, with published U-Pb and $^{40}Ar/^{39}Ar$ ages for Kaimai and Kakahu ranging from 2.2 to 2.8 Ma (Briggs et al., 2005; Pittari et al., 2021). The complex was emplaced during the late Pliocene to early Pleistocene transition between the Coromandel Volcanic Zone and the Taupō Volcanic Zone. The KRDC sits between two major regional structures, the Hauraki Rift to the west and the Tauranga Graben to the east, both of which were active during and after emplacement.

Despite its size, topographic prominence, and position within this transitional period of New Zealand volcanism, the KRDC has received no dedicated study. The complex was previously recognised as a separate volcanic centre, the Kaimai Volcanic Centre (Briggs et al., 2005), before being reincorporated into the Tauranga Volcanic Centre by Pittari et al. (2021). Prentice (2023) explicitly notes the absence of detailed descriptions or characterisation of the rhyolite lavas comprising the KRDC within the published literature. As a result, the architecture, eruptive

products, magmatic history, and regional significance of the complex remain poorly understood.

1.2 Research Aim and Objectives

This study applies modern volcanological, petrological, and geochemical techniques to provide the first detailed characterisation of the Kaimai Rhyolite Dome Complex, and to assess its place within the geological evolution of the Tauranga Volcanic Centre and the broader transition of the Coromandel Volcanic Zone to the Taupō Volcanic Zone.

The objectives of this study are to:

- identify and map discrete dome centres comprising the KRDC using field observation, petrographic and geochemical evidence, and GIS-based morphometric analysis;
- identify structural controls on dome emplacement across the complex;
- determine the mineralogy, and groundmass textures of KRDC dome rocks through optical microscopy, X-ray diffraction, and SEM-EDS analysis;
- whole-rock major and trace element compositions using X-ray fluorescence spectroscopy and laser ablation inductively coupled plasma mass spectrometry, and use these data to assess magmatic processes and source characteristics

The Kaimai Range, of which the KRDC forms a key landform, is a defining feature of the western skyline of Tauranga and is visible across the entire city and its harbour. State Highway 29 traverses the complex directly, providing one of the main road links between the Waikato and Bay of Plenty regions. The North–South Track and Rapurapu Track, both within the Kaimai-Mamaku Conservation Park, also pass through the study area and are popular with trampers and other recreational users. The findings of this study contribute to broader public understanding of the geological history of this prominent and well-travelled landscape.

1.3 Methods

The methods used to address the objectives of this study fall into three broad categories: (1) field-based investigation, including geological mapping, outcrop description, and sample collection across the KRDC and its surroundings; (2) GIS-based analysis, including the production of geological and morphometric maps and the calculation of dome dimensions, areas, volumes, and slope statistics; and (3) laboratory analysis, comprising optical microscopic petrography of thin sections, X-ray powder diffraction (XRD), scanning electron microscopy with energy-dispersive spectroscopy (SEM-EDS), whole-rock major and trace element geochemistry by X-ray fluorescence spectroscopy (XRF) and laser ablation inductively coupled plasma mass spectrometry (LA-ICP-MS), and zircon saturation thermometry.

Detailed descriptions of each method are presented in the relevant chapters. Additional raw data are presented in the appendices.

1.4 Study Area

The Kaimai Rhyolite Dome Complex is located at the southernmost extent of the Kaimai Range, North Island, New Zealand, approximately 32 km southwest of Tauranga and 75 km east of Hamilton (Figure 1.1). The Kaimai Range is part of a series of ranges that separate the Waikato Region in the west from the Bay of Plenty in the east, comprising the Coromandel Range to the north and the Mamaku Range to the south. To the west of the KRDC study area lie the Hauraki Plains and the Hauraki Rift, and to the east the Tauranga Basin and the Mamaku Ignimbrite sheet that buries the Omanawa Caldera, along with outcrops of Waitеariki Ignimbrite. Access to the complex is provided primarily by State Highway 29, which crosses the complex west to east, along with several DOC tracks through the Kaimai-Mamaku Conservation Park. The slopes of the KRDC are covered in dense native bush. This vegetation cover, combined with deep weathering and steep terrain, limits outcrop exposure across the complex, with most accessible outcrop located along conservation tracks, state highway cuttings, quarries, and farmland. A key feature of the KRDC is the surveillance radar installation operated by Airways New Zealand which sits atop Te Weraiti and is a prominent feature of the western Tauranga skyline.

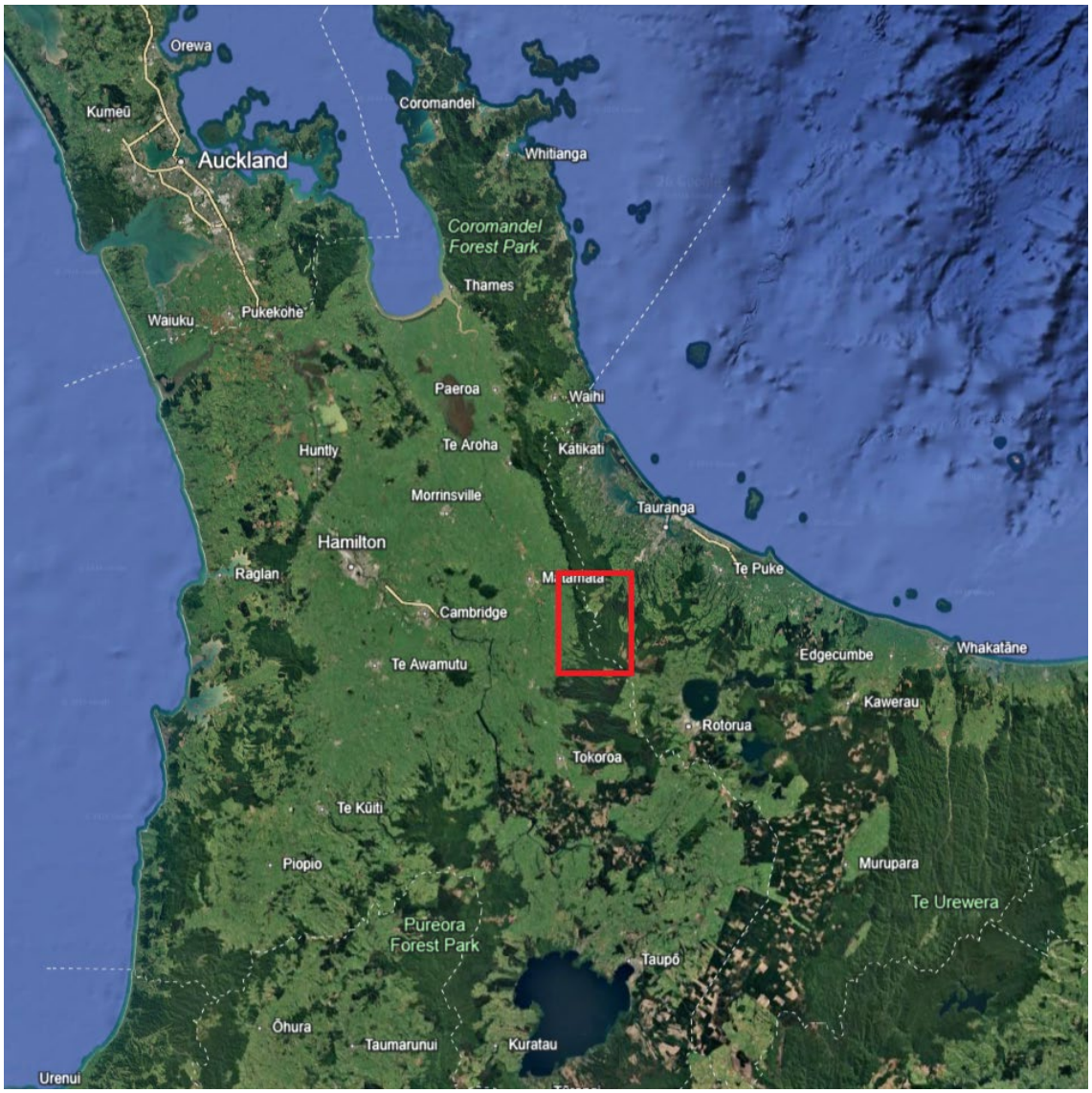

Figure 1.1: Satellite image of the central North Island showing the location of the Kaimai Rhyolite Dome Complex (red box). Key population centres of the North Island are also displayed, including Auckland, Hamilton, Tauranga, and Rotorua. Base image from Google Earth.

1.5 Thesis structure and chapter outline

Chapter 2 is a review of literature relevant to the regional geology of the study area, including the volcanological evolution of New Zealand, the tectonic setting of New Zealand, and the Coromandel Volcanic Zone (CVZ) and Taupō Volcanic Zone (TVZ). Discussion then narrows to the Tauranga Volcanic Centre, which straddles both, and the geological context within which the Kaimai Rhyolite Dome Complex is located.

Chapter 3 describes the geomorphology of the KRDC and its immediate surroundings, with emphasis on the identification of discrete dome centres, their

spatial distribution, structural controls on emplacement, and the morphometric characterisation of individual domes.

Chapter 4 presents the petrology, mineralogy, and geochemistry of the KRDC. This includes petrographic descriptions of the dome rocks based on optical microscopy, X-ray diffraction, and SEM-EDS analyses, as well as whole-rock major and trace element geochemistry determined by X-ray fluorescence spectroscopy and laser ablation inductively coupled plasma mass spectrometry.

Chapter 5 interprets the geomorphological, petrographic, and geochemical results to constrain the petrogenesis and emplacement history of the KRDC. The complex is then placed in regional context within the wider TgVC through comparison with the adjacent Waiteariki Ignimbrite and Mount Misery rhyolite series, and in global context through comparison with the Valles Caldera dome complex.

Chapter 6 synthesises the main findings of the study, presents conclusions, and outlines avenues for future work.

Chapter Two: Literature Review

2.1 New Zealand Geological Setting

New Zealand is located in the south-western Pacific Ocean and is characterised by diverse volcanic activity across the North Island and surrounding areas. New Zealand's volcanic landscape is shaped by a diverse tectonic setting, including subduction-related, intraplate, and oceanic crust volcanism (Mortimer & Scott, 2020). New Zealand's geological setting is primarily characterised by its position on the boundary between the Pacific and Australian plates, as part of the mostly submerged continent of Zealandia.

The primary activation of volcanism is attributed to plate collision processes within the last 25 million years, following a long period of rifting from Gondwanaland and subsequent thinning of the continental crust (Campbell et al., 2012). Subduction of the Pacific Plate beneath the North Island at the Hikurangi Trench drives modern volcanism, forming the North Island's modern volcanic configuration. The Taupō Volcanic Zone (TVZ) and Auckland Volcanic Field (AVF) have evolved over the past three million years, with intraplate volcanism progressively migrating northward along the western North Island — from the Okete lavas and Karioi, through the Ngatutura and South Auckland volcanic fields, to the modern AVF (Pittari et al., 2021).To the west of the TVZ is the Taranaki volcanic system, which represents an isolated arc volcano at the southern end of the modern arc. The Coromandel Zone (CVZ) is considered the precursor to the TVZ, with the transition occurring seamlessly 3 Ma (Prentice et al., 2025). It acts as a geological record of subduction-related volcanism of the Miocene-Pliocene, approximately between 18 Ma and 3.5 Ma (Julian 2016; Cole & Spinks, 2009; Adams et al., 1994). The CVZ also provides insights into arc volcanism and the transition from andesitic-dominated magmatism to rhyolitic volcanism. It potentially provides insights into how TVZ will progress into the future.

Zealandia's crustal structure exerts a strong control on volcanism. The extended continental crust has facilitated the development of both arc-related and, later, back-arc volcanic systems across the North Island. In the Taupō Volcanic Zone (TVZ), pronounced back-arc rifting of thinned continental crust has produced high magma fluxes through decompression melting and partial crustal melting, resulting in extensive silicic volcanism. In contrast, the configuration of the back-arc during the

Coromandel Volcanic Zone (CVZ) is less clearly defined. Volcanism in the CVZ largely developed in a subduction-arc setting, with only limited extensional deformation in its later stages. This late-stage extension, likely driven by slab rollback and gradual crustal thinning represents the early stages of back-arc development that ultimately evolved into the fully rifted Taupō Volcanic Zone.

2.1.1 Modern Volcanic Setting

New Zealand's modern volcanic setting consists of the TVZ and AVF, which are caused by subduction-related arc volcanism and intraplate basaltic fields, respectively (Pittari et al., 2021; Mortimer & Scott, 2020). The TVZ is the primary locus of Quaternary volcanism in New Zealand, featuring rhyolitic calderas, ignimbrite sheets, andesitic stratovolcanoes, and rhyolite/dacite lava domes (Shane 2017). Volcanism within the TVZ comprises three parts: the north (Whakatane Graben -Bay of Plenty), and the south (Tongariro Volcanic Centre), which are predominantly andesitic; and the central part, which is predominantly rhyolitic. This central area comprises nine caldera centres, the Omanawa caldera being the oldest at 2.1 Ma,. The AVF's modern volcanic configuration has been active since ~193 ka and comprises approximately 50 monogenetic volcanoes featuring a range of eruption styles from magmatic to phreatomagmatic (Cassidy et al., 1999; Hopkins et al., 2020). Eruptions typically begin with a phreatomagmatic phase, forming maar and tuff rings with tephra fall and base surges. These eruptions subsequently have magmatic phases, which form scoria cones and sometimes produce lava flows.

2.1.2 Taupō Volcanic Zone (TVZ)

The Taupō Volcanic Zone (TVZ) is located in the central North Island and is the most active rhyolitic volcanic system on Earth, characterised by frequent, voluminous silicic eruptions. It represents the continental crustal extension of the 2800 km-long Tonga–Kermadec arc, of which the TVZ forms the southernmost 300 km segment. This section accommodates the oblique subduction of the Pacific Plate's oceanic crust beneath the continental crust of the Australian Plate. Structurally, the TVZ is a back-arc basin comprising a complex system of calderas, rifts, and faults, with rhyolitic activity concentrated in the centre and andesitic volcanism occurring at its northern and southern margins (Cole & Spinks, 2009). Offshore, the system continues for approximately 150 km and features three parallel tectono-

morphological units: a frontal non-volcanic graben, a volcanic ridge, and a volcanic back-arc graben (Wright, 1992). The TVZ is commonly divided into three sections, with the central region containing nine major caldera centres dominated by rhyolitic volcanism. The southern section, known as the Tongariro Volcanic Centre, is characterised mainly by andesitic stratovolcanoes and associated lava flows (Cole, 1976), while the northern section encompasses the Whakatane Graben, dominated by andesitic volcanism associated with the active Whakaari/White Island volcano. The central TVZ exhibits the highest magma-output rates, likely due to enhanced crustal melting and magma flux driven by extension and decompression (Wilson et al. 1995; Barker et al. 2021).

Since approximately 3 Ma, the TVZ has remained volcanically active, and in the past 1 Ma it has erupted more than 104 km^3 of dominantly rhyolitic magma (Wilson et al., 1984). Most volcanism occurs within an area about 125 × 60 km and is expressed through a series of large, overlapping caldera systems, including the Rotorua, Okataina, Reporoa, Ohakuri, Whakamaru, Kapenga, Maroa, and Taupō calderas (Wilson et al., 1995; Cole et al., 2010; Pittari et al., 2021). All central TVZ calderas except Rotorua have experienced multiple episodes of collapse and resurgence associated with voluminous ignimbrite eruptions. These repeated collapse events reflect ongoing crustal subsidence in response to regional extension within the back-arc setting. The broader TVZ is undergoing progressive basement collapse, which facilitates magma ascent, fault propagation, and the formation of caldera structures. At its northern extent, the Omanawa Caldera within the Tauranga Volcanic Centre is now recognised as the earliest expression of the TVZ, marking the transition from subduction-dominated to rift-dominated silicic volcanism. The eruption of the Waiteariki Ignimbrite at approximately 2.1 Ma (Prentice et al., 2025) represents the first major caldera-forming event in the nascent TVZ and indicates that crustal thinning, fault development, and silicic magma generation were already underway by the early Pleistocene.

Magma genesis in the TVZ involves complex processes, including partial melting of the mantle wedge to produce basalts and andesites, and crustal melting for dacitic and rhyolitic compositions (Cole, 1981). The silicic magmas of the TVZ and adjacent Kermadec Arc exhibit both fractional crystallisation and crustal anatexis, wherein

portions of the crust melt and mix with ascending magmas (Saunders, 2009). Within the Taupō Volcanic Centre, rhyolitic magmas require assimilation of continental lithosphere (greywacke) and approximately 60–80 % fractional crystallisation (Saunders, 2009). Zircon-age spectra from the Taupō Volcanic Centre show a wide range of crystallisation ages; for example, post-26.5 ka eruptions display both young and inherited zircon populations, indicating remobilisation of older crystal mush and assimilation of surrounding crustal material (Charlier et al., 2004). These observations suggest that new magma batches frequently interacted with and rejuvenated older silicic reservoirs, incorporating antecrysts, phenocrysts, and occasional xenocrysts derived from Quaternary plutons or Mesozoic–Palaeozoic metasedimentary crust.

The tectonic evolution of the TVZ is closely linked to the oblique subduction of the Pacific Plate beneath the Australian Plate. This obliquity has generated significant crustal extension in the overriding plate, leading to lithospheric thinning and the development of a back-arc rift system. The Taupō Rift is a rapidly evolving continental intra-arc rift characterised by asymmetric narrowing, eastward migration, and southward propagation, influenced by subduction dynamics and magmatic processes (Villamor et al., 2017). The modern TVZ is extending at rates of 8–18 mm a^{-1}, promoting decompression melting in the mantle and facilitating magma ascent through the thinned crust (Wilson et al., 1995). This extensional regime accommodates a broad compositional spectrum of magmas, from basaltic-andesitic lavas at the margins to dacitic and voluminous rhyolitic eruptions in the central TVZ (Wilson et al., 2018). The development of back-arc basins plays a key role in controlling the storage and evolution of large silicic magma reservoirs, which can locally perturb stress fields and influence vent distribution (Bacon, 1985). The interplay between tectonic stretching, crustal assimilation, and magmatic differentiation therefore defines the volcano-tectonic character of the Taupō Volcanic Zone.

2.1.3 Coromandel Volcanic Zone (CVZ)

The Coromandel Volcanic Zone (CVZ) is an extinct volcanic arc located in the North Island of New Zealand, active from the late Miocene to early Pliocene, spanning approximately 18 to 4 Ma (Adams et al., 1994). It represents the earliest phase of

modern subduction-related volcanism along the current convergence margin. It is the onshore extension of the Colville Ridge and consists of the NE-SW trending belt of volcanic and intrusive rocks extending from Great Barrier Island in the north to the Kaimai Range in the south (Booden et al., 2012).

While the CVZ is the precursor to the TVZ, there is another volcanic arc that predates CVZ activity. The Northland arc was active from 25 Ma to 16 Ma, with many volcanic centres extinct by 19 Ma (Herzer, 1995). It consisted of twin belts of marine and subaerial andesitic volcanoes which trended north-west. It formed due to the subduction of the Pacific Plate beneath the Australian Plate, specifically involving the South Fiji Basin. Subduction occurred to initiate this arc in the late Oligocene and continued throughout the Early Miocene. The Three Kings Ridge arc was also active throughout this period, and it was an offshore arc to the northwest of Northland, New Zealand. The Three Kings Ridge arc and the Northland arcs were coeval until 20 Ma, with progressive southeast migration until the Northland arc died rapidly between 17 Ma in the northwest and 15 Ma in the southeast (Herzer et al., 2000). Today, many volcanoes have eroded or subsided, but remnants such as the Waitakere Ranges (andesitic, 22-16 Ma), the Waipoua Plateau (basaltic, 19-16 Ma), and features around Whangaroa Harbour and Whangarei Heads remain (Hayward, 1975, Hayward, 1993). These older offshore volcanic arc chains, along with the Colville Ridge, once formed the continuous NNE-trending proto-Kermadec (Vitiaz) Arc between the North Island of New Zealand and running past Tonga to northeast of Fiji (Pittari et al., 2021). The Northland arc extended southeast into the northern and western part of the CVZ, where andesitic volcanism continued. The extinction of the Northland arc is likely due to tectonic shifts and reorganisation of the subduction zone.

Volcanic succession from the Northland Arc through to the Taupō Volcanic Zone shows evolving arc volcanism in a dynamic plate tectonic setting that shows a trend over time from basalt and andesite-dominated shield and cone volcanism with very little silicic activity in the Northland Arc to andesite and rhyolite dominated volcanic activity in the CVZ to overwhelmingly silicic volcanism in the TVZ. The CVZ is the transitionary point where the volcanism shifts rapidly over time, and older parts of

the succession are well exposed, which allows for the opportunity to study the nascent development of the onshore development of this arc.

The early phase of the CVZ is characterised by the Coromandel Group Succession which between 18.0 ± 0.4 Ma and ~12 Ma, produced calc-alkaline basaltic andesite, andesite, and dacite (54.4–68.5 wt% SiO_2) in the northern Coromandel Peninsula, on Great Barrier Island, and within the northern Kiwitahi chain (Booden, 2012). Great Barrier Island is a key between the Northland Arc and the CVZ, which were coeval (Lindsay et al., 1999). The Great Barrier Island hosts rocks associated with both the Northland Arc and the CVZ and is comprised of calc-alkaline basaltic andesites to dacites, much like early CVZ products. Other notable formations from the early phase include the Port Charles andesites, which are dated to 19 Ma, located in the northern tip of the Coromandel Peninsula. These andesites, part of the Kuaotunu subgroup, consist of lava flows, autoclastic breccias, and minor pyroclastic deposits, including the construction of stratovolcanoes 10-15 km in diameter. Four subgroups are recognised in the Coromandel Peninsula and Great Barrier Island, with the most significant eruption aerial extent having a volume > 200 km^2. Coromandel Group volcanic rocks generally become progressively younger toward the south and east, consistent with the southward migration of arc volcanism in the CVZ during the Miocene to Pliocene (Skinner, 1986; Adams et al., 1994). Coromandel Group andesites are typically porphyritic, with 20–60% phenocrysts comprising plagioclase, orthopyroxene, clinopyroxene, and Fe–Ti oxides, set in a granular groundmass dominated by plagioclase laths and pyroxene microcrystals (Booden, 2012).

Localised mafic volcanism occurred across the northern Coromandel Peninsula and adjacent islands. This predominantly occurred in the Mercury Basalts (50.8–56.1 wt% SiO_2), which erupted between ~12 and 2.7 Ma in the Mercury Islands, eastern Great Barrier Island, and parts of the Coromandel Peninsula. These small-volume eruptions were typically Strombolian or Hawaiian in style, and the basalts are preserved as lava flows, spatter cones, and dikes intruding older rhyolites (Skinner, 1986; Adams et al., 1994; Briggs et al., 2005).

Silicic volcanism in the Coromandel Volcanic Zone (CVZ) began between 12.0 and 11.5 Ma on Great Barrier Island, approximately four million years after the onset of

intermediate to mafic volcanism (~16 Ma; Vincent, 2012).This marks the beginning of a shift to bimodal volcanism, with basalt–basaltic andesite and rhyolite erupted contemporaneously from ~12 to 7 Ma (Nicholson et al., 2004). Widespread rhyolitic volcanism is likely driven by extensional tectonics linked to the development of the Hauraki Rift. This rifting thinned the crust and facilitated decompression melting of the mantle, producing mafic magmas whose heat contributed to crustal melting and generation of silica-rich rhyolite. This period reflects a tectonic shift from mild compression or weak extension within the overriding Australian Plate to a strongly extensional setting, facilitating crustal thinning and enhanced magmatic activity. Rhyolitic volcanism intensified from 10 Ma to 8 Ma, culminating in significant caldera-forming eruptions such as the Carina Rock Ignimbrite, erupted from the early outer ring fault system of the Kapowai Caldera, and the Whitianga Caldera. Between 9 Ma and 7 Ma, bimodal basalt/basaltic andesite–rhyolite associations became prominent, coinciding with significant ignimbrite eruptions, caldera collapse, and postcaldera andesite volcanism (Adams et al., 1994). Another phase of bimodal eruptions occurred between ~6 and 5.5 Ma, followed by dominantly basaltic volcanism from 4.7 to 4.2 Ma. Volcanism also spread to the southern Colville Ridge around 5.5 Ma. Spatially, the locus of volcanism migrated irregularly eastward (~3 mm/yr) and southward (~8 mm/yr), resulting in progressively younger volcanic units to the south (Booden, 2012). The Waihi Caldera represents the youngest rhyolite-dominated volcanic centre associated with the southern extent of the Coromandel Volcanic Zone. Located northwest of Tauranga, it formed between approximately 3.9 and 3.5 Ma, marking one of the final phases of silicic volcanism within the CVZ (Briggs et al., 2005; Vincent, 2012; Pittari et al., 2021). U–Pb zircon geochronology constrains eruption ages of the Owharoa and Waikino ignimbrites, which are interpreted to record caldera-forming and post-caldera activity, at 3.76 ± 0.06 Ma and 3.48 ± 0.10 Ma, respectively (Vincent, 2012; Julian, 2016). These ages refine the eruptive chronology of the Waihi Caldera and highlight its role as the terminal expression of silicic volcanism in the Coromandel arc.

The tectonic and magmatic evolution from the extinct Colville Ridge arc to the presently active Kermadec Arc is closely tied to the progressive southward migration of volcanism within the CVZ (Wright, 1997). Following the cessation of the Northland Arc, volcanism persisted along the Colville Ridge between ~16.7 and 5.5

Ma, overlapping with the early basaltic to andesitic phases of CVZ development. Around 5.5 Ma, back-arc extension and slab rollback initiated the rifting of the Colville Ridge, leading to the formation of the Havre Trough — a key extensional back-arc basin — and the birth of the Kermadec Arc to the northeast. This tectonic reorganisation coincided with a marked southward shift in volcanic activity within the CVZ, as rhyolitic centres and calderas began forming progressively closer to the Tauranga region.

2.1.4 Alexandra Volcanic Group (including Okete volcanic field)

The Okete Volcanic Field represents one of the earliest phases of intraplate basaltic volcanism in the western North Island, active between approximately 2.7 and 2.3 Ma (Briggs et al., 2005; McLeod et al., 2022). The field comprises alkali basalt to hawaiite composition, lava flows, scoria cones, and monogenetic eruptive centres that formed along the Raglan-Aotea-Kawhia coastline. These lavas exhibit ocean-island basalt (OIB) like geochemical signatures, enriched in incompatible trace elements and isotopically distinct from the arc-related basalts/andesites/rhyolites of earlier Coromandel Volcanic Zone and the later Tauranga Volcanic Centre. Their intraplate character reflects the onset of back-arc extension and lithospheric thinning as subduction rollback progressed beneath the central North Island (McLeod et al., 2022).

A key feature of western North Island volcanism during this period is the coexistence of OIB like alkali basalts and subduction influenced andesites at the same volcanic centres. Recent structural and geochemical work shows that this duality results from a tear forming in the Pacific Plate, which allowed OIB like asthenosphere to upwell through the gap while adjacent regions continued to receive slab derived magmas (McLeod, 2020; McLeod et al., 2022). Consequently, centres such as Pirongia, Kakepuku, Karioi, and Te Kawa erupted both alkali basalts-hawaiite and hydrous andesite, often within overlapping time intervals. This combination provides strong evidence for a spatially complex mantle regime where mantle flow around propagating slab tear interacted with variable metasomatized mantle wedge components, The Okete Volcanic Field represents the earliest manifestation of this mixed intraplate-subduction mantle environment.

The Alexandra Volcanic Group (AVG), active between 2.74 and 1.60 Ma, records phases of basaltic to andesitic volcanism across the Waikato and King Country regions (Briggs, 1986; Briggs et al., 2005; McLeod, 2020). The AVG includes eroded volcanic centres such as Mt Pirongia, Kakepuku, Karioi, and Te Kawa, which were emplaced along NNE-SSW and NW-SE extensional faults marking the early development of the Taupō Rift (Pittari et al., 2021). These structural controls produced elongated volcanic alignments and complex, multi-vent edifices influenced by shifting magma supply and fault linked vent migration.

The AVG composition ranges from olivine basalt and basaltic andesite to hornblende andesite and dacite, indicating fractional crystallisation, magma mixing, and minor crustal assimilation within a subduction modified system (Briggs, 1986; McLeod, 2020). This contrasts with the uniform Okete Volcanic Field and reflects shallow crustal magma storage zones.

Importantly to this study, the AVG was contemporaneous with the earliest rhyolitic eruptions of the TgVC, both systems active between 2.7 and 2.2 Ma (Pittari et al., 2021; Prentice et al., 2022; McLeod et al., 2022). The AVG represents the mafic-intermediate counterpart to the TgVC within the same evolving back-arc environment. This contemporaneity demonstrates that slab rollback, lithospheric extension, and mantle upwelling simultaneously generated both basaltic-andesite and silicic magmas across the region, but at different depths and with differing degrees of crustal assimilation.

While intraplate volcanism persists in the northern North Island through the Auckland Volcanic Field (AVF), it is no longer directly coupled to the active back-arc magmatic environment that characterised the Okete and Alexandra volcanic episodes. The AVF is instead an intraplate monogenetic field generated within far-field extensional stresses related to the modern Taupō Rift, rather than the strongly evolving slab-rollback and slab-tear regime that influenced western North Island volcanism between 2.7 and 1.6 Ma.

2.2 Tauranga Volcanic Centre (TgVC)

The Tauranga Volcanic Centre (TgVC), located in the Western Bay of Plenty, represents a crucial transitional stage in the evolution of silicic volcanism between

the CVZ and TVZ. Volcanic deposits within the TgVC overlap spatially with the late silicic CVZ and are coeval with the early TVZ, and thus the TgVC represents the shift in volcano-tectonic setting of the arc (Briggs et al., 2005). The TgVC was active from 2.95 to 1.9 Ma and has been previously grouped into two volcanic centres, the Kaimai and Tauranga centres (Briggs et al., 2005).

The Kaimai centre, located at the southern tip of the greater Kaimai Range, includes the large voluminous rhyolite domes of Kaimai (2.86 ± 0.08 Ma), Kakahu (2.87 ±0.02 Ma) and the Waiteariki Ignimbrite (2.09 ± 0.03 Ma) (Briggs et al., 2005). The two rhyolite domes and Kaimai centre in general are poorly defined due to poor exposures, burial by younger ignimbrites, the voluminous Waiteariki Ignimbrite and Hauraki rift/fault uplift (Briggs et al., 2005). The definition of individual domes within the region is based primarily on limited evidence, consisting largely of $^{40}Ar/^{39}Ar$ age determinations and the spatial separation of topographic highs. The Kaimai and Kakahu domes, in particular, may represent parts of a single, continuous rhyolitic deposit rather than discrete volcanic centres. Additional peaks, such as Te Weraiti and Hiwiroa, could similarly expose portions of a complex of rhyolitic domes.

The remaining silicic lava domes, dated between 2.69 and 1.95 Ma, along with the ignimbrites of the Pāpāmoa Formation (2.4–1.9 Ma), were initially grouped within the Tauranga Volcanic Centre. Briggs et al. (2005) proposed a model that distinguished two separate volcanic centres; however, more recent work by Pittari et al. (2021) has revised this interpretation. A single Tauranga Volcanic Centre (TgVC) is now recognised, encompassing the successions of both former centres and all associated volcanic deposits across the greater Tauranga region, spanning from 2.95 to 1.9 Ma.

The TgVC preserves a diverse volcanic succession spanning a range of compositions and eruptive styles. It includes a series of dacite-rhyolitic lava domes and dome complexes (Minden Rhyolite Subgroup), an eroded andesitic stratovolcano (Otawa Formation), an isolated basaltic unit (Matakana Basalt), and two major pyroclastic sequences: the Waiteariki Ignimbrite (a Formation) and the Papamoa Formation.

2.2.1 Minden Rhyolite Subgroup

The Minden Rhyolite Subgroup comprises crystal-rich orthopyroxene-, hornblende-, and biotite-bearing rhyolite domes and dome complexes across the Tauranga Volcanic Centre (TgVC) and Bay of Plenty, north of the Taupō Volcanic Zone (Houghton & Cuthbertson, 1989; Leonard et al., 2010). Approximately 16 individual domes are recognised, including prominent landforms such as Mount Maunganui (252 m a.s.l.), Mount Minden (286 m a.s.l.), and Maungatūtū/Mt Misery (478 m a.s.l.) (Hollis, 1995).

These lavas are typically crystal-rich (up to 40% phenocrysts), except at Mt Maunganui and Bowentown, and have consistent mineral assemblages of plagioclase ± quartz ± orthopyroxene ± hornblende ± biotite (Hughes, 1993, Whitbread-Edwards, 1994; Hollis, 1995; Cook, 2016; Kinley, 2022). All are pervasively devitrified and commonly display spherulitic textures superimposed on flow structures (Hughes, 1993).

Briggs et al. (2005) subdivided the domes into four geochemical groups: (i) crystal-rich, hornblende-bearing Minden Peak domes; (ii) highly evolved, crystal-poor Mt Maunganui domes; (iii) less evolved Mangatawa domes with lower SiO_2; and (iv) Mount Misery domes, distinguished by high Zr contents (>200 ppm). Bowentown Rhyolite shares affinities with both Minden Peak and Mt Maunganui domes but is spatially isolated; its inclusion within the TgVC remains tentative (Pittari et al., 2021).

The Minden domes align along a NNE trend, inferred to reflect northeast-trending basement faults (Healy et al., 1964; Briggs et al., 1996), although no active structures have been confirmed. Overall, the spatial and geochemical clustering suggests that the domes represent genetically related silicic magmas, although no detailed geochemical studies of the TgVC have been conducted yet (Briggs et al., 2005).

2.2.2 Otawa Formation

The Otawa Formation consists of an eroded andesitic stratovolcano and associated andesitic to dacitic lava flows and volcanic breccias, which originally spanned approximately 35 km^2 on the eastern side of the TgVC. Today, these rocks form the

backbone of the Pāpāmoa Range and are overlain by a series of NNE-trending dacite to rhyolite lava domes belonging to the Minden Rhyolite Subgroup.

Volcanic rocks of the Otawa Formation are typically blue-grey, fine- to medium-grained, and display a porphyritic texture (Briggs et al., 1996). Plagioclase is the dominant phenocryst phase, with lesser orthopyroxene, Fe-Ti oxides, and occasional hornblende, clinopyroxene, and quartz, set within an intergranular to hyalopilitic groundmass. Accessory minerals include chlorite, apatite, zircon, and iron oxides and sulphides. Radiometric dating of andesite samples indicates volcanic activity occurred between 2.95 and 2.54 million years ago, representing the earliest recognised phase of volcanism within the TgVC (Stipp and McDougall, 1968).

Table 2.1: Volcanic stratigraphy and summary of published geochronological data for the Tauranga Volcanic Centre (TgVC)

Geological Map Unit[1]	Eruption Deposit(s)	K-Ar age[2] (Ma)	$^{40}Ar/^{39}Ar$ age[6] (Ma)	U-Pb zircon age[7] (Ma)	(U-Th)/He zircon age[7] (Ma)
Waiteariki Fm	Waiteariki Ignimbrite	2.18 ± 0.15 w 2.13 ± 0.17 p	2.09 ± 0.03*	-	2.25 ± 0.26
Papamoa Fm	Papamoa ignimbrites	-	2.40 ± 0.02 L 1.90 ± 0.10 U	2.21 ± 0.13	-
Minden Rhyolite Subgroup	Bowentown Dome	2.51 ± 0.25 (wr) 2.77 ± 0.31 (p) 2.89 ± 0.07[3]	-	2.83 ± 0.16 2.09 ± 0.39[8]	2.55 ± 0.59
	Minden Peak Dome	1.52 ± 0.23 (wr)	2.16 ± 0.03	2.135 ± 0.066*	2.04 ± 0.18
	Kaikaikaroro Dome	-	2.39 ± 0.06	-	-
	Maunganui Dome	-	2.35 ± 0.06	-	-
	Mangatawa Dome	2.36 ± 0.08 (wr) 2.28 ± 0.15 (p)	2.39 ± 0.13	2.31 ± 0.18*	2.45 ± 0.31
	Upuhue Dome	-	2.69 ± 0.04	2.530 ± 0.089*	2.84 ± 0.17
	Papamoa Dome	-	2.50 ± 0.03	2.25 ± 0.16*	2.88 ± 0.20
	Kopukairua Dome	-	2.20	2.53 ± 0.14*	2.69 ± 0.13
	Waitao Dome	-	-	2.64 ± 0.15	2.71 ± 0.14
	Waikite Dome	-	-	2.25 ± 0.10	2.37 ± 0.12
	Otanewainuku Dome	-	1.95 ± 0.02	-	-
	Puwhenua Dome	-	2.14 ± 0.04	-	-
	Mount Misery Dome	-	2.69 ± 0.03	-	-
	Kaimai Dome	-	2.86 ± 0.08	2.236 ± 0.038*	2.20 ± 0.49
	Kakahu Dome	-	2.87 ± 0.02	-	-
Matakana Fm	Basalt lava	2.7 ± 0.1[4]	-	-	-
Otawa Fm	Andesitic volcano	2.95 ± 0.30[5] 2.54 ± 0.05[5]	-	-	-

[1]Stratigraphic nomenclature follows Leonard et al. (2010) and Briggs et al. (1996); [2] K–Ar ages: wr = whole rock, p = plagioclase (Briggs et al., 2005); [3] Data from Pittari et al. (2021) and Prentice et al. (2022) weighted averages (95 % CI); [4] $^{40}Ar/^{39}Ar$ data from Cook (2016); italicised values = plateau ages (± 1σ); [5] (U–Th)/He zircon ages from Pittari et al. (2021).

2.2.3 Matakana Basalt

The Matakana Basalt is a dark grey, porphyritic basalt (52.3 wt.% SiO_2) exposed as a small island 30 metres offshore from Matakana Island. First noted by Henderson and Bartrum (1913) and later formally named by Hollis (1995), it contains abundant plagioclase phenocrysts (up to 5 mm), along with altered olivine (iddingsite), orthopyroxene, and Fe-Ti oxides, set within an intergranular groundmass. The basalt is hard, competent, and exhibits irregular jointing with early-stage spheroidal weathering. It represents the only known basaltic eruption within the Tauranga Volcanic Centre (TgVC).

Stratigraphic relationships are uncertain, but the basalt appears older than the Te Puna Ignimbrite and younger than the Minden Rhyolite, with a K-Ar age of 2.7 ± 0.1 Ma (Hollis, 1995). Paleomagnetic measurements show a normal polarity. A nearby gravity anomaly (-15 mGal) suggests a possible buried extension or underlying basement rocks (Stagpoole et al., 2020). Despite its small exposure, the Matakana Basalt provides essential insight into early, less silicic phases of volcanism within the TgVC.

2.2.4 Papamoa Formation

The Papamoa Formation is made up of a sequence of northward-dipping rhyolitic to dacitic ignimbrites interbedded with fall deposits, located along the eastern side of the TgVC (Briggs et al., 1996; Leonard et al., 2010). Five distinct ignimbrite units: the Welcome Bay Ignimbrite (previously Lower Pāpāmoa Ignimbrite), the Wharo Ignimbrite (previously Upper Pāpāmoa Ignimbrite), as well as the newly recognised Arateka Ignimbrite, Otawera Ignimbrite, and Unit A — an as yet unnamed ignimbrite (Namaliu, 2021, Prentice et al., 2022).

Petrographic and geochemical analyses show variations between the ignimbrites, with pumice clasts ranging from dacitic to andesitic compositions, suggesting magma mixing during eruption.

$^{40}Ar/^{39}Ar$ dating places the formation between 2.4 and 1.9 Ma (Briggs et al., 2005), while U–Pb zircon geochronology yields an age of 2.21 ± 0.13 Ma for the Otawera Ignimbrite (Pittari et al., 2021). Additional U–Pb zircon ages from Prentice et al.

(2022) further constrain early Tauranga Volcanic Centre activity, with the Welcome Bay, Wharo, and Arateka ignimbrites dated at 2.31 ± 0.046 Ma, 2.26 ± 0.046 Ma, and 2.25 ± 0.044 Ma, respectively. Although the vent location remains uncertain, the deposits' geochemistry and distribution suggest a local source within the eastern Tauranga Volcanic Centre.

2.2.5 Waitearikí Ignimbrite

The Waitearikí Ignimbrite, dated between 2.18 ± 0.031 Ma and 2.09 ± 0.029 Ma (Prentice et al., 2022), represents the ~2.1 Ma supereruption of approximately 870 ± 270 km^3 dense rock equivalent (DRE) of crystal-rich (~37%) rhyodacite magma from the newly defined Omanawa Caldera within the Tauranga Volcanic Centre (Prentice et al., 2025). The Omanawa Caldera has been identified through ignimbrite thickness variations, distinctive textural features, the presence of numerous silicic lava domes, and a pronounced negative gravity anomaly. This anomaly lies at the southern end of an asymmetrically rifted graben beneath the northern Mamaku Plateau. Although the caldera lacks obvious topographic expression, it is inferred to be buried beneath younger ignimbrites of the Taupō Volcanic Zone.

The Waitearikí Ignimbrite is primarily exposed in the Kaimai Range and across the Whakamarama Plateau, forming the gently sloping upper surface of the latter, which dips eastward beneath younger sediments of the Tauranga Basin. Key exposures occur in stream sections of the southern Kaimai Range and around McLaren Falls near Tauranga, where the ignimbrite reaches thicknesses of up to 150 m.

The deposit is a beige to grey, crystal-rich lapilli tuff, with an average crystal content of approximately 40 % and lithic fragments comprising less than 2 %. It is strongly welded and divided into at least two cooling units. The basal sequence consists of pumiceous lapilli tuffs and ash that grade upward into a densely welded middle zone characterised by lenticular structures and a eutaxitic texture, indicating high emplacement temperatures and syn-depositional deformation. The base is incipiently welded, ranging from pyroclastic breccia to fine tuff, and commonly shows moderate devitrification. The original unwelded top is typically eroded, leaving primarily welded sections preserved.

Petrographically, the Waiteariki Ignimbrite contains plagioclase, hornblende, orthopyroxene, and quartz as the dominant phases, with subordinate biotite and clinopyroxene. Pumice clasts are common in basal zones and display fiamme textures in welded sections, reflecting deformation under high-temperature emplacement conditions.

2.3 Kaimai Rhyolite Dome Complex

The Kaimai Rhyolite Dome Complex, part of the Minden Rhyolite Subgroup, comprises a series of coalesced, crystal-rich rhyodacitic to rhyolite domes forming the southernmost portion of the Kaimai Range. The Kaimai Range itself is an upfaulted block bounded to the west by the eroded scarp of the Hauraki Fault (Houghton & Cuthbertson, 1989). The complex includes the Kaimai, Kakahu, Te Weraiti, and Hiwiroa domes. Te Weraiti forms the northernmost dome of the complex, with the Kaimai Dome located immediately to the south and Kakahu Dome occupying the southernmost position within the range. Hiwiroa lies to the east of Kakahu and is separated from the main complex by the Atiamuri and Orakonui formations. The remainder of the dome complex forms a coalesced dome field, representing a laterally continuous expanse of rhyolitic lava. These domes record some of the earliest silicic volcanic activity associated with the Tauranga Volcanic Centre (TgVC), with $^{40}Ar/^{39}Ar$ ages on feldspar separates of 2.86 ± 0.08 Ma for the Kaimai Dome and 2.87 ± 0.02 Ma for the Kakahu Dome (Briggs et al., 2005). In contrast, U–Pb zircon and U–Th zircon ages for the Kaimai Dome are slightly younger at 2.236 ± 0.038 Ma (Pittari et al., 2021). Despite their significance, no detailed geochemical or petrographic analyses of these domes have yet been published, leaving substantial gaps in understanding their magmatic evolution, eruption styles, and relationship to broader tectonic and volcanic processes in the region.

Spatially, the Kaimai Rhyolite Dome Complex lies immediately west of the Omanawa Caldera, placing it along the inferred western structural boundary of the early caldera system. This proximity suggests that the emplacement of the domes may have been influenced by extensional faulting and magma ascent associated with the Omanawa Caldera's development and collapse (Prentice et al., 2025). The alignment of the domes along the southern Kaimai Range also coincides with the western margin of the Taupō Rift, indicating that the KRDC may represent an early phase of

fault-controlled silicic volcanism related to the initial propagation of Taupō Volcanic Zone rifting. Field mapping indicates that dome emplacement aligns subparallel to the western caldera boundary faults of Omanawa, suggesting syn-tectonic extrusion along the early Taupō Rift margin (Leonard et al., 2010).

Detailed petrographic and geochemical investigation of these domes, undertaken in this study, provides new constraints on magma evolution, crystallisation textures, and emplacement dynamics within the early Taupō Volcanic Zone.

2.4 Lava Domes

2.4.1 Definition and General Features

Lava domes are steep-sided, mound-like accumulations of viscous lava that form when degassed, silicic magma extrudes slowly onto the surface and piles up near the vent rather than flowing laterally, as occurs in low-viscosity basaltic eruptions such as those forming shield volcanoes. They are typically composed of rhyolitic to dacitic magma, with silica contents exceeding ~63 wt.% SiO_2 (Fink & Griffiths, 1998; Swanson et al., 1987). The high viscosity of silicic magmas reflects extensive polymerisation of SiO_4 tetrahedra within the melt, which forms a rigid network that restricts ion mobility and prevents fluid flow, causing lava to accumulate over the vent rather than spread laterally (Blake, 1990). This contrasts strongly with the extensive, low angle lava fields typical of basaltic volcanism.

Morphologically, lava domes exhibit a range of forms from small, “plug” like mounds to large, composite edifices several kilometres wide and hundreds of metres high (Fink, 1990). Dome morphology is primarily controlled by the effusion rate, magma viscosity, volatile content, and eruption duration (Fink & Anderson, 2000). High effusion rates or repeated extrusion events can generate coalesced dome complexes or rhyolitic lava fields, where individual domes overlap and merge, forming laterally continuous silicic terrain, such as observed within the Kaimai Rhyolite Dome Complex.

Internally, lava domes typically consist of a dense, crystalline core surrounded by a brecciated carapace and a talus apron formed by gravitational collapse (Calder et al., 2015). The upper portions often display pervasive flow banding resulting from shear

during extrusion, while the outer surfaces are marked by obsidian or devitrified glassy textures reflecting rapid cooling. Cooling-induced fracturing and brittle deformation along dome margins commonly lead to autobrecciation and block-and-ash flow deposits, particularly during partial dome collapse events (Swanson et al., 1987; Fink, 1990).

Lava domes are also key indicators of shallow magmatic processes, as their emplacement conditions preserve evidence of magma rheology, crystallisation, degassing, and post-emplacement cooling (Cashman & Blundy, 2013; Sparks et al., 2000). The occurrence of microtextures such as spherulites, microlite alignment, and crystallisation fronts within rhyolitic domes display undercooling and the kinetics of melt devitrification, making domes critical natural laboratories for studying magma ascent and solidification in silicic systems (Castro et al., 2008; Stevenson et al., 1993).

2.4.2 Formation Processes

Lava domes form through the slow extrusion of highly viscous magma, typically of dacitic to rhyolitic composition, from shallow magma chambers into volcanic conduits. As magma ascends, a combination of volatile exsolution, decompression, and crystallisation increases its viscosity, reducing the ability of the lava to flow laterally (Fink & Griffiths, 1998). The resulting effusion of degassed, crystal-rich lava accumulates near the vent. The degassing process also drives cyclic extrusion behaviour, with alternating phases of dome inflation and a pausing of extrusion which reflect fluctuations in conduit pressure and magma supply (Voight et al., 1999; Calder et al., 2015).

The effusion rate and magma viscosity are the principal controls on dome morphology and growth style (Fink & Anderson, 2000). At low effusion rates, new magma is injected into the dome's interior, inflating it from within, a process called endogenous growth. This produces massive, steep-sided domes with dense, crystalline interiors and limited surface lobes. At higher effusion rates, extrusion occurs externally at or above the dome surface, resulting in exogenous growth. Exogenous growth occurs when new lava overflows or breaches the outer crust, forming lobate flows or coulees that can extend several kilometres from the vent (Fink, 1990).

As extrusion continues, the outer surfaces of the dome cool and solidify to form a brittle carapace, which frequently fractures with continued internal effusion of magma. This process leads to autobrecciation and the development of a surrounding talus apron formed by gravitational collapse of unstable outer material. The accumulation of these breccias around the dome flanks reflects ongoing instability and marks the transition between the hot, ductile interior and the cooling, solidifying exterior (Calder et al., 2015).

If oversteepening, rapid degassing, or conduit pressurisation occurs, portions of the dome may collapse, generating block-and-ash flows or pyroclastic density currents (PDCs). Such events have been observed at Soufrière Hills and Chaitén, and similarly at Mount St. Helens, where large-scale gravitational failure of an overpressured dome triggered a lateral blast and PDCs that extended tens of kilometres from the vent (Lipman & Mullineaux, 1981). These collapses are often followed by renewed extrusion, producing alternating sequences of effusive and pyroclastic deposits.

2.4.3 Internal Structure and Evolution

Lava domes display a distinct internal architecture that reflects the mechanical and thermal evolution of highly viscous magma during and after emplacement. Typically, domes comprise three main zones: a dense crystalline core, a brecciated carapace, and a surrounding talus apron (Fink, 1990; Calder et al., 2015). These zones develop as magma cools and transitions from ductile flow within the interior to brittle deformation close to and at the surface.

The core represents the slowly cooled interior, where magma remains hot and viscous for extended periods. Continued internal flow under confinement produces shear-related flow banding, alignment of microlites, and late-stage crystallisation textures such as spherulites. This dense, crystalline material is highly resistant to weathering and is often all that remains in deeply eroded or uplifted domes, such as those within the Kaimai Rhyolite Dome Complex (KRDC).

Surrounding the core is the carapace, a brittle outer shell formed as the dome surface cools and solidifies during ongoing extrusion. The still-ductile interior continues to deform which exerts pressure on the carapace and causing it to fracture and collapse, generating autobreccia composed of angular fragments of obsidian,

pumice, and devitrified rhyolite. These fragments can become welded or cemented by subsequent lava emplacement. The carapace therefore represents the mechanical boundary between the core and the external environment, where deformation transitions from plastic flow to failure

The talus apron develops as carapace instability triggers gravitational collapse along the dome flanks, producing deposits of coarse, angular debris. This material can later be remobilised during renewed extrusion or partial dome collapse. Through time, repeated cycles of collapse and reworking can produce thick breccia accumulations that encircle the dome and record variations in extrusion rate, cooling, and gravitational instability.

Over geological timescales, erosion preferentially removes the weaker dome structures such as the carapace and talus materials, leaving the competent, flow-banded interiors exposed at the surface. Given the time elapsed since emplacement, the rhyolites of the KRDC likely represent the preserved dense interiors of once larger domes, with their outer layers long removed by erosion and denudation.

2.4.4 Flow Banding and Spherulite Development

Flow banding and spherulitic textures are key features of silicic lava domes and provide key insights into the deformation, cooling, and crystallisation history of rhyolitic magma. Flow banding forms during dome emplacement when highly viscous magma undergoes ductile shear either within the conduit or inside the slowly moving dome interior core. Layers of slightly different crystal contents, volatile concentrations or degrees of devitrification deform differentially, producing alternating light and dark bands. These bands may appear as planar, folded, or contorted laminations that record variations in strain rate and magma rheology during extrusion (Fink, 1990).

In the core of a dome, flow banding commonly reflects continuous laminar flow under high temperatures and slow cooling conditions. Near the margins, where transition between the ductile core and brittle carapace, flow bands may become highly folded or disrupted, merging into zones of autobreccia. In exhumed or eroded domes such as those of the KRDC, well developed flow banded rhyolite exposed at

the surface likely represents the preserved interiors of domes where the outer carapace has been removed by erosion.

Spherulites form during the late stages of dome cooling as glassy or partially crystalline lava devitrifies. They grow when silica rich melt becomes supersaturated and begins to crystallise, producing radial aggregates of quartz and feldspar that nucleate from discrete centres. Their size and abundance depend on cooling rate, undercooling, and volatile content: slow cooling in the dome interior favours large, well developed spherulites, whereas rapid quenching at the margins suppresses their growth. In many rhyolite domes, spherulites develop along flow bands or vesicle trails, marking former volatile pathways through the lava.

Experimental studies on silicate crystallisation demonstrate that crystal shape changes systematically with the degree of supercooling and the relative rates of crystal growth and atomic diffusion in the melt (Lofgren, 1971). At low levels of undercooling, atoms in the melt can move and attach to crystal surfaces fast enough to maintain smooth, well-formed faces, producing tabular or skeletal crystals that grow under near-equilibrium conditions. As the melt becomes more undercooled, crystals begin to grow faster than atoms can diffuse through the liquid to supply them evenly, causing unstable, fibrous growth. Under these conditions, crystals develop into dendritic and eventually spherulitic forms consisting of fine radiating fibres that grow outward from a nucleus. The exact shape of these aggregates, whether spherical, fan shaped, or elongated along flow bands, reflects the local cooling rate, deformation, and availability of volatiles within the lava.

Chapter Three: Geology and Geomorphology

3.1 Introduction

The morphology of the Kaimai Rhyolite Dome Complex provides important insights into its eruptive history, emplacement processes, and the tectonic controls that influenced its development. Rhyolitic lava is typically highly viscous and largely degassed at the time of emplacement, reducing ability to flow long distances. As a result, rhyolitic eruptions commonly produce steep-sided lava domes that grow predominantly through vertical accumulation rather than extensive lateral flow.

The resulting dome morphology therefore preserves key information about eruptive behaviour. Steep, blocky domes are generally indicative of viscous, effusive emplacement, whereas lobate dome margins suggest multiple phases of emplacement or incremental dome growth (Fink & Anderson, 2000; Calder et al., 2015). Clusters of domes may reflect migration of eruptive vents over time, while isolated dome remnants can represent erosional remnants of once larger volcanic edifices (Nasholds & Zimmerer, 2022). Consequently, geomorphological analysis of the Kaimai Rhyolite Dome Complex allows analysis on eruption style, vent distribution, and the long-term volcanic evolution of the complex.

Age constraints for the KRDC are provided by $^{40}Ar/^{39}Ar$ dating of the Kaimai and Kakahu domes at approximately 2.86–2.87 Ma (Briggs et al., 2005), subsequently refined for Kaimai by U-Pb zircon geochronology to 2.135 ± 0.066 Ma (Pittari et al., 2021). On either estimate, the KRDC has experienced significant erosion since emplacement. As a result, the original volcanic stratigraphy is likely incomplete, with contacts obscured or removed and lava flow margins partially or entirely eroded. In such settings, geomorphology becomes a primary tool for reconstructing the original volcanic architecture, including dome size, spatial distribution, and the location of eruptive centres.

In addition to erosion, parts of the complex have been modified by younger volcanic activity associated with the Taupō Volcanic Zone. Large ignimbrite sheets have partially buried portions of the complex, particularly along the eastern margin of the KRDC, obscuring original dome boundaries and further complicating stratigraphic

interpretations. Structural controls also influence the present-day morphology of the complex. Uplift along major faults bounding the Kaimai Range has modified topographic relief and may have altered the original orientation of dome structures, affecting interpretations of dome geometry and preservation. Together, erosion, burial by younger volcanic deposits, and tectonic uplift have significantly modified the original morphology of the KRDC, reinforcing the importance of geomorphological analysis in reconstructing its volcanic evolution.

3.2 Methods

The geomorphology of the Kaimai Rhyolite Dome Complex (KRDC) was examined using a combination of field observations, digital elevation model (DEM) analysis, and GIS-based morphometric calculations. Field observations were conducted across the Kaimai Main Dome and Te Weraiti (Figure 3.3) to identify lithological boundaries, ridge morphology, and erosional features that assisted in defining dome boundaries. Due to dense vegetation cover, limited exposure, and rugged terrain across the Kaimai Range, field observations were supplemented with remote sensing and digital terrain analysis. The highly eroded nature of the KRDC, combined with extensive soil development and dense forest cover, means that individual eruptive centres are not always readily distinguishable from direct field observation alone, necessitating the use of high-resolution topographic datasets to identify subtle geomorphological features.

Regional geological context and surrounding terrain units were interpreted using the Rotorua geological map (QMAP series) produced by GNS Science at a scale of 1:250,000. This dataset was used to identify surrounding lithological units, structural features, and areas where direct sampling was not possible. The QMAP data were also used to assist in identifying contacts between rhyolitic dome units and surrounding ignimbrites, sedimentary deposits, and volcanic formations.

Although the overall extent of the KRDC identified in this study is broadly consistent with the QMAP mapping, several boundaries between rhyolitic units and surrounding lithologies were modified based on geomorphological observations derived from DEM analysis, hillshade imagery, slope maps, and field observations.

In particular, dome margins and contacts interpreted from high-resolution topographic data differed locally from those shown in the QMAP dataset. These differences likely reflect the relatively coarse scale of the QMAP mapping (1:250,000) compared to the higher-resolution terrain data used in this study. Consequently, revised boundaries were defined where geomorphological evidence indicated alternative interpretations.

A high-resolution digital elevation model (DEM) of the KRDC was obtained from Land Information New Zealand, derived from an amalgamation of the most recent LiDAR surveys available. This dataset represents the highest-resolution topographic dataset currently available for the study area. The DEM was analysed using ArcGIS Pro 3.6.0. From this DEM, a series of terrain derivatives were generated, including hillshade models (045° and 315° illumination), contour maps (10 m and 20 m intervals), and slope maps. Hillshade models were used to enhance subtle topographic features and identify dome margins, ridge alignments, and potential eruptive centres. Contour maps were used to define dome morphology and identify breaks in slope, while slope maps assisted in distinguishing steep dome margins from surrounding terrain.

Dome boundaries were manually delineated within ArcGIS using a combination of DEM analysis, hillshade imagery, contour interpretation, slope calculations, field observations, and geological mapping. Geochemical data presented in Chapter 4 were also used to assist in distinguishing individual dome units where geomorphological boundaries were ambiguous. This integrated approach allowed identification of multiple dome centres within the KRDC.

Following dome identification, morphometric parameters were calculated using ArcGIS Pro and Python scripts executed within Jupyter Notebook. The DEM and dome polygon shapefile were used as inputs for raster and vector analysis. The calculated parameters included area, perimeter, maximum length, maximum width, elongation ratio, minimum elevation, maximum elevation, mean elevation, relief, mean thickness, maximum thickness, dome height, mean slope, maximum slope, and dome volume.

Length and width were calculated using minimum bounding geometry, with elongation defined as the ratio of maximum length to width. Volume and thickness calculations were derived using a base-level subtraction method, where the minimum elevation within each dome polygon was used as a reference surface.

These morphometric results were combined with field observations, geological mapping, structural interpretation, and geochemical data to define dome boundaries, identify eruptive centres, and interpret the emplacement and evolution of the Kaimai Rhyolite Dome Complex.

3.3 Regional Geomorphology

The Kaimai Rhyolite Dome Complex (KRDC) forms the southernmost extent of the Kaimai Range (Figure 1.1), which is part of a broader series of north–south trending ranges including the Coromandel Range (Figure 1.1) to the north and the Mamaku Range to the south (Figure 1.1). The Kaimai Range represents an uplifted structural block primarily composed of andesitic and rhyolitic volcanic rocks. This uplift is largely controlled by major fault systems, forming a horst structure bounded by the Hauraki Fault and Kerepehi Fault to the west (Figure 3.3). The range is also mantled in places by younger volcanic deposits, including volcanic ash, pumice, and ignimbrite sheets derived from later volcanic activity.

To the west of the Kaimai Range lies the Waikato Basin (Figure 3.3), which is characterised by volcanic-derived sedimentary deposits. These include the Hinuera Formation, consisting predominantly of pumiceous gravels, sands, and silts derived from reworked volcanic material. The basin also contains Tauranga Group alluvium, comprising pumice-, crystal-, and ash-rich sediments reworked from Quaternary ignimbrites. Additionally, ignimbrite units such as the Pokai Formation and Whakamaru Group are present, with the latter consisting of variably welded, crystal-rich rhyolitic ignimbrites, locally displaying columnar jointing (Figure 3.3).

Figure 3.1: View looking west-northwest from the Te Weraiti summit. The densely forested terrain immediately below the viewpoint corresponds to the Waiteariki Ignimbrite, which buries the eastern margin of Te Weraiti and partially obscures the dome boundary in this direction. Beyond the ignimbrite, the Tauranga Basin extends to the coast, with Mt Maunganui (Mauao) visible on the far left horizon. The dense vegetation cover across the ignimbrite and dome flanks is representative of the limited rock exposure encountered during field investigation across the KRDC.

To the south and east of the KRDC lies the Mamaku Plateau, an extensive ignimbrite surface erupted from the Rotorua Caldera (Milner et al., 2003). This ignimbrite forms a relatively subdued plateau morphology that has been dissected by gullies and valleys, and extends into the Mamaku Range. The presence of the Mamaku Plateau influences the eastern geomorphology of the KRDC, where younger ignimbrite deposits partially obscure older dome structures.

To the north of the KRDC, volcanic units associated with the Tauranga Volcanic Centre are present, including the Waiteariki Formation, an ignimbrite derived from the Omanawa Caldera (Prentice, 2023). Additional volcanic units in this region include the Whakamarama Group and the Uretara Formation, which comprise alternating andesite–dacite lava flows and pyroclastic breccias. These surrounding

volcanic terrains further highlight the complex volcanic and tectonic setting in which the Kaimai Rhyolite Dome Complex developed.

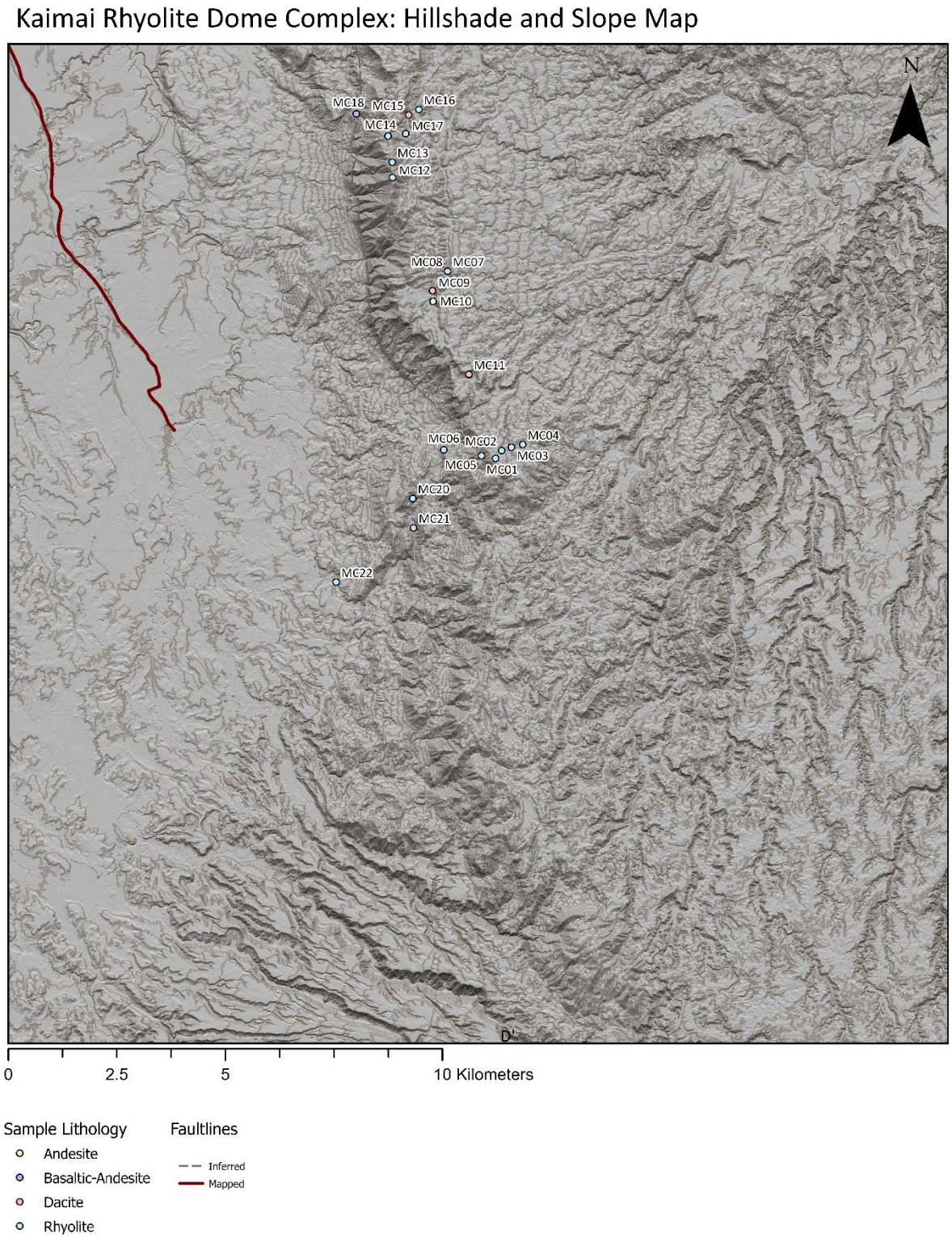

Figure 3.2: Hillshade and slope map of the Kaimai Rhyolite Dome Complex showing sample locations (MC01–MC22) classified by lithology (andesite, basaltic-andesite, dacite, and rhyolite). The mapped fault trace (solid red line) runs along the western margin of the complex and the dashed grey line is the inferred southern extent of the Hauraki Fault.. Scale bar in kilometres; north arrow indicated.

3.3.1 Geological Map and Cross-Sections

A geological map of the Kaimai Rhyolite Dome Complex field area (Figure 3.3) was compiled as part of this study to provide the first detailed geological map of the complex, combining field observations, interpretation of LiDAR derived topographic data, and published QMAP data. Geological cross sections are presented in Figure 3.4. The map delineates thirteen geological units within the KRDC boundary, including discrete dome units, basement exposure, undifferentiated rhyolite, and surrounding volcanic and sedimentary formations. Dome boundaries were established where geomorphological evidence from DEM analysis, hillshade imagery, slope maps, and contour interpretation indicated contacts between rhyolitic units and surrounding lithologies, with revisions made to QMAP boundaries where high-resolution topographic data indicated alternative interpretations. Where geomorphological boundaries were ambiguous, geochemical data presented in Chapter 4 were used to assist in unit differentiation. The map represents a significant revision of the previously published QMAP mapping of the area, identifying six discrete dome centres compared to the previous three, and documenting two previously unrecognised eastern dome units.

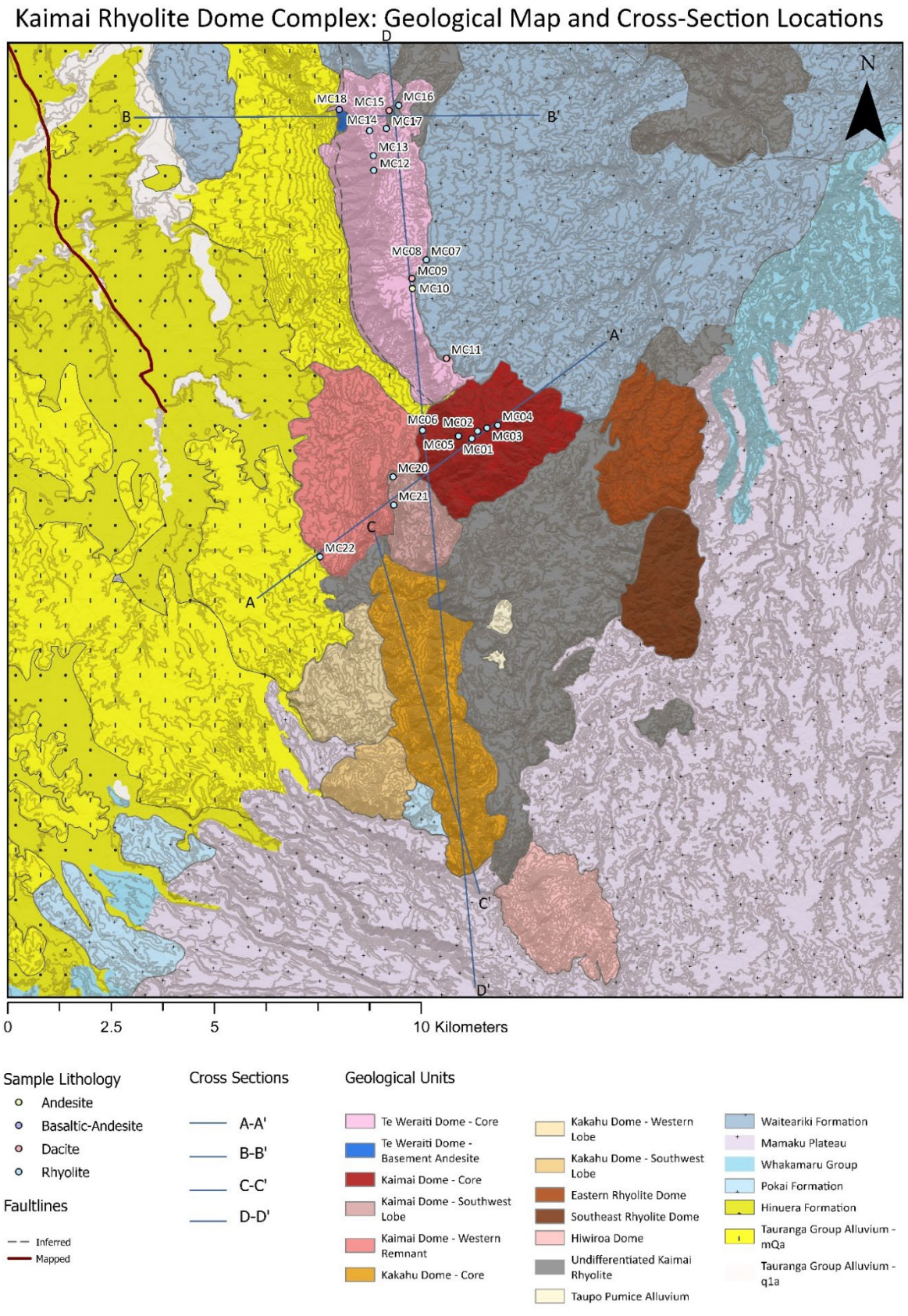

Figure 3.3: Geological map of the Kaimai Rhyolite Dome Complex and surrounding units.

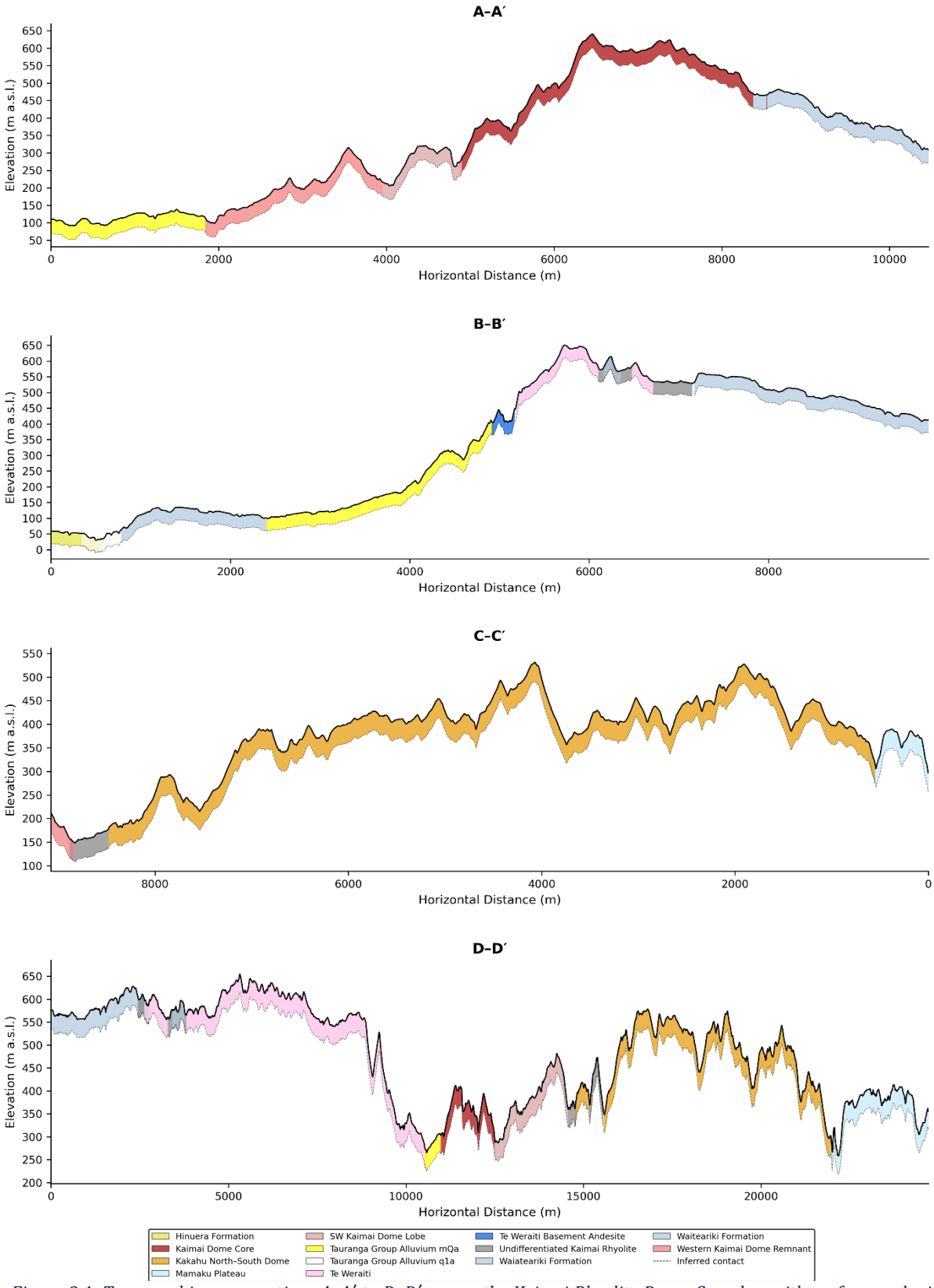

Figure 3.4: Topographic cross-sections A–A′ to D–D′ across the Kaimai Rhyolite Dome Complex, with surface geological units shaded to match the geological map (Figure 3.3). Unit boundaries were determined by intersecting each cross-section line with mapped dome and formation polygons. Profiles A–A′ and B–B′ traverse the complex from west to east, C–C′ runs along the range crest from north to south, and D–D′ extends north to south through the full length of the complex. The dashed line beneath each unit indicates the lack of subsurface data.

3.4 Morphological Overview

The Kaimai Rhyolite Dome Complex forms an elongated, north–south-trending silicic volcanic system extending approximately 25.8 km in length and 9.8 km in maximum width. This pronounced elongation suggests strong structural control on magma ascent and vent distribution, likely influenced by north–south-trending fault systems associated with the Kaimai Range. The linear arrangement of domes within the complex further supports a structurally controlled, fissure-related emplacement style, with eruptive centres aligned along fault-controlled pathways.

The KRDC forms a continuous volcanic ridge along the southern extent of the Kaimai Range, following the same north–south structural trend. This alignment indicates that regional tectonic structures not only influenced magma ascent but also controlled the overall morphology and distribution of rhyolitic dome emplacement across the complex.

The KRDC comprises multiple domes distributed along this north-south-trending ridge. From north to south, the principal dome centres include Te Weraiti, Kaimai, Western Kaimai Remnant/Kakahu continuation, Kakahu, then Hiwiroa, along with two smaller eastern domes and several rhyolitic “lobes”. These domes form a largely continuous and coalesced volcanic ridge, with individual dome centres overlapping and merging into one another along the length of the complex.

This overlapping morphology suggests prolonged and spatially migrating dome emplacement, with successive eruptions occurring along structurally controlled pathways. Such coalesced dome complexes are characteristic of long-lived silicic volcanic systems, where repeated dome growth produces an elongated composite volcanic ridge rather than isolated dome edifices.

3.4.1 Te Weraiti Dome

Te Weraiti forms one of the most prominent and morphologically distinct domes within the KRDC, characterised by its elongated north-south geometry and significant topographic relief. The dome extends approximately 8.34 km in length and 2.97 km in width, producing an elongation ratio of 2.81, indicating strong

structural control on emplacement. Te Weraiti covers an area of approximately 14.26 km^2 and represents the largest individual dome within the KRDC with an estimated volume of 1.16 km^3. Elevation within the dome ranges from 214 m to 765 m (a.s.l), producing a total relief of 550 m, the greatest within the complex. The dome is further characterised by steep slopes, with a mean slope of 24.7° and a maximum slope of 83.4° on the western ridge.

Figure 3.5: Rhyolite pinnacle exposed on the Te Weraiti ridge, viewed looking south along the western margin of the dome. The blocky, jointed rhyolite outcrop represents exhumed dome core material characteristic of a crystalline lava dome interior.

Morphologically, Te Weraiti forms a continuous north-south ridge with steep western margins and more irregular eastern slopes where the Waiteariki Ignimbrite buries it. The western margin appears sharply defined, likely influenced by structural uplift associated with faulting along the Kaimai Range. The elongated ridge morphology, combined with overlapping topographic highs along its length, suggests multiple phases of dome growth and vent migration along a structurally controlled pathway. This interpretation is further supported by geochemical

homogeneity throughout the Te Weraiti dome emplacement suggesting a continuous volcanic edifice rather than isolated dome centres.

Figure 3.6: View looking south along the Te Weraiti ridge, showing the Civil Aviation Secondary Surveillance Radar installation with the Te Weraiti summit visible on the ridge behind it. Prominent rhyolite pinnacles are exposed on the western flank of the ridge below the radar installation. The near-vertical rocky outcrops represent exhumed dome core material, with the blocky, jointed rhyolite texture characteristic of viscous silicic lava emplacement. The steep western margin dropping toward the Waikato Basin is visible to the right, illustrating the pronounced topographic relief and asymmetric morphology of Te Weraiti consistent with fault-influenced emplacement along the Kaimai Range front. The dense native vegetation cover across the dome flanks is indicative of the limited rock exposure encountered during field investigation.

3.4.2 Kaimai Dome

The Kaimai Dome Core forms a broad, elevated volcanic centre south of the Te Weraiti dome. The dome covers approximately 8.67 km^2 and extends 4.09 km in length and 2.83 km in width, producing an elongation ratio of 1.44, indicating a more equant morphology compared to the strongly elongated Te Weraiti dome. Elevation within the dome ranges from 267 m to 646 m (a.s.l), producing a relief of approximately 379 m. Slopes across the dome are moderately steep, with a mean

slope of 20.1° and a maximum slope of 76.8°, reflecting a moderately dissected but still prominent dome morphology. The Kaimai Dome Core has an estimated volume of approximately 0.67 km^3.

Morphologically, the Kaimai Dome Core forms a central elevated high with multiple overlapping ridges. The eastern margin forms a relatively abrupt topographic boundary against surrounding lower-relief terrain, whereas the western margin transitions into a broader, more complex topographic region consisting of lower-relief, eroded rhyolitic terrain. Unlike Te Weraiti, the western margin does not display consistently steep slopes and instead shows more subdued topography. The Kaimai Dome – Western Remnant appears highly eroded, characterised by lower relief and smoother topography relative to the central dome, and has an estimated volume of approximately 0.35 km^3. In contrast, the Kaimai Dome - Southwest Lobe forms a smaller elevated ridge extending southwest from the dome core, with an estimated volume of approximately 0.12 km^3.

Figure 3.7: View looking south toward one of the topographic highs of the Kaimai Dome Core. Scattered rhyolite boulders and float material are visible across the grassed dome flanks, representing weathered and displaced dome core material. Rocky outcrops are concentrated near the summit crest with soil development and grass cover increasing down the flanks. The limited continuous rock exposure across the dome is representative of field conditions encountered throughout the KRDC.

Together, these three units likely represent different preserved portions of a larger Kaimai Dome edifice. When combined, the total estimated volume of the Kaimai Dome is approximately 1.136 km^3, making it comparable in scale to the Te Weraiti dome and reinforcing interpretation of the Kaimai Dome as a major eruptive centre within the Kaimai Rhyolite Dome Complex. The transitional morphology between these units, combined with overlapping topographic highs and diffuse boundaries, indicates a complex volcanic morphology consisting of multiple overlapping dome units.

Field observations from the Kaimai Dome Core reveal well-developed flow banding and abundant spherulitic textures within rhyolitic outcrops. Flow banding is expressed as alternating bands of contrasting texture and crystallinity, while spherulites occur as radiating crystalline aggregates within the groundmass. These textures are characteristic of rhyolitic lava dome environments and consistent with emplacement of viscous silicic lava followed by devitrification during cooling.

3.4.3 Kakahu Dome

The Kakahu Dome possesses the highest elongation ratio in the complex at 3.158, exceeding even Te Weraiti at 2.807, producing a narrow blade-like ridge that is markedly more constricted laterally despite a comparable length of 8,014 m and 8,340 m respectively. The ridge runs almost parallel to the Kerepehi Fault and Hauraki Fault, suggesting strong structural control on magma ascent and emplacement. The ridge crest features two distinct topographic highs at 527 m and 531 m (a.s.l), separated by a prominent saddle, suggesting two discrete dome centres rather than a single continuous emplacement event. A single event fissure-controlled dome would show a continuous uniform crest with no significant breaks or changes in elevation, a consistent ridge width along its entire length, a smoother elevation profile, and no clear topographic highs.

The contacts with the Kakahu Dome - Southwest Lobe and the Kakahu Dome - Western Lobe differ. The Western Lobe features a reasonably sharp contact with a change in slope angle; the contours change character across it as it has a more rounded, lower relief form with widely spaced contours and gentler slopes and is interpreted as a morphologically distinct unit within the Kakahu system rather than a continuation of the primary dome. The Southwestern Lobe is more gradational in its contact, and the contours don't show a clear break between them, suggesting it may represent a continuation of the same emplacement event or a closely timed subsequent extrusion from the same source. The contrasting contact styles suggest that the sub-units within the Kakahu complex may not represent a single emplacement event, with the Western Lobe potentially recording a distinct eruptive episode relative to the N-S dome and SW Lobe. The Western Lobe has an area of 5.32 km^2 with a relief of 243 m and an elongation ratio of 1.299, while the Southwestern Lobe has an area of 3.10 km^2, a relief of 271 m, and an elongation ratio of 1.130. Both

sub-units display substantially lower elongation ratios than the primary N-S dome, indicating more equant, lobate forms consistent with point-source eruptions rather than fissure-controlled emplacement. The Southwest Lobe has a slightly higher relief than the Western Lobe, but both remain substantially lower than the 431 m of the primary Kakahu North–South Dome. The southern Kakahu contact is against the younger Mamaku plateau and thus current morphometrics represent minimum values due to truncation.

The combined Kakahu volume combining the 3 subunits totals to 0.922 km^3 making it the third largest complex within the KRDC.

3.4.4 Hiwiroa Dome

Hiwiroa represents the first of the more isolated dome units away from the primary N-S ridge trend, sitting separated from Kakahu by the Undifferentiated Kaimai Rhyolite and positioned to the southeast of the main complex. The dome displays a concentric contour pattern suggesting a centrally elevated dome form, along with sharp margins to the northwest and south against the Mamaku Plateau. It is one of the most equant major domes within the complex at an elongation ratio of 1.471, while a relief of 379 m indicates it maintains significant topographic expression above the surrounding ignimbrite surface. Hiwiroa's relief is comparable to the Kaimai Core at 379.3 m despite being spatially isolated. The equant form is consistent with point-source or localised conduit eruption. However, as the southern extents of the Kerepehi and Hauraki faults remain unmapped, the degree of structural control on its emplacement and eruptive history cannot be definitively determined. A small lobate protrusion extends from the southern margin of the dome, the origin of which is uncertain but may represent a late-stage extrusion or a preserved flow lobe. Hiwiroa features the highest volume density of any discrete dome within the complex, retaining substantial material relative to its footprint despite its isolated position, suggesting it is among the better-preserved domes within the KRDC.

3.4.5 Eastern Domes

The Eastern Rhyolite Dome and Southeast Rhyolite Dome were identified through LiDAR derived DEM analysis. The two domes display tighter contour spacing

compared to the Undifferentiated Kaimai Rhyolite, along with closed contours forming discrete topographic highs that separated them from the surrounding undifferentiated rhyolite. The closing contours form roughly circular patterns, indicating centrally elevated dome like forms rather than ridges or erosional features. Hillshade analysis confirmed this, showing organised morphological structure visibly distinct from the surrounding undifferentiated rhyolite and ignimbrite sheets to the east. The two domes have a less organised and less well defined morphology than the larger dome units, with lower relief and more subdued topography overall.

The Eastern Rhyolite Dome covers 7.34 km^2 with a relief of 292 m. The Southeast Rhyolite Dome covers 5.20 km^2 with a relief of 230 m, the lowest in the complex. Mean slopes are 19.72° and 23.40° respectively, with maximum slopes of 77.64° and 82.74°, both consistent with values across the broader complex. Their combined volume of approximately 0.675 km^3 represents a substantial previously unrecognised contribution to the total eruptive volume of the KRDC. No geochemical sampling was obtained from either unit, and their rhyolitic composition is inferred from spatial association with the KRDC and the rhyolite assignment in the QMAP.

3.4.6 Te Weraiti Basement Andesite

The Te Weraiti - Basement Andesite is exposed within a quarry operated by J Swap Contractors, located on the western margin of Te Weraiti along the Kaimai Range. This andesite represents the only known exposure of basement material beneath the KRDC. The quarry face reveals a sequence top to bottom: the Te Weraiti rhyolite at the top, an oxidised reddish-purple andesite underneath, a pale intermediate unit, and dark grey unoxidized fresh andesite at the base.

A sharp, well-defined contact is observed between the overlying Te Weraiti rhyolite and the oxidised andesite immediately beneath, with no gradational transition and an abrupt change in colour and texture. The oxidised reddish-purple zone present immediately beneath this contact may reflect hydrothermal alteration or thermal effects associated with Te Weraiti rhyolite emplacement.

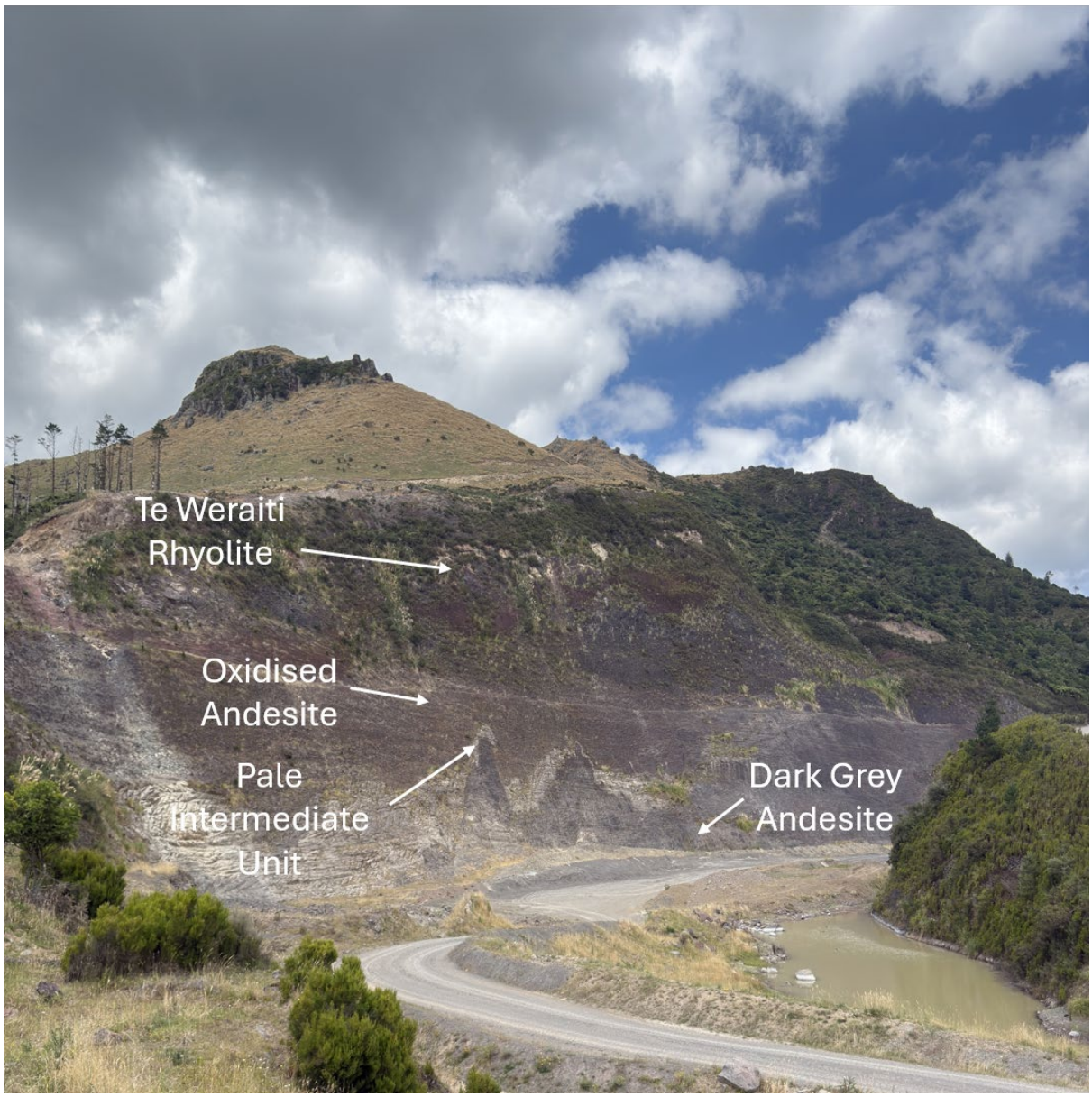

Figure 3.8: Field photograph of the J Swap Contractors quarry face, western margin of Te Weraiti, Kaimai Range. The quarry exposes the only known basement section beneath the KRDC, revealing a sequence from top to bottom of Te Weraiti Rhyolite, oxidised reddish-purple andesite, a pale intermediate unit, and dark grey unoxidized andesite. The sharp contact between the overlying rhyolite and the oxidised andesite may reflect fault juxtaposition associated with an inferred extension of the Hauraki Fault, though this interpretation remains uncertain. The pale intermediate unit displays irregular wavy contacts and may represent fault zone alteration material. View looking approximately south east. Sample MC18 (basaltic andesite) was collected from the dark grey andesite unit.

Within the andesite sequence, a pale intermediate unit is present between the oxidised andesite above and the dark grey unoxidised andesite below. Irregular wavy contacts are visible at the boundaries of this unit across the quarry face. An inferred extension of the Hauraki Fault runs through the quarry, and the pale intermediate unit may represent fault zone alteration material, with the wavy contacts reflecting fault-related deformation rather than primary flow or intrusive contacts. The sharpness of the rhyolite-andesite contact may similarly reflect fault

juxtaposition rather than a simple emplacement relationship, though this interpretation remains uncertain given the unconfirmed nature of the fault extension.

This exposure represents the only known window into the basement geology beneath the KRDC. While the lateral extent of the andesitic basement remains unknown without core sampling, it may underlie a broader portion of the complex. Further sampling of the individual units within the quarry face, combined with subsurface investigation, would be required to fully characterise the basement geology and fault zone alteration products beneath the KRDC.

3.4.7 Undifferentiated Kaimai Rhyolite

The Undifferentiated Kaimai Rhyolite is rhyolitic material within the KRDC boundary that lacks identifiable dome morphology. Its boundaries were delineated along contacts with surrounding sedimentary and ignimbrite units, consistent with QMAP classification. Despite covering an area of 36.57 km^2, it has a low mean thickness of 27.76 m, producing a relatively flat, spread-out unit at high elevations that distinguishes it fundamentally from dome units. Although its volume of 1.252 km^3 is comparable to the larger discrete internal dome complexes, its morphological character is sufficiently different that it is treated separately from dome unit comparisons throughout this study. It may represent heavily eroded dome structures, inter-dome material, or coalesced lava that has lost key morphological expressions over 2.2-2.8 Ma. Without field observations, geochemical sampling, or subsurface data its true origin cannot be determined, and represents a key area for future investigation.

3.5 Structural Setting

The Kaimai Rhyolite Dome Complex sits within the Hauraki Rift system, a NNW-trending half-graben active since the late Neogene (Persaud et al., 2016). At the time of dome emplacement, constrained by published $^{40}Ar/^{39}Ar$ (Briggs et al., 2005) and U-Pb zircon (Pittari et al., 2021) ages of 2.8 and 2.2 Ma respectively, the Hauraki Rift was transitioning as the locus of rifting migrated southward toward the nascent Taupō Rift at approximately 2–3 Ma (Persaud et al., 2016). The Hauraki Fault runs along the foot of the Kaimai Range, marking the eastern margin of the Hauraki Plains,

and the Kerepehi Fault runs through the central depression and is the currently active fault of the rift system (Persaud et al., 2016). Both faults trend approximately 340° (Persaud et al., 2016). The KRDC extends approximately 25.8 km in length, with overall N–S elongation parallel to the trend of the Hauraki and Kerepehi fault systems. The complex is bounded along its western margin by steep slopes that mark the topographic boundary between the Kaimai Range and the Hauraki Plains.

Geometric relationships between individual domes and the regional fault systems are described below. Te Weraiti, Kaimai, and Kakahu lie along a N–S trend parallel to the Hauraki and Kerepehi fault systems. Hiwiroa lies southeast of Kakahu, off the main N–S trend. The Eastern Domes lie east of the inferred fault extensions but remain approximately N–S oriented despite their off-axis position.

3.6 Morphometric Analysis

Morphometric parameters for all mapped units within the KRDC are presented in Table 3.1. The following section focuses on key patterns and their geological s

Table 3.1. *Morphometric parameters for all mapped units within the Kaimai Rhyolite Dome Complex (KRDC), ordered from north to south. Min = minimum, Max = maximum. All elevation and thickness values in metres (m), area in km², volume in km³, and slopes in degrees (°). The Te Weraiti Basement Andesite and Undifferentiated Kaimai Rhyolite are included for completeness but treated separately from discrete dome unit comparisons. Total KRDC row represents the combined extent of all mapped units within the complex boundary.*

Unit	Area (km²)	Perimeter (m)	Length (m)	Width (m)	Elongation Ratio	Volume (km3)	Min Elevation (m)
Te Weraiti	14.26	26642	8340	2971	2.807	1.16	214
Te Weraiti Dome - Basement Andesite	0.12	1478	562	290	1.938	0.001	395
Kaimai Dome - Core	8.97	13118	4086	2831	1.444	0.667	267
Kaimai Dome – Southwest Lobe	3.12	7341	2479	1834	1.352	0.116	176
Kaimai Dome - Western Remnant	10.7	16726	5233	3267	1.601	0.353	71
Kakahu Dome - Core	12.61	21855	8014	2538	3.158	0.597	170
Kakahu - Western Lobe	5.32	11873	3390	2610	1.299	0.159	108
Kakahu Dome - Southwest Lobe	3.1	7808	2287	2024	1.13	0.165	129
Eastern Rhyolite Dome	7.34	13989	4027	2594	1.553	0.325	229
Southeastern Rhyolite Dome	5.2	9995	3700	2004	1.847	0.35	314
Hiwiroa	6.53	14217	3876	2635	1.471	0.52	313
Undifferentiated Kaimai Rhyolite	36.87	76436	11373	4839	2.35	1.252	110
Total KRDC	114.14	221477	11373	4839	2.35	5.666	71

Unit	Max elevation (m)	Mean Elevation (m)	Relief (m)	Mean Thickness (m)	Max Thickness (m)	Mean Slope	Max Slope
Te Weraiti	765	523	550	92.83	412.46	24.69	83.4
Te Weraiti Dome - Basement Andesite	458	422	63	13.22	41.3	25.99	75.92
Kaimai Dome - Core	646	488	379	77.36	287.7	20.12	76.79
Kaimai Dome – Southwest Lobe	504	336	328	45.26	126.28	21.95	79.69
Kaimai Dome - Western Remnant	360	187	289	40.35	131.17	15.83	79.27
Kakahu Dome - Core	602	418	432	55.82	231.36	24.05	78.59
Kakahu - Western Lobe	351	233	243	41.93	126.36	17.61	80.59
Kakahu Dome - Southwest Lobe	400	289	271	61.04	212	22.88	69.59
Eastern Rhyolite Dome	522	397	292	47.22	119.72	19.72	77.64
Southeastern Rhyolite Dome	544	434	230	73.25	198.71	23.4	82.74
Hiwiroa	692	534	380	82.28	269.23	22.83	74.75
Undifferentiated Kaimai Rhyolite	638	384	528	27.76	165.08	17.89	79.04
Total KRDC	765	386	694	48.09	412.46	20.53	83.4

Morphometric analysis provides a valuable dataset for investigating volcanic complexes where field observations are limited by difficult terrain and dense vegetation cover, resulting in few accessible rock outcrops. For a complex of the age of the KRDC, spanning 2.2–2.8 Ma, prolonged erosion has significantly modified the original volcanic architecture, making it difficult to determine the true dimensions and character of individual dome structures without quantitative topographic analysis. The LiDAR-derived DEM enables high-resolution examination of dome morphology across the entire complex where direct field observation is not possible. No previous morphometric analysis of the KRDC has been undertaken, and the results presented here provide the first quantitative characterisation of the complex's geometry, volume distribution, and structural arrangement.

3.6.1 Elongation Ratios

Elongation ratios measure how stretched a dome is relative to its width, calculated as the ratio of long axis length to short axis width of the dome polygon. A ratio of 1.0 represents a perfectly circular planform, equally as wide as it is long. Ratios greater than 1.0 represent progressively more elongate forms, with values approaching 3.0 producing strongly blade-like geometries.

Elongation ratios across the KRDC range from 1.44 to 3.16 (Table 3.1). Te Weraiti and Kakahu have the highest elongation ratios at 2.81 and 3.16 respectively. The Undifferentiated Kaimai Rhyolite has an elongation ratio of 2.35, although as discussed in Section 3.4.7 this unit lacks identifiable dome morphology and its elongation ratio does not reflect a discrete dome geometry. The Eastern Domes record intermediate values of 1.55 and 1.85. The Kaimai Dome and Hiwiroa have the lowest elongation ratios at 1.44 and 1.47 respectively.

For the purposes of subsequent analysis, the domes are grouped into three categories based on their elongation ratios: highly elongate (Te Weraiti, Kakahu), moderately elongate (Eastern Domes), and approximately equant (Kaimai, Hiwiroa).

3.6.2 Volume Estimates

Volume provides a measure of the relative magnitude of eruptive output at each dome centre. Larger volumes indicate either larger individual eruptions, longer-lived eruptive episodes with multiple pulses, or both, and provide a measure of the

relative importance of each dome centre within the broader complex. The volume values presented here represent preserved volumes of dome cores rather than original erupted volumes, as approximately 2.2–2.8 Ma of erosion has removed carapace, talus, and outer dome material from all units. As a result, larger preserved volumes may reflect either greater original eruptive output or simply better preservation, and all values should be considered minimum estimates.

Te Weraiti and the Kaimai Dome Complex are the largest units within the complex at 1.160 km^3 and 1.136 km^3 respectively, despite displaying fundamentally different morphologies, Te Weraiti a strongly fault-controlled elongated ridge and the Kaimai complex a more equant point-source system. The Kakahu complex is the third largest at 0.922 km^3. The most significant volumetric finding of this study is the combined volume of the Eastern Domes at 0.675 km^3, which was entirely unrecognised prior to this study. Despite occupying a larger combined footprint than Hiwiroa, the Eastern Domes have a lower volume density reflecting their more subdued and partially buried character, yet their combined volume remains comparable to Hiwiroa at 0.520 km^3. The Undifferentiated Kaimai Rhyolite contributes a further 1.252 km^3, highlighting the substantial volume of rhyolitic material within the KRDC that cannot be attributed to discrete dome centres. The total preserved volume of the KRDC is 5.666 km^3.

3.6.3 Slope Angle

Mean and maximum slopes provide complementary information about the preservation state of dome units within the KRDC. Maximum slopes reflect structural or original dome margin features, while mean slopes capture the integrated character of the entire dome surface and overall preservation state. A well-preserved dome displays a steep core with near-vertical margins, relatively steep flanks close to original emplacement angles, and a correspondingly high mean slope. A heavily eroded dome may retain steep margin faces but displays progressively worn and smoothed flanks, producing a low mean slope as the majority of the surface has been reduced to gentler gradients.

Maximum slopes across the complex are consistently high, ranging from 74° to 83°. This consistency across units of varying size, morphology, and preservation state suggests that these are original dome margin features rather than erosional

products, if erosion were the primary control, significantly more variability in maximum slope would be expected. The exception is the Southwestern Kakahu Lobe at 69.59°, possibly reflecting its position as a secondary lobe with reduced structural support relative to the primary North–South dome.

Mean slopes show considerably more variability across the complex, ranging from 15.83° to 25.99°. Te Weraiti records the highest mean slope at 24.69°, consistent with it being the best-preserved dome surface within the complex. This elevated mean slope may also reflect post-emplacement uplift along the Hauraki Fault, which could have steepened the overall surface beyond original emplacement angles. In contrast, the Western Kaimai Dome Remnant records the lowest mean slope at 15.83° despite maintaining a maximum slope of 79.27°, indicating a heavily dissected surface where the western flank of the dome grades progressively into the surrounding Tauranga Group Alluvium.

The Eastern Domes display mean slopes of 19.72° and 23.40° with maximum slopes of 77.64° and 82.74° respectively. The combination of moderate maximum slopes and relatively low mean slopes is consistent with partial burial along their eastern margins by the Mamaku Plateau, which has smoothed the overall surface, while steeper original dome margin faces are preserved on their western and northern margins.

3.6.4 Thickness

Mean thickness is the average depth of a dome unit above its base reference surface and provides a measure of how much material is retained relative to the dome's footprint. Te Weraiti records the highest mean thickness at 92.83 m, which is consistent with it being the tallest and best-preserved dome within the complex. Hiwiroa is the second highest at 82.28 m despite its smaller footprint and spatially isolated position. This may reflect a methodological advantage, Hiwiroa's isolated position means its base reference surface is unaffected by the overlapping contacts of adjacent dome units, potentially allowing a more accurate thickness calculation than domes with overlapping components. The Kaimai Core at 77.36 m is comparable to Hiwiroa despite forming part of a considerably larger dome complex. The Western Kaimai Dome Remnant records a mean thickness of 40.35 m, consistent with the heavily dissected and eroded character described in Section 3.6.1. The

Eastern Rhyolite Dome and Southeastern Rhyolite Dome display mean thicknesses of 47.22 m and 73.25 m respectively. The higher thickness of the Southeastern Rhyolite Dome relative to the Eastern Rhyolite Dome despite similar footprint areas could reflect erosion differences, burial by the Mamaku Plateau, or greater original eruptive output. The Undifferentiated Kaimai Rhyolite records the lowest mean thickness at 27.76 m across an area of 36.87 km^2, reinforcing its character as a flat, coalesced sheet of rhyolitic material rather than a discrete dome edifice.

Chapter Four: Petrology of lavas

4.1 Petrography and Mineralogy

4.1.1 Methods

4.1.1.1 Thin Section

Twenty-two rock samples were cut into blocks approximately 4 cm × 2 cm, and the cut surfaces were ground flat using #600 polishing powder. The prepared surface of each block was mounted onto the frosted side of a glass petrographic microscope slide using Hillquist thin section resin and hardener mixed at a ratio of 2.3:1. Once the resin had cured, the mounted blocks were cut to a thickness of approximately 1 mm and subsequently ground to a final thickness of ~30 μm using a Struers Discoplan-TS thin section grinder. Coverslips were applied using Petropoxy 154 epoxy resin at a ratio of 10:1, and the slides were allowed to cure on a hotplate until fully set.

4.1.1.2 Optical Microscopy

Thin sections were examined using a petrographic microscope under both plane polarised light (PPL) and cross polarised light (XPL) to identify and describe mineral phases, crystal morphologies, groundmass textures, and alteration features. Attention was given to identifying phenocryst assemblages and characterising groundmass textures, including hyalopilitic, pilotaxitic, microcrystalline, and devitrified textures. The presence and relative abundance of spherulitic structures were also documented.

Mineral occurrence within each thin section was recorded qualitatively as Dominant, Abundant, Common, Minor, Trace, and Absent, and groundmass textures and spherulite shapes were noted for each sample.

4.1.1.3 Results

Thin section analysis was undertaken on 22 samples (MC01–MC22) collected from the Kaimai Rhyolite Dome Complex to characterise mineral assemblages, groundmass textures, and alteration features. The lavas are predominantly non-vesicular to weakly vesicular and commonly exhibit porphyritic textures with phenocrysts dispersed within a fine-grained groundmass. Phenocrysts are dominated by quartz, K-feldspar, and plagioclase, with subordinate biotite and

minor Fe–Ti oxide phases. Pyroxene is rare and occurs only in a small number of samples. Phenocrysts are typically euhedral to subhedral and occur as isolated crystals set in the groundmass.

The groundmass is predominantly microcrystalline to devitrified and commonly displays hyalopilitic, pilotaxitic, and microcrystalline mosaic textures. Spherulitic devitrification textures are widespread and commonly abundant, reflecting recrystallisation of originally glassy rhyolitic material during cooling. In some samples, flow alignment of microlitic feldspar produces weak trachytic textures.

Mineral assemblages, groundmass textures, and spherulite textures observed in thin section are summarised in Table 4.1.

Table 4.1: Mineral abundances and groundmass textures across the 22-sample suite determined by petrographic analysis. Phenocryst abundances use a six-tier scale: Dominant (>10%), Abundant (5–10%), Common (1–5%), Minor (<1%), Trace, and Absent. Samples MC01–MC10, MC12–MC14, MC16–MC17, MC19–MC21 are KRDC rhyolites; MC11 and MC15 are reclassified as Waiteariki Ignimbrite; MC18 is a parental basaltic andesite, MC22 is an unassigned rhyolite. Groundmass / devitrification texture descriptions follow the morphological framework of Lofgren (1974).

Sample	Quartz	K-feldspar	Plagioclase	Biotite	Pyroxene	Amphibole	Olivine	Fe-Ti oxides	Groundmass / devitrification texture
MC01	Minor	Trace	Common	Minor	Trace	Absent	Absent	Minor	Spherical, coalesced; concentric banded
MC02	Minor	Absent	Common	Minor	Absent	Absent	Absent	Minor	Spherical, banded, coalesced; episodic concentric
MC03	Minor	Absent	Common	Minor	Absent	Absent	Absent	Minor	Cryptospherulitic; quenched glass
MC04	Minor	Absent	Common	Common	Absent	Absent	Absent	Minor	Microspherulitic; vapour-phase silica patches
MC05	Trace	Absent	Common	Absent	Absent	Absent	Absent	Minor	Axiolitic; flow-band boundaries
MC06	Minor	Trace	Common	Minor	Absent	Absent	Absent	Minor	Spherical, banded, coalesced; mature
MC07	Minor	Absent	Common	Absent	Absent	Absent	Absent	Minor	Fan, coalesced; low nucleation density
MC08	Minor	Absent	Common	Absent	Absent	Absent	Absent	Minor	Spherical, coalesced; feldspar-nucleated
MC09	Minor	Absent	Common	Minor	Absent	Absent	Absent	Minor	Fragmental; spherulitic texture destroyed
MC10	Absent	Trace	Absent	Absent	Absent	Absent	Absent	Minor	No spherulitic organisation; kaolinitic matrix
MC11	Common	Absent	Abundant	Common	Absent	Common	Absent	Minor	Eutaxitic welded; no spherulites
MC12	Minor	Absent	Common	Common	Absent	Absent	Absent	Minor	Fan, coalesced; pervasive devitrification
MC13	Minor	Absent	Common	Absent	Absent	Absent	Absent	Minor	Microspherulitic + fan; granophyric intergrowths
MC14	Minor	Trace	Common	Common	Absent	Absent	Absent	Minor	Fan + spherical, coalesced; feldspar-nucleated
MC15	Common	Absent	Abundant	Common	Absent	Common	Absent	Minor	Hydrated glassy; perlitic fracturing;no spherulites
MC16	Minor	Absent	Common	Absent	Absent	Absent	Absent	Minor	Spherical + fan, coalesced; quartz-nucleated
MC17	Minor	Trace	Common	Absent	Absent	Absent	Absent	Minor	Spherical + fan, coalesced; radial extinction cross
MC18	Absent	Absent	Dominant	Absent	Common	Absent	Common	Minor	Pilotaxitic; no spherulites
MC19	Minor	Trace	Abundant	Common	Absent	Absent	Absent	Minor	Spherical + fan, coalesced; feldspar-nucleated
MC20	Minor	Trace	Common	Absent	Absent	Absent	Absent	Minor	Fan + microspherulitic, coalesced
MC21	Minor	Trace	Common	Minor	Absent	Absent	Absent	Minor	Spherical + fan, coalesced; concentric banded, perlitic
MC22	Minor	Minor	Common	Common	Common	Absent	Absent	Minor	Spherical + fan, coalesced; biotite-nucleated

4.1.1.4 Phenocrysts

Quartz

Quartz is a common phenocryst phase within the analysed samples (Table 4.1). It typically occurs as subhedral to anhedral crystals dispersed through the groundmass and is generally present in low to moderate abundance relative to feldspar phases.

Quartz also occurs as part of the microcrystalline groundmass in several samples, where it forms fine intergrowths with feldspar.

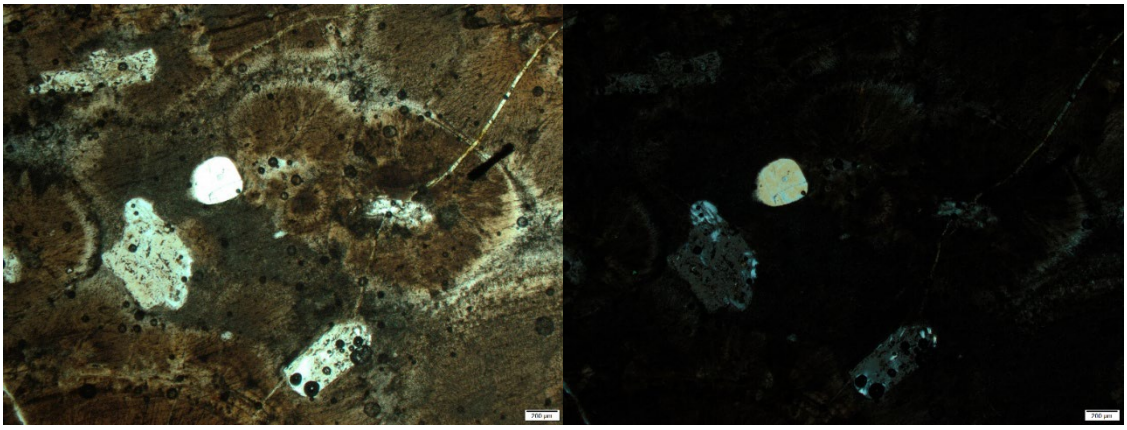

Figure 4.1: (a) plane-polarised light (PPL) and (b) crossed-polarised light (XPL). An anhedral quartz phenocryst (Qz) displays low first-order grey birefringence under XPL. Larger feldspar phenocrysts (Fsp) occur at centre-left and lower right. The groundmass is fine-grained with disseminated opaque minerals and spherulitic textures visible around the image margins. Scale bar = 200 µm.

K-Feldspar

K-feldspar (sanidine) occurs as a minor phenocryst phase present in some samples as subhedral to anhedral crystals within a fine-grained devitrified groundmass. Crystals are typically blocky to irregular in habit and range from approximately 200–500 µm in length. In plane-polarised light (PPL), feldspar crystals are colourless with low relief and commonly display fractures and inclusions. Under crossed polars (XPL), the crystals exhibit low-order interference colours and generally lack polysynthetic (albite) twinning, distinguishing them from plagioclase. Some grains display simple (Carlsbad) twinning. K-feldspar occurs as isolated phenocrysts set in the groundmass, which consists of a fine devitrified matrix locally displaying spherulitic textures.

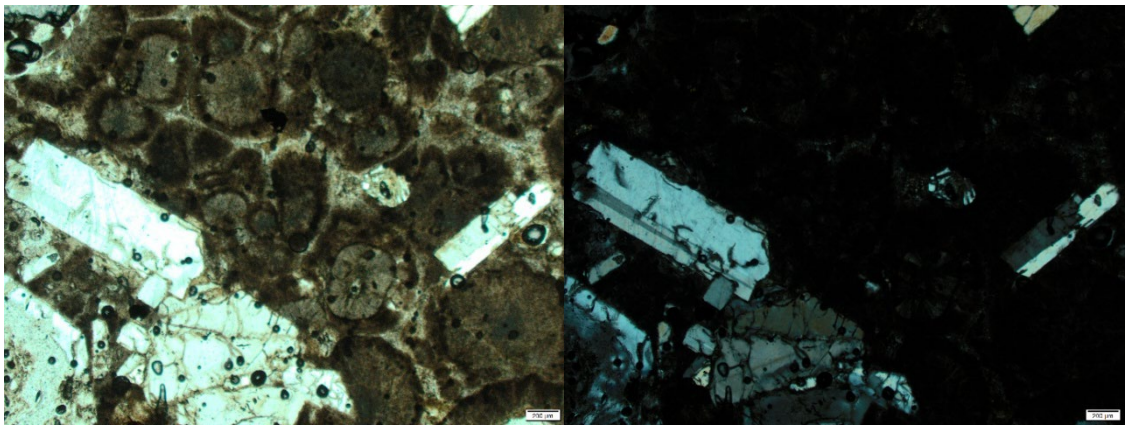

Figure 4.2: Photomicrographs of sample MC22 in (a) plane-polarised light (PPL) and (b) crossed-polarised light (XPL), illustrating the appearance of sanidine phenocrysts in the analysed sample suite. A subhedral sanidine phenocryst displays simple Carlsbad twinning under XPL, shown by two extinction domains separated by a single composition plane parallel to the long axis of the grain, together with low first-order grey interference colours. A second, smaller sanidine grain (right of centre) shows the same twin geometry. The surrounding groundmass is fine-grained and displays spherulitic textures. Scale bar = 200 µm.

Plagioclase

Plagioclase occurs as subhedral to euhedral phenocrysts set in the groundmass and is typically present as elongate to tabular crystals ranging from approximately 200–600 µm in length. In plane-polarised light (PPL), crystals are colourless with low relief and commonly display internal fractures and inclusions. Under cross polarised light (XPL), plagioclase crystals exhibit low-order interference colours and are characterised by polysynthetic (albite) twinning, expressed as parallel alternating lamellae across the crystals that produce a characteristic “piano-key” appearance. Some grains display irregular fracturing and occur both as isolated phenocrysts and as clustered crystals set in a fine-grained groundmass composed of microlitic feldspar and devitrified volcanic glass.

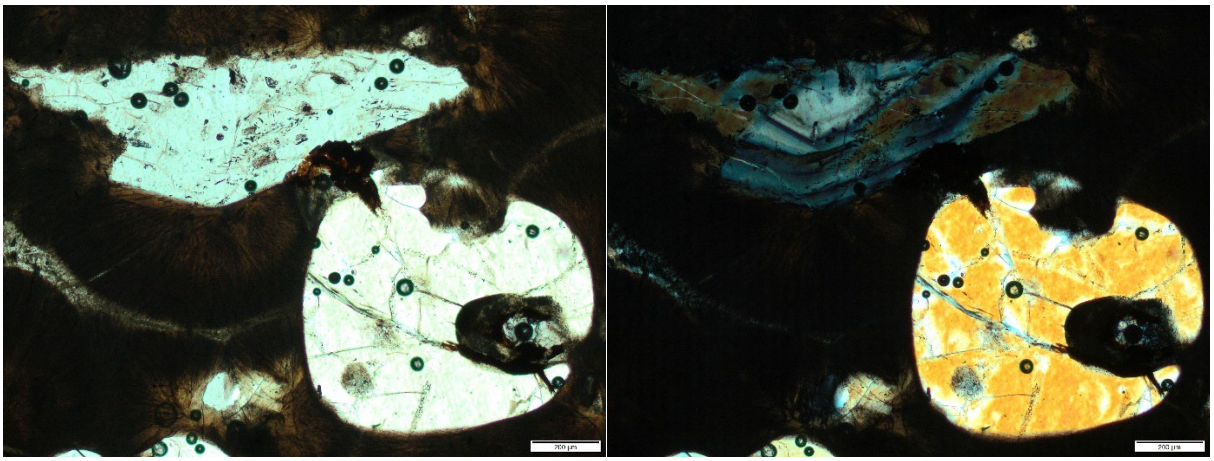

Figure 4.3: Photomicrographs of sample MC19 in (a) plane-polarised light (PPL) and (b) crossed-polarised light (XPL). A subhedral plagioclase phenocryst (Pl) displays polysynthetic twinning and compositional zoning visible as concentric bands of differing interference colour. The surrounding groundmass is pervasively devitrified with coarse spherulitic textures. Scale bar = 200 µm.

Biotite

Biotite occurs as elongate to subhedral lath-shaped grains. In plane polarised light, the crystals display strong brown pleochroism and well-developed cleavage parallel to their long axis. Grain sizes typically range from approximately 100–300 µm and many crystals contain small opaque inclusions. Under crossed polarised light, biotite commonly appears dark or exhibits low-order interference colours, with extinction occurring parallel to the cleavage traces. The biotite grains are commonly surrounded by a fine-grained spherulitic groundmass composed of radially arranged microlites. Some crystals show irregular margins and minor internal fractures.

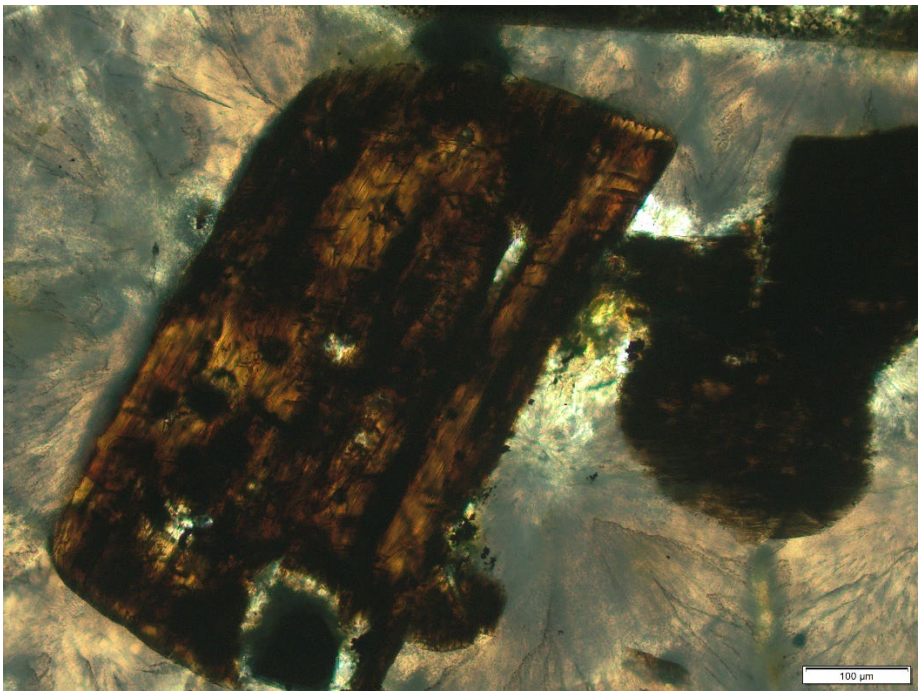

Figure 4.4: Plane-polarised light (PPL) photomicrograph of sample MC06 showing a subhedral elongate biotite phenocryst with characteristic brown body colour, well-developed cleavage, and prismatic habit. The surrounding groundmass is pervasively devitrified with coarse spherulitic textures. Scale bar = 100 µm.

Pyroxene

Pyroxene occurs as a minor mafic phase in several samples, forming subhedral to anhedral grains with stubby to irregular morphologies. Grain sizes typically range from approximately 0.05–0.35 mm, although locally larger altered mafic grains of up to ~0.4 mm are observed. In plane-polarised light (PPL), the crystals are pale to colourless and display moderately high relief relative to the surrounding groundmass. Under crossed polars (XPL), the grains exhibit moderate to high interference colours, consistent with clinopyroxene compositions such as augite. Pyroxene commonly occurs as isolated grains or small clusters within the groundmass and is associated with feldspar phases. In some samples, strongly altered mafic grains occur as irregular anhedral crystals displaying dark brown colours in PPL, making precise mineral identification uncertain and suggesting possible alteration of pyroxene or other Fe-rich mafic phases.

Fe-Ti oxides

Fe–Ti oxides occur as minor accessory phases in most samples, being present in all thin sections except MC13, MC16, MC17, and MC22. The grains are typically anhedral to subhedral and range in size from approximately ~0.02–0.20 mm. In plane-

polarised light (PPL), the crystals appear opaque and black, displaying very high relief relative to the surrounding groundmass. Fe–Ti oxides occur primarily as discrete grains set in the groundmass, although they are occasionally present as small inclusions within feldspar and mafic phases. Some grains display irregular margins and are locally clustered within the matrix.

4.1.1.5 Groundmass Texture

Groundmass textures observed across the analysed samples display a wide range of primary magmatic and secondary devitrification textures typical of silicic volcanic rocks. Primary groundmass textures include glassy, hyalopilitic, pilotaxitic, and trachytic varieties. Hyalopilitic to microcrystalline textures are common, occurring in samples such as MC01 and MC03, and consist of randomly oriented feldspar microlites within a glassy to microcrystalline matrix. In some samples, these microlites show preferred orientation producing flow-aligned trachytic-textured variants, such as the flow-aligned hyalopilitic texture observed in MC11. Pilotaxitic textures, characterised by sub-parallel alignment of feldspar microlites forming a felted microcrystalline framework, occur in MC04, while transitional textures between pilotaxitic and hyalopilitic groundmasses are present in MC18. Glassy and flow-banded groundmasses are observed in MC05, and locally transition into microlitic or devitrified textures, as seen in MC10 and MC15, which display glassy to microlitic or hyalopilitic devitrified groundmasses.

Spherulitic devitrification textures occur in ~12 of the 22 analysed samples, indicating widespread syn- to post-emplacement recrystallisation of silicic glass. Microcrystalline mosaic textures occur in MC02, reflecting extensive recrystallisation of original volcanic glass. Spherulitic devitrification textures are particularly abundant and occur in many samples including MC06, MC08, MC12, MC13, MC17, MC19, MC20, MC21, and MC22. These textures occur both as discrete spherulites and as densely packed spherulitic mosaics within the groundmass. In some cases, spherulites exhibit weak flow or trachytic alignment, as observed in MC14, or transition into fibrous axiolitic structures along fractures, as seen in MC21. Overall, the observed groundmass textures reflect variable cooling histories and widespread devitrification of silicic glass following emplacement.

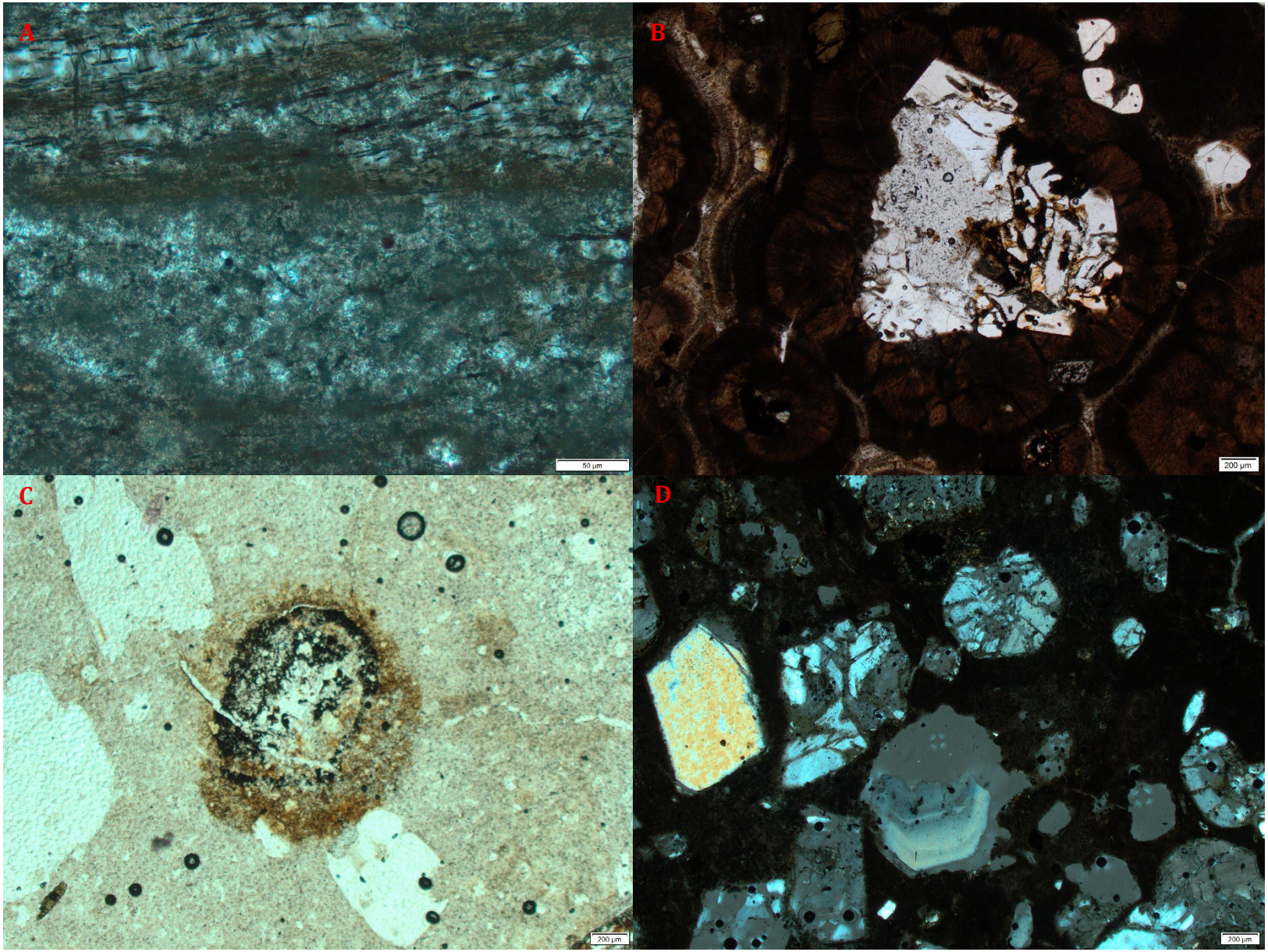

Figure 4.5: Representative groundmass textures in Kaimai Rhyolite Dome Complex samples. (A) Axiolitic devitrification in MC05, with fine fibres radiating from flow-band boundaries (scale bar = 50 µm). (B) Coalesced, concentric-banded spherulites in MC01, with a central lithophysal cavity (scale bar = 200 µm). (C) Microspherulitic groundmass in MC04 with vapour-phase cristobalite and tridymite patches (scale bar = 200 µm). (D) Crystal-rich, fragmental groundmass in MC09 with a near-isotropic matrix (scale bar = 200 µm).

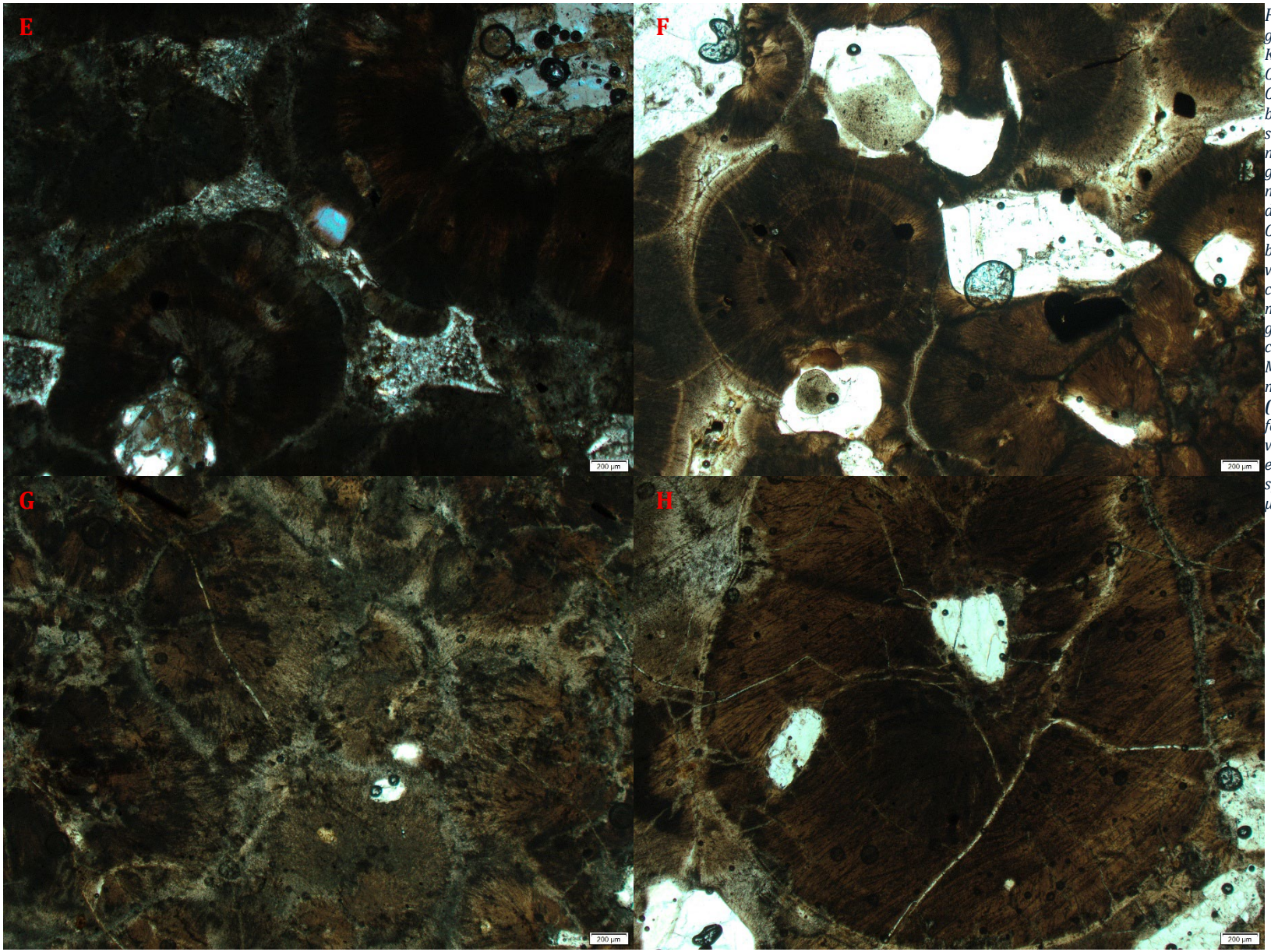

Figure 4.6: Devitrified groundmass textures in Kaimai Rhyolite Dome Complex samples. ***(E)*** *Coalesced, concentric-banded spherulites in MC02 set within an interlocking microcrystalline mosaic groundmass, indicating mature pervasive devitrification.* ***(F)*** *Coalesced, concentric-banded spherulites in MC06, with radial fibrous crystallites forming a mature devitrified groundmass.* ***(G)*** *Fan and coalesced spherulites in MC20 forming a microspherulitic framework.* ***(H)*** *Concentric-banded and fan spherulites in MC21, with perlitic cracking and exceptionally large, mature spherulites. Scale bars = 200 µm.*

4.1.1.6 Spherulites

Spherulitic textures are abundant throughout the analysed samples and represent the dominant groundmass devitrification texture within the rhyolitic units. Spherulites consist of radial aggregates of fibrous crystallites that nucleate at discrete sites and grow outward into the surrounding glassy matrix, forming circular to irregular radial structures ranging from ~20 μm to >2500 μm in diameter. Under plane-polarised light these features appear as dark brown to grey radial domains, often with clearly defined centres from which fibrous crystallites radiate outward. In many samples, adjacent spherulites impinge upon one another to form coalesced spherulites with polygonal boundaries where growth fronts intersect.

Well-developed examples of these textures occur in several samples, including MC06, MC08, MC12, MC13, MC17, MC19, MC20, MC21, and MC22, where spherulites occur both as discrete isolated structures and as densely packed aggregates that dominate the groundmass. In samples such as MC19 and MC22, spherulites commonly nucleate around pre-existing crystals, particularly feldspar phenocrysts, producing radial growth patterns that extend outward from phenocryst margins. In other instances, the nucleation occurs within the glassy groundmass itself, resulting in isolated circular spherulites that later impinge on neighbouring structures as crystallisation progresses.

The internal morphology of the spherulites varies considerably across the dataset. Many display well-developed radial fibrous textures, whereas others exhibit more complex internal structures including sectoral growth domains and concentric growth zoning. Several samples also contain features transitional between spherulitic and axiolitic textures, where fibrous crystallites nucleate along fractures or elongate nuclei rather than a single point.

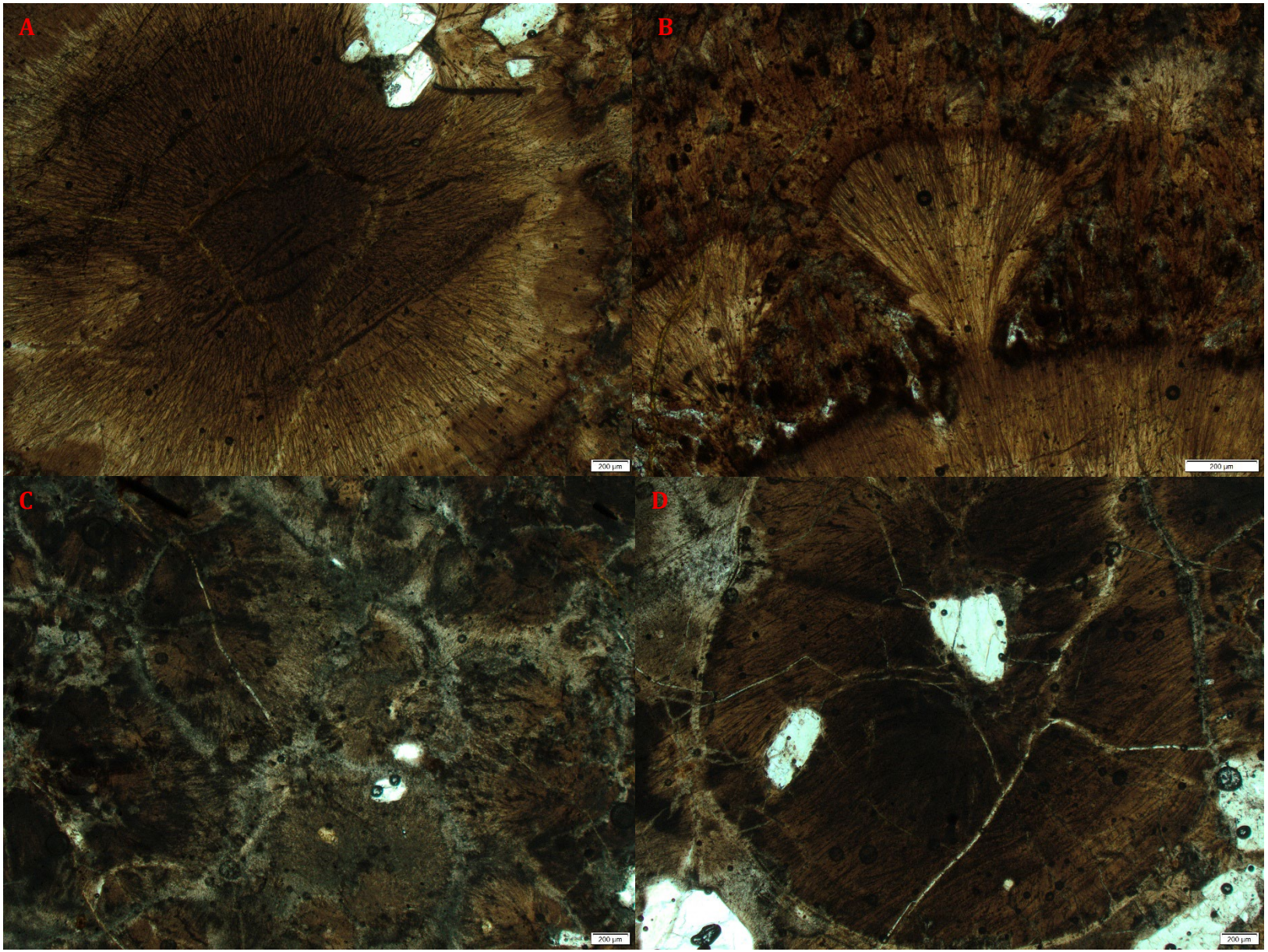

Figure 4.7: Representative spherulitic devitrification textures observed in the groundmass.
(A–B) Large, well-developed radial fibrous spherulites in MC14, characterised by fan-like crystallites radiating from central nucleation points within a devitrified groundmass. Adjacent spherulites locally impinge, producing irregular boundaries between growth domains.
(C) Spherulitic mosaic texture in MC20 formed by the impingement of numerous spherulites during devitrification of the glassy groundmass, producing a polygonal network of intersecting growth fronts.
(D) Spherulitic–axiolitic devitrification texture in MC21, where fibrous crystallites radiate outward from the margin of K-feldspar. Scale bars = 200 µm.

4.2 Scanning Electron Microscopy (SEM)

Scanning Electron Microscopy (SEM) was undertaken on four representative samples from the 22-sample dataset (MC02, MC05, MC08, and MC13) to characterise groundmass textures and mineral phase distributions at scales not resolvable using optical petrography. Samples consisted of the polished blocks produced during thin section preparation and were coated with a conductive platinum layer prior to analysis to minimise charging effect.

Imaging was conducted under high vacuum conditions using backscattered electron (BSE) and secondary electron (SE) detectors. SE imaging was used to characterise surface morphology and microtopography, while BSE imaging provided compositional contrast between mineral phases of differing mean atomic number.

Energy dispersive spectroscopy (EDS) was used to acquire elemental maps and semi-quantitative compositional data for groundmass, spherulites, and phenocrysts.

4.2.1 SEM Observations

Backscattered electron (BSE) imaging, which is sensitive to variations in mean atomic number, reveals predominantly homogeneous groundmasses characterised by uniform grey tones, indicating limited compositional variation at the microscale. Occasional phenocrysts are identifiable by subtle compositional contrast, with some displaying internal heterogeneity or inclusions. Secondary electron (SE) imaging on the polished blocks provides limited topographic information due to the flattened sample surface; however, SE contrast highlights fracture networks and localised zones of disruption that are less visible in BSE images. Overall, the SEM data indicate that microstructural features (fractures, disruption zones) are more prominent than compositional variation across the analysed samples.

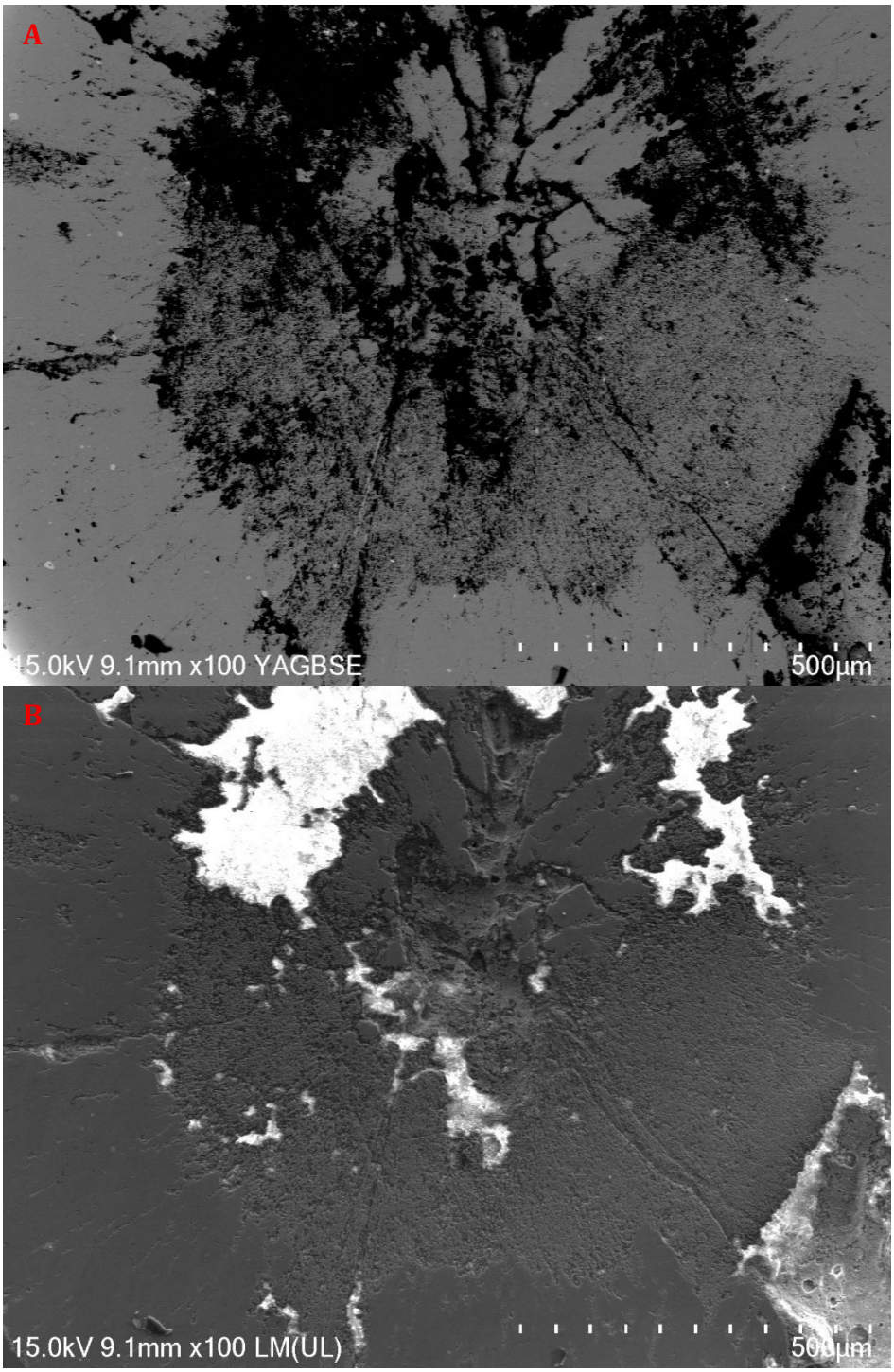

Figure 4.8: SEM (BSE and SE) images of sample MC02 showing a spherulite surrounded by groundmass. (A) BSE image displaying a well-developed spherulite characterised by radial compositional heterogeneity, with darker regions indicating relatively lower mean atomic number compared to the surrounding matrix. (B) Corresponding SE image of the same area revealing outward-propagating fractures aligned with the radial structure, consistent with spherulite growth and associated devitrification processes.

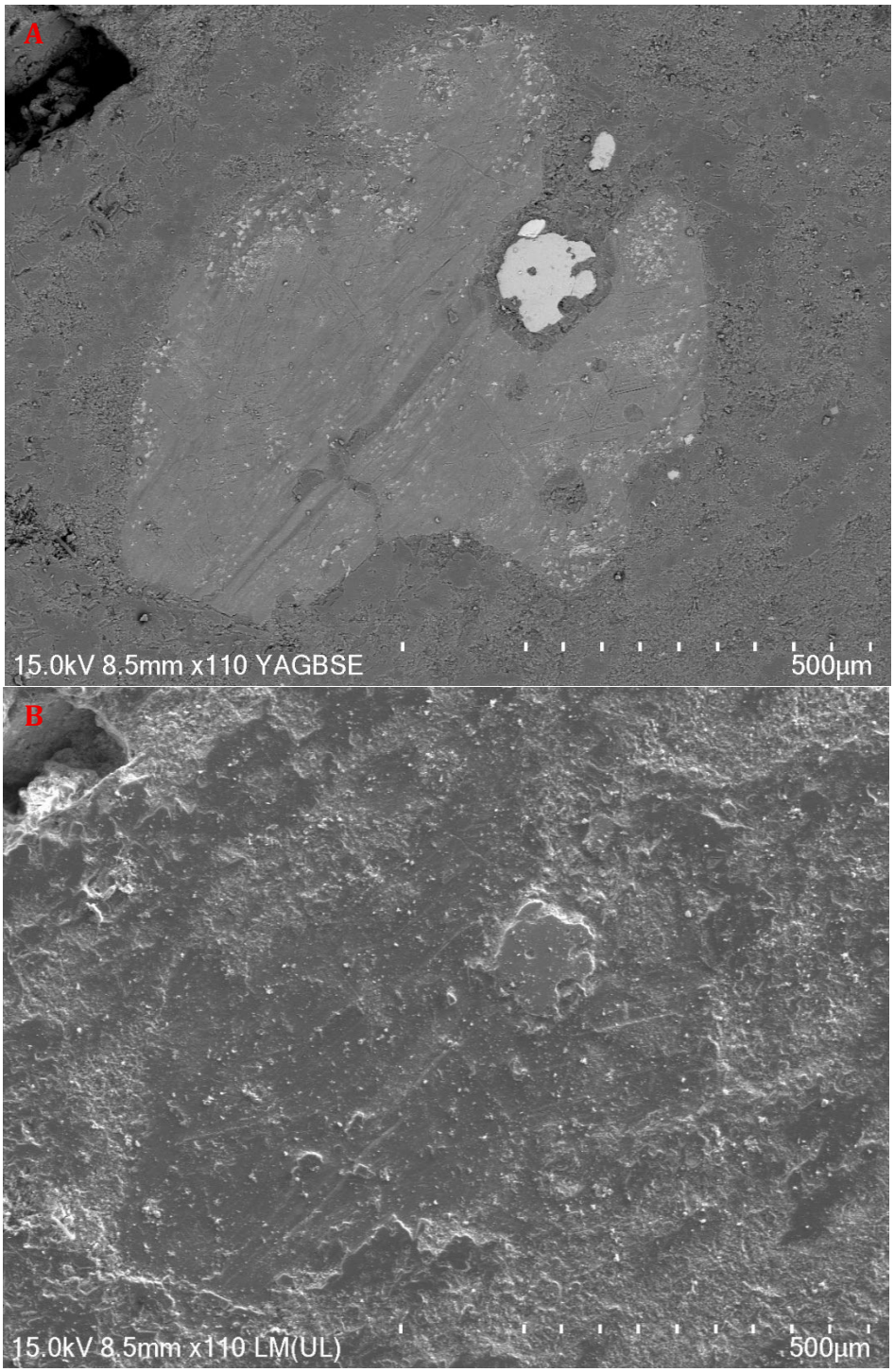

Figure 4.9: SEM (BSE and SE) images of sample MC05 showing phenocryst–groundmass relationships and associated microstructural features.
(A) BSE image of a large subhedral phenocryst exhibiting subtle internal compositional variation. The surrounding groundmass is comparatively homogeneous. A smaller, brighter inclusion within the phenocryst indicates a phase of higher mean atomic number.
(B) Corresponding SE image of the same area highlighting a network of microfractures and surface roughness within both the phenocryst and adjacent groundmass.

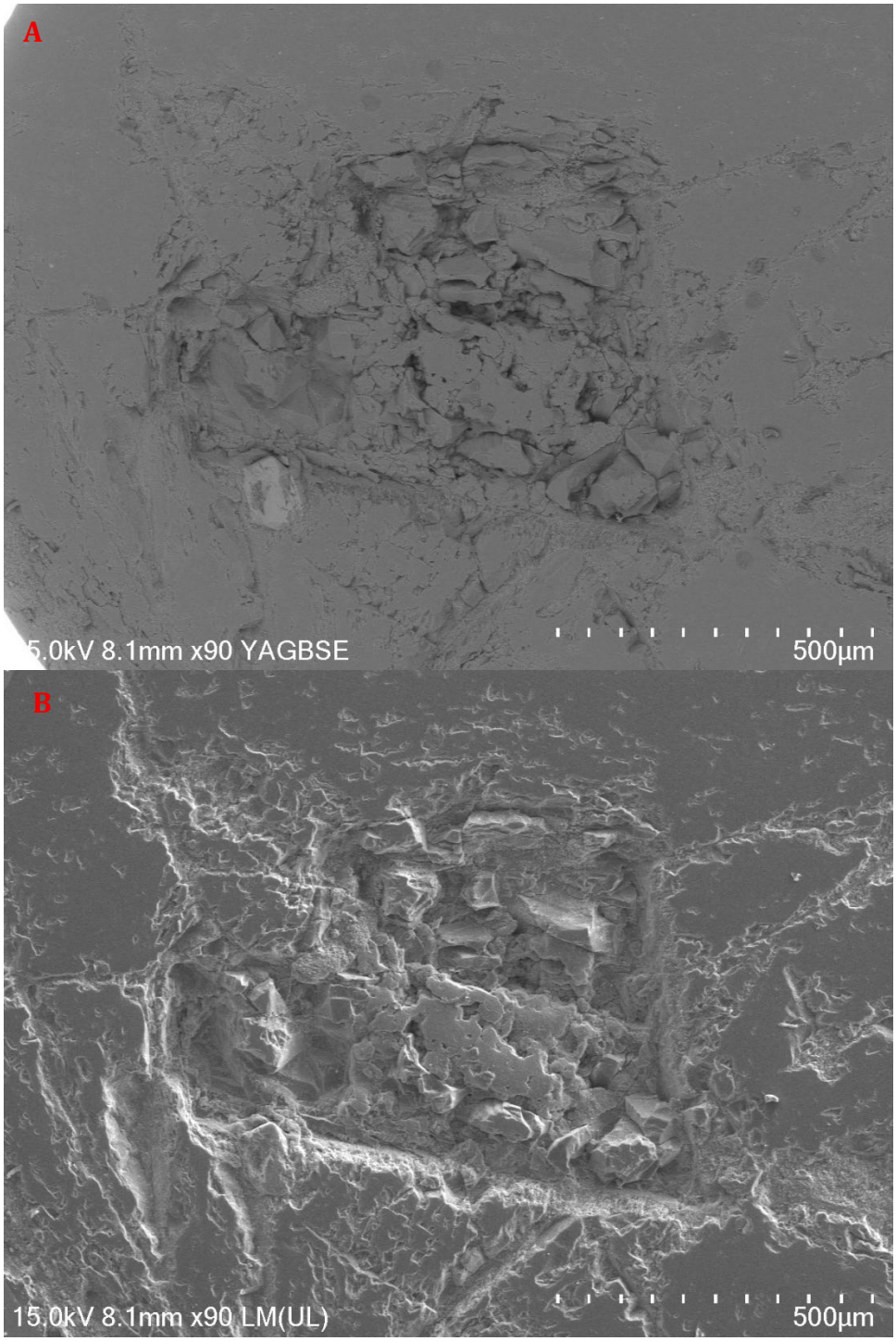

Figure 4.10: SEM (BSE and SE) images of sample MC08 showing a disrupted groundmass domain. (A) BSE image displaying an irregular domain with subtle compositional variation relative to the surrounding matrix. (B) Corresponding SE image revealing a highly fractured and roughened internal texture, with sharp boundaries between the disrupted domain and the surrounding groundmass.

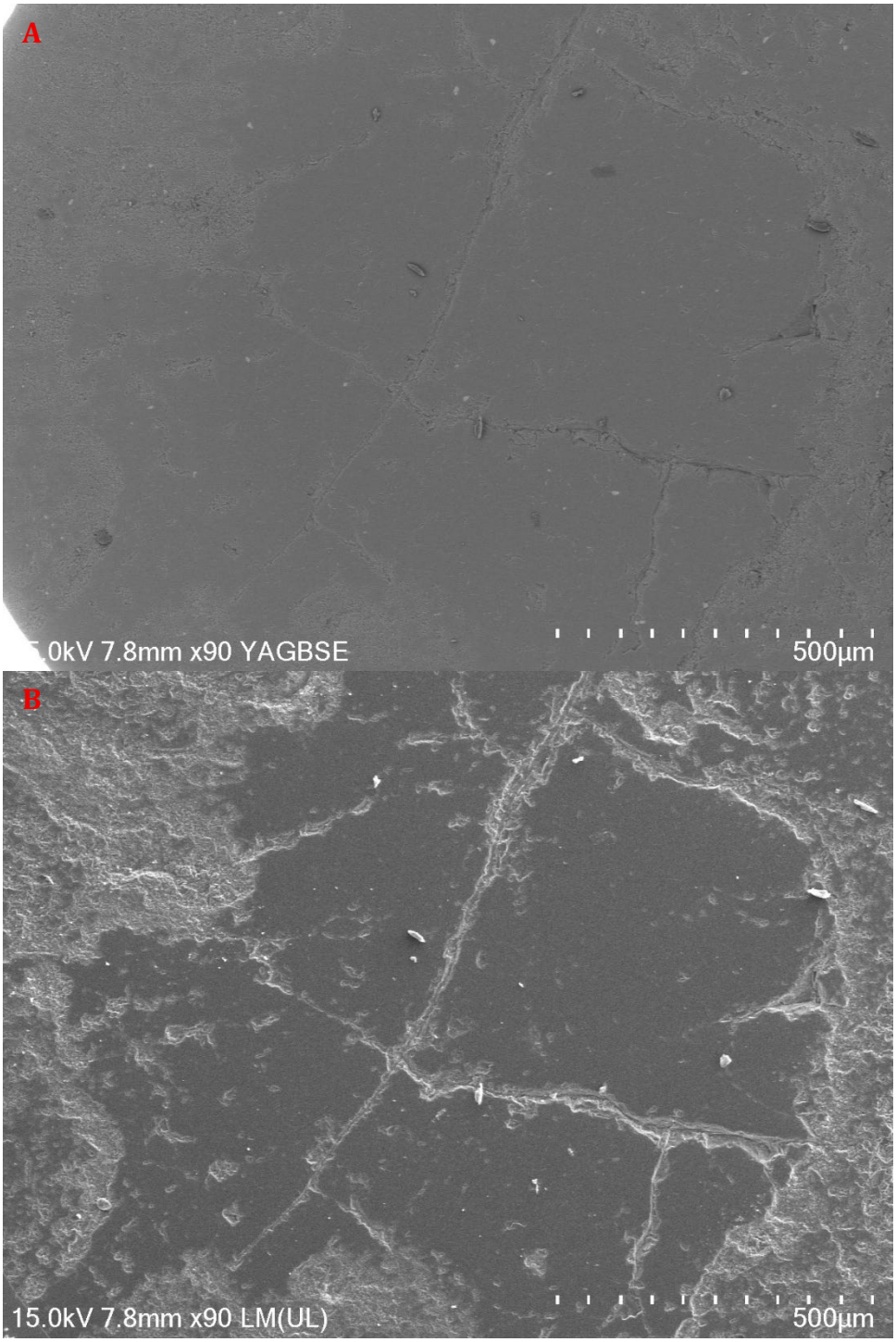

Figure 4.11: SEM (BSE and SE) images of sample MC13 showing fracture-controlled microstructural domains within a homogeneous groundmass.
(A) BSE image displaying a compositionally uniform groundmass with only subtle contrast between adjacent domains.
(B) Corresponding SE image revealing a well-developed network of fractures that define polygonal domains, with enhanced surface roughness and topographic expression along fracture boundaries.

4.2.2 Elemental Distribution (EDS)

MC02

Elemental mapping of sample MC02 reveals a predominantly homogeneous groundmass composition, with widespread enrichment in Si, consistent with a silica-rich matrix. Minor but diffuse concentrations of Al, Na, and K are also present throughout the groundmass, indicating feldspar compositions.

The groundmass exhibits limited compositional heterogeneity at this scale. Radiating spherulitic textures observed in SEM imaging are not associated with significant chemical differentiation and instead show only subtle variations in K and Al distribution, suggesting these features are primarily textural rather than compositional.

Discrete Fe-rich phases are present as small, irregularly distributed grains and clusters within the groundmass. Ca-bearing phases are comparatively rare and occur as minor, localised concentrations.

A distinct phenocryst is observed in some mapped characterised by elevated Ca, Na, and Al relative to surrounding groundmass. This phase is compositionally distinct and sharply bounded, contrasting with the groundmass matrix.

Irregular and linear zones of groundmass display slight elemental enrichment of Al and Fe which form discontinuous features across the sample. These structures cut across the groundmass and are independent of primary groundmass textures.

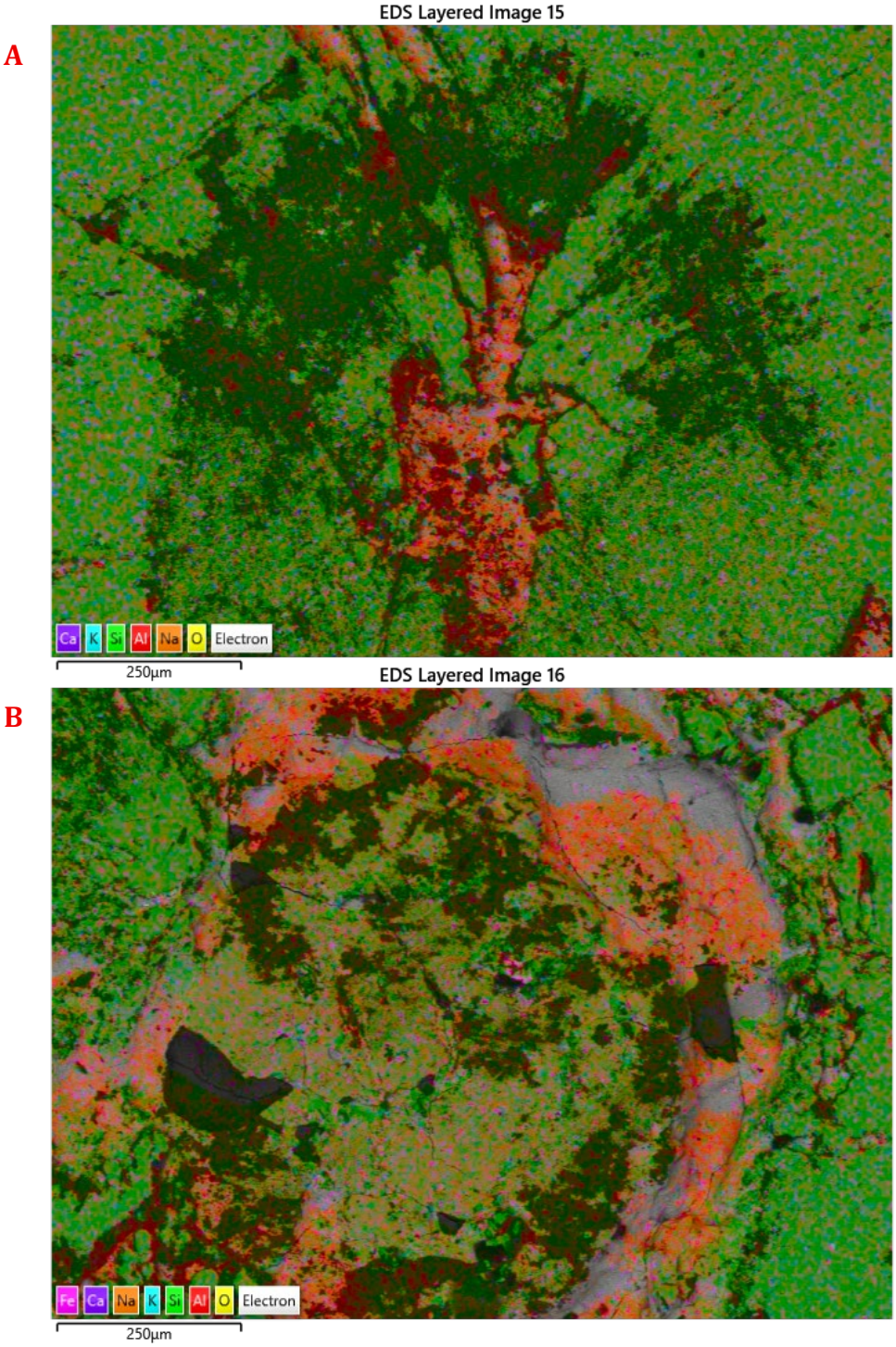

Figure 4.12: SEM–EDS elemental maps of sample MC02.
(A) Irregular, branching fracture network enriched in Al and Na, forming interconnected pathways through a predominantly Si-rich groundmass. These features define zones of localized chemical heterogeneity relative to the surrounding matrix.
(B) Semi-circular domain defined by compositional variation, with a relatively homogeneous Si-rich interior and margins enriched in Al, Na, and Fe. The boundary zone contains irregular concentrations of Fe-bearing phases and minor accessory material.

MC05

Elemental maps of sample MC05 show a predominantly Si-rich groundmass, with diffuse Na, K, and Al distributed throughout the matrix. The groundmass is broadly homogeneous at the microscale, with minor compositional variability expressed as irregular domains and linear features. These linear features are locally enriched in Fe, Ti, and Al, indicating concentration of minor phases or secondary material along fractures or boundaries.

One mapped area contains a compositionally distinct phenocryst, characterised by relative enrichment in Na and Al compared to the surrounding groundmass. This crystal is sharply defined and contains, or is spatially associated with, small accessory phases, including Zr-bearing and Fe–Ti-bearing grains.

Other domains display granular surface textures, consisting of fine aggregates enriched in Na, K, and Al, which occur along irregular surfaces and cavity margins.

One map also reveals a flow-banded domain within the groundmass, defined by compositional variation relative to the surrounding Si and Na-rich matrix. The flow-banded domain shows enrichment in Fe, Al, K, and Ti, and contains numerous small Fe–Ti-rich grains. Notably, Fe–Ti phases within the flow-banded domain appear relatively Fe-dominant, whereas those within the surrounding silica-rich matrix exhibit comparatively higher Ti contributions, indicating compositional variability between domains.

A

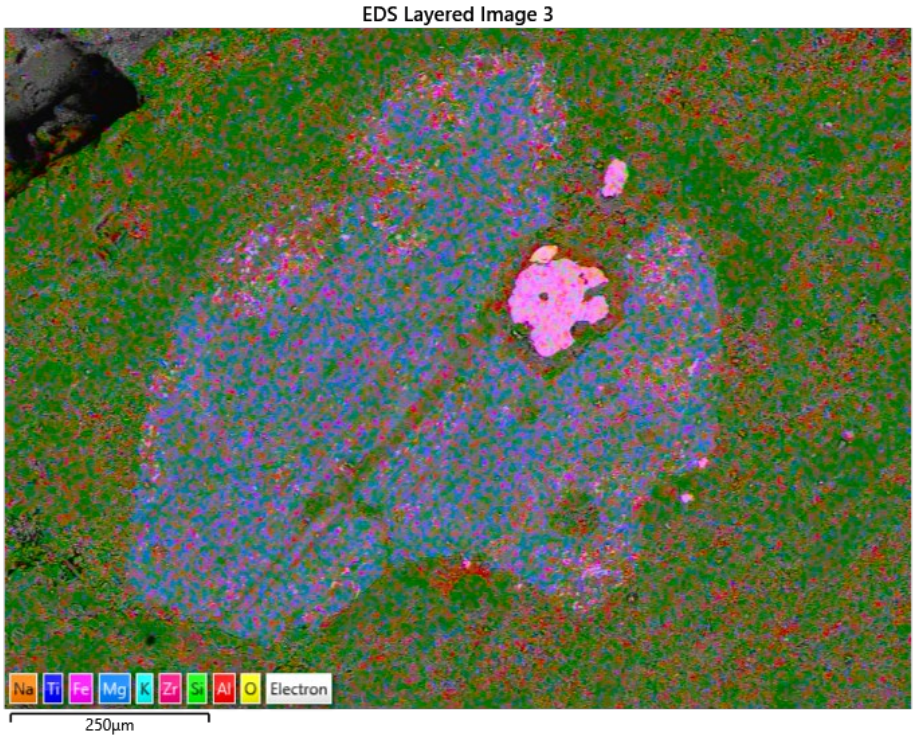

B

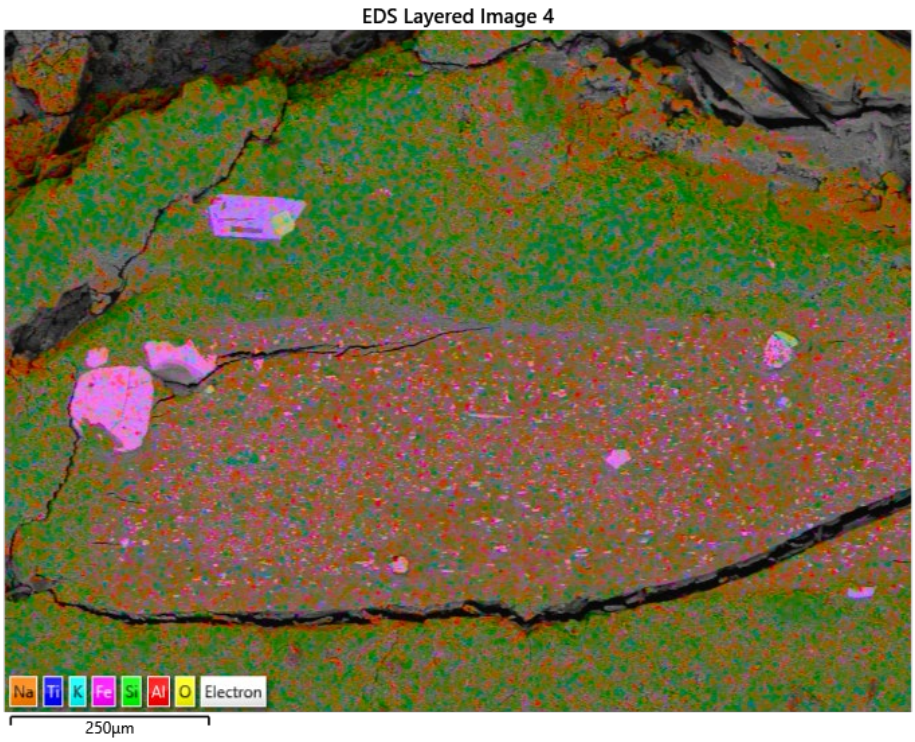

Figure 4.13: SEM–EDS elemental maps of sample MC05. (A) Compositionally distinct domain within a predominantly Si-rich groundmass, characterised by relative enrichment in Na, Al, and Fe compared to the surrounding matrix. Zr is present around the area but undefined. (B) Compositionally banded domain within the groundmass, defined by variation relative to the surrounding Si- and Na-rich matrix. The banded region is enriched in Fe, Al, K, and Ti, and contains numerous small Fe–Ti-rich grains.

MC08

Elemental mapping of sample MC08 reveals a predominantly Si-rich groundmass, with diffuse distribution of Na, K, and Al throughout the matrix. The groundmass is compositionally homogeneous within domains, but exhibits pronounced chemical variation along discontinuous linear and circular features.

Several mapped areas display well-defined circular to semi-circular areas, characterised by distinct boundaries enriched in Al, Fe, K and locally Ca relative to their interiors. Within these areas the groundmass is predominantly Si-dominant and chemically uniform, whereas the boundaries form interconnected networks of enriched material.

Irregular domains containing grains of Al and Fe are also present in higher concentrations. These occur along surfaces and discontinuities and contrast with the smoother, more homogenous groundmass.

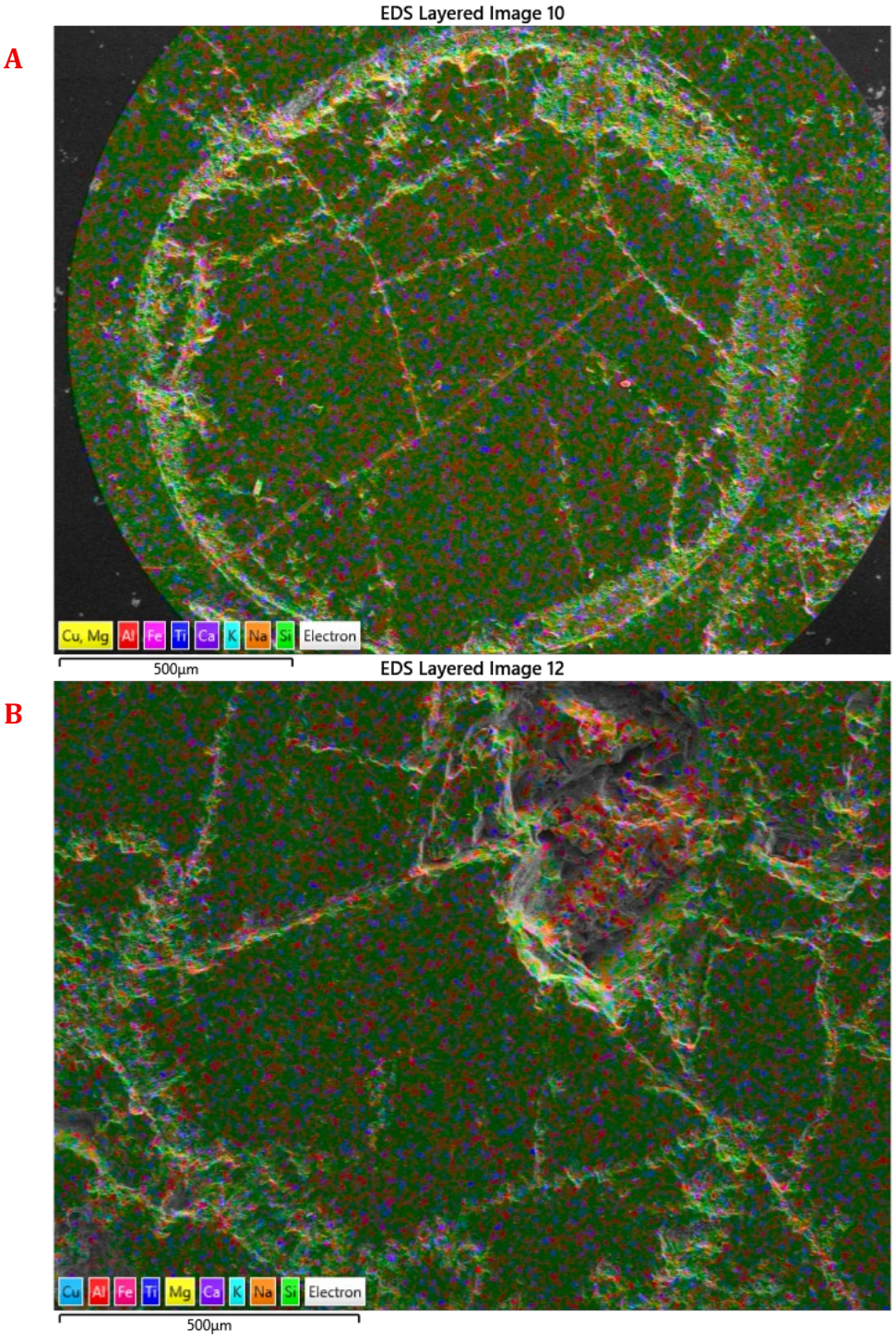

Figure 4.14: SEM–EDS maps of sample MC08

(A) Sub-circular domain within a predominantly Si-rich groundmass, defined by a network of curvilinear fractures and boundaries enriched in Al, Na, and Fe relative to the surrounding matrix.

(B) Fracture-controlled zone showing localized enrichment in Al, Na, Fe, and minor Ti. These enriched regions contrast with the more compositionally uniform Si-rich groundmass, indicating element redistribution along structural pathways.

MC13

Elemental mapping of sample MC13 reveals a predominantly Si-rich groundmass, with minor but pervasive concentrations of Al, K, and Na. The groundmass is compositionally uniform at the microscale, although it is cross-cut by several irregular to curvilinear fracture features.

These fractures are distinctly enriched in Al and Na relative to the surrounding matrix and form interconnected pathways throughout the sample. They represent zones of localized chemical heterogeneity, likely reflecting element redistribution along structural discontinuities.

One mapped area contains a compositionally distinct elongate phenocryst, characterised by relative enrichment in Na and Al, consistent with a feldspar phase. This crystal is sharply bounded and is spatially associated with Fe–Ti oxide grains as well as Zr-bearing groundmass.

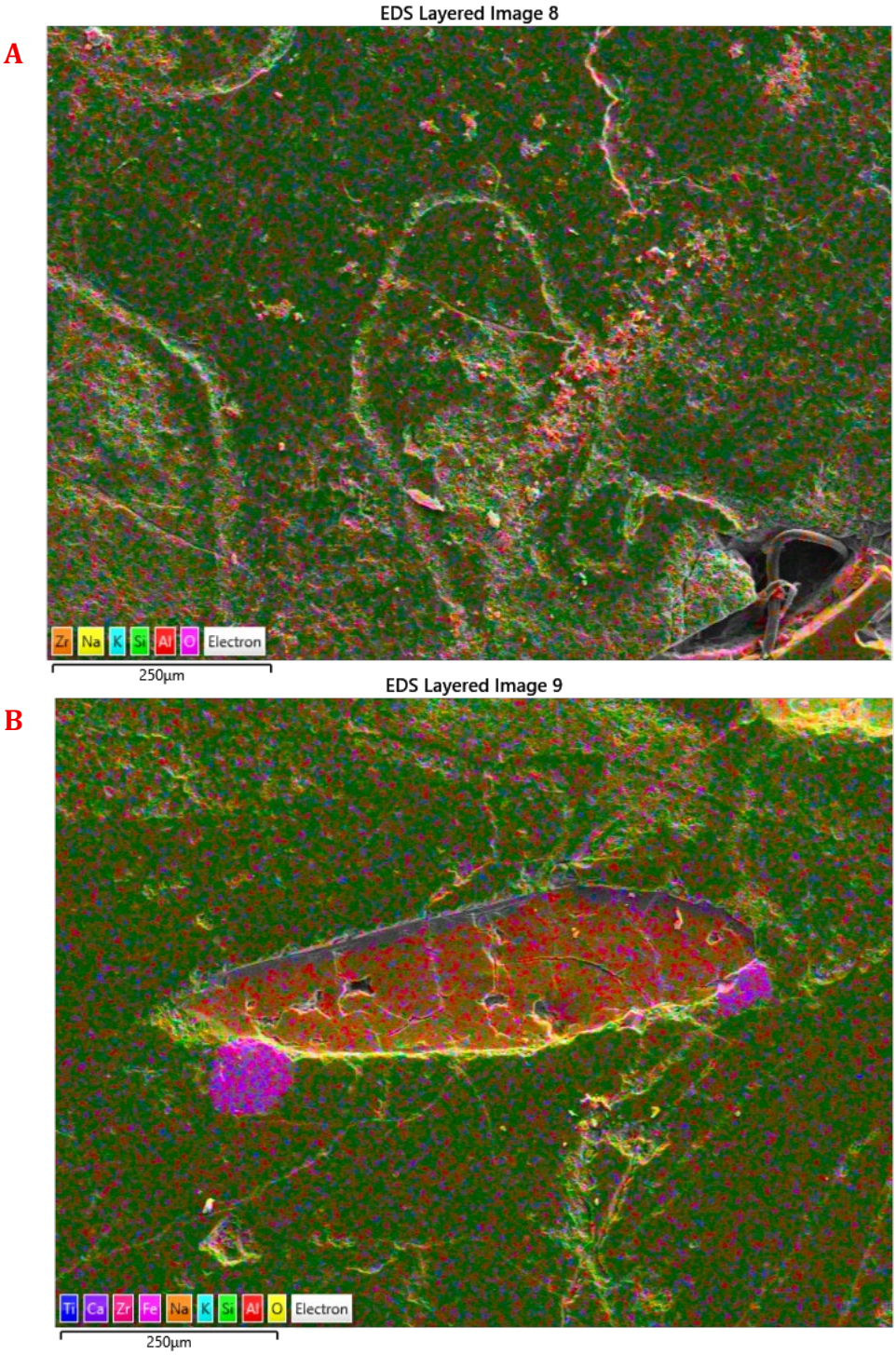

Figure 4.15: SEM–EDS maps of sample MC13

(A) Predominantly Si-rich groundmass cross-cut by a network of irregular to curvilinear fractures enriched in Al and Na, forming interconnected pathways of chemical heterogeneity

(B) Elongate, sharply bounded phenocryst enriched in Na and Al, consistent with a feldspar phase, set within a Si-rich groundmass. The phenocryst is spatially associated with Zr-bearing phases and Fe–Ti oxides, which occur as discrete accessory grains within the surrounding matrix.

4.3 X-Ray Powder Diffraction (XRD)

4.3.1 Methods

Bulk whole-rock samples were crushed to a fine powder using a tungsten-carbide ring mill to ensure homogenisation. Powdered samples were mounted as random aggregates and analysed using a Panalytical Empyrean Series 2 X-Ray Diffractometer housed in the STEM Division, University of Waikato.

The instrument was calibrated prior to analysis using a quartz standard to ensure accurate peak positioning. Diffraction patterns were collected over a 2θ range of 5–80° (Cu Kα radiation), with a counting time of 50 seconds per step.

Phase identification was performed using HighScore Plus (Malvern Panalytical) with reference to the ICDD Powder Diffraction File (PDF) database. Initial phase identification used the automatic search-match function. All phases were subsequently manually verified through inspection of the three strongest diagnostic reflections (d_1, d_2, d_3) for each mineral phase to ensure robust identification. Phase abundances were not quantified; XRD analysis was performed for qualitative phase identification only.

A separate XRD analysis was conducted on the heavy mineral fraction of sample MC18 following heavy liquid separation (SPT) as part of the zircon extraction workflow. These results are not directly comparable to the whole-rock diffraction patterns and are discussed in Section 4.5.3 and 5.3.

4.3.2 Results

XRD analysis was conducted on 22 samples (MC01–MC22 inc. heavy fraction MC18).

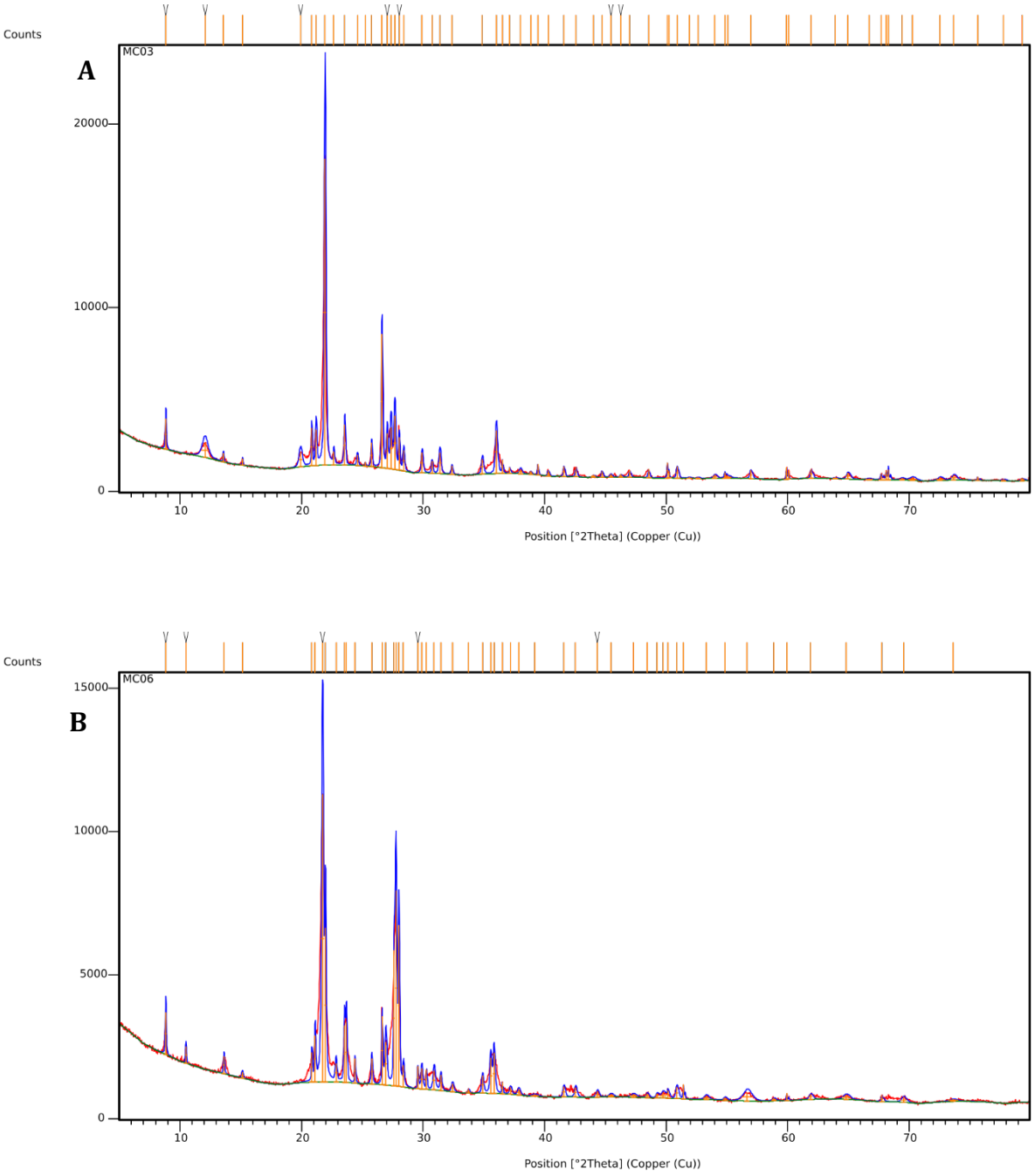

Figure 4.16: Representative X-ray diffraction patterns for selected samples from the Kaimai Rhyolite Dome Complex. (A) MC03, (B) MC06, (C) MC02, (D) MC11, (E) MC15 (Waiteariki Ignimbrite), (F) MC01, (G) MC10 (altered), and (H) MC18 (andesite). Rhyolitic samples are characterised by dominant cristobalite reflections at ~22° 2θ with subordinate quartz and feldspar peaks. The andesite sample MC18 displays reflections corresponding to albite and diopside.

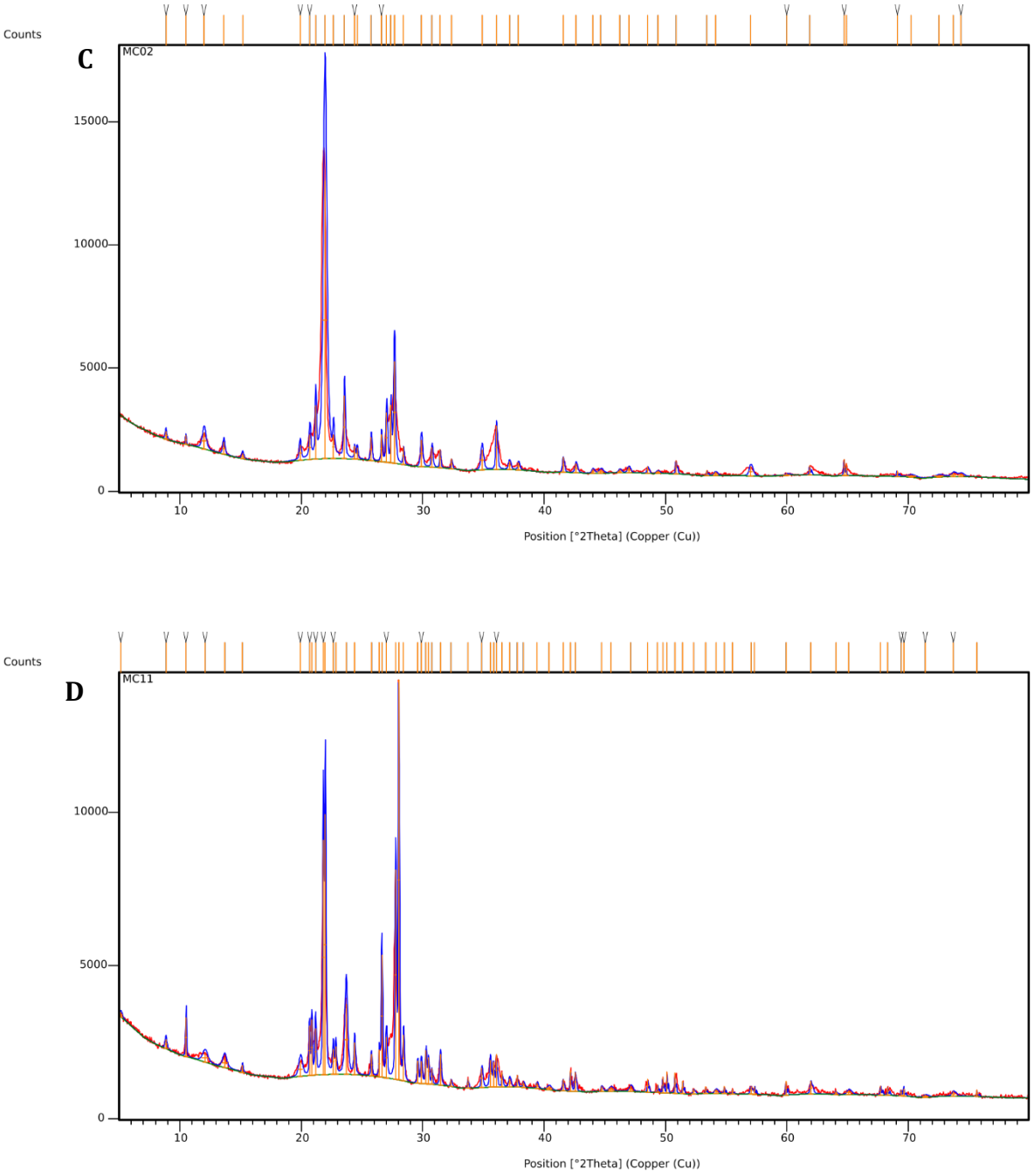

Figure 4.16 (Continued): (C) MC02 and (D) MC11 (Waitеariki Ignimbrite).

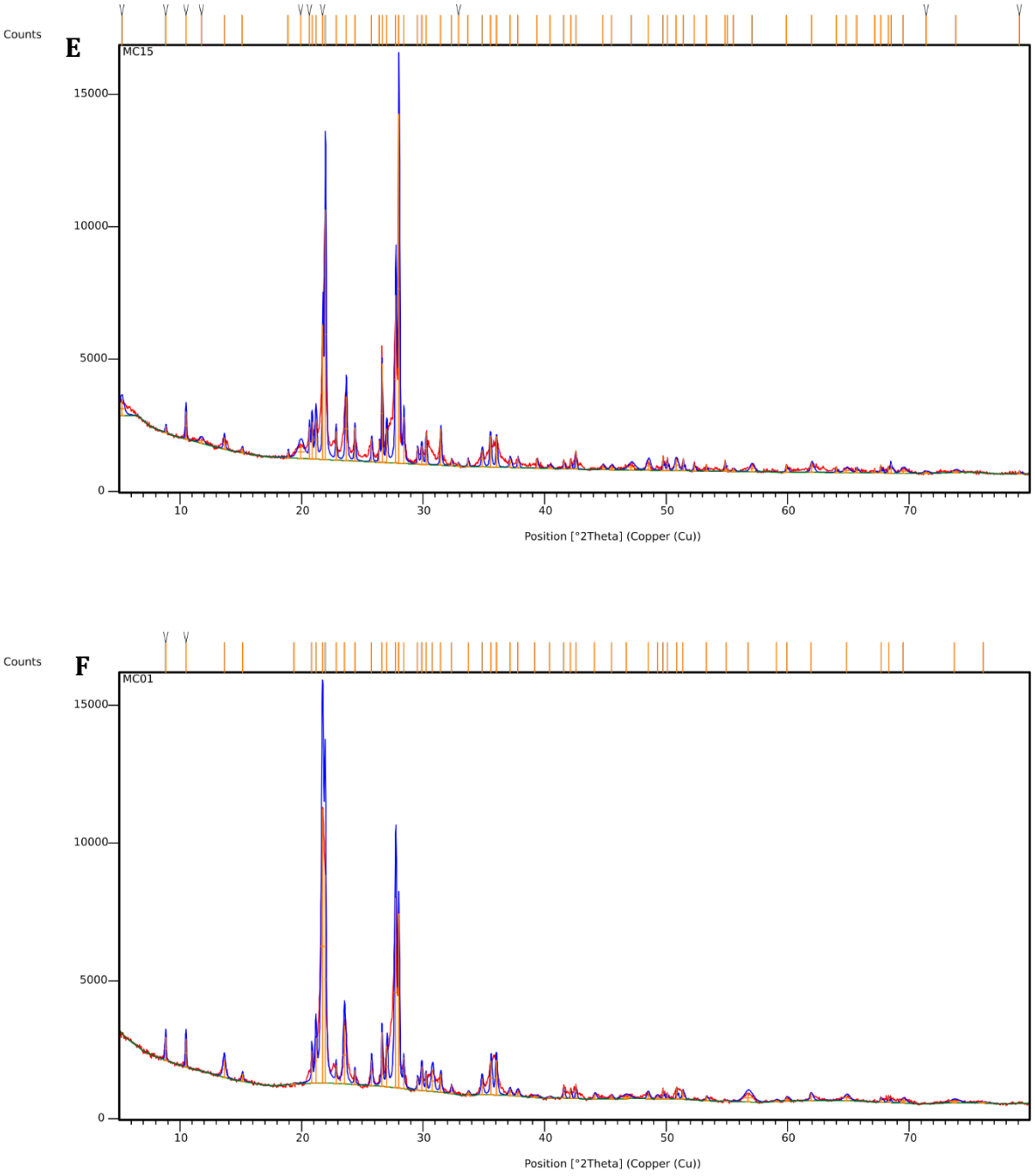

Figure 4.16 (Continued): (E) MC15 (Waitearikiki Ignimbrite) and (F) MC01.

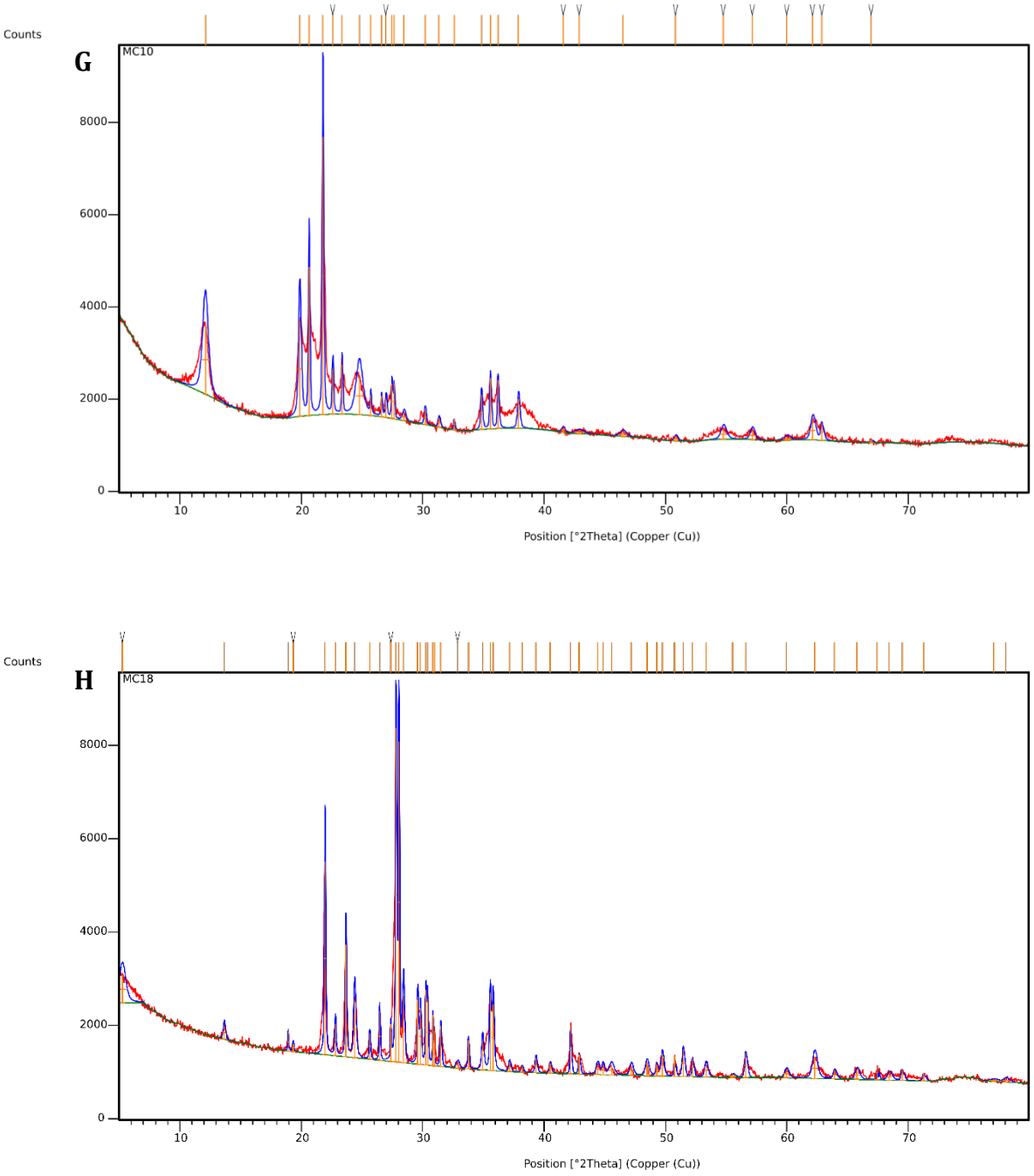

Figure 4.16 (Continued): (G) MC10 (altered) and (H) MC18 (andesite).

4.3.2.1 Silica Polymorph Assemblages (MC01–MC17, MC19–MC22)

Whole-rock XRD patterns for samples MC01-MC17 and MC19-MC22 are characterised by strong reflections corresponding to high-temperature silica polymorphs. All samples display a dominant reflection at approximately 22° 2θ (d ≈ 4.04 Å), accompanied by supporting reflections at approximately 36° 2θ (d ≈ 2.49 Å) and 31–32° 2θ (d ≈ 2.84 Å). These correspond to the three strongest reflections of cristobalite, which is identified as the principal crystalline silica phase in all rhyolitic samples. Cristobalite peaks are sharp and well resolved.

A subordinate reflection at approximately 26.6° 2θ (d ≈ 3.34 Å) confirms the presence of quartz in all samples. Quartz reflections are consistently of lower relative intensity compared to cristobalite in most samples.

Reflections within the 27–28° 2θ region are compatible with tridymite; however, significant peak overlap with cristobalite and feldspar reflections prevents unequivocal confirmation in the bulk powder patterns. No uniquely diagnostic tridymite-only reflections were resolved. Tridymite was flagged in MC10 by the automatic search–match routine in HighScore Plus and is therefore treated as tentative.

No broad amorphous feature was observed in the 20–30° 2θ region, and silica peaks are sharp and well defined.

Feldspar Phases

Feldspar phases are present across the majority of samples. Alkali feldspars consistent with sanidine, orthoclase and microcline were identified in multiple samples (e.g., MC02, MC03, MC04, MC05, MC07, MC08, MC12–MC17, MC19–MC22). Plagioclase feldspars were also detected in MC01, MC06, MC09, MC11, MC15, MC18, MC19.

Due to peak overlap between alkali feldspar and plagioclase polymorphs in bulk powder patterns, precise discrimination between individual feldspar species is limited.

Feldspar reflections are generally of lower relative intensity compared to cristobalite but are consistently present across the dataset.

Mafic and Alteration Phases

Mafic phases are volumetrically minor within the rhyolitic samples. A clinopyroxene phase was identified in MC01 by automatic phase matching within HighScore Plus. Diagnostic reflections compatible with clinopyroxene occur within the 29–31° 2θ region and at higher-angle positions; however, these reflections are of low intensity relative to dominant feldspar and silica peaks.

Low-intensity reflections between approximately 7–15° 2θ are present in several samples (e.g., MC03). These peaks are weak and lack consistent higher-order harmonic reflections required for definitive identification of 7 Å or 10 Å clay minerals. In most cases, the 24–25° 2θ region is dominated by overlapping feldspar and silica reflections, preventing confident resolution of kaolinite-type second-order peaks.

Kaolinite was flagged by automatic phase identification in MC10 and represents the only clay mineral suggested within the rhyolitic dataset. MC10 exhibits comparatively stronger low-angle intensity relative to other samples. No additional clay phases were confidently resolved in the remaining rhyolitic samples.

MC18 (Andesite)

Sample MC18 displays a diffraction distinct from the rhyolitic samples. The assemblage is characterised by albite and diopside with minor cristobalite. Diopside reflections are well resolved and occur at moderate relative intensity compared to the silica and feldspar phases.

The mineral assemblage differs from the cristobalite-dominated rhyolitic samples and reflects a more mafic bulk composition. No clay minerals were confidently identified in MC18.

Table 4.2: Summary of XRD-identified mineral phases across all analysed samples.

The table presents the distribution of silica polymorphs, feldspar phases (K-feldspar and plagioclase), mafic minerals, and alteration products identified by X-ray diffraction (XRD). Cristobalite is the dominant silica phase across most samples, with quartz present in several units. K-feldspar occurs predominantly as sanidine and orthoclase, with minor microcline, while plagioclase compositions range from albite to anorthite. Mafic phases are sparse but include clinopyroxene and diopside, and alteration minerals such as kaolinite are locally present.

Sample	Silica Polymorphs		K-Feldspar	Plagioclase	Mafic Phases	Clay/Alteration
MC01	Cristobalite	Quartz	Orthoclase	Anorthite	Clinopyroxene	
MC02	Cristobalite		Microcline			
MC03	Cristobalite	Quartz	Sanidine			
MC04	Cristobalite	Quartz	Sanidine			
MC05	Cristobalite	Quartz	Microcline			
MC06		Quartz	Sanidine	Albite		
MC07	Cristobalite		Sanidine			
MC08	Cristobalite		Sanidine			
MC09	Cristobalite	Quartz	Sanidine	Albite		
MC10	Cristobalite					Kaolinite
MC11		Quartz		Albite		
MC12	Cristobalite		Orthoclase			
MC13	Cristobalite		Sanidine			
MC14	Cristobalite		Microcline			
MC15	Cristobalite	Quartz	Orthoclase	Anorthite		
MC16	Cristobalite		Sanidine			
MC17	Cristobalite		Sanidine			
MC18 - bulk	Cristobalite			Albite	Diopside	
MC18 -HF					Diopside	
MC19		Quartz	Orthoclase	Anorthite		
MC20	Cristobalite	Quartz	Sanidine			
MC21	Cristobalite	Quartz	Sanidine			
MC22	Cristobalite		Sanidine			

4.4 X-Ray Fluorescence (XRF)

4.4.1 XRF Methods

Whole-rock samples were dried at 105 °C overnight to remove moisture prior to preparation. Dried samples were crushed to a fine, homogeneous powder using a tungsten-carbide ring mill.

Loss on Ignition (LOI)

Loss on ignition (LOI) was determined by heating approximately 1–2 g of powdered sample at 1100 °C for 1 hour. Weight loss or gain was calculated as a percentage of the initial mass.

Major Element Analysis

Major oxides were analysed using fused glass beads prepared at a flux-to-sample ratio of 10:1 (8.0 g flux : 0.8 g sample ± 0.003 g). Samples were fused at 1050 °C using a Claisse Neo automated fusion furnace with 0.1–0.2 g NH_4I as a releasing agent.

The flux composition ("12:22") consisted of 35.3 % lithium tetraborate and 64.7 % lithium metaborate.

Trace Element Analysis

Trace elements were analysed using pressed powder pellets prepared with polyvinyl alcohol (PVA) as a binder. Approximately 7–8 g of sample powder was mixed with ~0.7 g PVA prior to pellet pressing.

Instrumentation and Quality Control

All analyses were conducted using a Bruker S8 TIGER wavelength-dispersive X-ray fluorescence (WDS-XRF) spectrometer housed in the School of Science, University of Waikato.

USGS reference materials AGV-2, GSP-2, and RGM-2 were analysed at the beginning of the analytical session, after the first 11 samples (midway through the run), and again at the end of the session to monitor instrumental drift and analytical precision. These standards were selected to span a silica range comparable to that of the

analysed samples. Measured values showed good agreement with published reference compositions.

Two samples (MC09 and MC10) were re-analysed to confirm LOI values due to initially elevated results. The repeat analyses yielded consistent LOI values.

Data Treatment and Screening

Major element oxide concentrations were normalised to 100 wt.% on an anhydrous basis following subtraction of loss on ignition (LOI). Normalisation was applied to minimise the influence of volatile components and to allow direct comparison of primary major-element systematics between samples.

Samples with LOI > 5 wt.% were excluded from major-element trend analysis and Harker diagram interpretation, as elevated LOI indicates significant volatile-bearing secondary components that may obscure primary magmatic compositions. Under this criterion, MC09 (LOI = 7.24 wt.%) and MC10 (LOI = 12.14 wt.%) were excluded from major-element interpretation.

4.4.2 Results

Whole-rock major element compositions determined by X-ray fluorescence (XRF) are presented in Table 4.4. Major element concentrations are reported as wt.% and all iron is expressed as Fe_2O_3.

Loss on ignition (LOI) values for all analysed samples are shown in Table 4.4. Two samples (MC09 and MC10) yielded elevated LOI values (>5 wt.%) and were excluded from major-element trend analysis and Harker diagram interpretation shown in Table 4.3. Consequently, 20 samples are considered in the following major-element comparisons.

Table 4.3: Loss on ignition (LOI) values for whole-rock samples. Samples with LOI > 5 wt.% were excluded from geochemical interpretation.

Sample	LOI	Included
MC09	7.24	No
MC10	12.14	No

Table 4.4: Whole-rock major (wt.%) and trace element (ppm) compositions determined by X-ray fluorescence (XRF). Major element oxides are normalised to 100 wt.% on a volatile-free basis following subtraction of loss on ignition (LOI), and all Fe is expressed as Fe_2O_3.

Sample Name	**MC01**	**MC02**	**MC03**	**MC04**	**MC05**	**MC06**	**MC07**
Major elements (XRF, wt.%) (Normalised to 100% on LOI, volatile free; LOI and Total are original values; all Fe expressed as Fe_2O_3)							
SiO_2	74.07	75.80	74.17	74.81	74.35	74.22	77.61
TiO_2	0.28	0.26	0.32	0.31	0.30	0.28	0.12
Al_2O_3	13.95	15.24	17.62	15.56	17.08	14.04	13.18
Fe_2O_3	2.21	2.08	2.60	2.53	2.38	2.19	2.80
MnO	0.05	0.04	0.03	0.02	0.04	0.05	0.02
MgO	0.41	0.18	0.22	0.19	0.07	0.33	0.04
CaO	1.88	0.66	0.43	0.76	0.59	1.78	0.38
Na_2O	3.66	2.22	1.38	2.15	1.81	3.63	2.20
K2O	3.43	3.47	3.21	3.63	3.34	3.42	3.61
P_2O_5	0.07	0.06	0.04	0.04	0.04	0.06	0.03
LOI	0.78	3.07	4.87	3.50	4.62	1.03	3.28
Trace elements (XRF, ppm)							
Sc	6	7	4	4	6	5	6
V	24	18	27	27	23	26	13
Cr	7	0	0	0	0	0	0
Co	39	12	12	21	14	26	16
Ni	4	4	3	4	4	4	3
Cu	6	6	10	6	7	6	7
Zn	36	33	32	36	45	36	31
Ga	15	15	17	16	16	15	18
As	8	7	7	7	5	6	10
Rb	127	136	122	138	125	110	142
Sr	133	60	39	67	64	131	33
Y	22	55	16	13	21	16	23
Zr	148	154	169	164	157	150	134
Nb	6	7	7	7	7	6	8
Mo	4	4	4	4	4	4	4
Sn	2	5	6	2	4	3	5
Sb	3	3	3	1	2	3	3
Cs	1	6	2	2	1	1	8
Ba	808	799	631	712	865	842	681
La	21	142	18	7	33	17	12
Ce	47	50	35	34	39	48	43
Nd	26	91	19	14	21	21	21
Tl	1	1	1	1	1	1	1
Pb	12	14	13	14	15	14	16
Th	13	16	16	16	16	16	19
U	3	4	4	4	4	3	4

Table 4.4: Continued

Sample Name	MC08	MC11	MC12	MC13	MC14	MC15	MC16
Major elements (XRF, wt.%) (Normalised to 100% on LOI, volatile free; LOI and Total are original values; all Fe expressed as Fe_2O_3)							
SiO_2	77.01	69.88	76.59	76.76	76.67	69.03	76.53
TiO_2	0.10	0.47	0.10	0.10	0.10	0.42	0.10
Al_2O_3	13.17	17.25	13.11	13.49	13.35	17.53	13.50
Fe_2O_3	1.76	4.50	1.43	1.48	1.44	4.09	1.67
MnO	0.02	0.02	0.03	0.02	0.02	0.03	0.01
MgO	0.04	0.31	0.05	0.04	0.04	0.47	0.04
CaO	0.63	2.41	0.86	0.67	0.78	2.70	0.70
Na_2O	3.17	2.74	3.69	3.29	3.52	3.30	3.39
K_2O	4.07	2.37	4.12	4.13	4.05	2.39	4.03
P_2O_5	0.03	0.04	0.03	0.03	0.03	0.04	0.03
LOI	1.58	3.67	0.75	1.43	1.13	2.79	1.50
Trace elements (XRF, ppm)							
Sc	5	10	6	7	5	10	5
V	6	53	4	5	4	52	7
Cr	0	0	0	0	0	5	0
Co	24	21	42	19	22	21	22
Ni	3	3	3	3	3	3	3
Cu	5	5	5	5	5	9	6
Zn	35	55	36	31	35	81	31
Ga	16	20	15	16	15	19	16
As	9	7	9	9	8	5	9
Rb	153	84	153	152	148	90	146
Sr	48	163	61	53	55	180	53
Y	27	14	30	67	25	20	21
Zr	121	179	124	120	120	163	119
Nb	8	6	7	7	7	6	7
Mo	4	4	4	4	4	4	4
Sn	5	3	6	3	4	3	4
Sb	4	2	3	2	2	2	1
Cs	5	2	4	10	9	0	5
Ba	872	591	931	927	885	632	877
La	15	2	28	51	15	7	18
Ce	56	25	66	58	62	37	59
Nd	24	13	32	45	25	13	26
Tl	1	0	1	1	1	0	1
Pb	18	9	19	16	20	9	19
Th	19	10	17	17	17	10	17
U	5	3	4	3	4	3	4

Table 4.4: Continued

Sample Name	**MC17**	**MC18**	**MC19**	**MC20**	**MC21**	**MC22**
Major elements (XRF, wt.%) (Normalised to 100% on LOI, volatile free; LOI and Total are original values; all Fe expressed as Fe_2O_3)						
SiO2	76.21	56.82	73.86	77.78	76.39	72.22
TiO2	0.10	0.76	0.28	0.10	0.11	0.41
Al2O3	14.45	17.29	14.05	13.56	14.93	15.92
Fe2O3	1.39	7.26	2.25	1.55	1.53	2.86
MnO	0.02	0.13	0.04	0.02	0.03	0.02
MgO	0.03	5.05	0.38	0.08	0.08	0.22
CaO	0.67	8.55	1.95	0.38	0.56	1.65
Na2O	3.27	2.96	3.73	2.30	2.74	3.77
K2O	3.83	1.06	3.39	4.18	3.59	2.88
P2O5	0.03	0.13	0.07	0.04	0.03	0.05
LOI	2.33	0.52	1.40	2.31	2.47	2.13
Trace elements (XRF, ppm)						
Sc	5	25	6	6	6	7
V	5	191	29	3	5	26
Cr	0	108	0	0	0	0
Co	22	49	40	13	20	23
Ni	3	25	4	3	3	3
Cu	5	25	7	7	5	8
Zn	35	73	36	32	56	44
Ga	17	18	16	16	17	17
As	9	8	7	9	9	9
Rb	128	39	109	170	135	81
Sr	47	223	135	33	46	120
Y	23	19	24	22	30	29
Zr	119	95	155	117	123	274
Nb	7	4	6	8	7	7
Mo	4	4	4	4	4	5
Sn	5	4	3	4	4	3
Sb	2	2	1	2	2	2
Cs	0	4	2	3	6	2
Ba	890	270	836	742	944	786
La	17	1	23	17	37	33
Ce	64	29	60	41	43	52
Nd	25	13	23	23	41	29
Tl	1	0	1	1	1	1
Pb	20	3	11	22	23	14
Th	18	4	14	20	22	13
U	4	3	3	5	4	3

4.4.2.1 Major Element Compositions

Major element oxide concentrations for the analysed samples are presented in Table 4.4. Samples are grouped by lithology: KRDC rhyolite (17 samples), Waitеariki Ignimbrite (MC11, MC15), and a basement andesite collected from the JSWAP Quarry (MC18).

The KRDC rhyolite samples form a compositionally restricted high-silica suite, with SiO_2 ranging from 72.22 to 77.78 wt.% and most samples clustering between 73 and 77 wt.%. TiO_2 concentrations range from 0.10 to 0.41 wt.%, Al_2O_3 from 13.11 to 17.62 wt.%, and Fe_2O_3 from 1.39 to 2.86 wt.%. MgO ranges from 0.03 to 0.41 wt.% and CaO from 0.38 to 1.95 wt.%. MnO is consistently low, ranging from 0.01 to 0.05 wt.%. Alkali oxides show moderate variation, with Na_2O ranging from 1.38 to 3.77 wt.% and K_2O ranging from 2.22 to 4.18 wt.%. P_2O_5 concentrations are low, varying between 0.03 and 0.07 wt.%.

The Waitеariki Ignimbrite samples (MC11, MC15) record lower SiO_2 values of 69.88 and 69.03 wt.%, respectively, and systematically higher mafic components than the KRDC rhyolites. TiO_2 ranges from 0.42 to 0.47 wt.%, Al_2O_3 from 17.25 to 17.53 wt.%, and Fe_2O_3 from 4.09 to 4.50 wt.%. MgO values of 0.31–0.47 wt.% and CaO values of 2.41–2.70 wt.% both exceed the KRDC rhyolite ranges. Na_2O and K_2O range from 2.74–3.30 wt.% and 2.37–2.39 wt.%, respectively.

The basement andesite sample MC18 is compositionally distinct from both the KRDC and Waitеariki units. It records 56.82 wt.% SiO_2, 0.76 wt.% TiO_2, 17.29 wt.% Al_2O_3, 7.26 wt.% Fe_2O_3, 5.05 wt.% MgO, 8.55 wt.% CaO, 0.13 wt.% MnO, 2.96 wt.% Na_2O, 1.06 wt.% K_2O, and 0.13 wt.% P_2O_5. These values reflect its andesitic composition and position it as a candidate parental magma rather than a member of the KRDC rhyolite suite.

Trace element concentrations determined by XRF are also presented in Table 4.4.

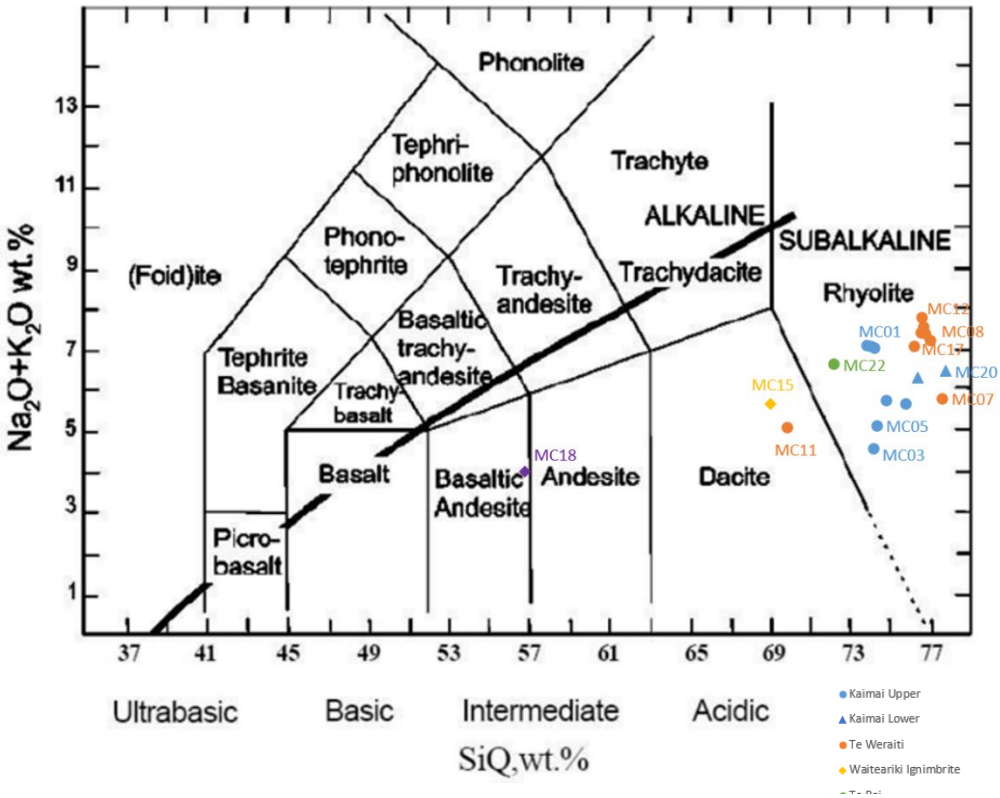

Figure 4.17: Total alkali–silica (TAS) classification diagram showing whole-rock compositions of analysed samples determined by XRF. Fields after Le Bas et al. (1986). Most samples plot within the rhyolite field, whereas several samples plot within the dacite field. One sample (MC18) plots within the andesite field.

4.4.2.2 Rock Classification

Whole-rock compositions plotted on the Total Alkali-Silica (TAS) diagram are shown in Figure 4.17. The majority of analysed samples plot within the rhyolite field, reflecting their high SiO_2 contents and elevated total alkali concentrations.

Several samples plot within the dacite field, reflecting slightly lower SiO_2 and total alkali contents relative to the rhyolitic compositions. Notably the Waitekariki Ignimbrite sits in this field along with a member of the Te Weraiti Unit. One sample MC18 plots within the Basaltic Andesite/Andesite field on the border and is identified as the Te Weraiti Basement Andesite.

Overall, the dataset is dominated by high-silica compositions, with the majority of samples plotting within the acidic compositional range, aside from MC18.

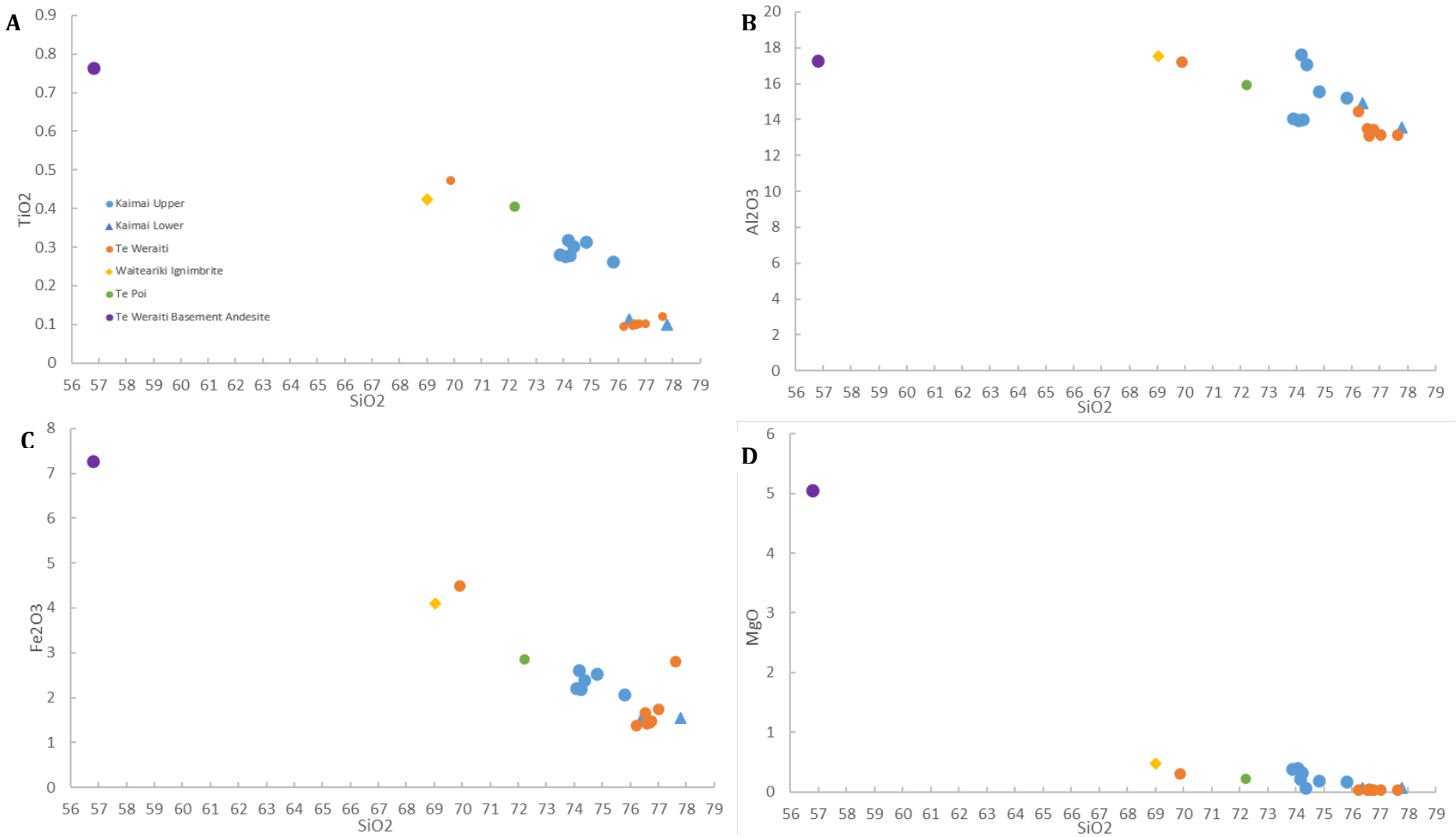

Figure 4.18: Major element Harker variation diagrams for XRF data. Panels show TiO_2 (A), Al_2O_3 (B), Fe_2O_3 (C), and MgO (D) plotted against SiO_2.

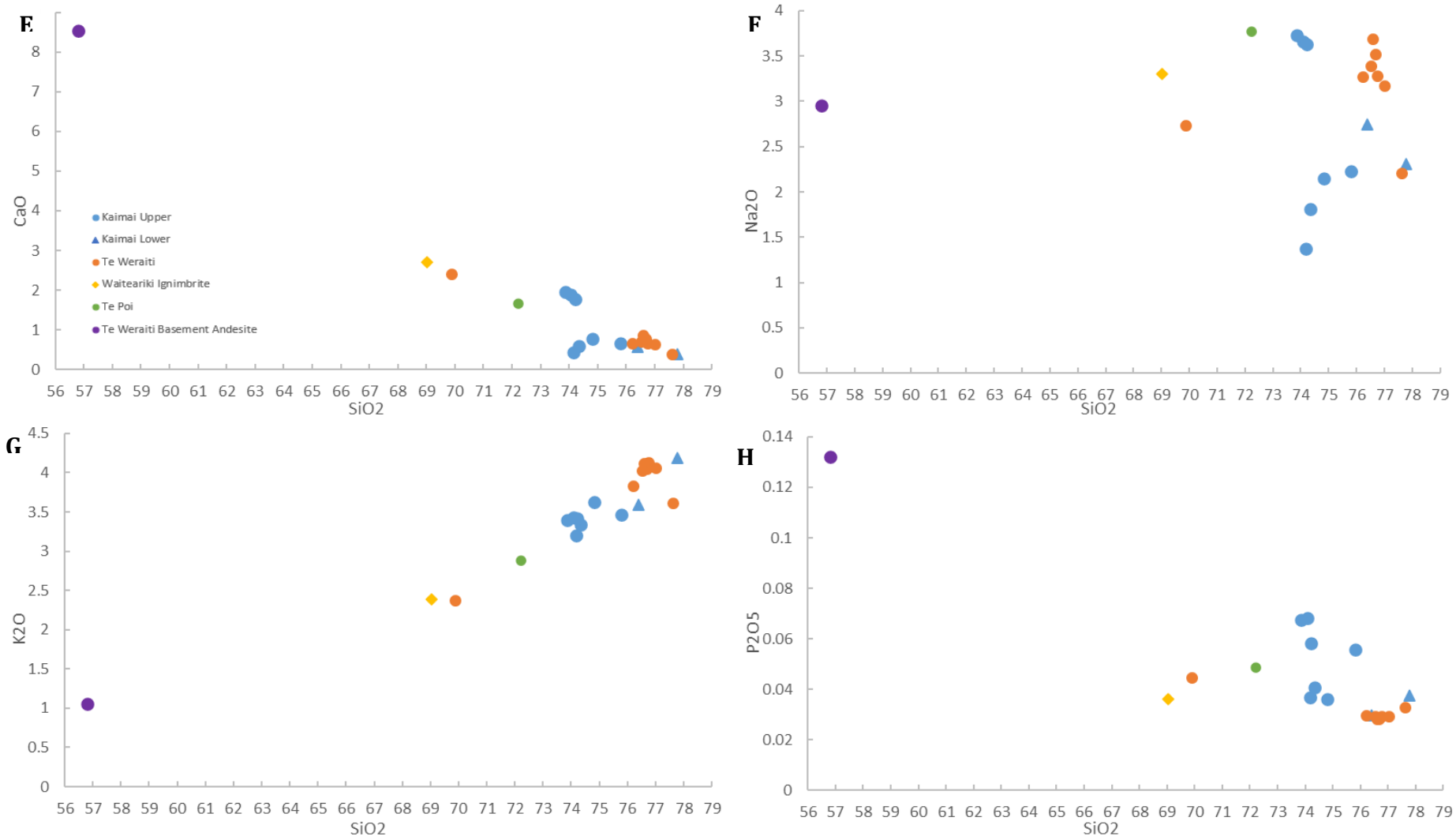

Figure 4.19: Major element Harker variation diagrams for XRF data. Panels show CaO (E), Na_2O (F), K_2O (G), and P_2O_5 (H) plotted against SiO_2.

4.4.2.3 Major Element Variation Diagrams

Major element variation diagrams plotted against SiO_2 are shown in Figure 4.18 and Figure 4.19. Several oxides display systematic relationships with increasing SiO_2. TiO_2, Fe_2O_3, MgO, and CaO generally decrease with increasing SiO_2, forming negative correlations across the dataset. In contrast, K_2O shows a positive relationship with SiO_2, whereas Na_2O displays moderate scatter and does not define a clear systematic trend. Al_2O_3 shows moderate variability across the compositional range, and P_2O_5 remains low in abundance throughout the dataset.

Most samples cluster between approximately 73 and 78 wt.% SiO_2. Kaimai Upper samples form a relatively tight cluster within this range, although some internal scatter is present in several oxides. Kaimai Lower samples overlap with the Kaimai Upper field and do not appear compositionally distinct on the major element variation diagrams. Te Weraiti samples also overlap with the Kaimai samples but generally plot toward the higher-SiO_2 end of the main silicic cluster.

The Waitеariki Ignimbrite plots separately from the main silicic cluster at lower SiO_2 values, whereas the Te Poi sample lies intermediate between the lower-SiO_2 samples and the main rhyolitic grouping. The Te Weraiti Basement Andesite plots distinctly apart from all other samples at substantially lower SiO_2 and higher TiO_2, Fe_2O_3, MgO, and CaO values.

4.5 LA-ICP-MS

4.5.1 Methods

Trace element concentrations were determined by laser ablation inductively coupled plasma mass spectrometry (LA-ICP-MS) using a RESOlution-SE 193 nm excimer laser ablation system coupled to an Agilent 8900 triple-quadrupole (QQQ) ICP-MS at the University of Waikato. The triple-quadrupole configuration enables effective removal of spectral interferences, improving detection limits and analytical accuracy for trace elements.

Analyses were performed directly on solid glass samples. Laser ablation was conducted using a 60 μm spot diameter, with an average fluence of ~5 J cm^{-2} and pulse energy of approximately 3.7 mJ. External calibration was achieved using NIST SRM 610 and 612 reference glasses, which were analysed repeatedly throughout the analytical session to monitor instrument stability and drift.

Data reduction was undertaken using *iolite*. Aluminium was employed as the internal standard during concentration calculation. Internal standard concentrations were derived from XRF major element analyses, with oxide weight percent values converted to elemental weight percent prior to import into the reduction workflow. Sample names in the internal standard file were matched precisely to the "Comment" field entries in the laser log file to ensure correct assignment of internal standard values to each ablation spot.

Time-resolved signals were inspected during data reduction to ensure stable signal intervals were selected for integration. Final trace element concentrations are reported in ppm.

Rare earth element (REE) concentrations were normalised to CI chondrite values for construction of REE patterns. Multi-element spider diagrams were normalised to primitive mantle values.

4.5.2 Results

Table 4.5: Whole-rock trace and rare earth element compositions (ppm) determined by laser ablation inductively coupled plasma mass spectrometry (LA-ICP-MS) on glass fusion beads.

Sample Name	**MC01**	**MC02**	**MC03**	**MC04**	**MC05**	**MC06**	**MC07**
Trace elements (LA-ICP-MS, ppm)							
Sc	6.47	6.38	6.94	6.01	6.8	6.24	5.67
V	33.86	27.26	36.91	33.8	33.8	31.2	18.99
Rb	114.5	115.5	114	113.2	113.5	95.2	129.7
Cs	5.79	5.09	4.42	5.03	3.74	6.1	6.04
Ba	717	681	581.8	599	780	730	616.5
Sr	119.3	51.8	32.36	60	56.42	114.7	25.87
Y	19.65	49.15	15.13	10.29	19.74	14	20.54
Zr	149.5	148.7	184.2	158.8	164.8	148.6	127.3
Nb	5.71	6.22	6.96	6.02	6.57	5.64	7.85
Ta	0.646	0.587	0.684	0.591	0.611	0.596	0.78
Ti	1979	1827	2303	2073	2167	1956	1113
La	23.35	108.1	22.64	12.64	33.12	21.52	18.18
Ce	38.97	37.72	29.1	23.42	36.18	35.23	32.85
Pr	4.56	23.65	3.79	2.35	5.42	4.03	4.28
Nd	16.89	84.1	13.13	8.79	19.12	14.89	16.96
Sm	3.33	14.63	2.09	1.55	3.14	2.64	3.91
Eu	0.573	2.46	0.333	0.26	0.618	0.519	0.368
Gd	3.11	12.42	2.05	1.49	2.97	2.41	3.59
Tb	0.456	2.024	0.349	0.247	0.464	0.326	0.553
Dy	3.02	12.13	2.23	1.64	2.85	2.31	3.75
Ho	0.642	2.15	0.475	0.34	0.636	0.444	0.753
Er	1.88	6.06	1.52	1.1	1.69	1.44	2.17
Tm	0.301	0.808	0.223	0.16	0.251	0.206	0.334
Yb	2.16	5.68	1.47	1.35	1.83	1.57	2.16
Lu	0.339	0.765	0.23	0.191	0.277	0.226	0.325
Pb	12.537	12.153	13.750	12.983	14.153	13.043	16.600
Th	11.51	13.08	13.95	11.67	13.56	11.66	16.42
U	2.56	3.22	2.99	2.74	2.86	2.512	2.98

Table 4.5 (Continued)

Sample Name	**MC08**	**MC11**	**MC12**	**MC13**	**MC14**	**MC15**	**MC16-17**
Trace elements (LA-ICP-MS, ppm)							
Sc	6.25	10.85	6.34	6.49	6.35	11.82	6.29
V	13.88	63.9	12.51	12.11	12.4	60.1	14.12
Rb	136.4	74.97	137.9	138.4	137.24	78.8	133.5
Cs	7.2	3.07	7.4	6.26	7.27	3.22	6.73
Ba	741	529.6	802.2	794	776.2	550.2	766.1
Sr	39.63	152.5	50.97	42.75	45.77	160.4	43.57
Y	23.84	12.17	26.32	59.64	22.4	17.43	18.7
Zr	114.8	184.9	116.7	112.6	111.9	176.4	112.6
Nb	6.69	6.29	6.16	6.42	6.45	5.58	6.29
Ta	0.616	0.547	0.67	0.582	0.66	0.426	0.621
Ti	1000	3310	1020	1002	1004	2907	996
La	20.94	11.85	25.87	41.07	22.64	14.87	21.51
Ce	41.55	23.19	48.04	41.38	44.2	26.52	41.36
Pr	4.81	2.566	6	9.16	5.22	3.09	4.67
Nd	18.89	9.98	23.14	36.2	19.15	12.18	17.85
Sm	3.97	2	4.81	7.85	3.93	2.35	3.59
Eu	0.419	0.628	0.564	1.09	0.43	0.699	0.427
Gd	3.79	1.72	4.27	8.33	3.72	2.54	3.08
Tb	0.604	0.303	0.686	1.361	0.587	0.412	0.52
Dy	4.17	2.05	4.42	8.95	3.91	2.53	3.37
Ho	0.841	0.445	0.916	1.995	0.82	0.578	0.688
Er	2.46	1.36	2.78	5.8	2.31	1.9	1.88
Tm	0.364	0.227	0.391	0.785	0.318	0.262	0.26
Yb	2.62	1.62	2.93	5.6	2.42	1.82	1.88
Lu	0.36	0.245	0.389	0.841	0.327	0.328	0.26
Pb	15.080	10.433	15.393	13.843	15.327	9.673	14.543
Th	14.06	7.93	13.32	13.83	13.8	7.31	13.73
U	3.023	1.769	2.79	2.72	2.84	1.584	2.63

Table 4.5 (Continued)

Sample Name	MC18	MC19	MC20	MC21	MC22
Sc	22.5	8.44	6.76	5.54	7.39
V	146.1	42.24	14.29	12.66	30.35
Rb	25.61	121.8	162.6	114.4	65.4
Cs	1.477	7.68	7.71	7.06	3.276
Ba	192.9	926	661.3	728.7	646
Sr	170.2	154.3	26.41	34.5	102.3
Y	14.27	27.54	20.18	24.16	25.26
Zr	72.25	189.6	114.1	109.7	257.1
Nb	2.7	7.27	7.62	6.43	6.35
Ta	0.224	0.817	0.824	0.643	0.552
Ti	4079	2583	1040	1002	2594
La	6.82	33.41	21.82	30.37	31.48
Ce	14.36	48.3	36.07	36.36	37.38
Pr	1.826	6.61	4.37	8.03	6.13
Nd	8.16	23.96	16.89	30.23	23.17
Sm	2.13	4.57	3.76	5.98	4.36
Eu	0.667	0.838	0.37	0.622	0.928
Gd	2.3	3.94	3.3	5.05	4.12
Tb	0.38	0.681	0.614	0.714	0.619
Dy	2.47	4.24	3.55	4.46	3.81
Ho	0.509	0.907	0.7	0.921	0.878
Er	1.53	2.72	2.16	2.45	2.52
Tm	0.215	0.396	0.29	0.362	0.375
Yb	1.448	2.84	2.26	2.44	2.54
Lu	0.216	0.447	0.285	0.365	0.374
Pb	4.087	16.120	17.223	16.747	12.687
Th	2.205	14.51	16.31	14.66	9.68
U	0.489	3.25	3.11	2.83	2.073

Trace elements concentrations determined by LA-ICP-MS are presented in Table 4.5. Concentrations of incompatible elements such as Rb and Ba vary significantly across the dataset, whereas high field strength elements (HFSE) including Nb, Ta, Zr, and Y show a narrower compositional range. Rb concentrations range from 25.61 to 162.6 ppm, while Ba varies from 72.25 to 926 ppm. Sr concentrations range from 25.87 to 170.2 ppm. Among the HFSE, Zr ranges from 72.25 to 257.1 ppm, Nb from 2.70 to 7.85 ppm, Ta from 0.224 to 0.824 ppm, and Y from 10.29 to 59.64 ppm.

Most samples fall within relatively restricted compositional ranges; however sample MC18 is distinct, displaying notably lower concentrations of incompatible elements including Rb, Ba, Zr, Nb, Ta, Pb, Th, and U relative to the rest of the dataset, while

exhibiting much higher concentrations of Sr, V, and Ti. Additional variation is observed in MC13, which shows elevated rare earth element concentrations, and MC22, which contains the highest Zr concentration recorded in the dataset.

4.5.2.1 Rare Earth Elements

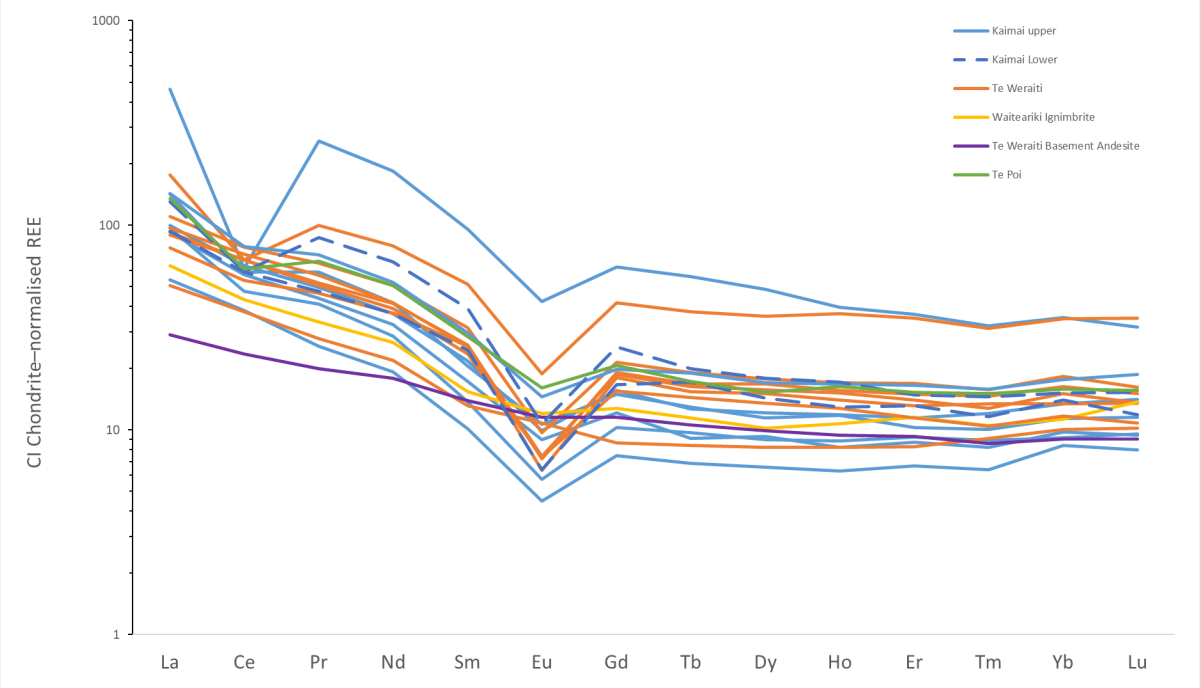

Figure 4.20: Chondrite-normalised rare earth element (REE) patterns for samples from the Tauranga Volcanic Centre analysed by LA-ICP-MS. Normalisation values are from Sun and McDonough (1989). All samples show enrichment of light rare earth elements (LREE) relative to heavy rare earth elements (HREE) and display negative Eu anomalies of variable magnitude.

Chondrite-normalised rare earth element (REE) patterns for all analysed samples are shown in Figure 4.20. All samples display enrichment in light rare earth elements (LREE) relative to heavy rare earth elements (HREE). Lanthanum concentrations are elevated relative to the middle and heavy REE, producing steep slopes from La to Sm. In contrast, the HREE (Gd–Lu) display relatively flat patterns with limited variation between samples. A pronounced negative Eu anomaly is present in all samples, with the magnitude of the anomaly varying between units. Overall, the REE patterns are broadly similar in shape across the dataset, although samples from the Kaimai Upper unit display slightly higher overall REE abundances compared to the other units. Samples from Te Weraiti, the Waitеariki Ignimbrite, and Te Poi define broadly comparable REE patterns, whereas the Te Weraiti Basement Andesite is characterised by lower overall REE abundances, particularly within the LREE, while maintaining a similar HREE pattern.

4.5.2.2 Primitive Mantle-Normalised

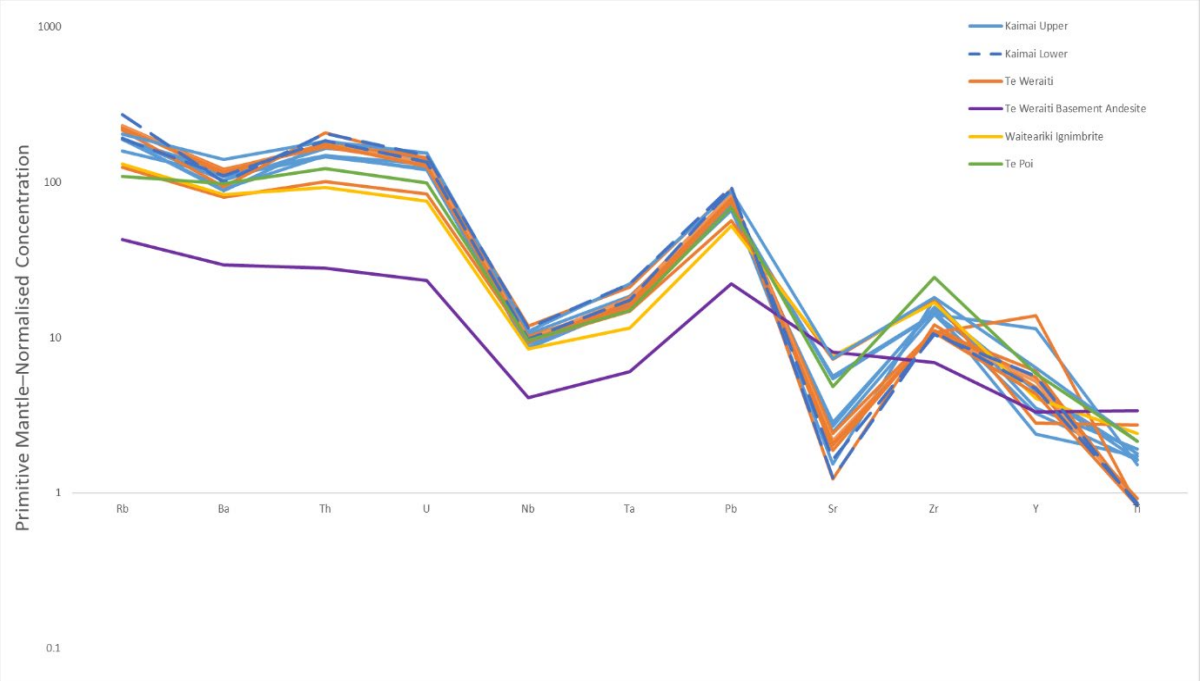

Figure 4.21: Primitive mantle-normalised multi-element spider diagram for samples from the Tauranga Volcanic Centre analysed by LA-ICP-MS. Normalisation values are from Sun and McDonough (1989). All samples display enrichment in large-ion lithophile elements (LILE) relative to high-field strength elements (HFSE), with pronounced Nb–Ta troughs and positive Pb anomalies. Variations between eruptive units are expressed primarily in amplitude rather than overall pattern shape.

Primitive mantle-normalised multi-element patterns are shown in Figure 4.21. All samples display enrichment in large-ion lithophile elements (LILE; Rb, Ba, Th, and U) relative to high-field strength elements (HFSE; Nb and Ta). A pronounced negative Nb-Ta anomaly is present in all samples, accompanied by a positive Pb anomaly. Strontium also displays a strong negative anomaly relative to neighbouring elements. Overall, the multi-element patterns are broadly similar between units, with variations occurring primarily in the overall amplitude of enrichment rather than in the shape of the patterns. The sample of the Te Weraiti Basement Andesite displays lower overall trace element abundances relative to the other units. Minor variability is observed in the Zr and Y concentrations between units.

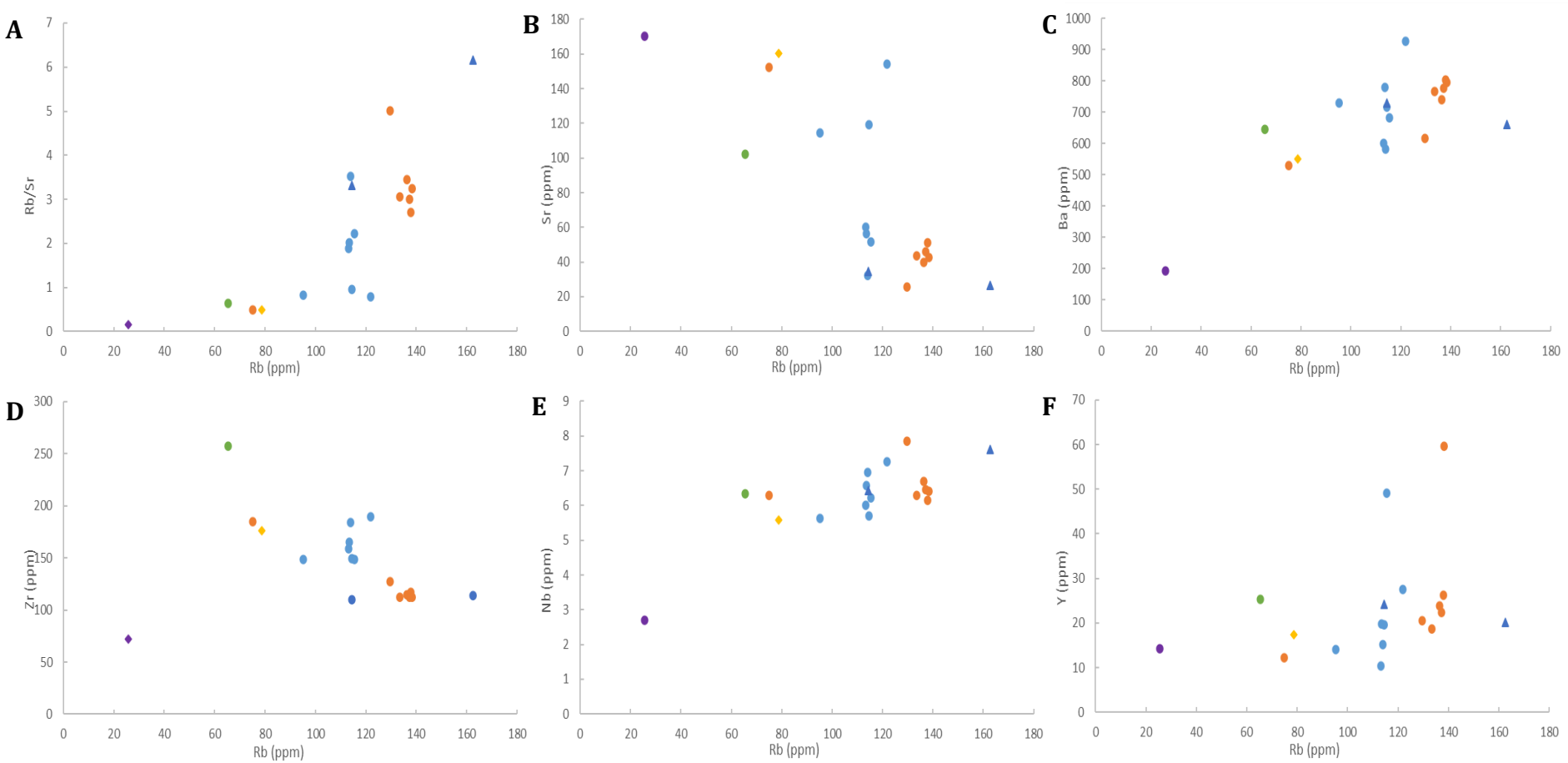

Figure 4.22: Trace element variation diagrams for samples from the Kaimai Rhyolite Dome Complex. Element concentrations (ppm) are plotted against Rb (ppm) to illustrate trace element behaviour during magmatic differentiation. (A) Rb/Sr vs Rb, (B) Sr vs Rb, (C) Ba vs Rb, (D) Zr vs Rb, (E) Nb vs Rb, (F) Y vs Rb.

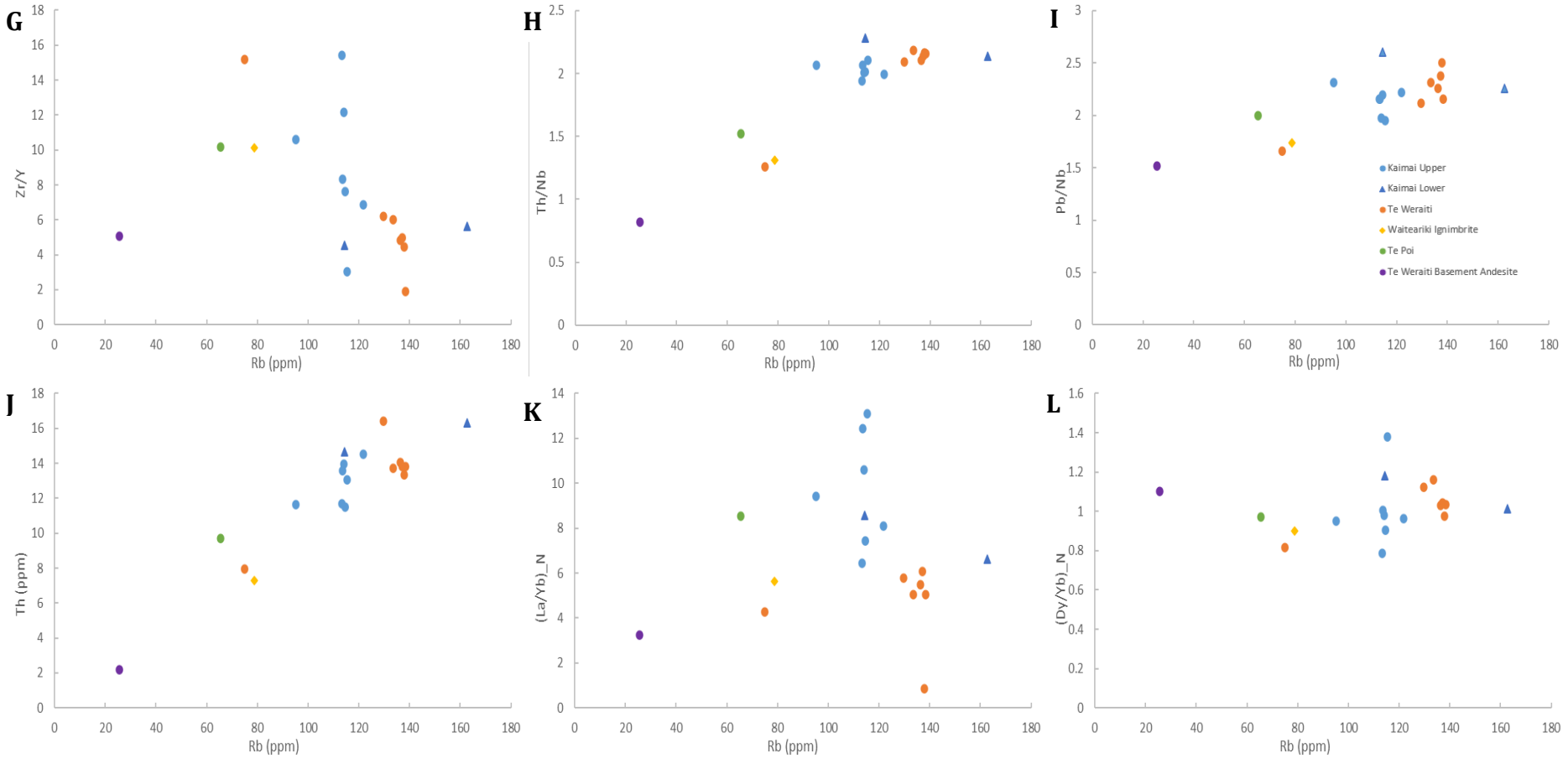

Figure 4.22 (Continued): Trace element variation diagrams for samples from the Kaimai Rhyolite Dome Complex. (G) Zr/Y vs Rb, (H) Th/Nb vs Rb, (I) Pb/Nb vs Rb, (J) Th vs Rb, (K) (La/Yb)N vs Rb, (L) (Dy/Yb)N vs Rb.

4.5.2.3 Trace Element Variation against Rb

Trace element variation diagrams for selected elements plotted against Rb are shown in Figure 4.22. The ratio Rb/Sr increases with increasing Rb, reflecting progressive enrichment of Rb relative to Sr across the dataset. In contrast, Sr concentrations generally decrease with increasing Rb, although considerable scatter is present. Ba displays a weak positive correlation with Rb, with higher Ba concentrations generally associated with higher Rb values. Zr exhibits a weak bell-shaped relationship with Rb, with concentrations increasing at moderate Rb values before decreasing at higher Rb concentrations; most samples cluster between approximately 110 and 190 ppm. Nb concentrations show a slight increase with increasing Rb, although scatter is present across the dataset. Y concentrations display considerable variability and do not define a clear trend with Rb.

Trace element ratios also show variable behaviour. Zr/Y displays moderate scatter with no clear correlation with Rb, whereas Th/Nb and Pb/Nb ratios generally increase with increasing Rb. Th concentrations also increase with increasing Rb, defining a broadly positive relationship. Rare earth element ratios show limited systematic variation, with La/Yb displaying moderate scatter across the dataset and Dy/Yb remaining relatively constant with increasing Rb.

Samples from Te Weraiti define a relatively tight cluster across the diagrams, with the exception of one sample that plots closer to the Waitearikiki Ignimbrite. The Kaimai Upper and Lower samples display greater scatter but occupy broadly similar compositional fields. The Te Weraiti Basement Andesite plots distinctly from the other units but generally follows the same overall trends. The Te Poi sample plots close to the Waitearikiki Ignimbrite and follows similar trends across the diagrams.

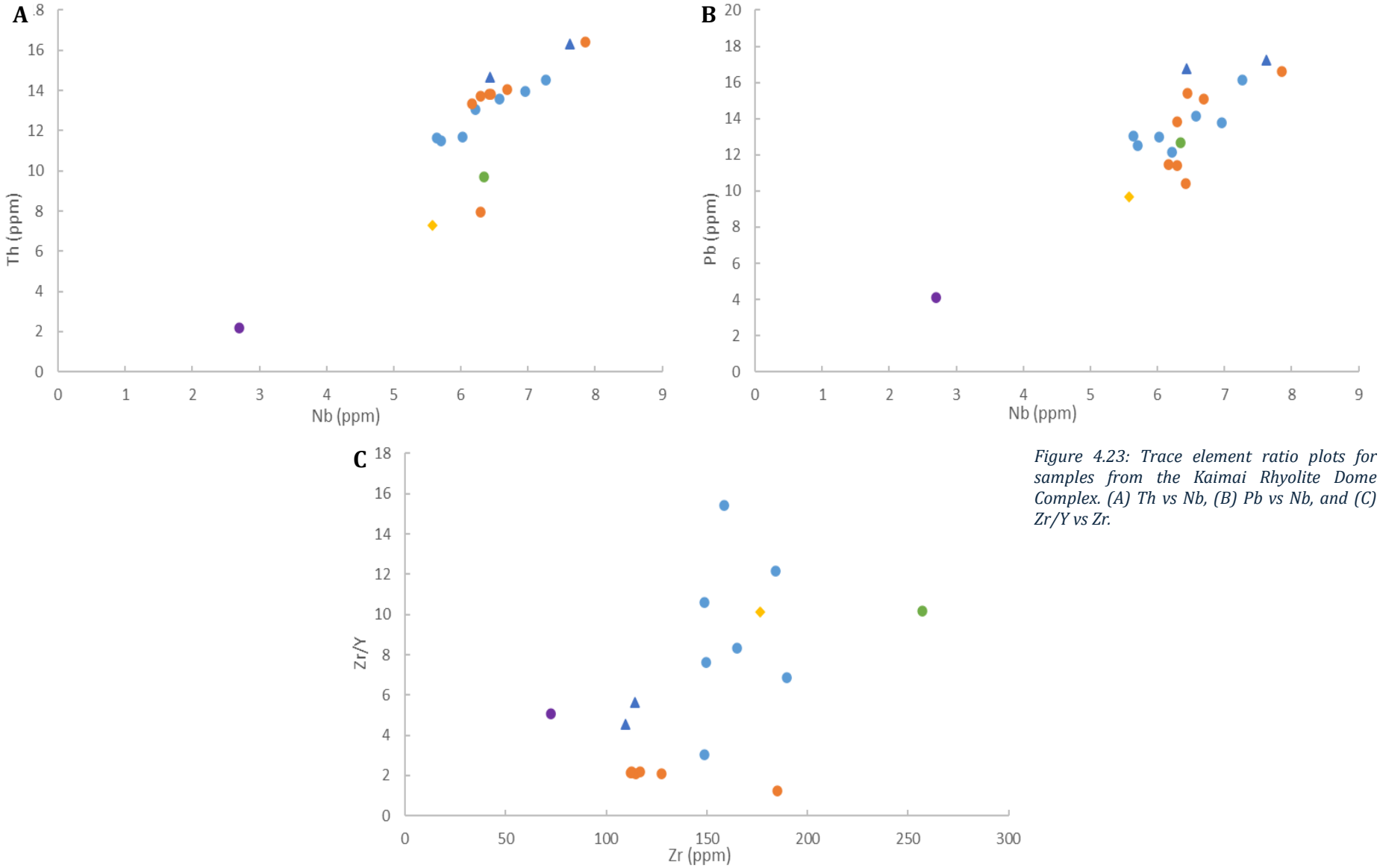

Figure 4.23: Trace element ratio plots for samples from the Kaimai Rhyolite Dome Complex. (A) Th vs Nb, (B) Pb vs Nb, and (C) Zr/Y vs Zr.

4.5.2.4 Trace Element Ratios

Trace element ratio diagrams are shown in Figure 4.23. Th and Pb both display positive correlations with Nb, with concentrations increasing systematically across the dataset. Most samples form a clustered trend between approximately 5–8 ppm Nb, whereas the Te Weraiti Basement Andesite plots distinctly at lower Nb, Th, and Pb concentrations.

The Zr/Y vs Zr diagram shows considerable scatter across the dataset. Most samples cluster between approximately 100 and 200 ppm Zr, although several samples extend to higher Zr concentrations. The Te Weraiti Basement Andesite again plots at comparatively low Zr and Zr/Y values relative to the other units. Overall, the samples define broadly similar compositional fields, with differences expressed mainly through variations in trace element abundance rather than distinct compositional grouping.

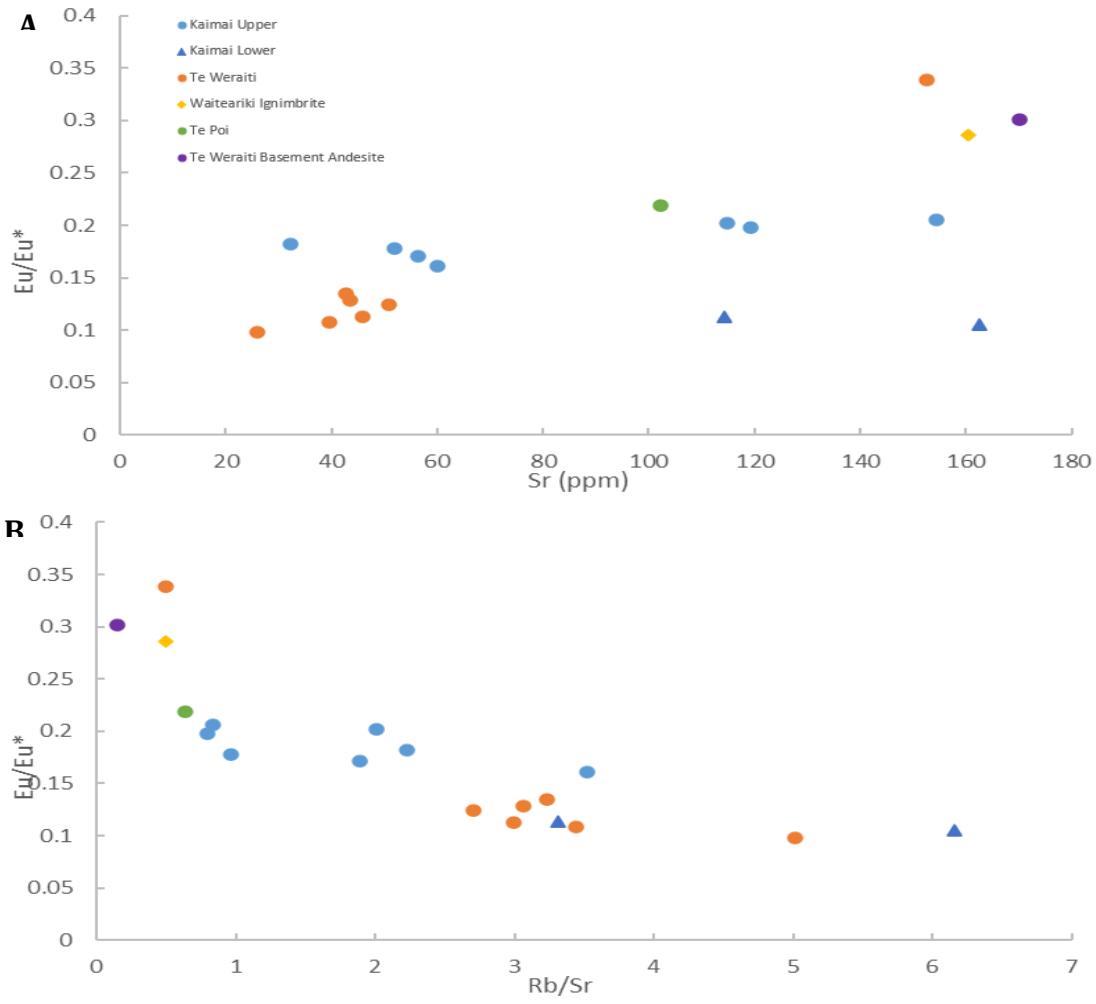

Figure 4.24: Eu anomaly variation diagrams for samples from the Kaimai Rhyolite Dome Complex. (A) Eu/Eu vs Sr and (B) Eu/Eu* vs Rb/Sr.*

Eu anomaly variation diagrams are shown in Figure 4.24. Eu/Eu* values across the dataset range from approximately 0.10 to 0.35. The *Eu/Eu vs Sr** diagram shows a weak positive relationship, with higher Eu/Eu* values generally associated with higher Sr concentrations. The Kaimai Lower samples deviate slightly from this trend and display a comparatively flatter relationship. In contrast, the *Eu/Eu vs Rb/Sr** diagram shows an overall negative relationship, with Eu/Eu* values decreasing as Rb/Sr increases.

Samples from Te Weraiti form a relatively tight cluster in both diagrams, whereas samples from the Kaimai Upper and Lower units display greater scatter. The Te Weraiti Basement Andesite plots distinctly from the main sample population, similar to the Waitearikiki Ignimbrite, with both units exhibiting comparatively higher Eu/Eu* and Sr values, and lower Rb/Sr values relative to the other units.

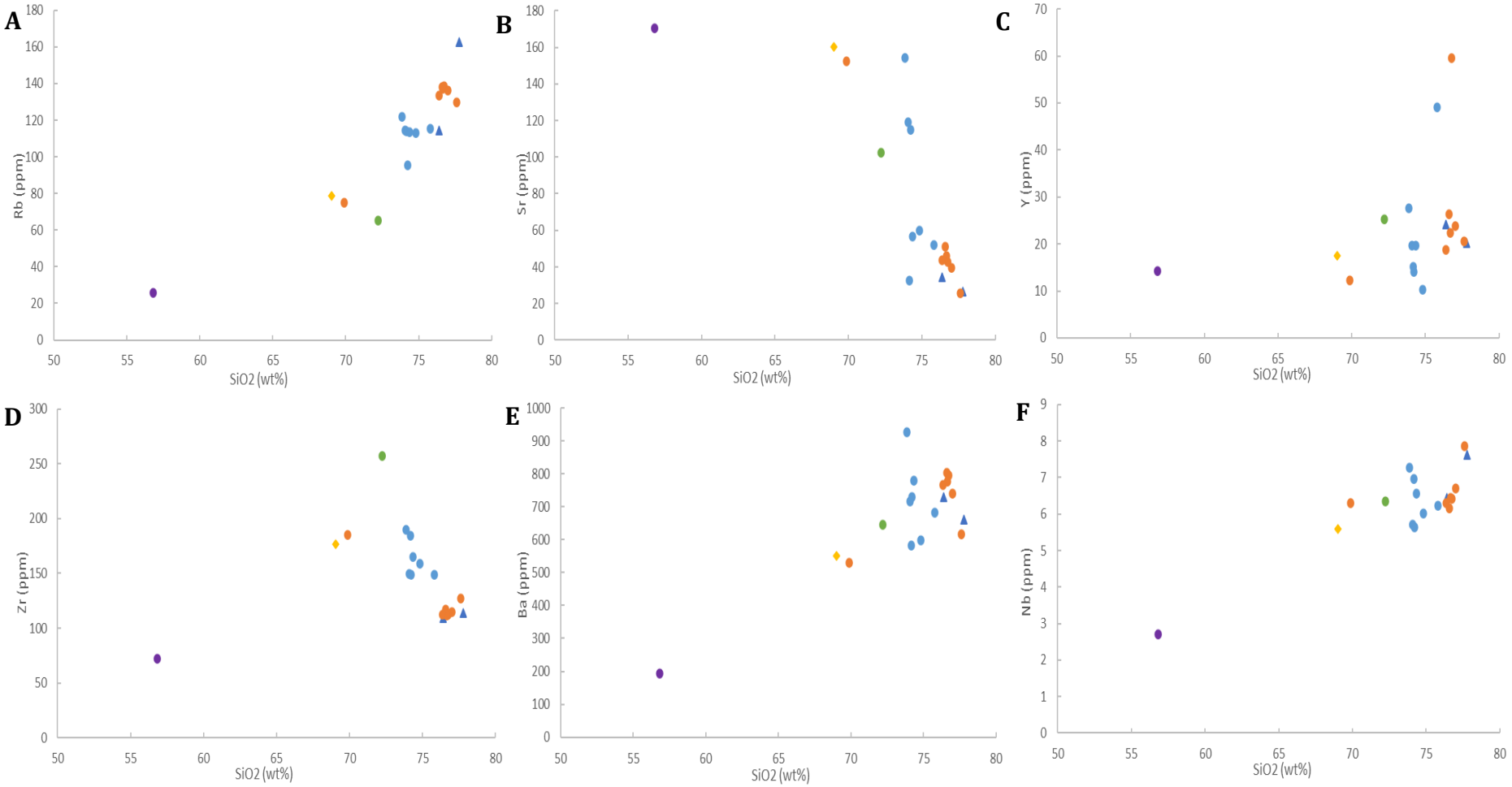

Figure 4.25: Trace element variation diagrams for samples from the Kaimai Rhyolite Dome Complex showing trace element concentrations plotted against SiO_2 (wt%). (A) Rb vs SiO_2, (B) Sr vs SiO_2, (C) Y vs SiO_2, (D) Zr vs SiO_2, (E) Ba vs SiO_2, and (F) Nb vs SiO_2.

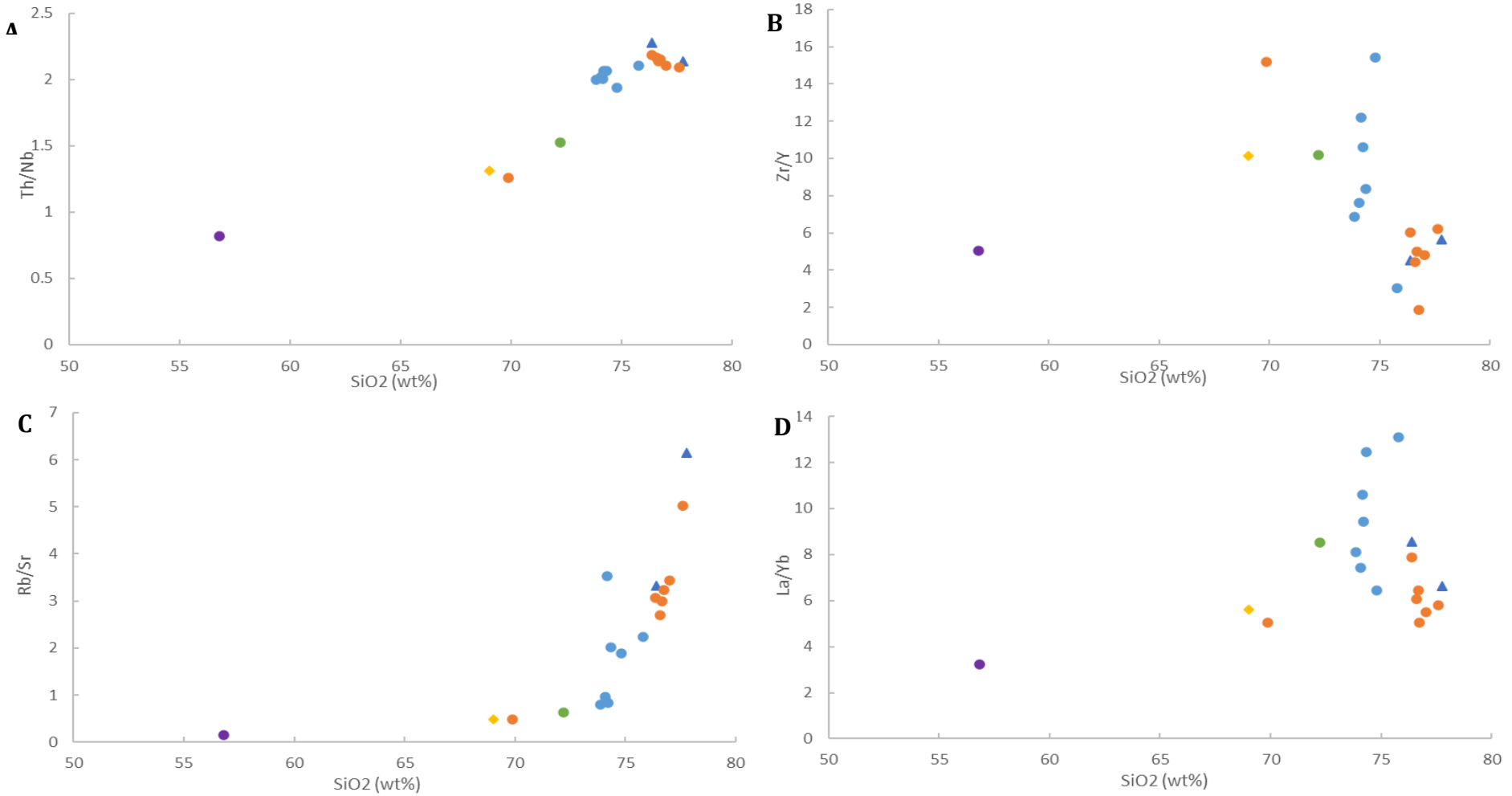

Figure 4.26: Trace element ratio diagrams for samples from the Kaimai Rhyolite Dome Complex showing element ratios plotted against SiO_2 (wt%). (A) Th/Nb vs SiO_2, (B) Zr/Y vs SiO_2, (C) Rb/Sr vs SiO_2, and (D) La/Yb vs SiO_2.

4.5.2.5 Trace Element Variation against SiO_2

Trace element variation diagrams for selected elements plotted against SiO_2 are shown in Figure 4.25. Rb, Ba, and Nb generally increase with increasing SiO_2. In contrast, Sr displays a negative relationship with SiO_2, with concentrations decreasing as silica increases, although some scatter is present. Zr shows a weak bell-shaped trend, with concentrations increasing at intermediate SiO_2 values before decreasing at higher SiO_2. Y displays moderate scatter and does not define a clear systematic trend with SiO_2.

Trace element ratio variation diagrams plotted against SiO_2 are shown in Figure 4.26. Th/Nb displays a positive relationship with SiO_2, with higher Th/Nb ratios occurring at higher silica contents. In contrast, Zr/Y displays a weak right-skewed bell-shaped relationship with SiO_2, with higher values occurring at intermediate to moderately high silica contents and lower values at the highest SiO_2 concentrations. Rb/Sr displays a steep positive relationship with SiO_2, with ratios increasing markedly toward higher silica compositions. La/Yb displays moderate variability but generally higher values at higher SiO_2 concentrations.

Samples from the Kaimai Upper and Lower units display moderate variability in Th/Nb, Zr/Y, Rb/Sr, and La/Yb ratios, although most values cluster within a similar compositional range. Te Weraiti samples define a relatively tight cluster across the diagrams, indicating limited variation in trace element ratios within this unit. The Te Weraiti Basement Andesite plots distinctly from the other units and is characterised by lower Th/Nb, Rb/Sr, and La/Yb ratios relative to the main sample population. In contrast, the Waitearikiki Ignimbrite and Te Poi samples plot within the broader range of ratios defined by the other units and generally follow the same overall compositional trends.

4.5.3 Zircon Separation and imaging

Zircon is a common accessory mineral in silicic volcanic rocks and is widely used for geochronological analysis because it incorporates uranium and thorium during crystallisation while excluding lead. Zircon separation was undertaken on selected samples from the Kaimai Rhyolite Dome Complex with the original intention of obtaining U-Pb ages to constrain the timing of dome emplacement. A suitable zircon population was successfully extracted; however, a substantial proportion of the separated grains was lost during the final mounting and polishing stage, and the remaining population was insufficient for robust geochronological analysis. The remaining zircons were instead examined to document zircon morphology and internal structures.

4.5.3.1 Zircon Separation

Whole-rock samples were dried at approximately 100 °C prior to processing. Samples were first reduced to fist-sized fragments using a rock saw and hammer, before further size reduction using a rock jaw crusher to produce pebble-sized material. The crushed material was subsequently pulverised using a BICO pulveriser to produce grains approximately ≤0.5 mm in diameter.

Heavy mineral separation was undertaken to concentrate zircon from the bulk sample. Initial density separation was carried out using a Gemini shaking table to isolate dense mineral fractions. The heavy mineral fraction was then dried at 100 °C prior to further processing.

Magnetic minerals were first removed using a Frantz vertical magnetic separator. The remaining material was then subjected to density separation using sodium polytungstate (SPT) heavy liquid with a specific gravity of approximately 2.85, isolating minerals with densities greater than this threshold.

Following heavy liquid separation, the heavy mineral fraction was further processed using a Frantz inclined magnetic separator to refine the non-magnetic mineral concentrate. The resulting heavy mineral fraction was examined under a binocular microscope, and zircon grains present were hand-picked using fine tweezers and pick.

4.5.3.2 Zircon Examination by optical and cathodoluminescence microscopy

Sample MC18 (andesite) did not yield zircons. Zircon grains recovered from MC12 were examined using optical microscopy and cathodoluminescence (CL) imaging to characterise grain morphology and size. The recovered zircons occur as a small cluster of predominantly elongate prismatic crystals with well-developed crystal faces (Figure 4.27A). The grains display euhedral to subhedral morphologies, with several crystals preserving intact prism faces and terminations. Figure 4.28 shows a small cluster of zircon grains displaying predominantly broken and irregular zircon fragmentations with incomplete crystal terminations and incomplete crystal faces. The grains range from subhedral to anhedral in form.

The same zircons shown in Figure 4.27A were then examined under microscope to determine approximate crystal dimensions (Figure 4.27B). Two representative grains shown in Figure 4.27 range from 370–391 μm in length, while the broader recovered population shown in Figure 4.29 ranges from 80–237 μm in length and 24–117 μm in width. The crystals are transparent to translucent under optical microscopy and display internal luminescence features under cathodoluminescence imaging.

Figure 4.29 shows a representative sample of zircon grains under optical microscopy to measure grain dimensions. Measured grain lengths range from approximately 80-237 μm, with widths of approximately 24–117 μm. Despite the fragmented nature of several grains, the elongate prismatic habit preserved in some crystals is consistent with zircon crystallisation in a silicic magmatic system.

Only a small number of zircon grains were recovered from the sample; however, the grains are well preserved and suitable for morphological characterisation.

Sample MC18 did yield a significant heavy mineral fraction following separation. This fraction was analysed using X-ray diffraction (XRD) and is presented in Table 4.2. The analysis identified diopside as the dominant mineral present within the heavy fraction.

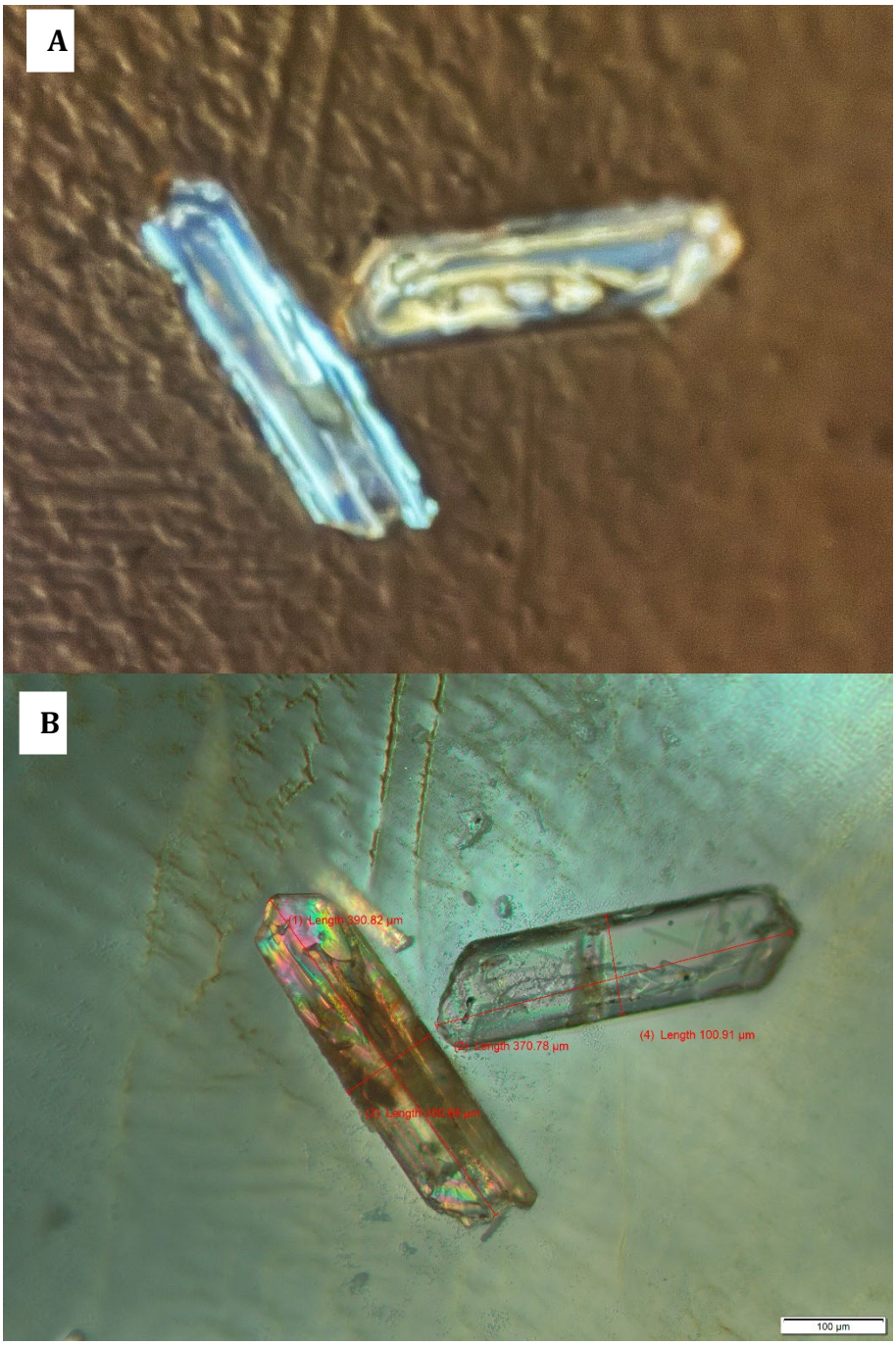

Figure 4.27: Zircon grains recovered from sample MC12.
(A) Two elongate prismatic zircon crystals displaying well-developed euhedral crystal faces typical of magmatic zircon.
(B) Representative zircon grains showing measured crystal dimensions. Grain lengths range from approximately 370–391 µm, with widths of approximately 100 µm. Scale bar = 100 µm.

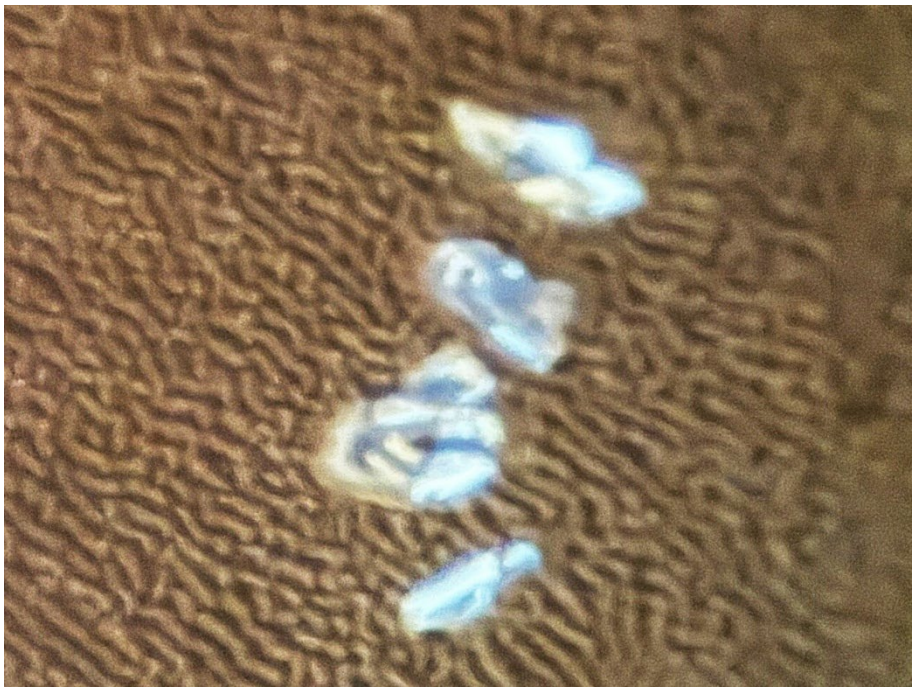

Figure 4.28: Zircon grains recovered from sample MC12 under cathodoluminescence. Cluster of zircon grains showing predominantly elongate prismatic crystal morphologies, they are primarily fractured/broken zircon grains and are not well preserved.

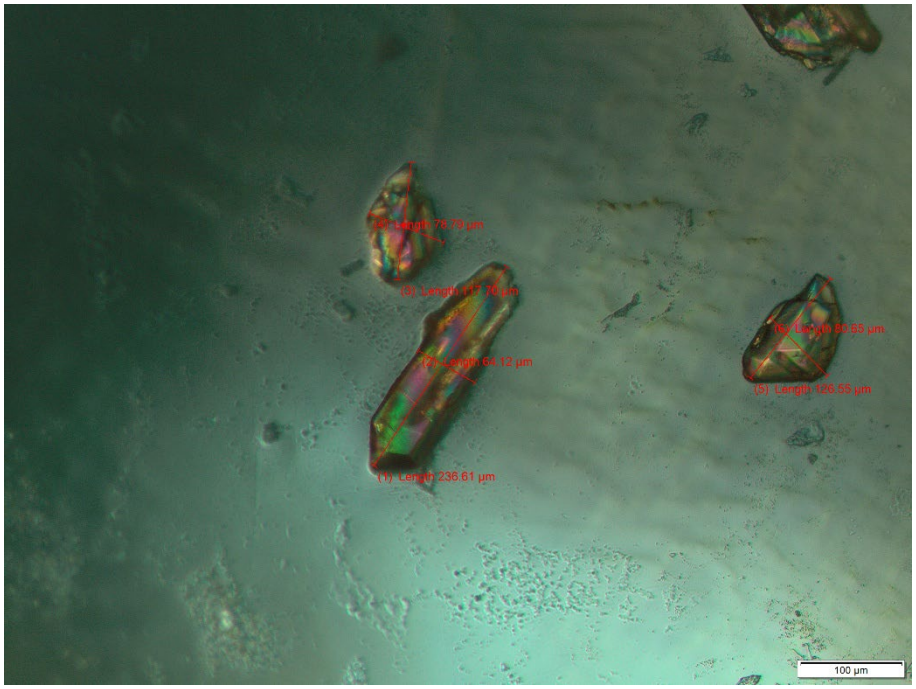

Figure 4.29: Representative zircon grains from sample MC12 under microscope showing measured crystal dimensions. Grain lengths range from approximately 80–237 µm, with widths of approximately 24–117 µm. Crystal morphologies are predominantly elongate prismatic with well-developed crystal faces typical of magmatic zircon. Scale bar = 100 µm.

Chapter Five: Discussion

5.1 Revised Architecture

The silicic volcanic rocks of the southern Kaimai Range have historically been mapped as part of the Minden Rhyolite Subgroup, a collective unit of all rhyolite and rhyodacite domes within the Tauranga Volcanic Centre (Leonard et al., 2010). At the 1:250,000 scale of the QMAP Rotorua sheet, the KRDC is represented as an undifferentiated body of flow-banded rhyolite to rhyodacite lava within the Minden Rhyolite Subgroup with no internal dome boundaries resolved. The three dome names, Kaimai, Kakahu, and Te Weraiti appear in the published literature (Briggs et al., 2005; Pittari et al., 2021; Prentice et al., 2025), but these domes have never been systematically mapped with defined boundaries or characterised in detail. Prentice (2023) explicitly notes that no detailed descriptions or characterisation of the rhyolite lavas comprising the Kaimai-Kakahu-Te Weraiti dome complex exists within published literature. The peak of Hiwiroa is labelled on the QMAP as a topographic high but has not been recognised as a discrete dome unit in any prior study. More recently, Prentice et al. (2025) identified the dome complex to run along the inferred northwestern structural boundary of the newly defined Omanawa Caldera, the source of the ~870 ± 270 km^3 DRE Waitеariki super-eruption at ~2.1 Ma, further underscoring the need for detailed mapping and characterisation of these dome lavas.

This study addresses this gap by resolving the undifferentiated rhyolite of the southern Kaimai Range into six discrete dome centres, Te Weraiti, Kaimai, Kakahu, Hiwiroa, and two previously undocumented eastern domes, which was done using high-resolution 1 m LiDAR derived DEM analysis, hillshade, and slope mapping, field observations, and geochemical data. For the three previously named domes, this study provides the first defined dome boundaries, morphometric parameters, and geochemical characterisation. Hiwiroa is recognised here for the first time as a discrete dome unit on the basis of its distinct topographic expression, elongation ratio, and spatial separation from the main N-S dome corridor. The two eastern domes are entirely new identifications, situated within the area mapped as undifferentiated Minden Rhyolite on the QMAP. Despite being topographically expressed, these domes were not recognised as discrete eruptive centres in any

prior study. Their identification here is based on morphometric and geomorphological analysis of the LiDAR-derived DEM. Their eastern margins are partially buried by younger deposits of the Mamaku Plateau, which limits the preserved extent of these units but does not obscure the dome edifices themselves. While they sit off-axis from the main N-S corridor, both domes maintain a N-S orientation consistent with the regional structural trend. Compositional differences confirmed through XRF and LA-ICP-MS analysis were used to support unit differentiation between Kaimai and Te Weraiti where geomorphological boundaries were ambiguous.

The mapping demonstrates that the KRDC is not a single rhyolite body but a coalesced composite dome ridge comprising multiple eruptive centres distributed along a 25.8 km north-south corridor. The continuous ridge morphology, overlapping dome margins visible in cross-section, and the absence of clear inter-dome topographic differences along much of the complex indicate that successive dome emplacements merged along a structurally controlled pathway. This style of coalesced dome emplacement is consistent with prolonged, spatially migrating effusive volcanism along fault-controlled conduits in extensional settings. The total preserved volume of the KRDC is estimated at 5.67 km^3, a substantial effusive output that, combined with the Waiteariki supereruption and other eruptive products, underscores the significance of the southern TgVC as a major centre of silicic magmatism during the late Pliocene.

The recognition of six dome centres has implications for eruption frequency and the duration of dome-building volcanism within the complex. Published $^{40}Ar/^{39}Ar$ ages constrain the Kaimai and Kakahu domes to 2.86 ± 0.08 Ma and 2.87 ± 0.02 Ma respectively (Briggs et al., 2005), with a U-Pb zircon age of 2.236 ± 0.038 Ma also reported for the Kaimai dome (Pittari et al., 2021). Attempts to obtain U-Pb zircon ages for Te Weraiti and the Te Weraiti Basement Andesite were unsuccessful (Section 4.5.3). Te Weraiti, Hiwiroa, and the eastern domes therefore remain undated, and the temporal spacing and directional migration of dome emplacement cannot be resolved without further geochronological work. The stratigraphic relationship between all KRDC domes and the Waiteariki Ignimbrite, which onlaps the eastern flanks of the dome complex (Prentice et al., 2025), confirms that dome

emplacement predated the ~2.1 Ma supereruption. The identification of geochemically distinct Waiteariki Ignimbrite material (MC11) within the mapped extent of Te Weraiti provides further evidence for this stratigraphic relationship and indicates that the Waiteariki pyroclastic density current flowed against and around the pre-existing dome edifices.

5.2 Structural Controls

The Kaimai Rhyolite Dome Complex is located on the edge of the Hauraki Rift, a NNW-trending, active intra-continental rift that extends more than 250 km from Waiheke Island to the Taupō Volcanic Zone in the south (Hochstein & Ballance, 1993). Two principal faults define the southern rift segment: the Hauraki Fault, which runs along the foot of the Kaimai Range and is now considered inactive, and the Kerepehi Fault, which forms the active central depression fault (Persaud et al., 2016). Both faults trend approximately 340°, consistent with the overall NNW to N-S elongation of the KRDC. At the time of KRDC emplacement between approximately 2.87 and 2.2 Ma, the Hauraki Rift was undergoing a critical tectonic transition as the locus of rifting migrated southward toward the nascent Taupō Rift (Persaud et al., 2016). Seismic reflection data across the central rift indicate a temporal decrease in faulting density, suggesting the rift was more tectonically active during the Pliocene than at present (Fromont, 2017), consistent with active fault-controlled magma ascent during the late Pliocene to early Pleistocene period of KRDC dome emplacement. In addition to the Hauraki Rift, Prentice et al. (2025) identified an asymmetrical rifted graben running through the TgVC with NE-trending faults and placed the Omanawa Caldera at the southern end of this structure. The KRDC therefore sits at the intersection of two structural systems: the Hauraki Rift to the west and the TgVC graben to the east. Both systems likely influenced magma ascent pathways and dome emplacement geometry across the complex, although the parallelism between the Hauraki Fault and the steep western slopes of the KRDC suggests this structure exerted the more direct control on dome emplacement.

Elongation ratios calculated for individual dome units define two distinct emplacement modes, ranging from strongly fault-controlled to point-source dominated. The distribution of elongation ratios across the KRDC is bimodal, with a

clear gap between the highly elongate Te Weraiti and Kakahu (2.81–3.16) and the more equant remaining domes (1.44–1.85). This bimodality suggests fundamentally different magma ascent pathways for the two groups. Te Weraiti and Kakahu record the highest elongation ratios within the complex at 2.807 and 3.158 respectively, both trending parallel to the Hauraki and Kerepehi fault systems. These values are consistent with dome emplacement along fault planes or fissures rather than eruption from central vents, where magma ascends through a linear structural weakness rather than a singular conduit. In contrast, Kaimai and Hiwiroa are more equant with elongation ratios of 1.444 and 1.471 respectively, suggesting that emplacement came from a singular conduit or point source with less direct fault control. Despite this, the Kaimai dome sits along the same N-S corridor as Te Weraiti and Kakahu, indicating that regional fault architecture still influenced its emplacement. The two eastern domes have elongation ratios of 1.553 and 1.847, making them more linear than Kaimai and Hiwiroa but substantially less elongated than Te Weraiti and Kakahu. Both maintain a N-S orientation parallel to the main corridor, reflecting the regional extensional stress field rather than direct fault plane control. This variable structural influence within a single dome complex indicates that magma exploited different structural weaknesses along the same rift corridor, producing a range of dome geometries that record the interplay between regional structures and localised conduit geometries.

Steep western margins observed across the complex provide additional evidence for fault influence on dome morphology. Maximum slope values exceed 75° along the western flanks of Te Weraiti (83.4°), Kaimai (76.8°), Kakahu (78.59°), and both eastern domes (77.64°, 82.74°), producing scarps that contrast with the more moderate eastern slopes. These steep western margins are spatially consistent with the Hauraki Fault. Two processes may account for these features. Syn-emplacement fault control would produce inherently steep western contacts where magma ascended along or against the fault plane, while post-emplacement tectonic uplift along the Hauraki Fault would steepen originally gentler dome margins through differential displacement. Both processes likely contributed, as the Hauraki Fault was active during and after dome emplacement. Houghton and Cuthbertson (1989) documented at least 400 m of displacement of the Waiteariki Ignimbrite along the Hauraki Fault, and Briggs et al. (2005) constrained the most rapid period of fault

development in the southern rift segment to between 2.09 ± 0.03 Ma and 1.34–1.21 Ma — a period that directly postdates KRDC dome emplacement and overlaps with the Waitеariki supereruption. This magnitude of displacement confirms that significant tectonic activity occurred along the western margin of the KRDC during and shortly after dome growth.

Post-emplacement caldera collapse associated with the ~2.1 Ma Waitеariki supereruption may also have contributed to the asymmetric morphology of the dome complex. The KRDC sits along the inferred northwestern margin of the Omanawa Caldera (Prentice et al., 2025), and subsidence of the caldera floor during or after the supereruption would have preferentially affected the eastern margins of domes situated along this boundary. This would produce an apparent eastward tilt that compounds the effect of westward uplift along the Hauraki Fault, with both processes generating the same surface expression of steep western scarps and more moderate eastern slopes. A third contributing factor is the burial of eastern dome flanks by the Mamaku Plateau and by the older deposits of the Waitеariki Ignimbrite itself along the flanks of Te Weraiti and Kaimai domes, which further reduces the topographic expression of these domes along their eastern flanks. The relative contributions of Hauraki Fault uplift, caldera-related subsidence, and depositional burial to the observed asymmetry cannot be separated with the current dataset, but all three processes are consistent with the geological setting and likely acted in combination.

Several structural uncertainties remain that limit interpretation across the full extent of the complex. Elongation ratios reflect the preserved geometry of dome cores rather than original emplacement geometry, and may be influenced by differential erosion or post-emplacement tectonic modification. The 2.2–2.8 Ma age of the complex means that prolonged erosion has likely modified the original dome shapes, particularly along the steep western margins where the Hauraki Fault has been active during and after emplacement. At its southern end, the Hauraki Rift is concealed beneath the Mamaku Ignimbrite (Hochstein & Ballance, 1993), and the southern extensions of both the Hauraki and Kerepehi faults are unmapped in the area surrounding the KRDC. The degree of structural control on Hiwiroa and the eastern domes therefore cannot be definitively determined without subsurface data.

Hiwiroa's position southeast of the main N-S corridor, away from the mapped extent of the Hauraki and Kerepehi faults, could represent a later phase of emplacement along the southward-migrating corridor, or it may reflect eruption along a secondary fault splay not expressed at the present-day surface. The eastern domes sit east of the mapped fault traces, and the possibility of unmapped fault splays beneath the Mamaku Plateau and Undifferentiated Kaimai Rhyolite cannot be ruled out. The precise structural relationship between the KRDC and the Omanawa Caldera boundary is also uncertain, as the caldera margin is inferred from gravity data (Stagpoole et al., 2021) rather than direct structural or stratigraphic evidence. Subsurface geophysical investigation, such as gravity surveying, magnetic profiling, or seismic reflection, would be required to resolve fault geometry beneath the Mamaku Plateau and to determine whether unmapped structures influenced the positions of the eastern and southern dome units relative to the Hauraki Rift faults, the TgVC graben, and the Omanawa Caldera margin.

5.3 Petrographic and Mineralogical Significance

Petrographic data are available for two of the six identified dome centres: Kaimai and Te Weraiti. The remaining four domes — Kakahu, Hiwiroa, and the two eastern domes — were characterised through LiDAR-derived morphology and morphometric analysis only, as no samples were collected from these centres. Across both sampled domes, the phenocryst assemblage is consistent: plagioclase + quartz ± biotite ± sanidine ± pyroxene, with plagioclase as the dominant feldspar. This mineralogical consistency across two adjacent dome centres, spanning approximately 10 km of the 25.8 km N–S corridor, supports derivation from the same or a closely related magma source. Hornblende is entirely absent from all KRDC dome lavas, in contrast to the Waiteariki Ignimbrite, which contains plagioclase + hornblende + orthopyroxene + quartz ± biotite (Prentice et al., 2025). This distinction confirms that the KRDC dome lavas and the Waiteariki Ignimbrite represent separate magmatic lineages. K-feldspar occurs both as minor phenocryst phase (sanidine) and as a product of groundmass devitrification; the two occurrences are distinguished by texture, with phenocrysts forming euhedral to subhedral crystals and devitrification K-feldspar forming fine to coarse fibrous intergrowths within spherulites.

The Kaimai Dome was sampled across two sites: the upper JSWAP Farm site and the lower Rapurapu track. The upper site (MC01–MC06, MC19) displays variable devitrification maturity, ranging from initial crystallisation in quenched margins (MC03) to pervasive spherulitic groundmass in dome interior samples (MC01, MC06). MC05 displays axiolitic texture developed along flow bands, representing structurally controlled devitrification within the dome interior. The lower site (MC20–MC21) is characterised by pervasive mature devitrification with coalesced spherulites; MC21 records the largest spherulites in the sampled regions of the KRDC (200–3000+ μm). Nucleation across the Kaimai Upper samples is dominantly homogeneous, occurring within the groundmass rather than nucleating on pre-existing phenocrysts. The variation in spherulite development and size across these samples reflects differences in thermal history related to position within the dome rather than compositional differences between samples.

Te Weraiti dome rhyolites (MC07–MC08, MC12–MC14, MC16–MC17) display consistently well-developed spherulitic devitrification. MC07 has the lowest nucleation density of any KRDC sample, with the largest fan spherulites, consistent with the slowest-cooling dome interior sampled in this study. In contrast to Kaimai samples, spherulite nucleation in Te Weraiti occurs preferentially on pre-existing phenocrysts rather than within the groundmass. This difference in nucleation style between the two domes may reflect differences in cooling rate or phenocryst abundance. Te Weraiti is the largest dome by mapped area (14.26 km^2), and the consistently large spherulite sizes and mature devitrification textures are consistent with the slower cooling expected in a thicker dome.

XRD analysis identifies both cristobalite and sanidine in KRDC groundmasses. These phases are interpreted as forming fine-scale intergrowths within spherulites, consistent with the alkali feldspar–cristobalite spherulitic devitrification assemblage characteristic of rhyolitic glasses (Lofgren, 1971; Moore, 1983). Individual phases within spherulites could not be resolved under SEM-EDS due to insufficient compositional contrast between spherulites and the surrounding groundmass. The same devitrification assemblage has been documented in other Minden Rhyolite Subgroup domes, including the Hahei domes (Moore, 1983) and Mount Misery (Kinley, 2022), indicating this is a regional characteristic of these

lavas. The pervasive devitrification of KRDC groundmasses means that primary glass compositions cannot be obtained, unlike the Waitеariki Ignimbrite where Prentice et al. (2025) were able to analyse matrix glass. The absence of spherulitic devitrification textures in MC11 and MC15 supports the reclassification of MC11 as Waitеariki Ignimbrite, as dome lavas characteristically devitrify to produce spherulitic textures (Lofgren, 1971) whereas welded ignimbrites develop eutaxitic fabrics.

MC22 was collected from an exposure below the bush line on the lower southwestern slopes of the KRDC, east of SH28 and south of SH29 near Te Poi. The sample was identified in the field as containing hornblende and pyroxene; however, petrographic examination in this study found no amphibole in thin section. Mafic phenocrysts include brown subhedral to euhedral crystals with high birefringence and iron oxide rims, identified as clinopyroxene based on crystal habit, with minor platy brown crystals tentatively identified as biotite. Plagioclase is the dominant feldspar phase, occurring as euhedral tabular laths with well-developed albite twinning. No K-feldspar phenocrysts were observed; K-feldspar is present only as a groundmass devitrification product (sanidine identified by XRD). The resulting assemblage — plagioclase + clinopyroxene + biotite, lacking K-feldspar phenocrysts, quartz, and hornblende — is distinct from both the KRDC dome lavas (K-feldspar- and quartz-bearing) and the Waitеariki Ignimbrite (hornblende-bearing). The groundmass is pervasively spherulitic with coalesced spherulites ranging from 100–1500 μm, including concentric-banded forms and fan spherulites nucleated heterogeneously on mafic phenocrysts. The geochemical characteristics and stratigraphic implications of MC22 are discussed in Section 5.5.

Several samples require specific data quality considerations. MC02 displays elevated light rare earth element concentrations (La = 108 ppm compared with 22–31 ppm for adjacent samples), the cause of this enrichment is uncertain, and MC02 LREE data are excluded from petrogenetic interpretations. MC10 contains a clay mineral identified as kaolinite by routine powder XRD, though clay specific preparation was not undertaken and other 7 Å clay minerals such as halloysite cannot be excluded. The presence of a secondary clay phase indicates alteration, whether hydrothermal or surficial weathering, and major element geochemistry for this sample is

considered compromised. MC11 yields an XRD assemblage of quartz + albite, contrasting with the cristobalite + sanidine assemblage characteristic of all KRDC dome lavas, which provides further support for its reclassification as Waitearikiri Ignimbrite. MC18 yielded a diopside-dominated heavy mineral fraction with no zircon recovered, confirming its mafic composition and explaining the unsuccessful geochronological analysis of this sample.

5.4 Petrogenesis

The KRDC dome lavas are calc-alkaline, medium-K rhyolites (73.86–77.78 wt.% SiO_2 normalised) that plot within the rhyolite field on the TAS diagram. Their primitive mantle-normalised spider diagrams display a clear subduction-related signature with Nb–Ta troughs, enrichment in LILE (Rb, Ba, Th), and positive Pb anomalies. Chondrite-normalised REE patterns are LREE-enriched with negative Eu anomalies, consistent with plagioclase fractionation. MC18, a basement andesite sampled beneath the Te Weraiti dome, plots as a basaltic andesite on the TAS diagram (56.8 wt.% SiO_2), extending the compositional range from basaltic andesite to rhyolite within the sampled suite. These geochemical characteristics are consistent with the broader TgVC and TVZ subduction setting.

Major element Harker diagrams show coherent negative trends for TiO_2, Al_2O_3, Fe_2O_3, CaO, and P_2O_5 with increasing SiO_2, consistent with fractional crystallisation. MgO decreases but shows limited variation across the rhyolite samples due to low concentrations at these SiO_2 values and MC18 skewing the plotted field. Decreasing CaO and Al_2O_3 indicate plagioclase fractionation from the melt, while decreasing Fe_2O_3 and TiO_2 indicate Fe–Ti oxide removal. K_2O increases with SiO_2, consistent with K-feldspar being a late-crystallising phase that has not been significantly removed from the melt. MC11 and MC15 follow the same major element trends as the KRDC dome lavas, indicating a broadly similar fractionation history for the Waitearikiri Ignimbrite. MC22 follows these trends but decouples on key trace elements. MC18 sits at lower SiO_2 but lies on the extension of all major element trends, supporting its potential role as a parental composition.

Trace element variation diagrams display clear evidence for plagioclase-dominated fractionation across the KRDC rhyolites. Eu/Eu* decreases as Rb/Sr increases,

recording the progressive removal of plagioclase from the melt. Both Eu and Sr are compatible in plagioclase and are co-depleted as fractionation proceeds, while Rb is incompatible in the fractionating assemblage and concentrates in the residual melt. This relationship is reinforced by decreasing Sr with increasing SiO_2 and Rb across the suite. Rather than decreasing with differentiation, Ba correlates positively with Rb across the rhyolites. Ba is compatible in both K-feldspar and biotite, and its enrichment with increasing differentiation indicates that neither phase was being significantly removed from the melt. This is consistent with the increasing K_2O trend on major element Harker diagrams and supports the petrographic observation that K-feldspar is a minor late-crystallising phase in the KRDC assemblage. The limited extent of K-feldspar fractionation preserved sufficient K_2O in the residual melt, providing the compositional budget for pervasive sanidine + cristobalite spherulitic intergrowths in KRDC groundmasses. Chondrite-normalised (Dy/Yb)_N ratios are flat at 0.8-1.1 across all rhyolites, indicating no heavy rare earth element fractionation. This confirms the absence of hornblende and garnet in the fractionating assemblage, consistent with the hornblende-absent mineralogy in Section 5.3.

KRDC rhyolites share a fractionation history but are not compositionally homogeneous. Kaimai Upper, Kaimai Lower, and Te Weraiti overlap on major element Harker diagrams and share a consistent phenocryst assemblage, suggesting derivation from the same or closely related magma source. However, trace element ratios reveal significant scatter. Zr/Y ranges from 1.89 to 15.43 and (La/Yb)_N from 5.3 to 13.0 at similar SiO_2 values. This scatter and variation indicate a heterogenous reservoir. Te Weraiti samples tend towards higher Rb, lower Sr, and deeper Eu anomalies than Kaimai Upper, though the broader compositions overlap. Kaimai Lower extends to the highest SiO_2, Rb, and Rb/Sr values in the suite, possibly reflecting a more evolved batch from the same magma source. This internal variability is consistent with episodic eruption from an evolving reservoir, with each dome emplacement along the structurally controlled N-S corridor potentially sampling a slightly different composition. The absence of both geochemical and geochronological data for Hiwiroa, Kakahu, and the eastern domes, and the lack of geochronological constraints for Te Weraiti, means that the sequence and any directional migration of dome emplacement cannot currently be resolved.

One non-rhyolitic unit occurs within the mapped extent of the KRDC. The Te Weraiti Basement Andesite (MC18) is a basaltic andesite (56.8 wt.% SiO_2) exposed beneath the Te Weraiti dome in a quarry operated by J Swap Contractors (Matamata Metal Supplies) on the western slopes of the Kaimai Range. MC18 sits on the extension of all major element Harker trends established by the KRDC rhyolites, and its diopside-bearing heavy mineral fraction confirms its mafic composition (Section 5.3). These relationships are consistent with MC18 representing a potential parental composition for the KRDC dome lavas. If MC18 is a parent and FC is the dominant process, incompatible elements should enrich in the daughter rhyolites while compatible elements deplete. Incompatible trace elements relative to MC18 enrich as expected with Rb (4.92 times), Th (6.25 times), U (5.82 times), Pb (3.53 times), La (3.66 times), Nd (2.42 times), Nb (2.44 times), and Zr (1.89 times). Plagioclase-compatible trace elements Sr (0.36 times) and Eu (0.80 times) deplete as expected. Ba is the exception in comparison to other compatible traces, enriching at 3.78 times despite being compatible in K-feldspar and biotite. The positive Ba-Rb correlation shows that K-feldspar was not materially fractionated. F values for incompatible elements range from 0.16 to 0.53, a threefold variation. A single-stage fractional crystallisation process should have a consistent F value across all elements, and this spread indicates that a single fractionation step cannot account for observed compositions through FC alone. Ba enrichment and this spread suggest that simple fractional crystallisation cannot explain the KRDC lavas, and that additional processes, such as crustal material assimilation, influenced the system. Prentice (2023) identified Otawa33, an Otawa Formation andesite, as the least-evolved magma within the TgVC and modelled it as the parental composition for the low-$^{87}Sr/^{86}Sr$ Minden Rhyolite pathway. MC18, an independent andesite from a different location, similar in SiO_2 to Otawa33, yields comparable directional relationships with the KRDC lavas. However, without $^{87}Sr/^{86}Sr$ isotopic data for MC18 or the KRDC dome lavas, a co-genetic relationship cannot be confirmed. MC18 may represent an older, unrelated andesite predating the KRDC, rather than a true parent, and further isotopic analysis is required to resolve this question.

The KRDC lavas and Waiteariki Ignimbrite represent distinct magmatic lineages. Prentice (2023) placed Kaimai in the low-$^{87}Sr/^{86}Sr$ group, produced by 70–80% crystallisation of Otawa33, while Waiteariki Ignimbrite is in the high-$^{87}Sr/^{86}Sr$

group, linked to the Omanawa Caldera system via AFC. The mineralogical and geochemical data presented in this study support this assignment KRDC samples contain minor K-feldspar and lack hornblende, whereas the Waiteariki Ignimbrite is hornblende-bearing and K-feldspar-free. KRDC has a higher average Rb of 126 ppm, a lower average Sr of 60 ppm, and deeper Eu anomalies. Waiteariki has a lower average Rb of 77 ppm, a higher average Sr of 156 ppm, and weaker Eu anomalies. On bivariate trace element diagrams, Waiteariki consistently plots off the main KRDC trends, despite overlapping in SiO_2. MC11, originally mapped as a Te Weraiti sample, is reclassified as Waiteariki Ignimbrite based on the following evidence. On major and trace element Harker plots, MC11 plots with Waiteariki sample MC15, not with the KRDC rhyolites. MC11's XRD assemblage of quartz and albite contrasts with the cristobalite and sanidine of KRDC dome lavas. MC11 also lacks the spherulitic devitrification textures pervasive in KRDC groundmasses. These observations confirm that Waiteariki Ignimbrite material overlaps the eastern margins of Te Weraiti, consistent with the stratigraphic relationship described in Section 5.1. Assignment of KRDC to the low-$^{87}Sr/^{86}Sr$ pathway is supported by mineralogy and geochemistry but remains unconfirmed without isotopic data for KRDC dome lavas.

5.5 CVZ-TVZ Transition and Regional Context

The KRDC sits at a transitional period of volcanism in New Zealand, between the CVZ and the TVZ. The CVZ spanned approximately 18 to 3 Ma, with volcanism migrating southward from Great Barrier Island down to Waihi over this period (Booden et al., 2012; Pittari et al., 2021). TVZ onset is established at 2.0 to 1.8 Ma (Wilson & Rowland, 2016; Chambefort et al., 2014), and the TgVC sits between these two volcanic zones in both time and character. The KRDC therefore records the transition between CVZ style and TVZ style volcanism.

The CVZ is characterised as subduction-arc volcanism driven by arc magmatism with limited extension, structurally controlled by faulting in a E-NE to NE trend. The zone is primarily andesitic to dacitic in the north, and moving south volcanism became dominated by more silicic compositions of dacite and rhyolite through slab rollback and the first extensional phase. This activity came in the form of domes and small calderas with eruptive volumes typically less than 30 km^3 (Briggs et al., 2005). The

TVZ, in contrast, is characterised by subduction-arc volcanism coupled with strong back-arc rifting, where thinned continental crust produces high magma fluxes, dominant caldera systems, and individual eruptions generating 30 to 1500 km^3 (Wilson et al., 2009). Prentice et al. (2025) have reclassified the TgVC as the earliest silicic expression of the TVZ, as its structural position within the Old Taupō Rift and the TgVC graben, along with the character of volcanism in the TgVC, is more aligned with the TVZ than the CVZ. The approximately 2.1 Ma Waitearikiki supereruption, with an estimated volume of 870 ± 270 km^3 DRE (Prentice et al., 2025), exceeds any known CVZ caldera eruption and sits firmly within the TVZ eruptive range.

The KRDC therefore presents a transitional story. Its lavas share compositional and petrographic features with the older CVZ Minden Rhyolite products yet were emplaced within the structural setting of the early TVZ. The following section examines what this transitional position records about regional volcanic evolution, with comparisons to other Minden Rhyolite dome complexes across the CVZ and TgVC.

Among the Minden Rhyolite dome complexes of the TgVC, the KRDC has the largest documented volume at 5.67 km^3, making it the most volumetrically significant effusive silicic centre within the TgVC. The Mount Misery dome series (Pukunui, Maungatūtū/Mount Misery, and Greenpark) is another Minden Rhyolite dome complex within the TgVC, sitting on the opposite (eastern) margin of the Omanawa Caldera (Kinley, 2022). The KRDC and Mount Misery series share features that support their common Minden Rhyolite Subgroup assignment, including spherulitic groundmass devitrification with cristobalite and sanidine, and both are endogenous silicic domes within the TgVC.

Despite these similarities, the two suites are compositionally and petrographically distinct and represent separate magma batches from independent plumbing systems. The Mount Misery domes have SiO_2 contents of 72.11–73.29 wt.%, Zr concentrations of 174–252 ppm, and a phenocryst assemblage of plagioclase + quartz ± clinopyroxene ± orthopyroxene (Kinley, 2022). The KRDC lavas have higher SiO_2 at 73.86–77.78 wt.%, lower Zr at 109.7–189.6 ppm, and a phenocryst assemblage of plagioclase + quartz ± biotite ± sanidine ± pyroxene, with plagioclase as the dominant feldspar. Minor primary sanidine in the KRDC, absent from Mount

Misery, is one petrographic feature distinguishing the KRDC from the Mount Misery series. MC22, although collected from within the broader KRDC field area and originally provided for analysis with the KRDC suite, returns a Zr content (257 ppm) that falls within the Briggs et al. (2005) high-Zr range and is reclassified as a separate unassigned rhyolite as discussed below.

The SiO_2–Zr relationship in both the KRDC and Mount Misery reflects zircon-saturation-controlled evolution, but they do not follow the same trend. At comparable SiO_2 contents of 72–74 wt.%, Mount Misery consistently carries higher Zr than equivalent KRDC samples, indicating that the two suites evolved from magmas with different starting conditions, whether in melt temperature, source composition, or prior fractionation history. Zircon saturation thermometry (Watson and Harrison, 1983; Boehnke et al., 2013; Appendix V) supports this interpretation. Mean melt temperatures of ~799°C (Watson and Harrison, 1983) or ~768°C (Boehnke et al., 2013) are calculated for the KRDC main rhyolite suite, which spans a wide internal range (768–869°C) reflecting episodic tapping of an evolving reservoir (Section 5.4). Mount Misery fresh samples (LOI <2.5%; Kinley, 2022) give a more tightly constrained mean of ~837°C or ~806°C across a narrow 827–845°C range. The mean 40°C offset in suite means is consistent with the KRDC representing a cooler, more evolved population tapped over a longer evolutionary window, while Mount Misery represents a more thermally homogeneous, less-evolved batch.

The presence of minor primary sanidine in some KRDC samples, absent from the Mount Misery series, is consistent with this thermal and compositional difference. Sanidine saturation in silicic melts is favoured by lower temperatures, lower water contents, and higher K_2O activity in the residual liquid. The cooler, more evolved KRDC melts approached or marginally crossed the sanidine saturation threshold prior to eruption, producing minor K-feldspar phenocrysts. The hotter, less evolved Mount Misery melts did not reach sanidine saturation until groundmass devitrification during post-emplacement cooling, producing sanidine only as a devitrification product rather than a primary phenocryst.

The KRDC and Mount Misery series therefore represent separate magma batches that shared a common petrogenetic process. Both belong to the Minden Rhyolite Subgroup and record the same general petrogenetic process of zircon-fractionation-

controlled evolved rhyolites erupting as endogenous domes, but from separate plumbing systems tapped at different evolutionary stages — Mount Misery as a hotter, less-evolved, high-Zr suite, and the KRDC as a cooler, more-evolved, moderate-Zr suite with a distinct phenocryst assemblage including primary K-feldspar. The independent Kinley (2022) study therefore supports the interpretation that the TgVC hosted multiple compositionally and thermally distinct Minden Rhyolite magma batches rather than a single regional source.

The KRDC, while younger than the CVZ, shares compositional and petrographic features with older CVZ domes but differs in structural setting. The Hahei domes (Bluff, Hahei, Hot Water Beach, and Moturoa) are ~7.8 Ma Minden Rhyolite Subgroup domes on the eastern Coromandel Peninsula, characterised by Moore (1983) with a fission-track age from Rutherford (1978). These domes share lithological features with the KRDC as they are flow-banded rhyolites which feature spherulitic devitrification of both cristobalite and sanidine confirmed by XRD and feature plagioclase + quartz phenocrysts. The Hahei domes have internal variation of phenocryst assemblages with biotite rhyolite (Hahei Dome, Bluff Dome), biotite-hornblende rhyolite (Hot Water Beach Dome), and pyroxene rhyolite (Moturoa Dome), each dome recording a compositionally distinct magma batch. The KRDC shows a similar pattern of internal compositional variation, but rather than representing separate distinct magma batches, it records continuous tapping of the same evolving reservoir at different stages of evolution. The Hot Water Beach Dome specifically is an amalgamation of lavas from two or more contemporaneous fissures (Moore, 1983), similar to this study's interpretation of the fissure-controlled portions of the KRDC. The cristobalite-sanidine spherulitic devitrification is consistent across the CVZ-TgVC from ~7.8 Ma (Hahei) to ~2.2 Ma (KRDC), confirming it as a persistent regional feature. Despite these similarities, the key difference lies in the structures that enabled their emplacement. The Hahei dome fissures trend E to NE, reflecting the CVZ structural setting, whereas the KRDC fissures trend N-S, reflecting the Hauraki Rift, Old Taupō Rift, and Tauranga Graben. Same emplacement mechanism, different tectonic setting.

MC22 is a rhyolite sample collected by M. Prentice during fieldwork for Prentice (2023) and provided for analysis as part of this study. The locality is west of the main

Kaimai Dome (below the bush line near Te Poi, south of SH29, east of SH28). LiDAR shows no dome edifice at the sample location nor any significant morphology and shows up on the QMAP as Tauranga Group Alluvium. MC22 phenocryst assemblage is plagioclase + clinopyroxene + biotite ± minor sanidine, lacking quartz and hornblende, thus differing from both the Waitеariki Ignimbrite and most of the KRDC. The presence of clinopyroxene as a major mafic phase, combined with the absence of quartz, are the key features distinguishing MC22 from KRDC dome lavas. The sample's geochemistry consistently sits off trend from the KRDC, the SiO_2 sits lower than the main KRDC (73.86–77.78 wt.%) at 72.22 wt.%, Zr of 257 ppm which is the highest in this study's dataset, a lower Rb 65 ppm, lower Th 9.7 ppm, and a much higher Sr of 102 ppm compared to the KRDC of 56 ppm. Thermometry supports a higher temperature of 850°C but closer to the mean of Mount Misery's fresh rhyolites at 837°C but with differing phenocryst assemblage. MC22 represents a compositionally distinct exposure within the broader TgVC area but due to differences with the KRDC it is not classified as part of the KRDC magmatic system. The origin of this sample is unknown due to the lack of morphology and compositional/petrographic similarities. However, the presence of MC22 suggests a broader range of composition within the TgVC. It is a further piece of evidence that the existing TgVC framework does not fully accommodate all volcanism within it.

The KRDC is the youngest effusive Minden Rhyolite dome complex in a series of volcanism running from the CVZ to the TgVC ~7.8–2.2 Ma in a southward migrating trend. The KRDC is compositionally consistent with older CVZ Minden Rhyolites but is emplaced through rift-controlled structures of the Hauraki Fault, Old Taupō Rift, and the Tauranga Graben. The KRDC is therefore the physical rock record of CVZ magmatism channelled through emerging TVZ structures.

The Minden Rhyolite Subgroup is a CVZ-wide classification for rhyolite to rhyodacite flow-banded lavas that lumps together compositionally and petrographically distinct dome complexes across the whole CVZ and TgVC. Within the TgVC, four compositional groups were defined by Briggs et al. (2005) prior to the merger of the Kaimai Volcanic Centre and Tauranga Volcanic Centre into a single centre (Pittari et al., 2021): the Minden Peak Group (crystal-rich hornblende rhyolites ± biotite ± orthopyroxene), the Mount Maunganui Group (crystal-poor biotite rhyolites ±

hornblende ± orthopyroxene), the Mangatawa Group (crystal-rich hornblende-orthopyroxene rhyolites and dacites ± biotite), and the Mount Misery Group (crystal-rich hornblende-orthopyroxene rhyolites). The KRDC does not fit any of these groups. Hornblende is a defining phenocryst phase in all four groups and is absent from the KRDC, and minor primary K-feldspar (sanidine) is observed in some KRDC samples but is absent from all four groups. The KRDC compositional range also does not match any of the four groups on SiO_2 or Zr content. Kinley's (2022) petrographic study found no hornblende in Mount Misery samples, contradicting the current framework. The TgVC Minden Rhyolite Subgroup, while fitting with the general trends of the CVZ Minden Rhyolite Subgroup, erupted from different structural controls. A revised TgVC-specific stratigraphic framework should incorporate the KRDC as a distinct formally named unit along with the other TgVC dome units. This would bring the TgVC in line stratigraphically with how other TVZ centres deal with stratigraphy.

Chapter Six: Conclusions and Summaries

6.1 Conclusions

The overall conclusions of the study are outlined below:

- The Kaimai Rhyolite Dome Complex comprises six discrete dome centres rather than a single undifferentiated rhyolite unit. These are Te Weraiti, Kaimai, Kakahu, Hiwiroa, the Eastern Dome, and the Southeastern Dome. None of the domes were recognised as discrete units until this study. Te Weraiti, Kaimai, and Kakahu were peak names from the Southern Kaimai Range, Te Weraiti is the peak name, Kaimai takes its name from the range itself, and Kakahu from a nearby stream. These names referred to topographic features only, not to formally define dome units. The Eastern and Southeastern Domes were not previously recognised as separate units and are informally named herein. Hiwiroa is recognised here for the first time as a discrete dome unit along with the Eastern, and Southeastern Domes on the basis of their distinct topographic expression, elongation ratio, and geomorphology.
- The KRDC covers a total mapped area of approximately 114 km^2 with an estimated volume of 5.7 km^3. The six discrete dome centres account 77 km^2 and 4.4 km^3, with the remainder attributed to the undifferentiated KRDC rhyolite unit defined as rhyolite within the bounds of the KRDC that could not be assigned to an individual dome due to the lack of geomorphology and topographic features. This volume is comparable to individual post-caldera dome systems at the Valles Caldera, New Mexico (Nasholds & Zimmerer, 2022).
- A three-tier framework of structural control on dome emplacement is identified within the KRDC, ranging from fault-controlled fissure emplacement (Te Weraiti, Kakahu), through intermediate point-source emplacement within a fault corridor (Kaimai), to minimal direct fault control (Hiwiroa, Eastern and Southeastern Domes). This was done using elongation ratios display the geomorphology and shape of these domes. The bimodal distribution of these elongation ratios across the complex supports two distinct emplacement modes rather than a continuous spectrum, indicating that magma exploited different structural weaknesses along the N-S corridor.

- Steep western margins across the complex, with maximum slopes exceeding 75°, are consistent with the influence of the Hauraki Fault during and after dome emplacement. At least 400 m of post-emplacement displacement of the Waitеariki Ignimbrite along this fault has been documented (Houghton & Cuthbertson, 1989), and Briggs et al. (2005) used this constraint together with new $^{40}Ar/^{39}Ar$ ages to bracket the most rapid period of rift development in the southern Hauraki segment to between 2.09 ± 0.03 Ma and 1.34–1.21 Ma, a period that directly postdates KRDC dome emplacement.
- KRDC rhyolites of the Te Weraiti and Kaimai Domes contain a phenocryst assemblage of plagioclase, quartz, and biotite, with minor sanidine. Plagioclase is the dominant feldspar phase. XRD analyses confirm sanidine, orthoclase, microcline, and cristobalite are present in groundmasses as low-temperature devitrification products formed during post-emplacement cooling.
- Three samples that were obtained within the undifferentiated Kaimai rhyolite are now reclassified on the basis of petrographic, XRD, and geochemical evidence. MC11 and MC15 are classified as Waitеariki Ignimbrite which have influenced KRDC unit boundaries (Figure 3.3). MC18 is reinterpreted as a possible parental basaltic andesite rather than a KRDC rhyolite. The identification of geochemically distinct Waitеariki Ignimbrite material within the previously mapped extent of Te Weraiti indicates that the Waitеariki pyroclastic density current flowed against and around the pre-existing dome edifices.
- KRDC rhyolites are high-silica (74–78 wt% SiO_2), high-K calc-alkaline to shoshonitic, and predominantly peraluminous (A/CNK = 1.05–2.70). MC18 the potential parental basaltic andesite is metaluminous (A/CNK = 0.80), consistent with a mantle-derived mafic source. Trace element signatures across the sample suite are characteristic of arc-related silicic volcanism, including pronounced Nb–Ta troughs, positive Pb anomalies, and LREE enrichment relative to HREE.
- The Te Weraiti and Kaimai Domes are geochemically distinguishable. Te Weraiti samples cluster tightly at high SiO_2 (76.2–77.6 wt%) and K_2O (3.61–4.13 wt%), with most samples crossing into shoshonitic K_2O fields. Kaimai

samples span a wider compositional range (SiO_2 73.9–77.8 wt%, K_2O 3.21–4.18 wt%) and are predominantly high-K calc-alkaline. Te Weraiti is the more evolved of the two sampled domes. This compositional distinction supports the recognition of Te Weraiti and Kaimai as discrete eruptive centres rather than single coalesced dome.

- Compositional variation across the complex is best explained by assimilation-fractional crystallisation (AFC) rather than fractional crystallisation alone (FC). The peraluminous major element signature, combined with trace element variability inconsistent with pure FC, supports a significant crustal contribution to the KRDC magmas. Zircon saturation thermometry yields mean melt temperatures of ~799 °C (Watson & Harrison, 1983) and ~768 °C (Boehnke et al., 2013) for the rhyolite suite, with individual samples spanning 768–869 °C, reflecting episodic tapping of an evolving reservoir. Sample MC22 (Kaimai Lower Western Slopes) is an outlier in both location and composition (SiO_2 72.2 wt%, K_2O 2.88 wt%, A/CNK 1.29) and is the least evolved rhyolite sample analysed. The lack of associated dome morphology means it cannot be assigned to any of the six discrete dome centres, thus its origin remains an avenue for future investigation.
- The KRDC shares petrographic and geochemical similarities with the Mount Misery rhyolite series (Kinley, 2022), supporting interpretation that both are of the same fractionation pathway but at different points of evolution. The complex contributes to a growing record of voluminous silicic volcanism within the Tauranga Volcanic Centre.

6.2 Future Work

This study has identified the architecture, petrology, and geochemistry of the Kaimai Rhyolite Dome Complex but there have been significant limitations that could expand on the interpretation and provide further insight into the complex.

Extending the sampled area to Hiwiroa, Kakahu, the Eastern Dome, and the Southeastern Dome would be beneficial and would test whether the petrographic

and geochemical interpretations developed for Kaimai and Te Weraiti apply across the complex.

Geochronology of Te Weraiti, Hiwiroa, the Eastern Dome, and the Southeastern Dome would resolve the temporal sequence of dome emplacement across the complex. Attempts to obtain U-Pb zircon ages for Te Weraiti during this study were unsuccessful but not due to a lack of zircons in the sample.

Detailed field investigation of MC22 would determine whether it represents an isolated dome remnant, a lower-slope expression of either Kaimai or Kakahu, or an unrelated rhyolite body. Since current data cannot confidently assign it to any discrete dome unit, further work would build on the current understanding of the KRDC.

Sr-Nd isotopic comparison between the KRDC, Mount Misery rhyolite, the other TgVC Minden Rhyolite domes, the Waiteariki Ignimbrite, and the potential parental basaltic andesite (MC18) would test whether MC18 represents a true parental composition and whether the KRDC and Waiteariki Ignimbrite share a connected magmagenesis.

Subsurface investigation of the southern Hauraki and Kerepehi Faults beneath and adjacent to the KRDC and the Mamaku Plateau is required, as structural controls on the eastern and southern dome units cannot be determined from surface mapping alone.

Revision of the TgVC Minden Rhyolite Subgroup classification is also recommended. All TVZ volcanic centres have independent stratigraphic frameworks despite compositional similarities across centres, but the TgVC currently retains the regional CVZ stratigraphic legacy despite being recognised by Pittari et al. (2021) and Prentice (2023) as the first silicic centre of the early TVZ. The KRDC does not fit any of the four compositional groups defined by Briggs et al. (2005), and Kinley's (2022) petrographic results contradict the existing framework. This revision is beyond the scope of any single dome study but would bring the TgVC into stratigraphic alignment with other Taupō Volcanic Zone centres.

Chapter Seven: Bibliography

Adams, C.J., Graham, I.J., Seward, D., Skinner, D.N.B., and Moore, P.R., 1994, Geochronological and geochemical evolution of late Cenozoic volcanism in the Coromandel Peninsula, New Zealand: New Zealand Journal of Geology and Geophysics, v. 37, p. 359–379, doi: 10.1080/00288306.1994.9514626.

AusIMM, 2023, The Australasian Institute of Mining and Metallurgy: Ausimm.com, https://www.ausimm.com/publications/conference-proceedings/1997-ausimm-new-zealand-branch-annual-conference/the-coromandel-epithermal-gold-silver-province-a-result-of-collision-of-the-northland-and-colville-volcanic-arcs-in-northern-new-zealand/ (accessed April 2025).

Bacon, C.R., 1985, Implications of silicic vent patterns for the presence of large crustal magma chambers: Journal of Geophysical Research, v. 90, p. 11243, doi: 10.1029/JB090iB13p11243.

Barker, S.J., Wilson, C.J.N., Illsley-Kemp, F., Leonard, G.S., Mestel, E.R.H., Mauriohooho, K., and Charlier, B.L.A., 2021, Taupō: an overview of New Zealand's youngest supervolcano: New Zealand Journal of Geology and Geophysics, v. 64, p. 320–346, doi: 10.1080/00288306.2020.1792515.

Bernstein, M., Pavez, A., Varley, N., Whelley, P., and Calder, E.S., 2013, Rhyolite lava dome growth styles at Chaitén Volcano, Chile (2008–2009): Interpretation of thermal imagery: Andean Geology, v. 40, doi: 10.5027/andgeov40n2-a07.

Blake, S., 1990, Viscoplastic models of lava domes, in Fink, J.H., ed., Lava Flows and Domes: IAVCEI Proceedings in Volcanology, v. 2, Springer-Verlag, Heidelberg, p. 88–126.

Boehnke, P., Watson, E.B., Trail, D., Harrison, T.M., and Schmitt, A.K., 2013, Zircon saturation re-revisited: Chemical Geology, v. 351, p. 324–334, doi: 10.1016/j.chemgeo.2013.05.028.

Booden, M.A., Smith, I.E.M., Mauk, J.L., and Black, P.M., 2012, Geochemical and isotopic development of the Coromandel Volcanic Zone, northern New Zealand, since 18 Ma: Journal of Volcanology and Geothermal Research, v. 219–220, p. 15–32, doi: 10.1016/j.jvolgeores.2012.01.005.

Briggs, R.M., 1986a, Volcanic rocks of the Waikato Region, western North Island, and some possible petrologic and tectonic constraints on their origin, in Smith, I.E.M., ed., Late Cenozoic Volcanism in New Zealand: Royal Society of New Zealand Bulletin, v. 23, p. 76–91.

Briggs, R.M., Hall, G.J., Harmsworth, G.R., Hollis, A.G., Houghton, B.F., Hughes, G.R., Morgan, M.D., and Whitbread-Edwards, A.R., 1996, Geology of the Tauranga area, sheet U14, scale 1:50,000: University of Waikato Department of Earth Sciences Occasional Report 22, co-published with Bay of Plenty Regional Council and Institute of Geological and Nuclear Sciences, Hamilton, New Zealand, https://www.nzgs.org/libraries/geology-of-the-tauranga-area-text/.

Briggs, R.M., Houghton, B.F., McWilliams, M., and Wilson, C.J.N., 2005, $^{40}Ar/^{39}Ar$ ages of silicic volcanic rocks in the Tauranga–Kaimai area, New Zealand: Dating the transition between volcanism in the Coromandel Arc and the Taupo Volcanic Zone: New Zealand Journal of Geology and Geophysics, v. 48, p. 459–469, doi: 10.1080/00288306.2005.9515126.

Calder, E.S., Lavallée, Y., Kendrick, J.E., and Bernstein, M., 2015, Lava dome eruptions, in Sigurdsson, H., Houghton, B., McNutt, S.R., Rymer, H., and Stix, J., eds., The Encyclopedia of Volcanoes (2nd ed.): Academic Press, p. 343–362, doi: 10.1016/B978-0-12-385938-9.00018-3.

Campbell, H.J., Mortimer, N., and Raine, J.I., 2012, Geology of Zealandia, in Mortimer, N., ed., New Zealand–New Caledonia: compilation map and overview: GNS Science Miscellaneous Series.

Carter, L., Alloway, B., Shane, P., and Westgate, J., 2004, Deep-ocean record of major late Cenozoic rhyolitic eruptions from New Zealand: New Zealand Journal of Geology and Geophysics, v. 47, p. 481–500, doi: 10.1080/00288306.2004.9515071.

Carter, L., Shane, P., Alloway, B., Hall, I.R., Harris, S.E., and Westgate, J.A., 2003, Demise of one volcanic zone and birth of another—A 12 m.y. marine record of major rhyolitic eruptions from New Zealand: Geology, v. 31, p. 493, doi: 10.1130/0091-7613(2003)031<0493:DOOVZA>2.0.CO;2.

Cashman, K.V., and Blundy, J., 2013, Petrological cannibalism: the chemical and textural consequences of incremental magma body growth: Contributions to Mineralogy and Petrology, v. 166, p. 703–729, doi: 10.1007/s00410-013-0895-0.

Cassidy, J., and Locke, C.A., 2010, The Auckland volcanic field, New Zealand: Geophysical evidence for structural and spatio-temporal relationships: Journal of Volcanology and Geothermal Research, v. 195, p. 127–137, doi: 10.1016/j.jvolgeores.2010.06.016.

Cassidy, J., France, S.J., and Locke, C.A., 1999, Gravity and magnetic investigations of maar volcanoes, Auckland Volcanic Field, New Zealand: Journal of Volcanology and Geothermal Research, v. 89, p. 49–58, doi: 10.1016/S0377-0273(98)00121-X.

Castro, J.M., Beck, P., Tuffen, H., Nichols, A.R.L., Dingwell, D.B., and Martin, M.C., 2008, Timescales of spherulite crystallization in obsidian inferred from water concentration profiles: American Mineralogist, v. 93, p. 1816–1822, doi: 10.2138/am.2008.2904.

Chambefort, I., Lewis, B., Wilson, C.J.N., Rae, A.J., Coutts, C., Bignall, G., and Ireland, T.R., 2014, Stratigraphy and structure of the Ngatamariki geothermal system from new zircon U-Pb geochronology: Implications for Taupo Volcanic Zone evolution: Journal of Volcanology and Geothermal Research, v. 274, p. 51–70, doi: 10.1016/j.jvolgeores.2014.01.015.

Charlier, B.L.A., Wilson, C.J.N., Lowenstern, J.B., Blake, S., van Calsteren, P.W., and Davidson, J.P., 2005, Magma generation at a large, hyperactive silicic volcano (Taupo, New Zealand) revealed by U–Th and U–Pb systematics in zircons: Journal of Petrology, v. 46, p. 3–32, doi: 10.1093/petrology/egh060.

Cioni, R., and Funedda, A., 2005, Structural geology of crystal-rich, silicic lava flows: A case study from San Pietro Island (Sardinia, Italy): Geological Society of America Special Paper, v. 396, p. 1–14, doi: 10.1130/0-8137-2396-5.1.

Cole, J., and Lewis, K.B., 1981, Evolution of the Taupo–Hikurangi subduction system: Tectonophysics, v. 72, p. 1–21, doi: 10.1016/0040-1951(81)90084-6.

Cole, J.W., 1976, Distribution and tectonic setting of late Cenozoic volcanism in New Zealand: Royal Society of New Zealand Bulletin, v. 10, p. 239–252.

Cole, J.W., and Spinks, K.D., 2009, Caldera volcanism and rift structure in the Taupo Volcanic Zone, New Zealand: Geological Society, London, Special Publications, v. 327, p. 9–29, doi: 10.1144/SP327.2.

Cole, J.W., Spinks, K.D., Deering, C.D., Nairn, I.A., and Leonard, G.S., 2010, Volcanic and structural evolution of the Okataina Volcanic Centre; dominantly silicic volcanism associated with the Taupo Rift, New Zealand: Journal of Volcanology and Geothermal Research, v. 190, p. 123–135, doi: 10.1016/j.jvolgeores.2009.08.011.

Cook, E.T., 2016, Felsic volcanism in the eastern Waihi area: process origins of the Corbett and Ratarua ignimbrites and the Hikurangi Rhyolite [M.Sc.(Research) thesis]: University of Waikato, Hamilton, New Zealand, 224 p.

Cooper, G.F., 2014, The dynamics of large-scale silicic magmatic systems: case studies from Mangakino Volcanic Centre, Taupo Volcanic Zone, New Zealand [Ph.D. thesis]: Victoria University of Wellington, doi: 10.26686/wgtn.17006218.v1.

Davey, F.J., Henrys, S.A., and Lodolo, E., 1995, Asymmetric rifting in a continental back-arc environment, North Island, New Zealand: Journal of Volcanology and Geothermal Research, v. 68, p. 209–238, doi: 10.1016/0377-0273(95)00014-L.

Deering, C.D., Bachmann, O., Dufek, J., and Gravley, D.M., 2011, Rift-related transition from andesite to rhyolite volcanism in the Taupo Volcanic Zone (New Zealand) controlled by crystal–melt dynamics in mush zones with variable mineral assemblages: Journal of Petrology, v. 52, p. 2243–2263, doi: 10.1093/petrology/egr046.

Downs, D.T., 2014, Evolution of the intra-arc Taupo–Reporoa Basin within the Taupo Volcanic Zone of New Zealand: Geosphere, v. 10, p. 185, doi: 10.1130/GES00965.1.

Ellis, S., Heise, W., Kissling, W., Villamor, P., and Schreurs, G., 2014, The effect of crustal melt on rift dynamics: case study of the Taupo Volcanic Zone: New Zealand Journal of Geology and Geophysics, v. 57, p. 453–458, doi: 10.1080/00288306.2014.972961.

Fink, J.H., 1983, Structure and emplacement of a rhyolitic obsidian flow: Little Glass Mountain, Medicine Lake Highland, northern California: Geological Society of America Bulletin, v. 94, p. 362–380, doi: 10.1130/0016-7606(1983)94<362:SAEOAR>2.0.CO;2.

Fink, J.H., and Anderson, S.W., 2000, Lava domes and coulees, in Sigurdsson, H., et al., eds., Encyclopedia of Volcanoes: Academic Press, San Diego, p. 307–319.

Fink, J.H., and Griffiths, R.W., 1998, Morphology, eruption rates, and rheology of lava domes: Insights from laboratory models: Journal of Geophysical Research: Solid Earth, v. 103, p. 527–545, doi: 10.1029/97JB02838.

Fink, J.H., ed., 1987, The emplacement of silicic domes and lava flows: Geological Society of America Special Paper, v. 212, 145 p.

Fink, J.H., ed., 1990, Lava flows and domes: emplacement mechanisms and hazard implications: IAVCEI Proceedings in Volcanology, v. 2, Springer-Verlag, Heidelberg, doi: 10.1007/978-3-642-74379-5.

Fromont, A.R., 2017, A seismic investigation of the evolution and structure of the Kerepehi Fault, in the context of the Hauraki Rift, New Zealand [Ph.D. thesis]: University of Auckland, Auckland, New Zealand.

Hale, A.J., and Wadge, G., 2008, The transition from endogenous to exogenous growth of lava domes with the development of shear bands: Journal of Volcanology and Geothermal Research, v. 171, p. 237–257, doi: 10.1016/j.jvolgeores.2007.12.016.

Hamilton, A.R., Campbell, K.A., Rowland, J.V., Barker, S., and Guido, D., 2018, Characteristics and variations of sinters in the Coromandel Volcanic Zone:

application to epithermal exploration: New Zealand Journal of Geology and Geophysics, v. 62, p. 531–549, doi: 10.1080/00288306.2018.1519514.

Hayward, B., 1993, The tempestuous 10 million year life of a double arc and intra-arc basin – New Zealand's Northland Basin in the Early Miocene: Sedimentary Basins of the World, v. 2, p. 113–142.

Hayward, B.W., 1975, Waipoua Basalt and the geology of Maunganui Bluff: Tane, v. 21, p. 121–138.

Healy, J., Schofield, J.C., and Thompson, B.N., 1964, Sheet 5 — Rotorua (1st ed.). Geological Map of New Zealand 1:250,000: New Zealand Geological Survey, Department of Scientific and Industrial Research.

Henderson, J., and Bartrum, J.A., 1913, The geology of the Aroha Subdivision, Hauraki, Auckland: New Zealand Geological Survey Bulletin, v. 16, p. 1–127.

Herzer, R., Mascle, J., Davy, B., Ruellan, E., Mortimer, N., Laporte, C., and Duxfield, A., 2000, New constraints on the New Zealand–South Fiji Basin continent–back-arc margin: Comptes Rendus de l'Académie des Sciences – Series IIA – Earth and Planetary Science, v. 330, p. 701–708, doi: 10.1016/S1251-8050(00)00185-3.

Herzer, R.H., 1995, Seismic stratigraphy of a buried volcanic arc, Northland, New Zealand and implications for Neogene subduction: Marine and Petroleum Geology, v. 12, p. 511–531, doi: 10.1016/0264-8172(95)91506-K.

Hochstein, M.P., and Ballance, P.F., 1993, Hauraki Rift: a young, active, intra-continental rift in a back-arc setting, in Ballance, P.F., ed., South Pacific Sedimentary Basins, v. 2, Elsevier, p. 295–305.

Hodder, A.P.W., 1984, Late Cenozoic rift development and intra-plate volcanism in northern New Zealand inferred from geochemical discrimination diagrams: Tectonophysics, v. 101, p. 293–318, doi: 10.1016/0040-1951(84)90118-5.

Hollis, A.G., 1995, Volcanic geology of the central Tauranga Basin, New Zealand [M.Sc. thesis]: University of Waikato, Hamilton, New Zealand.

Hopkins, J.L., Lowe, D.J., and Horrocks, J.L., 2021, Tephrochronology in Aotearoa New Zealand: New Zealand Journal of Geology and Geophysics, v. 64, p. 153–200, doi: 10.1080/00288306.2021.1908368.

Hopkins, J.L., Smid, E.R., Eccles, J.D., Hayes, J.L., Hayward, B.W., McGee, L.E., van Wijk, K., Wilson, T.M., Cronin, S.J., Leonard, G.S., Lindsay, J.M., Németh, K., and Smith, I.E.M., 2021, Auckland Volcanic Field magmatism, volcanism, and hazard: a review: New Zealand Journal of Geology and Geophysics, v. 64, p. 213–234, doi: 10.1080/00288306.2020.1736102.

Houghton, B.F., and Cuthbertson, A.S., 1989, Sheet T14 BD – Kaimai. Geological Map of New Zealand 1:50,000: Wellington, New Zealand Department of Scientific and Industrial Research.

Hughes, G.R., 1993, Volcanic geology of the eastern Tauranga Basin and Papamoa Range [M.Sc. thesis]: University of Waikato, Hamilton, New Zealand.

Julian, H.A., 2016, Volcanology of the Owharoa and Waikino ignimbrites, Waihi, Coromandel Volcanic Zone [M.Sc.(Tech.) thesis]: University of Waikato, Hamilton, New Zealand.

Kinley, T., 2022, Volcanic history of the Mount Misery Rhyolite Domes, Tauranga Volcanic Centre [M.Sc.(Research) thesis]: University of Waikato, Hamilton, New Zealand, 137 p.

Le Bas, M.J., Le Maitre, R.W., Streckeisen, A., and Zanettin, B., 1986, A chemical classification of volcanic rocks based on the total alkali–silica diagram: Journal of Petrology, v. 27, p. 745–750, doi: 10.1093/petrology/27.3.745.

Leonard, G.S., Begg, J.G., and Wilson, C.J.N. (compilers), 2010, Geology of the Rotorua area, scale 1:250,000: Lower Hutt, Institute of Geological & Nuclear Sciences 1:250,000 Geological Map 5, 102 p. + 1 folded map, ISBN 978-0-478-19778-5.

Leonard, G.S., Calvert, A.T., Hopkins, J.L., Wilson, C.J.N., Smid, E.R., Lindsay, J.M., and Champion, D.E., 2017, High-precision $^{40}Ar/^{39}Ar$ dating of Quaternary basalts from Auckland Volcanic Field, New Zealand, with implications for eruption rates and paleomagnetic correlations: Journal of Volcanology and

Geothermal Research, v. 343, p. 60–74, doi: 10.1016/j.jvolgeores.2017.05.033.

Lindsay, J.M., Worthington, T.J., Smith, I.E.M., and Black, P.M., 1999, Geology, petrology, and petrogenesis of Little Barrier Island, Hauraki Gulf, New Zealand: New Zealand Journal of Geology and Geophysics, v. 42, p. 155–168, doi: 10.1080/00288306.1999.9514837.

Lipman, P.W., and Mullineaux, D.R., eds., 1981, The 1980 eruptions of Mount St. Helens, Washington: U.S. Geological Survey Professional Paper, v. 1250, doi: 10.3133/pp1250.

Lofgren, G., 1970, Experimental devitrification rate of rhyolite glass: Geological Society of America Bulletin, v. 81, p. 553–560, doi: 10.1130/0016-7606(1970)81[553:EDRORG]2.0.CO;2.

Lofgren, G., 1971a, Experimentally produced devitrification textures in natural rhyolitic glass: Geological Society of America Bulletin, v. 82, p. 111–124, doi: 10.1130/0016-7606(1971)82[111:EPDTIN]2.0.CO;2.

Lofgren, G., 1974, An experimental study of plagioclase crystal morphology; isothermal crystallization: American Journal of Science, v. 274, p. 243–273, doi: 10.2475/ajs.274.3.243.

Lofgren, G.E., 1971b, Spherulitic textures in glassy and crystalline rocks: Journal of Geophysical Research, v. 76, p. 5635–5648, doi: 10.1029/JB076i023p05635.

Lowe, D.J., 2011, Tephrochronology and its application: a review: Quaternary Geochronology, v. 6, p. 107–153, doi: 10.1016/j.quageo.2010.08.003.

McLeod, O.E., 2020, Geology of Mount Pirongia and the Alexandra Volcanic Group [Ph.D. thesis]: University of Waikato, Hamilton, New Zealand, https://researchcommons.waikato.ac.nz/items/f33db8f0-e306-481f-a2c2-ebf856210c69.

McLeod, O.E., Brenna, M., Briggs, R.M., and Pittari, A., 2022, Slab tear as a cause of coeval arc–intraplate volcanism in the Alexandra Volcanic Group, New Zealand: Lithos, v. 408–409, p. 106564, doi: 10.1016/j.lithos.2021.106564.

McLeod, O.E., Pittari, A., Brenna, M., and Briggs, R.M., 2020, Geology of the Pirongia Volcano, Waikato, scale 1:30,000 geological map: Geoscience Society of New Zealand Miscellaneous Publication, v. 156, 60 p.

Milner, D.M., Cole, J.W., and Wood, C.P., 2003, Mamaku Ignimbrite: a caldera-forming ignimbrite erupted from a compositionally zoned magma chamber in Taupo Volcanic Zone, New Zealand: Journal of Volcanology and Geothermal Research, v. 122, p. 243–264, doi: 10.1016/S0377-0273(02)00504-8.

Moore, P.R., 1983, Rhyolite domes and pyroclastic rocks (Whitianga Group) of the Hahei area, Coromandel Peninsula: Journal of the Royal Society of New Zealand, v. 13, p. 79–92, doi: 10.1080/03036758.1983.10415339.

Mortimer, N., and Scott, J.M., 2020, Volcanoes of Zealandia and the Southwest Pacific: New Zealand Journal of Geology and Geophysics, v. 63, p. 371–377, doi: 10.1080/00288306.2020.1713824.

Namaliu, M., 2021, Volcanic geology of the early Pleistocene ignimbrite succession in the western Papamoa Region, Bay of Plenty [M.Sc. thesis]: University of Waikato, Hamilton, New Zealand, 111 p.

Nasholds, M.W.M., and Zimmerer, M.J., 2022, High-precision $^{40}Ar/^{39}Ar$ geochronology and volumetric investigation of volcanism and resurgence following eruption of the Tshirege Member, Bandelier Tuff, at the Valles caldera: Journal of Volcanology and Geothermal Research, v. 431, p. 107624, doi: 10.1016/j.jvolgeores.2022.107624.

Nicholson, K.G., Black, P.McL., Hoskin, P.W.O., and Smith, I.E.M., 2004, Silicic volcanism and back-arc extension related to migration of the Late Cainozoic Australian–Pacific plate boundary: Journal of Volcanology and Geothermal Research, v. 131, p. 295–306, doi: 10.1016/S0377-0273(03)00382-2.

Persaud, M., Villamor, P., Berryman, K., Ries, W., Cousins, J., Litchfield, N., and Alloway, B., 2016, The Kerepehi Fault, Hauraki Rift, North Island, New Zealand: active fault characterisation and hazard: New Zealand Journal of Geology and Geophysics, v. 59, p. 117–135, doi: 10.1080/00288306.2015.1127826.

Pittari, A., Prentice, M.L., McLeod, O.E., Yousef Zadeh, E., Kamp, P.J.J., Danišík, M., and Vincent, K.A., 2021, Inception of the modern North Island (New Zealand) volcanic setting: spatio-temporal patterns of volcanism between 3.0 and 0.9 Ma: New Zealand Journal of Geology and Geophysics, v. 64, p. 250–272, doi: 10.1080/00288306.2021.1915343.

Prentice, M., Pittari, A., and Kilgour, G., 2025, The Waiteariki Ignimbrite: eruption of a large-volume, monotonous intermediate ignimbrite at the dawn of the Taupō Volcanic Zone, New Zealand: Journal of Petrology, v. 66, doi: 10.1093/petrology/egaf052.

Prentice, M., Pittari, A., Lowe, D.J., Kilgour, G., Kamp, P.J.J., and Namaliu, M., 2022, Linking proximal ignimbrites and coeval distal tephra deposits to establish a record of voluminous Early Quaternary (2.4–1.9 Ma) volcanism of the Tauranga Volcanic Centre, New Zealand: Journal of Volcanology and Geothermal Research, v. 429, p. 107595, doi: 10.1016/j.jvolgeores.2022.107595.

Prentice, M.L., 2023, Silicic volcanism of the Tauranga Volcanic Centre and the climactic Waiteariki supereruption at the dawn of the Taupō Volcanic Zone [Ph.D. thesis]: University of Waikato, Hamilton, New Zealand.

Rowland, J.V., Wilson, C.J.N., and Gravley, D.M., 2010, Spatial and temporal variations in magma-assisted rifting, Taupo Volcanic Zone, New Zealand: Journal of Volcanology and Geothermal Research, v. 190, p. 89–108, doi: 10.1016/j.jvolgeores.2009.05.004.

Ruppel, C., 1995, Extensional processes in continental lithosphere: Journal of Geophysical Research: Solid Earth, v. 100, p. 24187–24215, doi: 10.1029/95JB02955.

Rutherford, N.F., 1978, Fission track age and trace element geochemistry of some Minden Rhyolite obsidians: New Zealand Journal of Geology and Geophysics, v. 21, p. 443–448, doi: 10.1080/00288306.1978.10424070.

Saunders, K.E., 2009, Micro-analytical studies of the petrogenesis of silicic arc magmas in the Taupo Volcanic Zone and southern Kermadec Arc, New

Zealand [Ph.D. thesis]: Victoria University of Wellington, doi: 10.26686/wgtn.16959340.v1.

Shane, P., 2000, Tephrochronology: a New Zealand case study: Earth-Science Reviews, v. 49, p. 223–259, doi: 10.1016/S0012-8252(99)00058-6.

Shane, P., 2017, The southern end of the Pacific Ring of Fire: Quaternary volcanism in New Zealand, in Shulmeister, J., ed., Landscape and Quaternary Environmental Change in New Zealand: Atlantis Advances in Quaternary Science, v. 3, Atlantis Press, Paris, p. 35–66, doi: 10.2991/978-94-6239-237-3_2.

Skinner, D.N.B., 1986, Neogene volcanism of the Hauraki Volcanic Region, in Smith, I.E.M., ed., Late Cenozoic Volcanism in New Zealand: Royal Society of New Zealand Bulletin, v. 23, p. 21–47.

Smith, I.E.M., ed., 1986, Late Cenozoic volcanism in New Zealand: Royal Society of New Zealand Bulletin, v. 23, 371 p.

Sparks, R.S.J., Murphy, M.D., Lejeune, A.M., Watts, R.B., Barclay, J., and Young, S.R., 2000, Control on the emplacement of the andesite lava dome of the Soufrière Hills volcano, Montserrat by degassing-induced crystallization: Terra Nova, v. 12, p. 14–20, doi: 10.1046/j.1365-3121.2000.00267.x.

Stagpoole, V., Miller, C., Caratori Tontini, F., Brakenrig, T., and Macdonald, N., 2021, A two million-year history of rifting and caldera volcanism imprinted in new gravity anomaly compilation of the Taupō Volcanic Zone, New Zealand: New Zealand Journal of Geology and Geophysics, v. 64, p. 358–371, doi: 10.1080/00288306.2020.1848882.

Stevenson, R.J., Briggs, R.M., and Hodder, A.P.W., 1993, Emplacement history of a low-viscosity, fountain-fed pantelleritic lava flow: Journal of Volcanology and Geothermal Research, v. 57, p. 39–56, doi: 10.1016/0377-0273(93)90030-U.

Stipp, J.J., and McDougall, I., 1968, The geochronology and petrogenesis of the Cenozoic volcanics of North Island, New Zealand [Ph.D. thesis]: The Australian National University, Canberra.

Sun, S.-S., and McDonough, W.F., 1989, Chemical and isotopic systematics of oceanic basalts: implications for mantle composition and processes, in Saunders, A.D., and Norry, M.J., eds., Magmatism in the Ocean Basins: Geological Society, London, Special Publications, v. 42, p. 313–345, doi: 10.1144/GSL.SP.1989.042.01.19.

Swanson, S.E., Naney, M.T., Westrich, H.R., and Eichelberger, J.C., 1989, Crystallization history of Obsidian Dome, Inyo Domes, California: Bulletin of Volcanology, v. 51, p. 161–176, doi: 10.1007/BF01067953.

Uyeda, S., and Kanamori, H., 1979, Back-arc opening and the mode of subduction: Journal of Geophysical Research, v. 84, p. 1049, doi: 10.1029/JB084iB03p01049.

Villamor, P., Berryman, K.R., Ellis, S.M., Schreurs, G., Wallace, L.M., Leonard, G.S., Langridge, R.M., and Ries, W.F., 2017, Rapid evolution of subduction-related continental intraarc rifts: The Taupo Rift, New Zealand: Tectonics, v. 36, p. 2250–2272, doi: 10.1002/2017TC004715.

Vincent, K.A., 2012, U-Pb dating of silicic volcanic rocks of the eastern Coromandel Peninsula [M.Sc. thesis]: University of Waikato, Hamilton, New Zealand.

Voight, B., Sparks, R.S.J., Miller, A.D., Stewart, R.C., Hoblitt, R.P., Clarke, A., Ewart, J., Aspinall, W.P., Baptie, B., Calder, E.S., Cole, P., Druitt, T.H., Hartford, C., Herd, R.A., Jackson, P., Lejeune, A.M., Lockhart, A.B., Loughlin, S.C., Luckett, R., Lynch, L., Norton, G.E., Robertson, R., Watson, I.M., Watts, R., and Young, S.R., 1999, Magma flow instability and cyclic activity at Soufrière Hills Volcano, Montserrat, British West Indies: Science, v. 283, p. 1138–1142, doi: 10.1126/science.283.5405.1138.

Watson, E.B., and Harrison, T.M., 1983, Zircon saturation revisited: temperature and composition effects in a variety of crustal magma types: Earth and Planetary Science Letters, v. 64, p. 295–304, doi: 10.1016/0012-821X(83)90211-X.

Whitbread-Edwards, A.N., 1994, Volcanic geology of the western Tauranga Basin [Ph.D. thesis]: University of Waikato, Hamilton, New Zealand.

Wilson, C.J.N., and Rowland, J.V., 2016, The volcanic, magmatic and tectonic setting of the Taupo Volcanic Zone, New Zealand, reviewed from a geothermal perspective: Geothermics, v. 59, p. 168–187, doi: 10.1016/j.geothermics.2015.06.013.

Wilson, C.J.N., Charlier, B.L.A., Fagan, C.J., Spinks, K.D., Gravley, D.M., Simmons, S.F., and Browne, P.R.L., 2009, U-Pb dating of zircon in subsurface, hydrothermally altered pyroclastic deposits and implications for subsidence in a magmatically active rift: Taupo Volcanic Zone, New Zealand: Journal of Volcanology and Geothermal Research, v. 191, p. 69–78, doi: 10.1016/j.jvolgeores.2010.01.001.

Wilson, C.J.N., Gravley, D.M., Leonard, G.S., and Rowland, J.V., 2018, Volcanism in the central Taupo Volcanic Zone, New Zealand: tempo, styles and controls, in Sigurdsson, H., et al., eds., Geological Society of London on behalf of The International Association of Volcanology and Chemistry of the Earth's Interior, p. 225–247, doi: 10.1144/IAVCEl002.12.

Wilson, C.J.N., Houghton, B.F., McWilliams, M.O., Lanphere, M.A., Weaver, S.D., and Briggs, R.M., 1995, Volcanic and structural evolution of Taupo Volcanic Zone, New Zealand: a review: Journal of Volcanology and Geothermal Research, v. 68, p. 1–28, doi: 10.1016/0377-0273(95)00006-G.

Wilson, C.J.N., Rogan, A.M., Smith, I.E.M., Northey, D.J., Nairn, I.A., and Houghton, B.F., 1984, Caldera volcanoes of the Taupo Volcanic Zone, New Zealand: Journal of Geophysical Research, v. 89, p. 8463, doi: 10.1029/JB089iB10p08463.

Wright, I.C., 1992, Shallow structure and active tectonism of an offshore continental back-arc spreading system: the Taupo Volcanic Zone, New Zealand: Marine Geology, v. 103, p. 287–309, doi: 10.1016/0025-3227(92)90021-9.

Wright, I.C., 1997, Morphology and evolution of the remnant Colville and active Kermadec arc ridges south of 33°30′ S: Marine Geophysical Researches, v. 19, p. 177–193, doi: 10.1023/A:1004266932113.

Appendix I: Locality and sample catalogue

Appendix 1: Locality and sample catalogue

Sample ID	Field Locality	Latitude	Longitude	Elevation	Unit/Dome Assignment	Rock Type	XRF	LA-ICP-MS	XRD	Thin Section	SEM-EDS
MC01	JSWAP FARM	-37.8807	175.9362	642.709	Kaimai Dome - Core	Rhyolite	✓	✓	✓	✓	-
MC02	JSWAP FARM	-37.879	175.9378	606.186	Kaimai Dome - Core	Rhyolite	✓	✓	✓	✓	✓
MC03	JSWAP FARM	-37.8782	175.9403	586.696	Kaimai Dome - Core	Rhyolite	✓	✓	✓	✓	-
MC04	JSWAP FARM	-37.8776	175.9432	602.688	Kaimai Dome - Core	Rhyolite	✓	✓	✓	✓	-
MC05	JSWAP FARM	-37.8802	175.9326	537.844	Kaimai Dome - Core	Rhyolite	✓	✓	✓	✓	✓
MC06	JSWAP FARM	-37.8792	175.9226	349.261	Kaimai Dome - Core	Rhyolite	✓	✓	✓	✓	-
MC07	NORTH-SOUTH TRACK	-37.8421	175.9222	557.293	Te Weraiti Dome - Core	Rhyolite	✓	✓	✓	✓	-
MC08	NORTH-SOUTH TRACK	-37.8421	175.9222	557.293	Te Weraiti Dome - Core	Rhyolite	✓	✓	✓	✓	✓
MC09	NORTH-SOUTH TRACK	-37.8462	175.9184	558.155	Te Weraiti Dome - Core	Altered Rhyolite	✓	✓	✓	✓	-
MC10	NORTH-SOUTH TRACK	-37.8484	175.9186	554.057	Te Weraiti Dome - Core	Altered Rhyolite	✓	✓	✓	✓	-
MC11	TRACK	-37.8634	175.9286	561.084	Waiteariki Formation	Ignimbrite	✓	✓	✓	✓	-
MC12	JSWAP QUARRY	-37.823	175.907	754.414	Te Weraiti Dome - Core	Rhyolite	✓	✓	✓	✓	-
MC13	JSWAP QUARRY	-37.8198	175.9068	745.114	Te Weraiti Dome - Core	Rhyolite	✓	✓	✓	✓	✓
MC14	JSWAP QUARRY	-37.8144	175.9055	690.505	Te Weraiti Dome - Core	Rhyolite	✓	✓	✓	✓	-
MC15	JSWAP QUARRY	-37.8099	175.9107	568.709	Waiteariki Formation	Ignimbrite	✓	✓	✓	✓	-
MC16	JSWAP QUARRY	-37.8087	175.9133	564.678	Te Weraiti Dome - Core	Rhyolite	✓	✓	✓	✓	-
MC17	JSWAP QUARRY	-37.8138	175.9101	599.916	Te Weraiti Dome - Core	Rhyolite	✓	✓	✓	✓	-
MC18	JSWAP QUARRY	-37.81	175.897	418.111	Te Weraiti Dome - Basement Andesite	Basaltic-Andesite	✓	✓	✓	✓	-
MC19	JSWAP FARM	-37.8807	175.9362	642.709	Kaimai Dome - Core	Rhyolite	✓	✓	✓	✓	-
MC20	RAPURAPU TRACK	-37.8895	175.9149	281.312	Kaimai Dome - Southwest Lobe	Rhyolite	✓	✓	✓	✓	-
MC21	RAPURAPU TRACK	-37.8956	175.9154	204.183	Kaimai Dome - Southwest Lobe	Rhyolite	✓	✓	✓	✓	-
MC22	TE POI	-37.9074	175.8956	108.335	Unassigned	Rhyolite	✓	✓	✓	✓	-

Appendix II: XRD

MC01

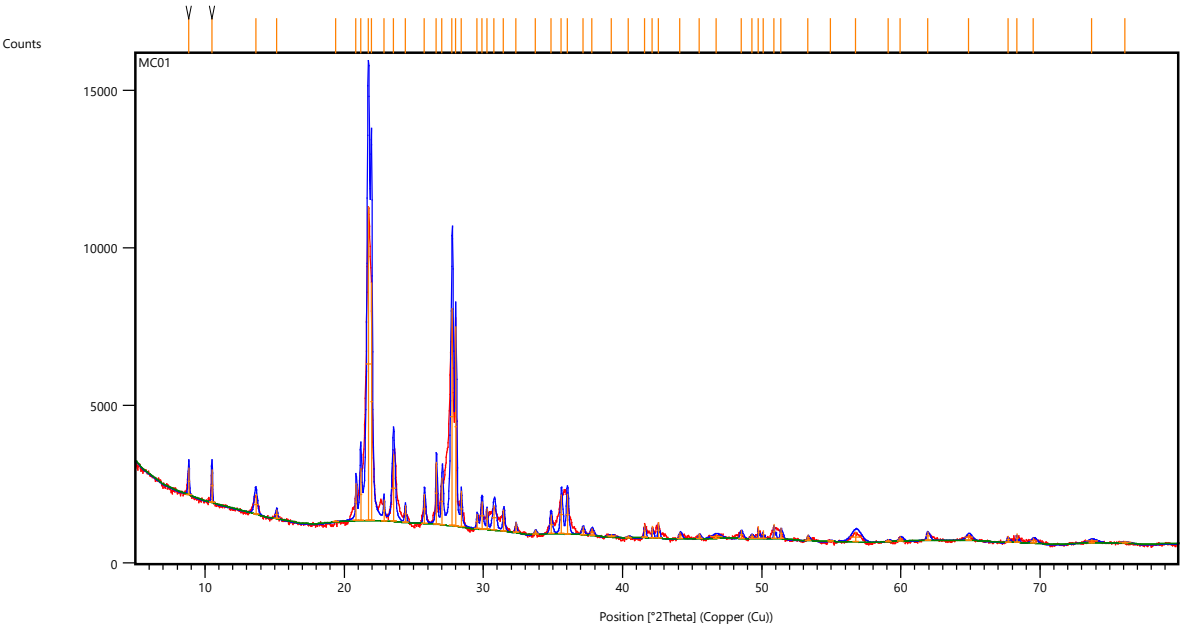
Counts
MC01
15000
10000
5000
0
10
20
30
40
50
60
70
Position [°2Theta] (Copper (Cu))

MC02

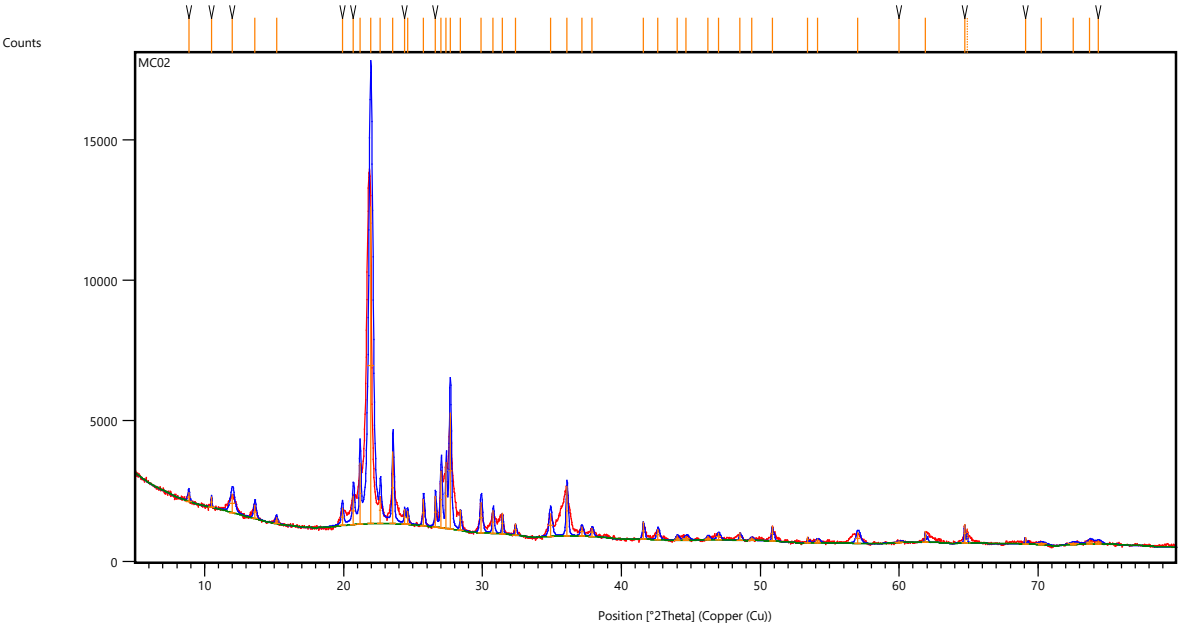
Counts
MC02
15000
10000
5000
0
10
20
30
40
50
60
70
Position [°2Theta] (Copper (Cu))

MC03

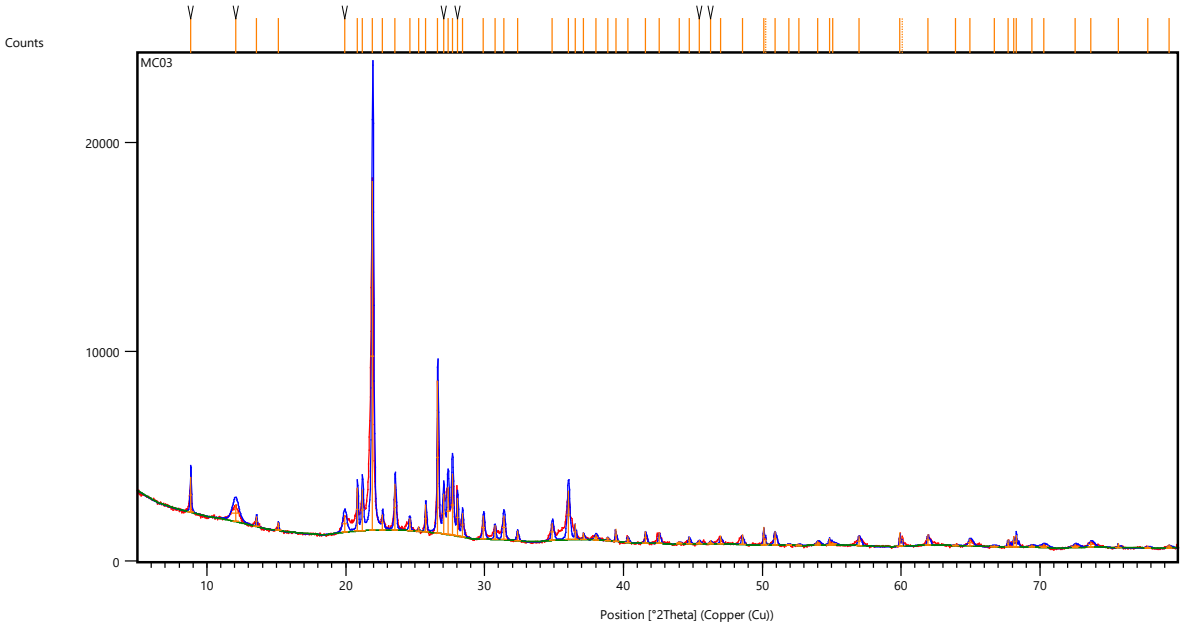
Counts
MC03
20000
10000
0
10
20
30
40
50
60
70
Position [°2Theta] (Copper (Cu))

MC04

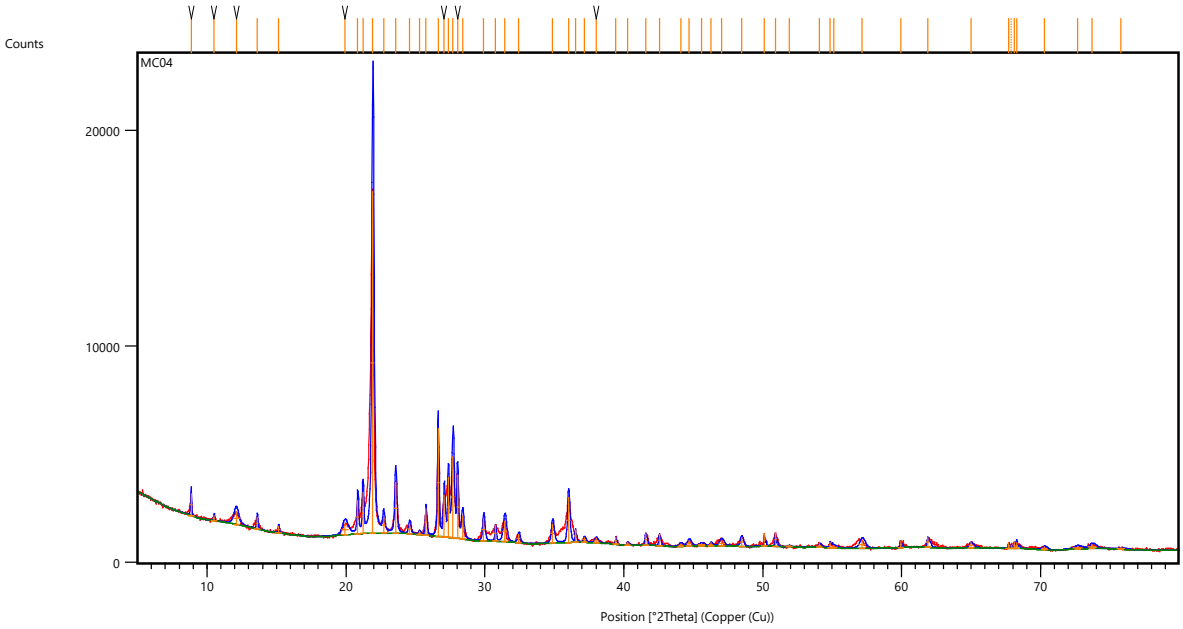
Counts
MC04
20000
10000
0
10
20
30
40
50
60
70
Position [°2Theta] (Copper (Cu))

MC05

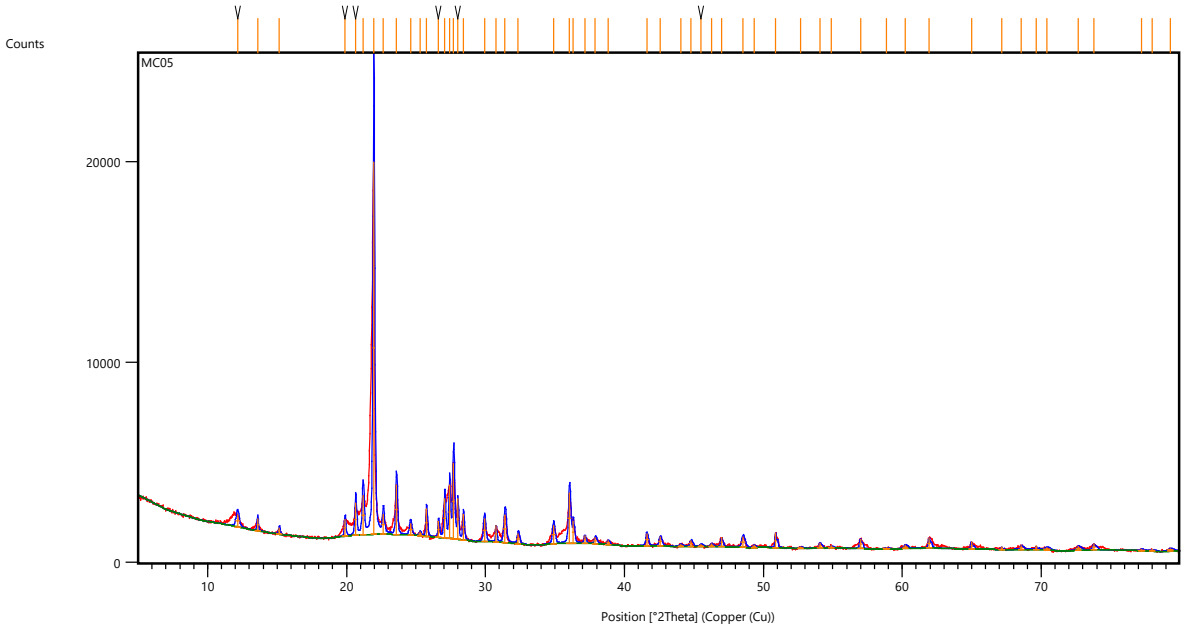
Counts
MC05
20000
10000
0
10
20
30
40
50
60
70
Position [°2Theta] (Copper (Cu))

MC06

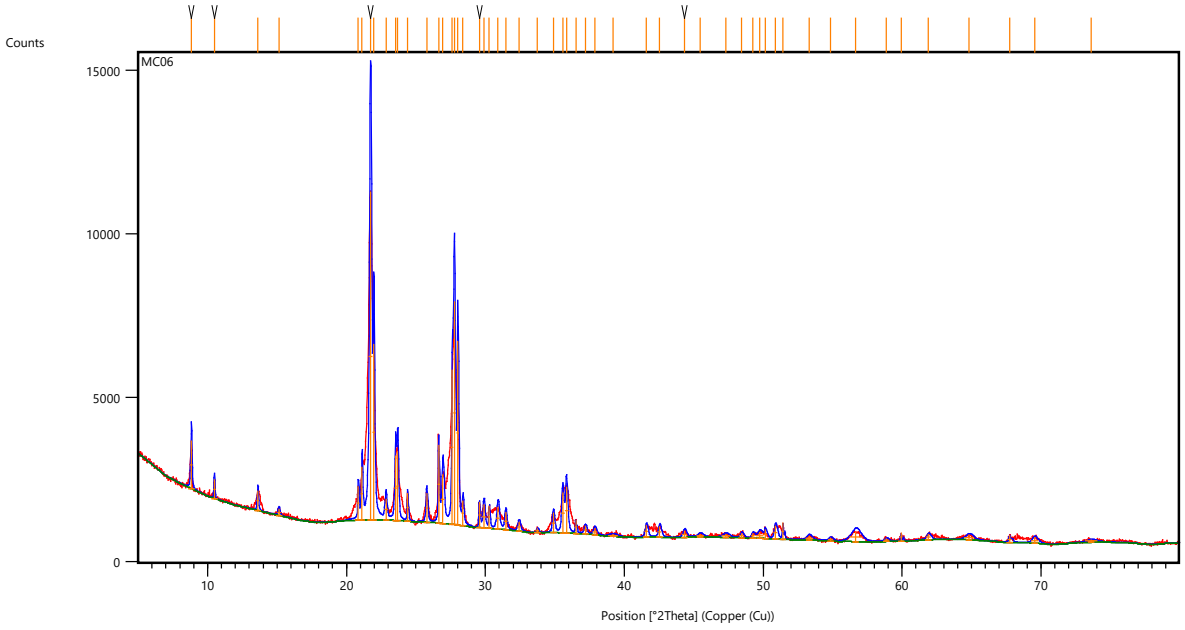
Counts
MC06
15000
10000
5000
0
10
20
30
40
50
60
70
Position [°2Theta] (Copper (Cu))

MC07

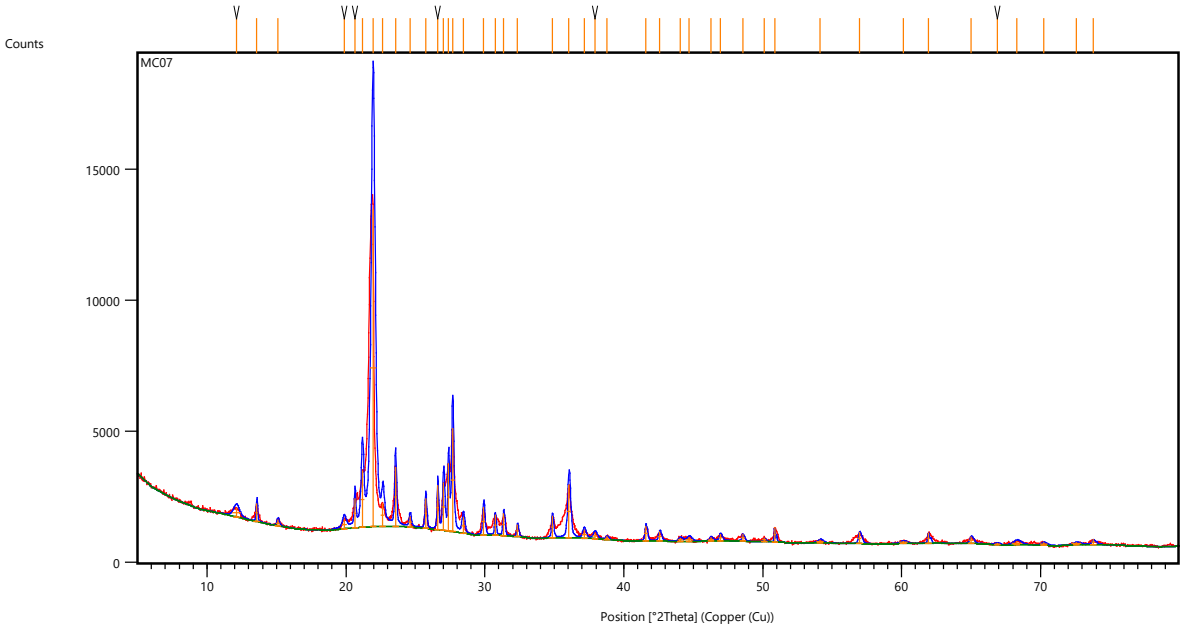
Counts
MC07
15000
10000
5000
0
10
20
30
40
50
60
70
Position [°2Theta] (Copper (Cu))

MC08

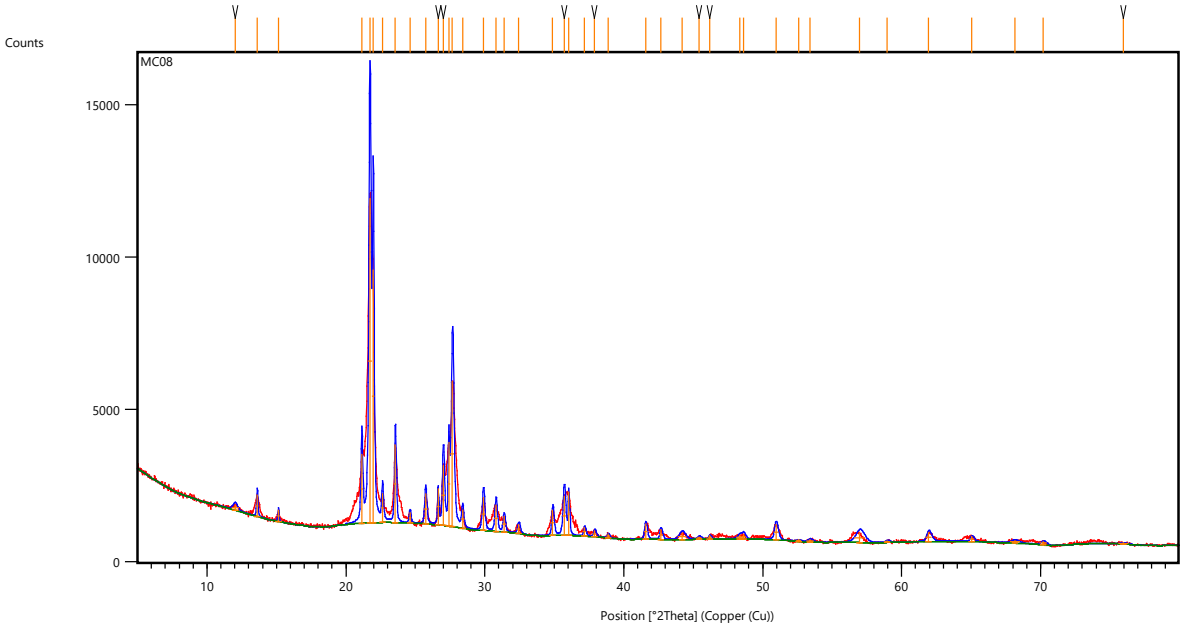
Counts
MC08
15000
10000
5000
0
10
20
30
40
50
60
70
Position [°2Theta] (Copper (Cu))

MC09

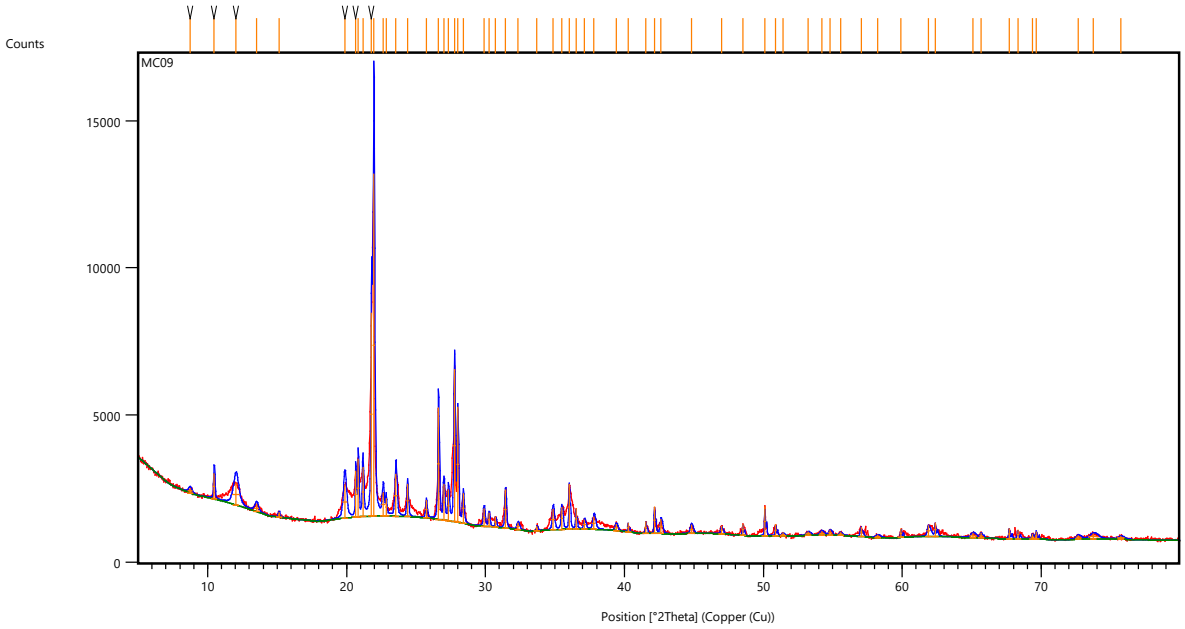
Counts
MC09
15000
10000
5000
0
10
20
30
40
50
60
70
Position [°2Theta] (Copper (Cu))

MC10

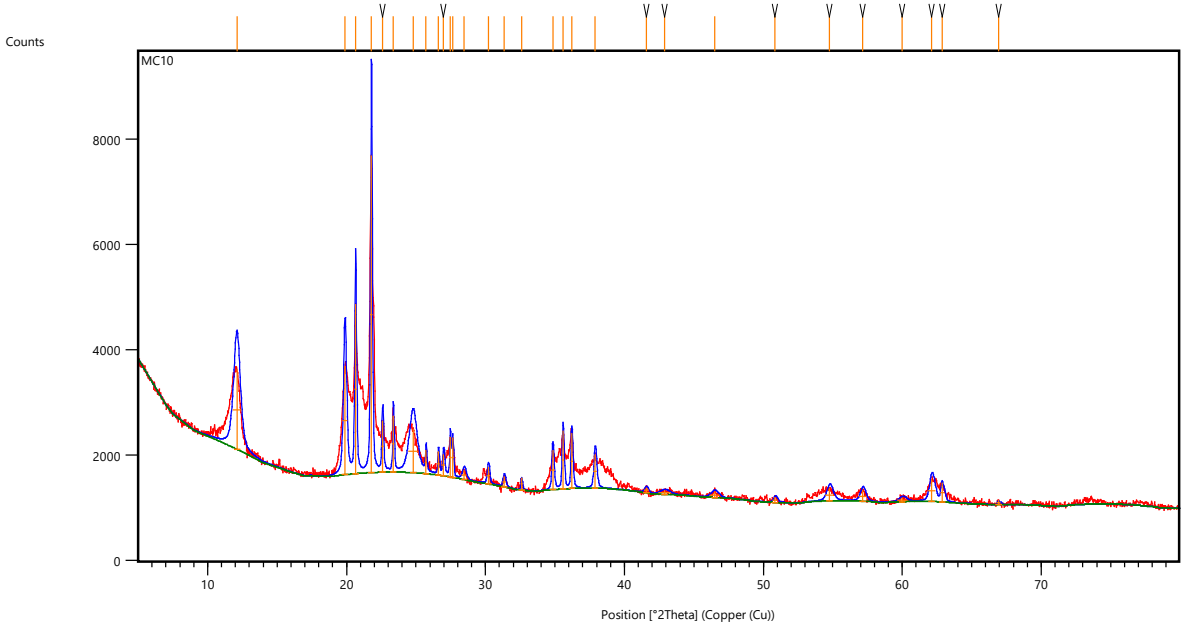
Counts
MC10
8000
6000
4000
2000
0
10
20
30
40
50
60
70
Position [°2Theta] (Copper (Cu))

MC11

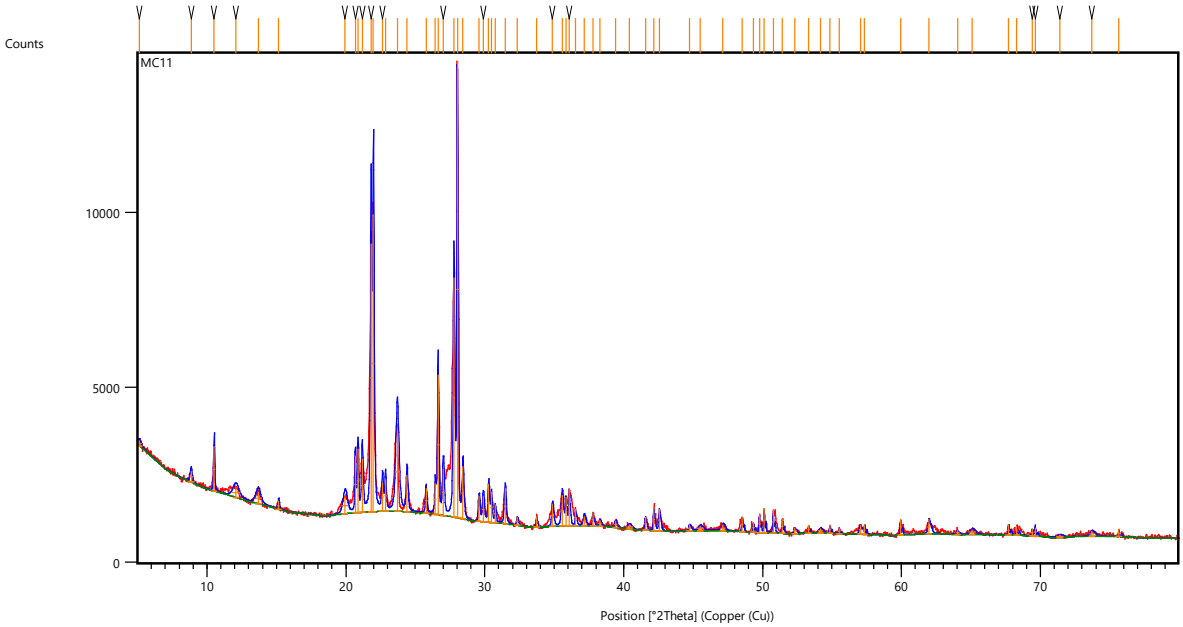
Counts
MC11
10000
5000
0
10
20
30
40
50
60
70
Position [°2Theta] (Copper (Cu))

MC12

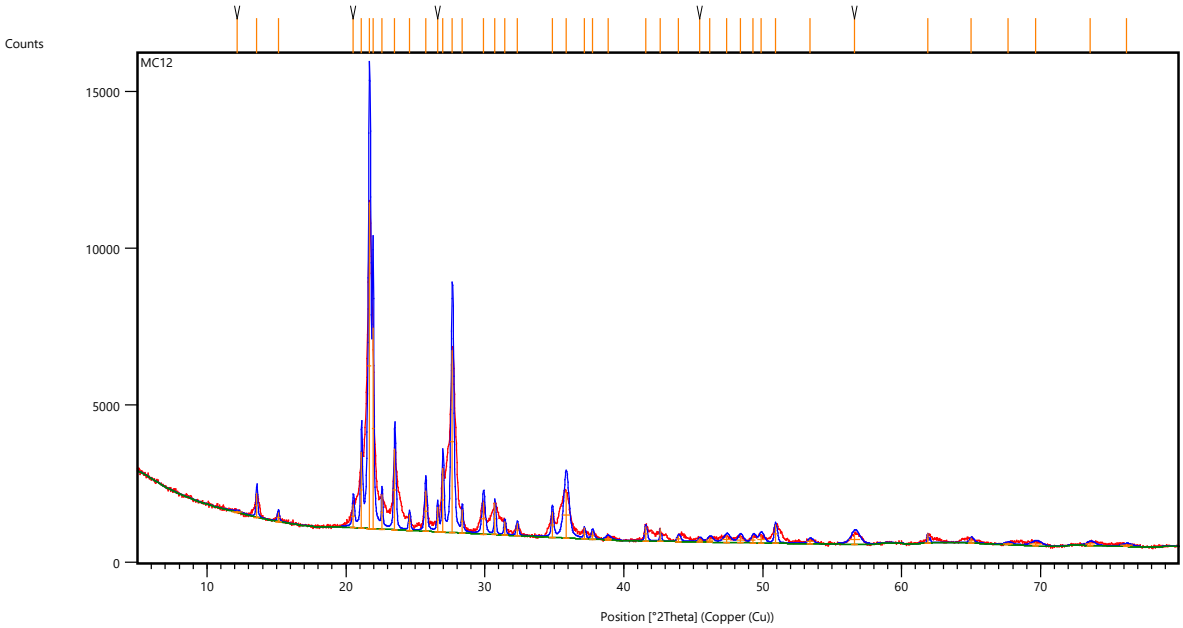
Counts
MC12
15000
10000
5000
0
10
20
30
40
50
60
70
Position [°2Theta] (Copper (Cu))

MC13

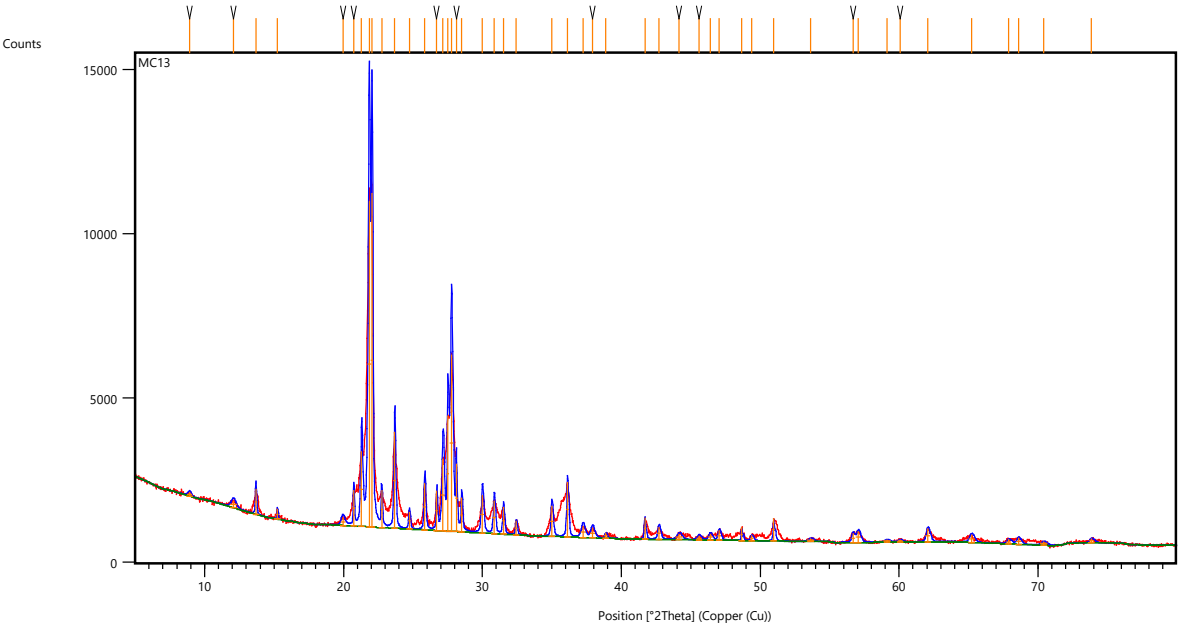
Counts
MC13
15000
10000
5000
0
10
20
30
40
50
60
70
Position [°2Theta] (Copper (Cu))

MC14

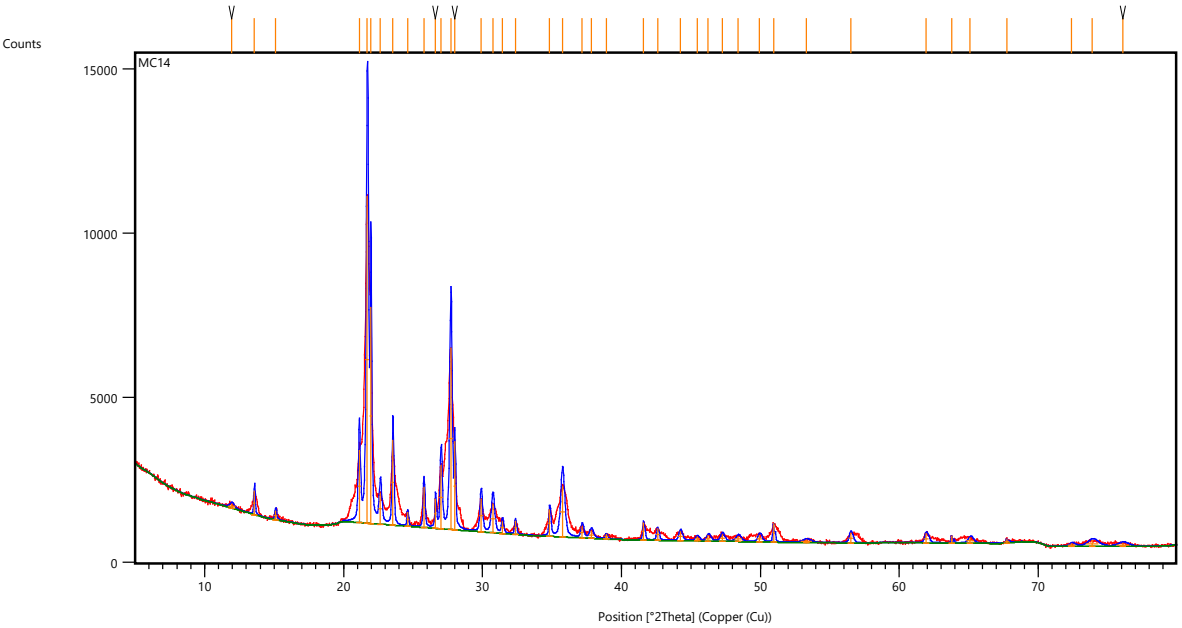
Counts
MC14
15000
10000
5000
0
10
20
30
40
50
60
70
Position [°2Theta] (Copper (Cu))

MC15

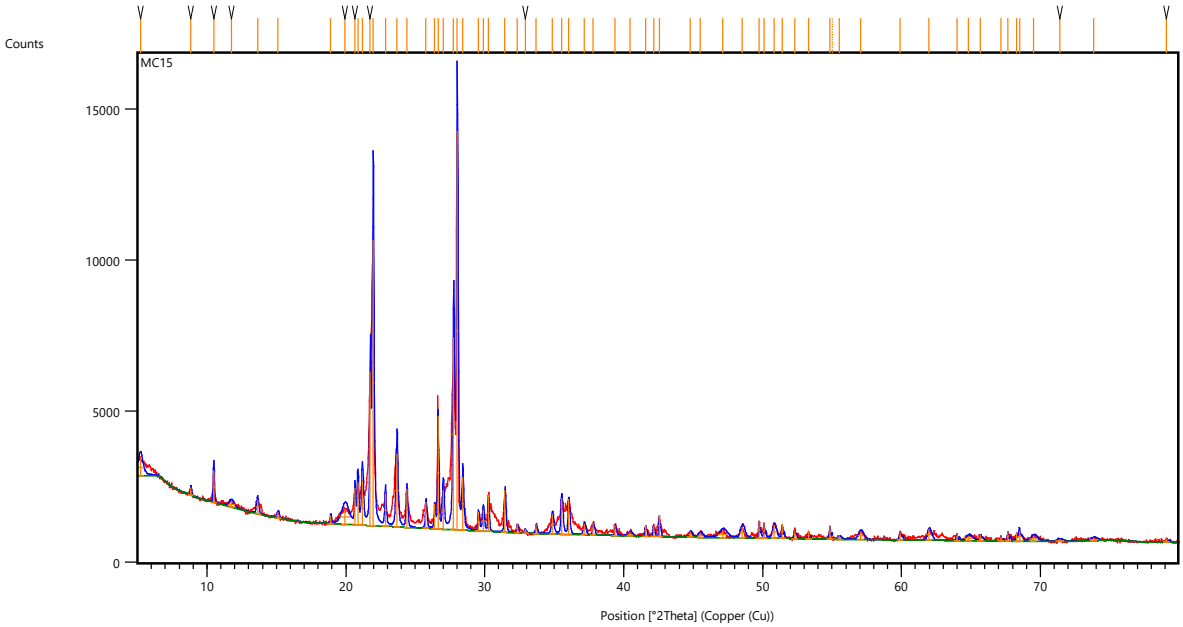
Counts
MC15
15000
10000
5000
0
10
20
30
40
50
60
70
Position [°2Theta] (Copper (Cu))

MC16

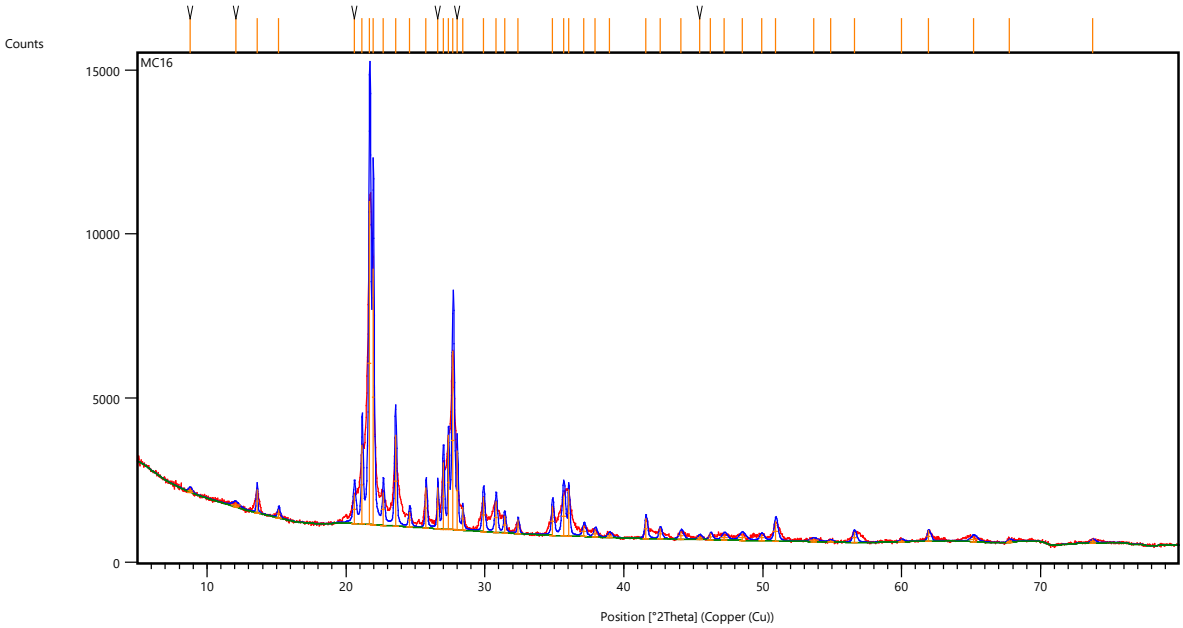
Counts
MC16
15000
10000
5000
0
10
20
30
40
50
60
70
Position [°2Theta] (Copper (Cu))

MC17

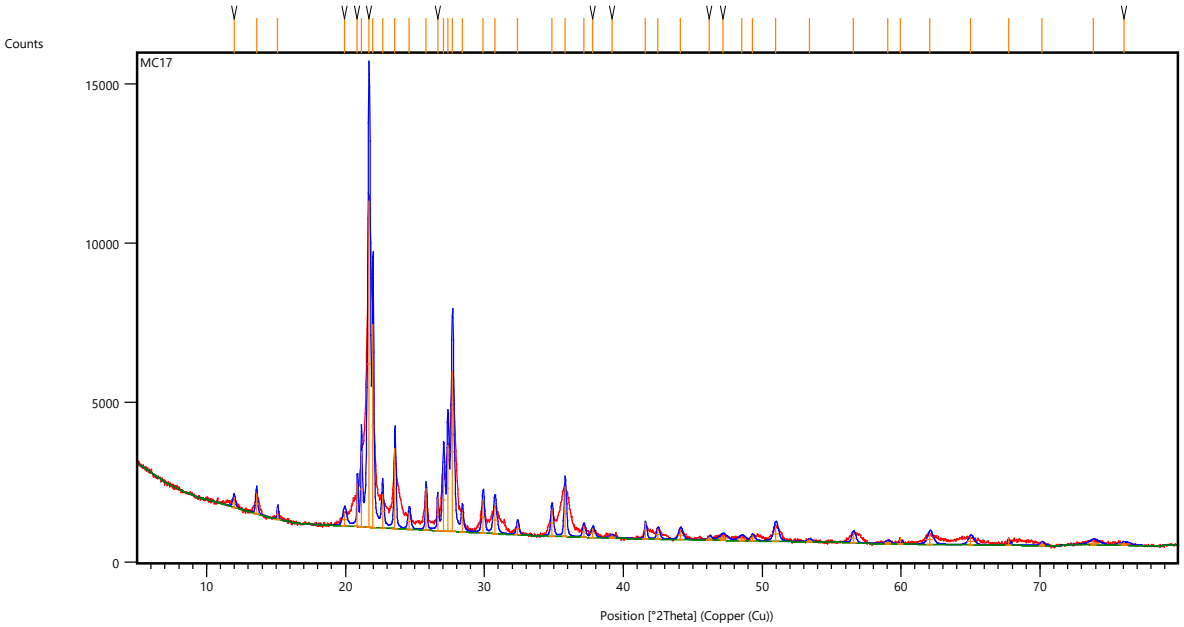
Counts
MC17
15000
10000
5000
0
10
20
30
40
50
60
70
Position [°2Theta] (Copper (Cu))

MC18

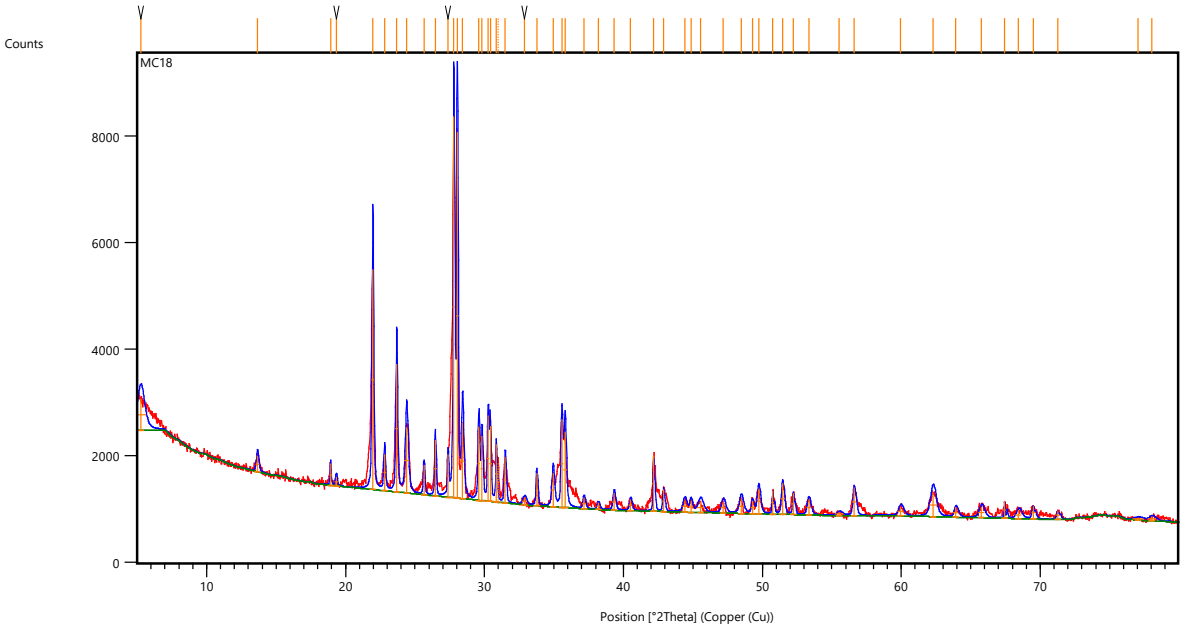
Counts
MC18
8000
6000
4000
2000
0
10
20
30
40
50
60
70
Position [°2Theta] (Copper (Cu))

MC18 Heavy Fraction

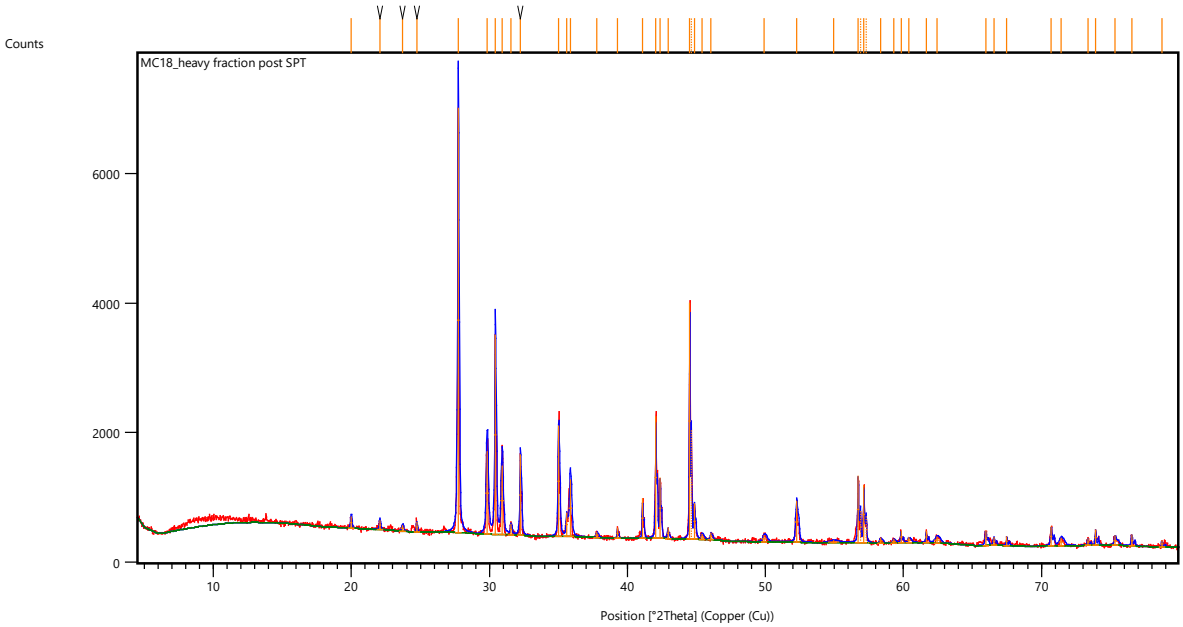

MC19

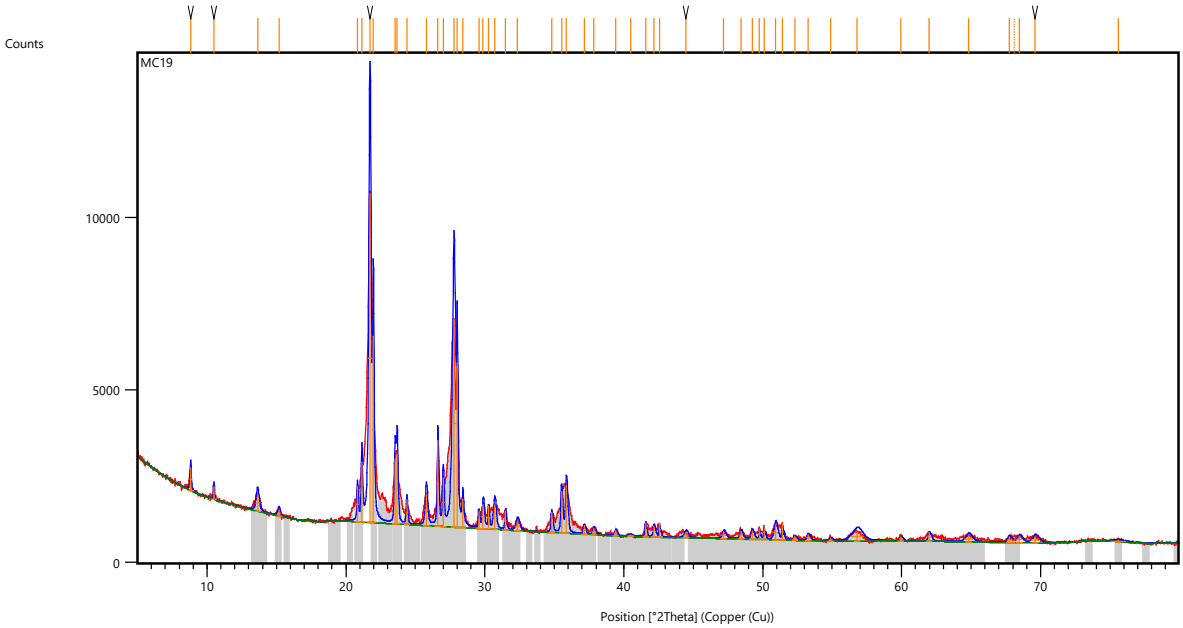

MC20

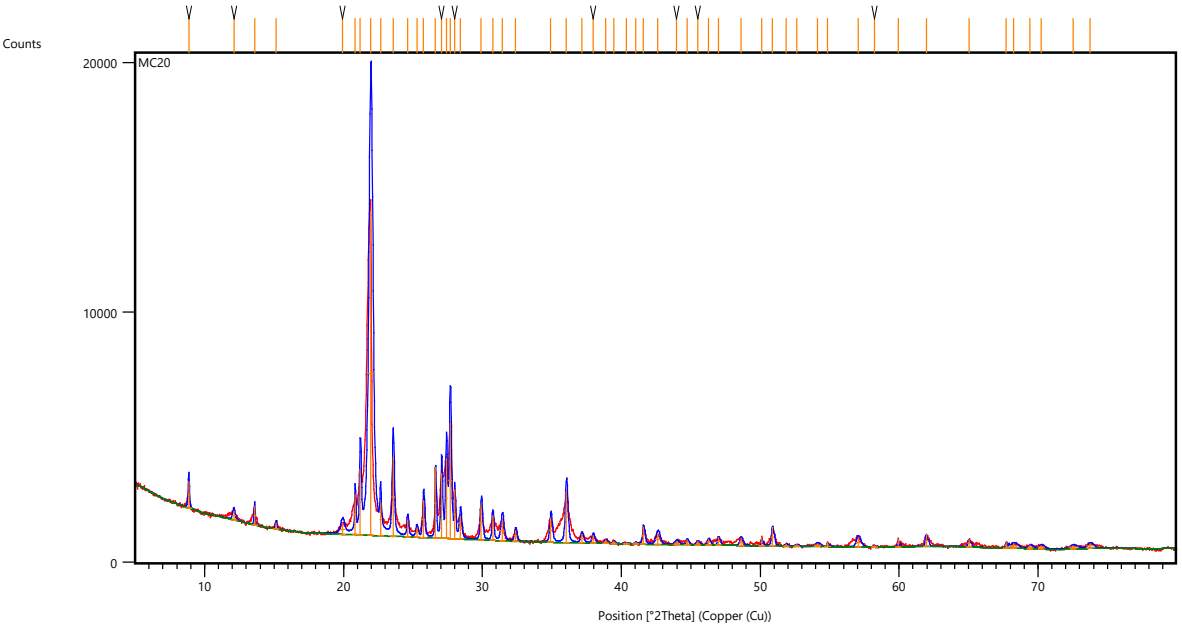
Counts
MC20
20000
10000
0
10
20
30
40
50
60
70
Position [°2Theta] (Copper (Cu))

MC21

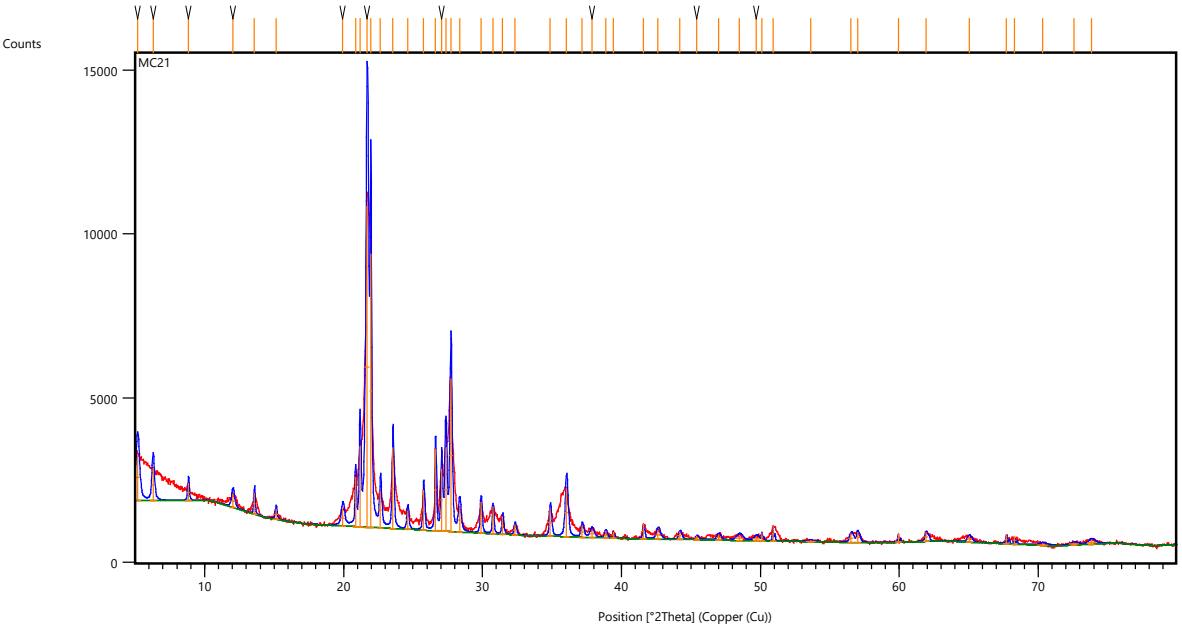
Counts
MC21
15000
10000
5000
0
10
20
30
40
50
60
70
Position [°2Theta] (Copper (Cu))

MC22

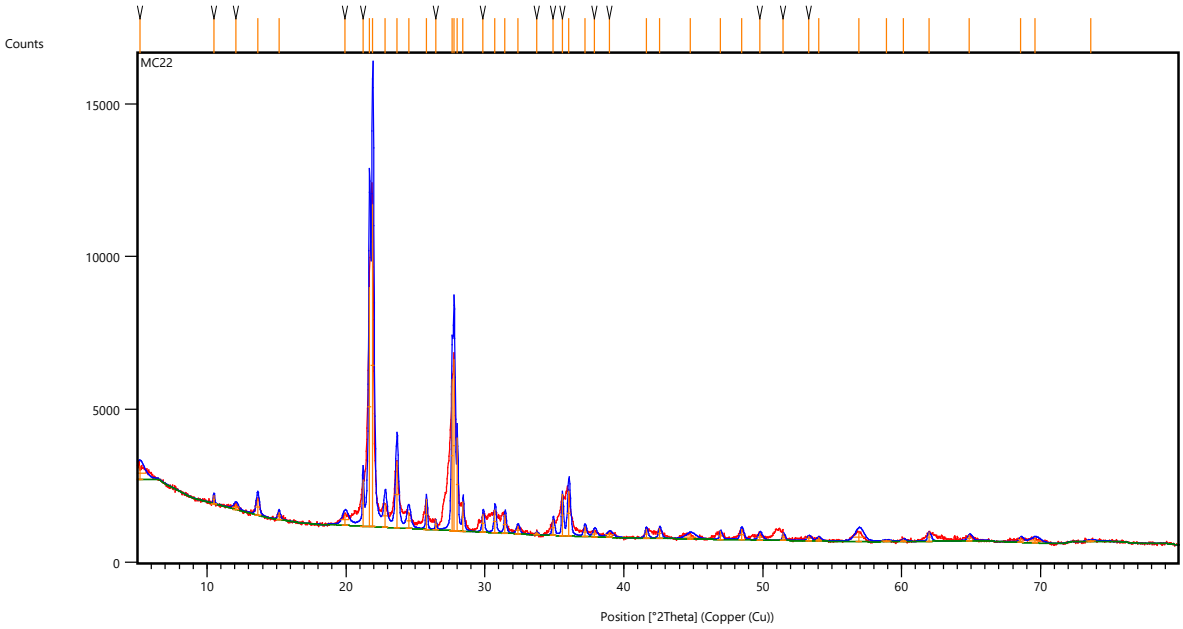
Counts
MC22
15000
10000
5000
0
10
20
30
40
50
60
70
Position [°2Theta] (Copper (Cu))

Appendix III: XRF Raw

Appendix 2: Raw whole-rock major and trace element compositions of samples MC01–MC22 determined by X-ray fluorescence (XRF) spectrometry.

Sample Name	**MC01**	**MC02**	**MC03**	**MC04**	**MC05**	**MC06**	**MC07**
Major elements (XRF, wt.%)							
(Raw data; all Fe expressed as Fe2O3)							
SiO_2	73.66	73.69	70.8	72.41	71.31	73.75	75.41
TiO_2	0.275	0.256	0.305	0.304	0.291	0.277	0.116
Al_2O_3	13.87	14.82	16.82	15.06	16.38	13.95	12.81
Fe_2O_3	2.19376	2.0195	2.48575	2.45091	2.28566	2.17621	2.72469
MnO	0.052	0.038	0.024	0.019	0.038	0.045	0.015
MgO	0.405	0.171	0.206	0.18	0.065	0.325	0.035
CaO	1.874	0.637	0.409	0.74	0.566	1.771	0.367
Na_2O	3.642	2.162	1.316	2.077	1.737	3.609	2.141
K2O	3.41	3.37	3.06	3.51	3.2	3.4	3.51
P_2O_5	0.068	0.054	0.035	0.035	0.039	0.058	0.032
LOI (%)	0.78	3.07	4.87	3.5	4.62	1.03	3.28
Sum (%)	100.335	100.383	100.396	100.371	100.638	100.494	100.534
Trace elements (XRF, ppm)							
Sc	6	7	4	4	6	5	6
V	24	18	27	27	23	26	13
Cr	7	0	0	0	0	0	0
Co	39	12	12	21	14	26	16
Ni	4	4	3	4	4	4	3
Cu	6	6	10	6	7	6	7
Zn	36	33	32	36	45	36	31
Ga	15	15	17	16	16	15	18
As	8	7	7	7	5	6	10
Rb	127	136	122	138	125	110	142
Sr	133	60	39	67	64	131	33
Y	22	55	16	13	21	16	23
Zr	148	154	169	164	157	150	134
Nb	6	7	7	7	7	6	8
Mo	4	4	4	4	4	4	4
Sn	2	5	6	2	4	3	5
Sb	3	3	3	1	2	3	3
Cs	1	6	2	2	1	1	8
Ba	808	799	631	712	865	842	681
La	21	142	18	7	33	17	12
Ce	47	50	35	34	39	48	43
Nd	26	91	19	14	21	21	21
Tl	1	1	1	1	1	1	1
Pb	12	14	13	14	15	14	16
Th	13	16	16	16	16	16	19
U	3	4	4	4	4	3	4

Appendix 1: Continued

Sample Name	MC08	MC09	MC10	MC11	MC12	MC13	MC14
Major elements (XRF, wt.%)							
(Raw data; all Fe expressed as Fe2O3)							
SiO_2	76.12	63.46	53.7	67.45	75.94	75.79	76.16
TiO_2	0.101	0.508	1.048	0.456	0.1	0.1	0.098
Al_2O_3	13.02	19.87	23.63	16.65	13	13.32	13.26
Fe_2O_3	1.73479	4.85029	8.35808	4.34326	1.42164	1.46267	1.43268
MnO	0.02	0.032	0.121	0.023	0.026	0.02	0.021
MgO	0.038	0.23	0.248	0.301	0.048	0.039	0.036
CaO	0.621	1.135	0.219	2.325	0.85	0.657	0.777
Na_2O	3.135	1.353	0.241	2.64	3.655	3.244	3.5
K2O	4.02	1.66	0.61	2.29	4.08	4.08	4.02
P_2O_5	0.029	0.044	0.04	0.043	0.028	0.029	0.028
LOI (%)	1.58			3.67	0.75	1.43	1.13
Sum (%)	100.509	100.439	100.387	100.265	100.003	100.286	100.568
			Trace elements (XRF, ppm)				
Sc	5	9	18	10	6	7	5
V	6	57	133	53	4	5	4
Cr	0	0	4	0	0	0	0
Co	24	24	30	21	42	19	22
Ni	3	4	9	3	3	3	3
Cu	5	10	19	5	5	5	5
Zn	35	67	94	55	36	31	35
Ga	16	22	27	20	15	16	15
As	9	7	7	7	9	9	8
Rb	153	64	35	84	153	152	148
Sr	48	83	24	163	61	53	55
Y	27	15	10	14	30	67	25
Zr	121	200	235	179	124	120	120
Nb	8	6	7	6	7	7	7
Mo	4	5	5	4	4	4	4
Sn	5	3	4	3	6	3	4
Sb	4	2	3	2	3	2	2
Cs	5	1	3	2	4	10	9
Ba	872	426	291	591	931	927	885
La	15	6	0	2	28	51	15
Ce	56	24	10	25	66	58	62
Nd	24	13	5	13	32	45	25
Tl	1	1	0	0	1	1	1
Pb	18	11	7	9	19	16	20
Th	19	11	9	10	17	17	17
U	5	3	3	3	4	3	4

Appendix 1: Continued

Sample Name	MC15	MC16	MC17	MC18	MC19	MC20	MC21
Major elements (XRF, wt.%)							
(Raw data; all Fe expressed as Fe2O3)							
SiO_2	66.98	75.66	74.87	56.78	73.14	76.39	74.87
TiO_2	0.41	0.095	0.094	0.763	0.279	0.098	0.111
Al_2O_3	17.01	13.35	14.2	17.28	13.91	13.32	14.63
Fe_2O_3	3.96818	1.6494	1.36505	7.25853	2.23064	1.52086	1.50401
MnO	0.032	0.014	0.016	0.125	0.043	0.023	0.031
MgO	0.46	0.035	0.033	5.044	0.376	0.075	0.074
CaO	2.619	0.697	0.658	8.541	1.926	0.374	0.551
Na_2O	3.199	3.356	3.212	2.954	3.689	2.262	2.688
K2O	2.32	3.98	3.76	1.06	3.36	4.11	3.52
P_2O_5	0.035	0.029	0.029	0.132	0.067	0.037	0.029
LOI (%)	2.79	1.5	2.33	0.52	1.4	2.31	2.47
Sum (%)	99.916	100.454	100.658	100.517	100.535	100.61	100.584
Trace elements (XRF, ppm)							
Sc	10	5	5	25	6	6	6
V	52	7	5	191	29	3	5
Cr	5	0	0	108	0	0	0
Co	21	22	22	49	40	13	20
Ni	3	3	3	25	4	3	3
Cu	9	6	5	25	7	7	5
Zn	81	31	35	73	36	32	56
Ga	19	16	17	18	16	16	17
As	5	9	9	8	7	9	9
Rb	90	146	128	39	109	170	135
Sr	180	53	47	223	135	33	46
Y	20	21	23	19	24	22	30
Zr	163	119	119	95	155	117	123
Nb	6	7	7	4	6	8	7
Mo	4	4	4	4	4	4	4
Sn	3	4	5	4	3	4	4
Sb	2	1	2	2	1	2	2
Cs	0	5	0	4	2	3	6
Ba	632	877	890	270	836	742	944
La	7	18	17	1	23	17	37
Ce	37	59	64	29	60	41	43
Nd	13	26	25	13	23	23	41
Tl	0	1	1	0	1	1	1
Pb	9	19	20	3	11	22	23
Th	10	17	18	4	14	20	22
U	3	4	4	3	3	5	4

Appendix 1: Continued

Sample Name	MC22
SiO_2	71.14
TiO_2	0.4
Al_2O_3	15.68
Fe_2O_3	2.81578
MnO	0.023
MgO	0.215
CaO	1.629
Na_2O	3.713
K2O	2.84
P_2O_5	0.048
LOI (%)	2.13
Sum (%)	100.724
Sc	7
V	26
Cr	0
Co	23
Ni	3
Cu	8
Zn	44
Ga	17
As	9
Rb	81
Sr	120
Y	29
Zr	274
Nb	7
Mo	5
Sn	3
Sb	2
Cs	2
Ba	786
La	33
Ce	52
Nd	29
Tl	1
Pb	14
Th	13
U	3

Appendix IV: LA-ICP-MS Raw Geochemical Data

Appendix 3:Major and trace element concentrations determined by LA-ICP-MS. All concentrations are reported in parts per million (ppm), with associated 2σ analytical uncertainties listed beneath each value.

Sample Name	MC01	MC02	MC03	MC04	MC05	MC06	MC07
Major element concentrations (ppm)							
Al	492000	495000	603000	589000	576000	503000	485000
Al (2σ)	32000	33000	41000	41000	37000	31000	29000
K	26090	25220	24700	24570	25840	25460	27550
K (2σ)	270	330	380	530	380	340	330
Ti	1979	1827	2303	2073	2167	1956	1113
Ti (2σ)	26	35	30	65	27	31	18
Trace element concentrations (ppm)							
Sc	6.47	6.38	6.94	6.01	6.8	6.24	5.67
Sc (2σ)	0.22	0.27	0.23	0.24	0.29	0.33	0.24
V	33.86	27.26	36.91	33.8	33.8	31.2	18.99
V (2σ)	0.69	0.64	0.53	1.3	0.73	0.52	0.53
Rb	114.5	115.5	114	113.2	113.5	95.2	129.7
Rb (2σ)	1.7	1.4	2.2	2.7	1.8	1.4	2.6
Sr	119.3	51.8	32.36	60	56.42	114.7	25.87
Sr (2σ)	1.3	0.85	0.58	1.5	0.82	1.5	0.42
Y	19.65	49.15	15.13	10.29	19.74	14	20.54
Y (2σ)	0.34	0.69	0.29	0.33	0.39	0.27	0.43
Zr	149.5	148.7	184.2	158.8	164.8	148.6	127.3
Zr (2σ)	1.8	2.5	3	3.8	1.8	1.7	2.2
Nb	5.71	6.22	6.96	6.02	6.57	5.64	7.85
Nb (2σ)	0.21	0.3	0.24	0.26	0.28	0.15	0.2
Cs	5.79	5.09	4.42	5.03	3.74	6.1	6.04
Cs (2σ)	0.22	0.16	0.17	0.25	0.17	0.21	0.15
Ba	717	681	581.8	599	780	730	616.5
Ba (2σ)	11	10	8.5	15	10	13	8.4
La	23.35	108.1	22.64	12.64	33.12	21.52	18.18
La (2σ)	0.36	1.5	0.42	0.42	0.49	0.38	0.58
Ce	38.97	37.72	29.1	23.42	36.18	35.23	32.85
Ce (2σ)	0.63	0.78	0.59	0.78	0.6	0.68	0.48
Pr	4.56	23.65	3.79	2.35	5.42	4.03	4.28
Pr (2σ)	0.15	0.39	0.12	0.12	0.12	0.13	0.13
Nd	16.89	84.1	13.13	8.79	19.12	14.89	16.96
Nd (2σ)	0.71	2	0.62	0.43	0.62	0.44	0.61
Sm	3.33	14.63	2.09	1.55	3.14	2.64	3.91
Sm (2σ)	0.22	0.75	0.23	0.11	0.28	0.24	0.28
Eu	0.573	2.46	0.333	0.26	0.618	0.519	0.368
Eu (2σ)	0.054	0.13	0.042	0.046	0.056	0.045	0.034
Gd	3.11	12.42	2.05	1.49	2.97	2.41	3.59
Dy	3.02	12.13	2.23	1.64	2.85	2.31	3.75
Dy (2σ)	0.18	0.57	0.15	0.13	0.19	0.15	0.24
Ho	0.642	2.15	0.475	0.34	0.636	0.444	0.753
Ho (2σ)	0.039	0.12	0.039	0.023	0.036	0.042	0.045
Er	1.88	6.06	1.52	1.1	1.69	1.44	2.17
Er (2σ)	0.12	0.27	0.13	0.12	0.11	0.12	0.15
Yb	2.16	5.68	1.47	1.35	1.83	1.57	2.16
Yb (2σ)	0.17	0.4	0.11	0.16	0.21	0.13	0.2
Lu	0.339	0.765	0.23	0.191	0.277	0.226	0.325
Lu (2σ)	0.027	0.053	0.022	0.02	0.03	0.03	0.03
Pb	13.05	12.6	14.25	13.65	14.79	13.61	17.37
Pb (2σ)	0.69	0.79	0.85	0.7	0.59	0.77	0.92
Th	11.51	13.08	13.95	11.67	13.56	11.66	16.42
Th (2σ)	0.36	0.38	0.33	0.43	0.33	0.27	0.34
U	2.56	3.22	2.99	2.74	2.86	2.512	2.98
U (2σ)	0.11	0.16	0.15	0.12	0.11	0.092	0.15

Appendix 2: Continued

Sample Name	MC08	MC09	MC10	MC11	MC12	MC13	MC14
Major element concentrations (ppm)							
Al	386000	893000	1.39E+06	713000	387100	391200	386100
Al (2σ)	7300	66000	84000	54000	5700	7300	4300
K	31130	13630	5375	18460	32230	32240	32170
K (2σ)	420	200	40	220	290	330	210
Ti	1000	3649	7481	3310	1020	1002	1004
Ti (2σ)	14	49	59	43	13	19	18
Trace element concentrations (ppm)							
Sc	6.25	11.53	22.31	10.85	6.34	6.49	6.35
Sc (2σ)	0.26	0.56	0.42	0.23	0.33	0.3	0.19
V	13.88	68	175.4	63.9	12.51	12.11	12.4
V (2σ)	0.43	1.2	1.9	1	0.37	0.34	0.37
Rb	136.4	58.2	28.77	74.97	137.9	138.4	137.24
Rb (2σ)	2.2	1.2	0.35	0.96	1.9	1.8	0.99
Sr	39.63	78.6	18.88	152.5	50.97	42.75	45.77
Sr (2σ)	0.72	1.3	0.41	1.3	0.72	0.71	0.56
Y	23.84	15.04	9.4	12.17	26.32	59.64	22.4
Y (2σ)	0.49	0.43	0.21	0.31	0.47	0.9	0.33
Zr	114.8	211.5	250.7	184.9	116.7	112.6	111.9
Zr (2σ)	1.9	3.5	2.3	1.8	1.1	1.2	1.9
Nb	6.69	7.25	7.89	6.29	6.16	6.42	6.45
Nb (2σ)	0.24	0.22	0.21	0.12	0.19	0.24	0.22
Cs	7.2	2.6	2.11	3.07	7.4	6.26	7.27
Cs (2σ)	0.23	0.064	0.1	0.18	0.25	0.23	0.25
Ba	741	393.5	279.4	529.6	802.2	794	776.2
Ba (2σ)	11	5.7	3.8	5.2	7.3	8.1	8.8
La	20.94	11.28	1.809	11.85	25.87	41.07	22.64
La (2σ)	0.5	0.3	0.094	0.22	0.46	0.64	0.43
Ce	41.55	25.63	9.99	23.19	48.04	41.38	44.2
Ce (2σ)	0.74	0.49	0.22	0.37	0.75	0.56	0.69
Pr	4.81	2.78	0.437	2.566	6	9.16	5.22
Pr (2σ)	0.12	0.14	0.03	0.083	0.13	0.17	0.12
Nd	18.89	11.38	1.9	9.98	23.14	36.2	19.15
Nd (2σ)	0.77	0.72	0.17	0.47	0.82	1.1	0.53
Sm	3.97	2.46	0.533	2	4.81	7.85	3.93
Sm (2σ)	0.29	0.28	0.098	0.2	0.49	0.49	0.28
Eu	0.419	0.39	0.121	0.628	0.564	1.09	0.43
Eu (2σ)	0.054	0.066	0.022	0.059	0.079	0.11	0.069
Gd	3.79	2.36	0.711	1.72	4.27	8.33	3.72
Dy	4.17	2.43	1.31	2.05	4.42	8.95	3.91
Dy (2σ)	0.25	0.2	0.14	0.17	0.29	0.49	0.23
Ho	0.841	0.516	0.353	0.445	0.916	1.995	0.82
Ho (2σ)	0.044	0.052	0.024	0.039	0.043	0.083	0.049
Er	2.46	1.63	1.185	1.36	2.78	5.8	2.31
Er (2σ)	0.14	0.18	0.089	0.12	0.14	0.23	0.13
Yb	2.62	1.81	1.44	1.62	2.93	5.6	2.42
Yb (2σ)	0.22	0.2	0.11	0.17	0.22	0.35	0.22
Lu	0.36	0.286	0.221	0.245	0.389	0.841	0.327
Lu (2σ)	0.028	0.028	0.019	0.021	0.029	0.064	0.029
Pb	15.54	12.07	12.08	10.91	16.06	14.59	15.83
Pb (2σ)	0.61	0.47	0.4	0.43	0.53	0.64	0.65
Th	14.06	8.89	8.01	7.93	13.32	13.83	13.8
Th (2σ)	0.33	0.24	0.26	0.21	0.26	0.26	0.34
U	3.023	1.9	1.865	1.769	2.79	2.72	2.84
U (2σ)	0.096	0.12	0.075	0.072	0.13	0.15	0.087

Appendix 2: Continued

Sample Name	MC15	MC16-17	MC18	MC19	MC20	MC21	MC22
Major element concentrations (ppm)							
Al	670000	369300	993000	469000	370000	409200	562000
Al (2σ)	48000	7800	68000	26000	5700	6300	40000
K	18510	31610	6725	32630	34190	25520	20110
K (2σ)	250	240	66	390	310	260	340
Ti	2907	996	4079	2583	1040	1002	2594
Ti (2σ)	25	14	26	29	16	17	37
Trace element concentrations (ppm)							
Sc	11.82	6.29	22.5	8.44	6.76	5.54	7.39
Sc (2σ)	0.25	0.27	0.43	0.26	0.37	0.25	0.29
V	60.1	14.12	146.1	42.24	14.29	12.66	30.35
V (2σ)	0.91	0.5	1.3	0.66	0.47	0.33	0.5
Rb	78.8	133.5	25.61	121.8	162.6	114.4	65.4
Rb (2σ)	2.1	1.3	0.44	1.6	1.5	1.3	1.1
Sr	160.4	43.57	170.2	154.3	26.41	34.5	102.3
Sr (2σ)	1.2	0.94	1.1	2	0.51	0.64	1.9
Y	17.43	18.7	14.27	27.54	20.18	24.16	25.26
Y (2σ)	0.34	0.4	0.25	0.42	0.45	0.47	0.55
Zr	176.4	112.6	72.25	189.6	114.1	109.7	257.1
Zr (2σ)	2.7	1.6	0.54	2.3	1.5	1.7	4.6
Nb	5.58	6.29	2.7	7.27	7.62	6.43	6.35
Nb (2σ)	0.2	0.18	0.13	0.23	0.28	0.21	0.2
Cs	3.22	6.73	1.477	7.68	7.71	7.06	3.276
Cs (2σ)	0.13	0.2	0.07	0.27	0.25	0.25	0.094
Ba	550.2	766.1	192.9	926	661.3	728.7	646
Ba (2σ)	6.5	7.8	2.2	13	8.1	9	11
La	14.87	21.51	6.82	33.41	21.82	30.37	31.48
La (2σ)	0.31	0.42	0.14	0.44	0.36	0.52	0.61
Ce	26.52	41.36	14.36	48.3	36.07	36.36	37.38
Ce (2σ)	0.32	0.61	0.22	1	0.75	0.67	0.72
Pr	3.09	4.67	1.826	6.61	4.37	8.03	6.13
Pr (2σ)	0.11	0.11	0.053	0.17	0.15	0.14	0.15
Nd	12.18	17.85	8.16	23.96	16.89	30.23	23.17
Nd (2σ)	0.44	0.61	0.28	0.67	0.62	0.99	0.72
Sm	2.35	3.59	2.13	4.57	3.76	5.98	4.36
Sm (2σ)	0.27	0.3	0.16	0.34	0.42	0.52	0.38
Eu	0.699	0.427	0.667	0.838	0.37	0.622	0.928
Eu (2σ)	0.059	0.042	0.036	0.069	0.054	0.054	0.082
Gd	2.54	3.08	2.3	3.94	3.3	5.05	4.12
Dy	2.53	3.37	2.47	4.24	3.55	4.46	3.81
Dy (2σ)	0.2	0.27	0.15	0.15	0.22	0.18	0.18
Ho	0.578	0.688	0.509	0.907	0.7	0.921	0.878
Ho (2σ)	0.054	0.059	0.029	0.05	0.062	0.051	0.058
Er	1.9	1.88	1.53	2.72	2.16	2.45	2.52
Er (2σ)	0.11	0.13	0.083	0.14	0.16	0.16	0.14
Yb	1.82	1.88	1.448	2.84	2.26	2.44	2.54
Yb (2σ)	0.14	0.13	0.099	0.22	0.26	0.2	0.2
Lu	0.328	0.26	0.216	0.447	0.285	0.365	0.374
Lu (2σ)	0.036	0.033	0.019	0.04	0.029	0.05	0.031
Pb	10.18	15.19	4.16	17.12	18.19	17.7	13.07
Pb (2σ)	0.53	0.75	0.15	0.95	0.83	0.72	0.55
Th	7.31	13.73	2.205	14.51	16.31	14.66	9.68
Th (2σ)	0.15	0.34	0.081	0.33	0.33	0.35	0.27
U	1.584	2.63	0.489	3.25	3.11	2.83	2.073
U (2σ)	0.083	0.14	0.036	0.14	0.12	0.11	0.09

Appendix V: Zircon Saturation Thermometry

Appendix 4: Zircon saturation temperatures calculated for samples MC01–MC22 from the Kaimai Rhyolite Dome Complex (KRDC). Cation fractions (Si, Al, Ca, Na, K) are reported as molar ratios used to calculate the compositional parameter M = (Na + K + 2Ca)/(Al × Si) following Watson and Harrison (1983). Zr concentrations are in parts per million (ppm). Saturation temperatures (°C) are calculated using both the original Watson and Harrison (1983) calibration (T °C W&H) and the revised Boehnke et al. (2013) calibration (T °C B). Dome assignments are based on field mapping (Chapter 3).

Sample Name	Dome	Si	Al	Ca	Na	K	M	Zr (ppm)	T (°C) W&H	T (°C) B
MC01	Kaimai	0.69	0.15	0.02	0.07	0.04	1.36	149.50	783.25	737.43
MC02	Kaimai	0.72	0.17	0.01	0.04	0.04	0.78	148.70	826.72	808.88
MC03	Kaimai	0.71	0.20	0.00	0.03	0.04	0.52	184.20	869.23	872.35
MC04	Kaimai	0.71	0.17	0.01	0.04	0.04	0.80	158.80	831.65	814.41
MC05	Kaimai	0.71	0.19	0.01	0.03	0.04	0.63	164.80	848.73	841.89
MC06	Kaimai	0.70	0.16	0.02	0.07	0.04	1.32	148.60	785.48	741.20
MC07	Te Weraiti	0.74	0.15	0.00	0.04	0.04	0.84	127.30	807.88	783.74
MC08	Te Weraiti	0.73	0.15	0.01	0.06	0.05	1.12	114.80	777.56	738.04
MC09	Te Weraiti	0.65	0.24	0.01	0.03	0.02	0.47	211.50	888.05	898.83
MC10	Te Weraiti	0.59	0.31	0.00	0.01	0.01	0.10	250.70	940.58	985.54
MC11	Waitewariki	0.66	0.19	0.02	0.05	0.03	1.00	184.90	829.87	805.00
MC12	Te Weraiti	0.72	0.14	0.01	0.07	0.05	1.28	116.70	767.62	721.51
MC13	Te Weraiti	0.72	0.15	0.01	0.06	0.05	1.14	112.60	774.95	734.55
MC14	Te Weraiti	0.72	0.15	0.01	0.06	0.05	1.21	111.90	769.48	726.00
MC15	Waitewariki	0.65	0.19	0.03	0.06	0.03	1.13	176.40	814.99	782.35
MC16	Te Weraiti	0.72	0.15	0.01	0.06	0.05	1.15	112.60	773.75	732.61
MC17	Te Weraiti	0.72	0.16	0.01	0.06	0.05	1.04	112.60	782.32	746.46
MC18	Basement	0.53	0.19	0.09	0.05	0.01	2.35	72.25	662.77	577.53
MC19	Kaimai	0.69	0.16	0.02	0.07	0.04	1.37	189.60	803.25	760.47
MC20	Kaimai	0.74	0.15	0.00	0.04	0.05	0.90	114.10	793.64	764.48
MC21	Kaimai	0.72	0.17	0.01	0.05	0.04	0.87	109.70	792.07	763.42
MC22	Unassigned	0.68	0.18	0.02	0.07	0.03	1.14	257.10	849.92	824.27

Appendix 5: Zircon saturation temperatures calculated for reference samples from the Pukunui and Greenpark domes. Cation fractions (Si, Al, Ca, Na, K) are reported as molar ratios used to calculate the compositional parameter M = (Na + K + 2Ca)/(Al × Si) following Watson and Harrison (1983). Zr concentrations are in parts per million (ppm). Saturation temperatures (°C) are calculated using both the original Watson and Harrison (1983) calibration (T °C W&H) and the revised Boehnke et al. (2013) calibration (T °C B). Dome assignments are based on field mapping (Chapter 3).

Sample Name	Dome	Si	Al	Ca	Na	K	M	Zr (ppm)	T (°C) W&H	T (°C) B
2TB	Pukunui	0.69	0.16	0.02	0.07	0.04	1.31	234	827.01	790.53
2CB	Pukunui	0.68	0.16	0.02	0.07	0.04	1.26	242	834.82	801.92
3CB	Pukunui	0.69	0.17	0.02	0.07	0.04	1.23	244	837.67	806.25
S1.1	Pukunui	0.69	0.17	0.02	0.06	0.04	1.14	245	845.42	818.87
S4DAR	Greenpark	0.68	0.18	0.02	0.06	0.04	1.15	238	842.03	814.5
S6DAR	Greenpark	0.68	0.18	0.02	0.07	0.04	1.2	232	835.47	804.75

Appendix VI: SEM-EDS

MC02

EDS Layered Image 15

Na Kα1,2

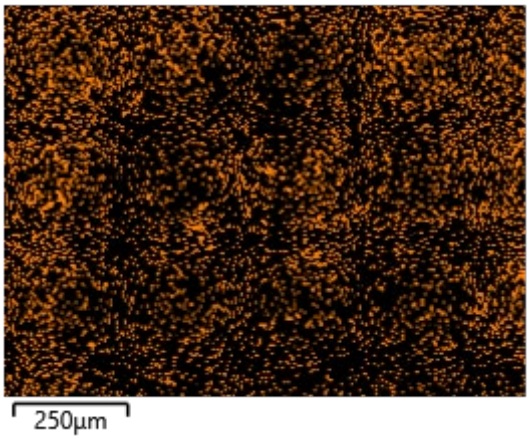

Al Kα1

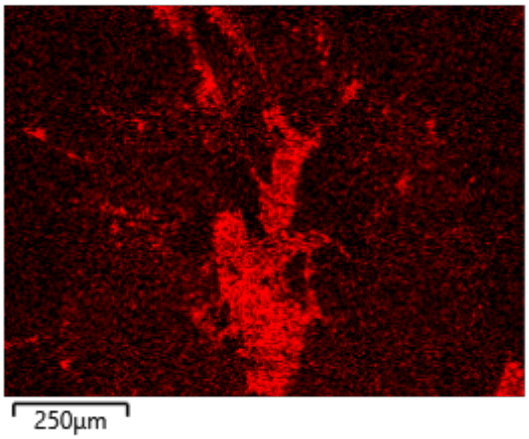

Si Kα1

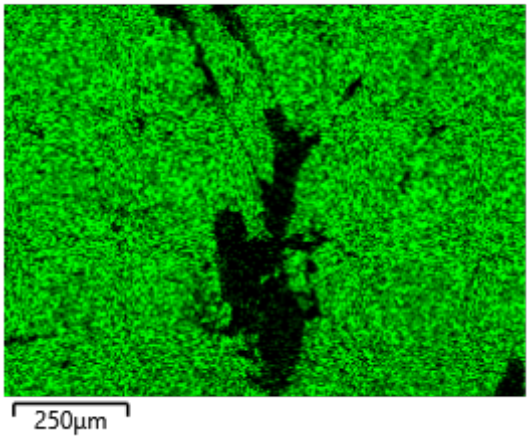

K Kα1

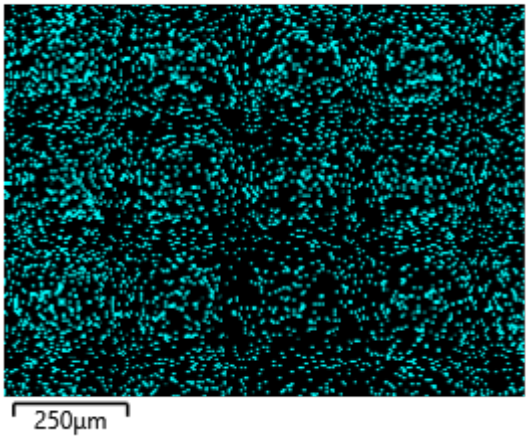

Ca Kα1

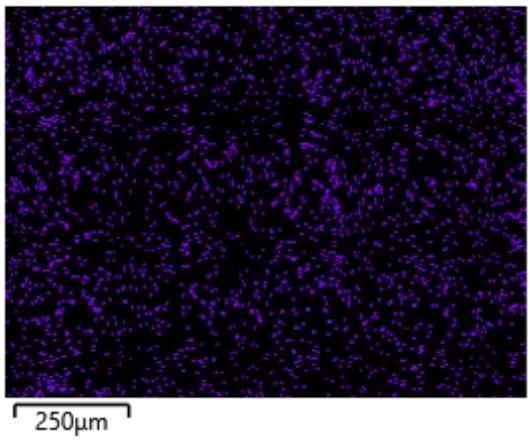

EDS Layered Image 16

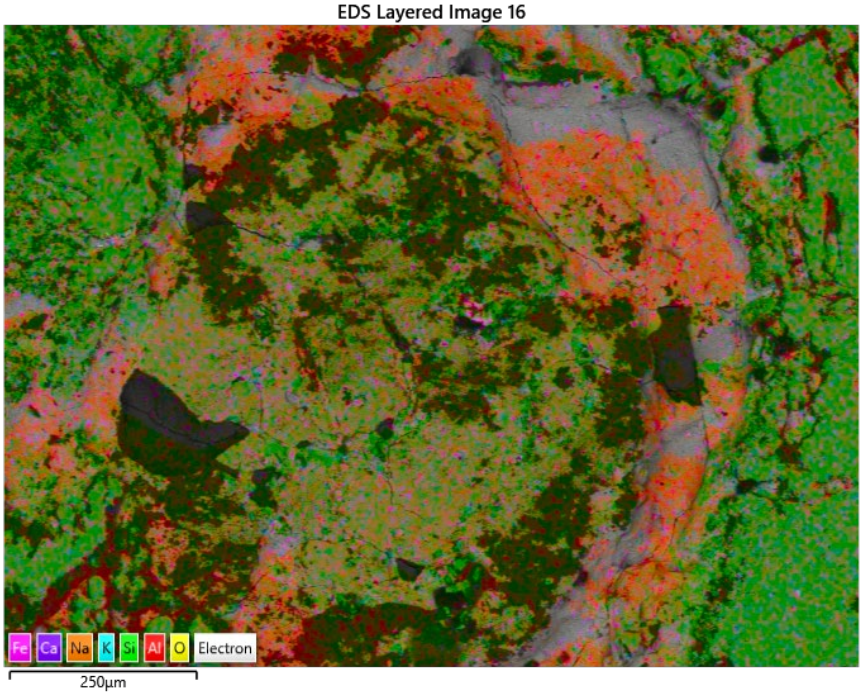

Na Kα1,2

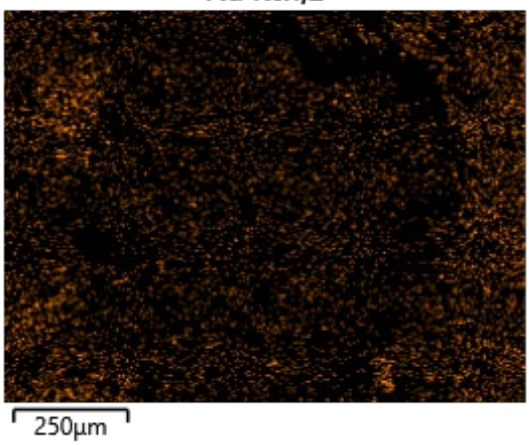

Al Kα1

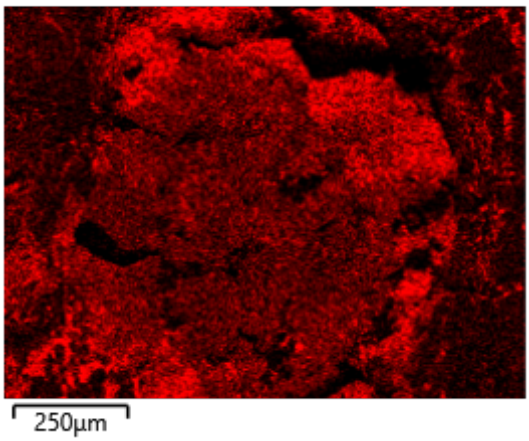

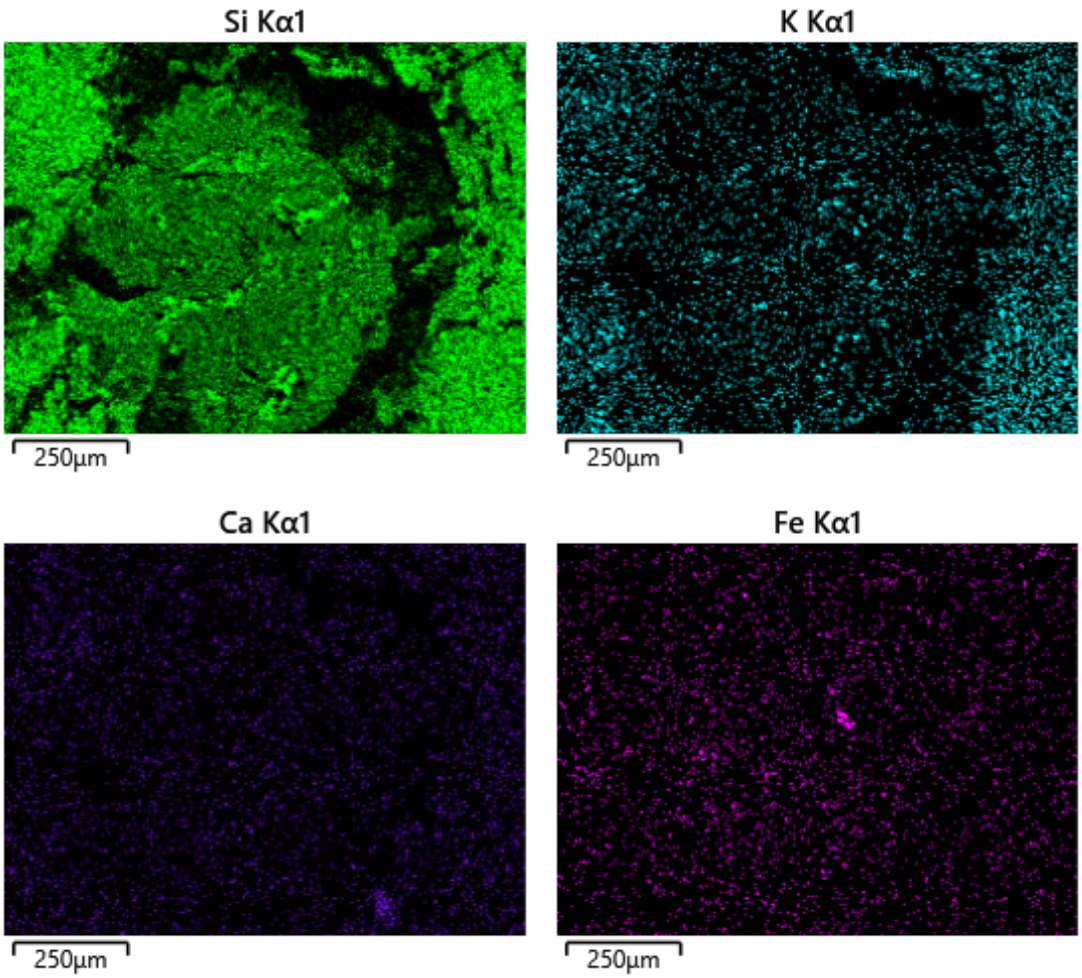
Si Kα1
250µm
K Kα1
250µm
Ca Kα1
250µm
Fe Kα1
250µm

MC05

EDS Layered Image 3

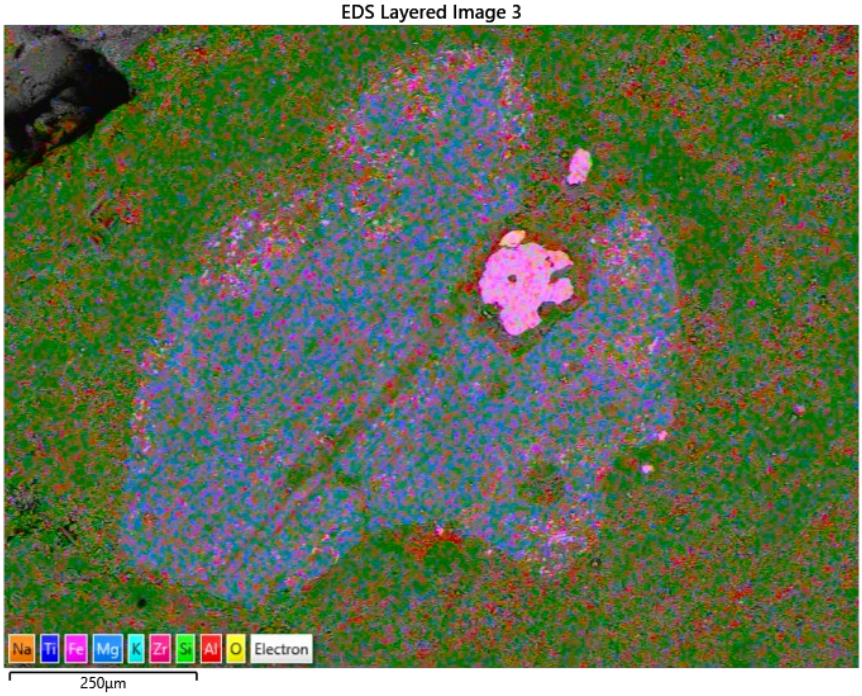

Na Kα1,2

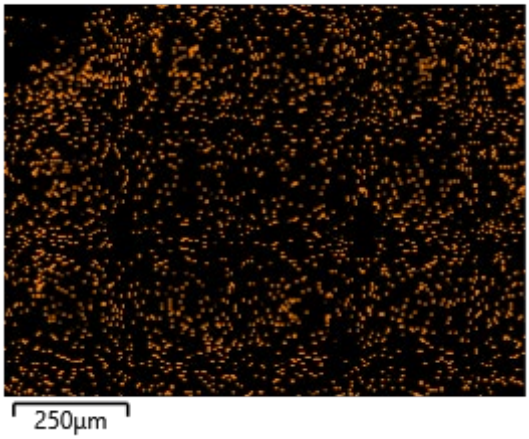

Mg Kα1,2

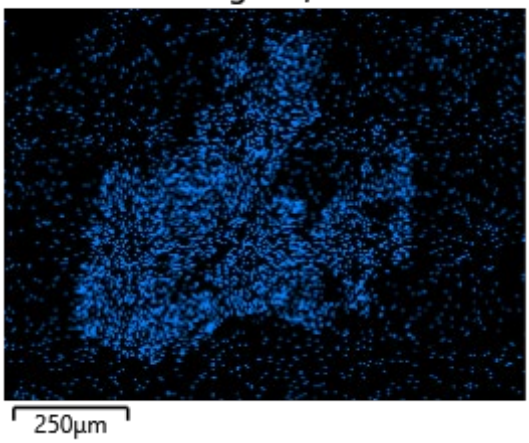

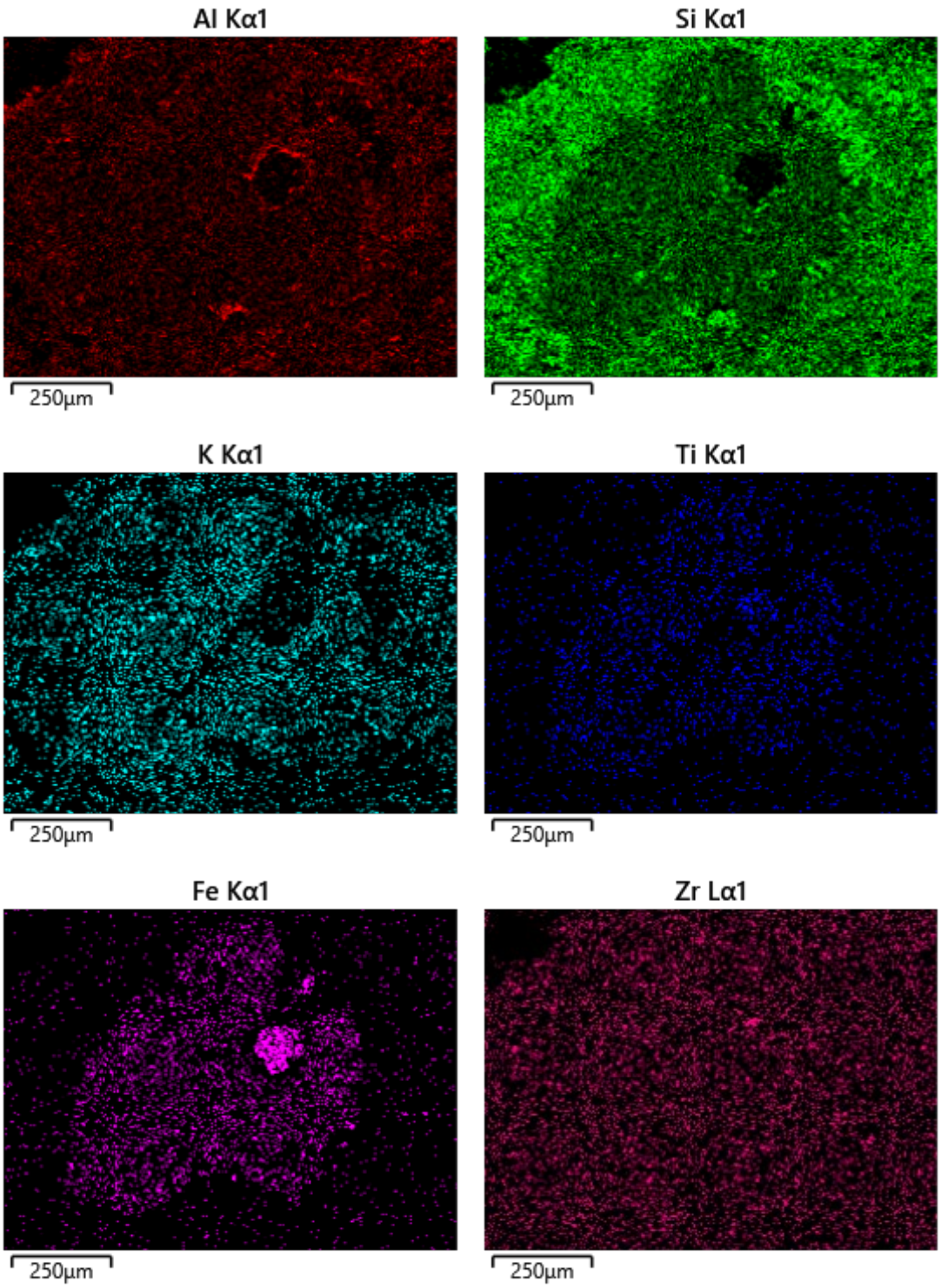
Al Kα1
250µm
Si Kα1
250µm
K Kα1
250µm
Ti Kα1
250µm
Fe Kα1
250µm
Zr Lα1
250µm

EDS Layered Image 4

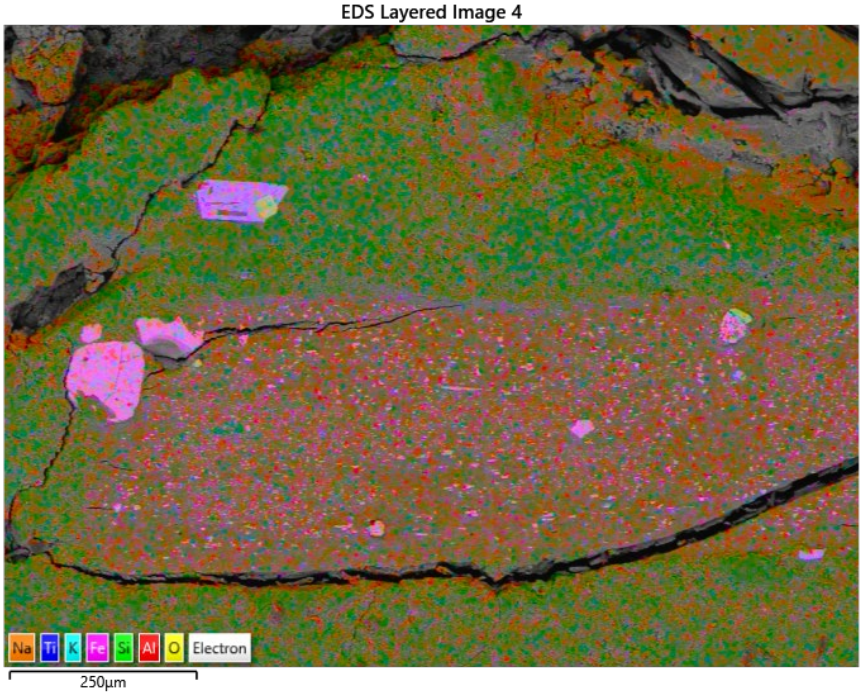

Na Kα1,2

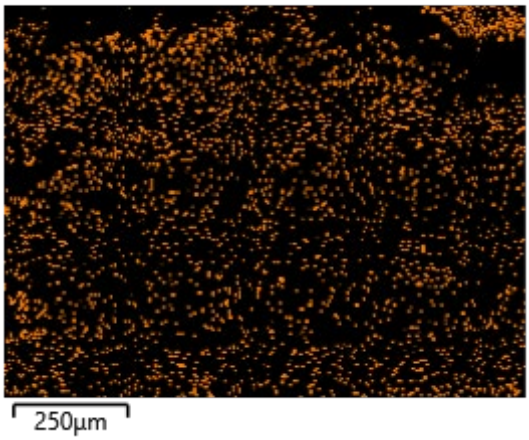

Al Kα1

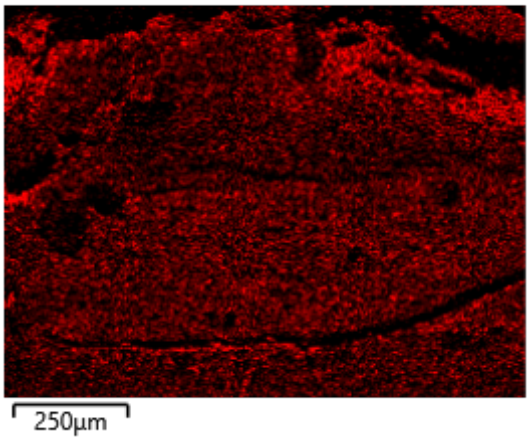

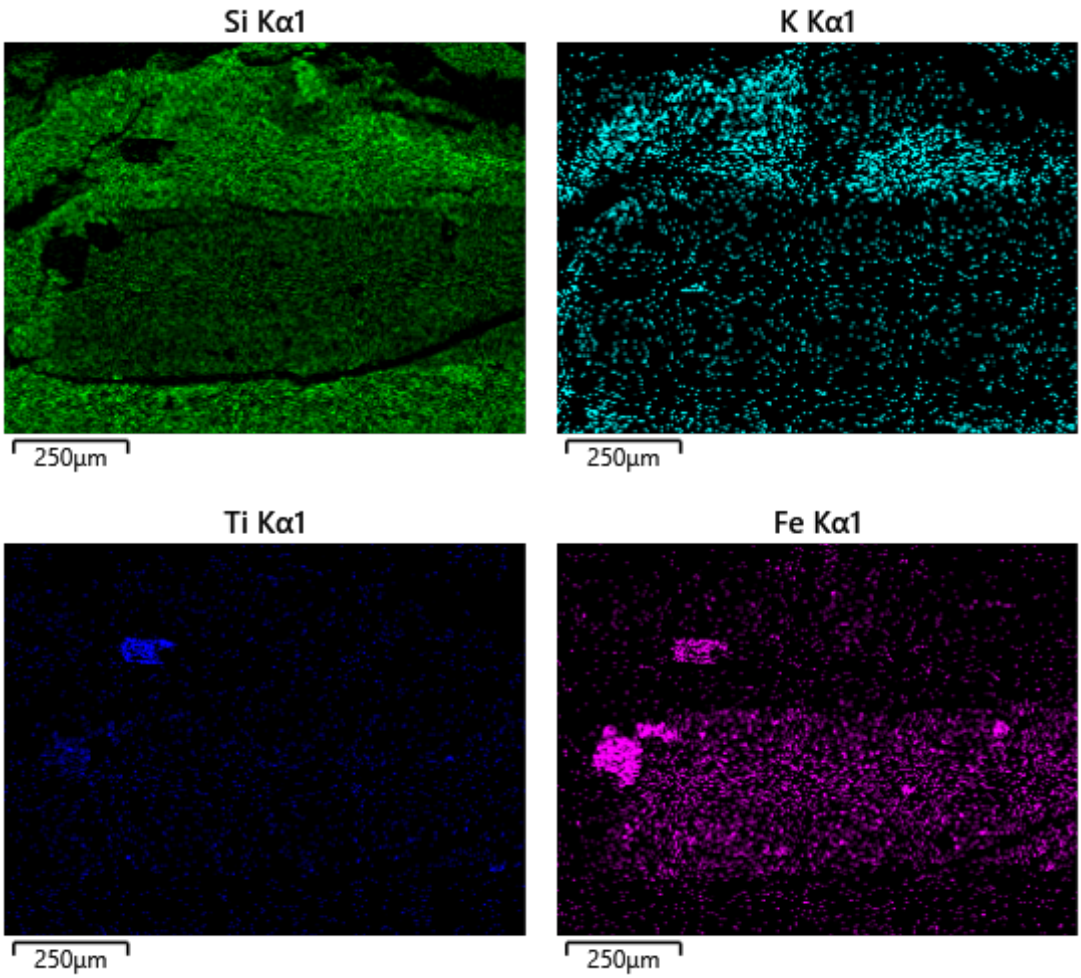
Si Kα1
250µm
K Kα1
250µm
Ti Kα1
250µm
Fe Kα1
250µm

MC08

EDS Layered Image 10

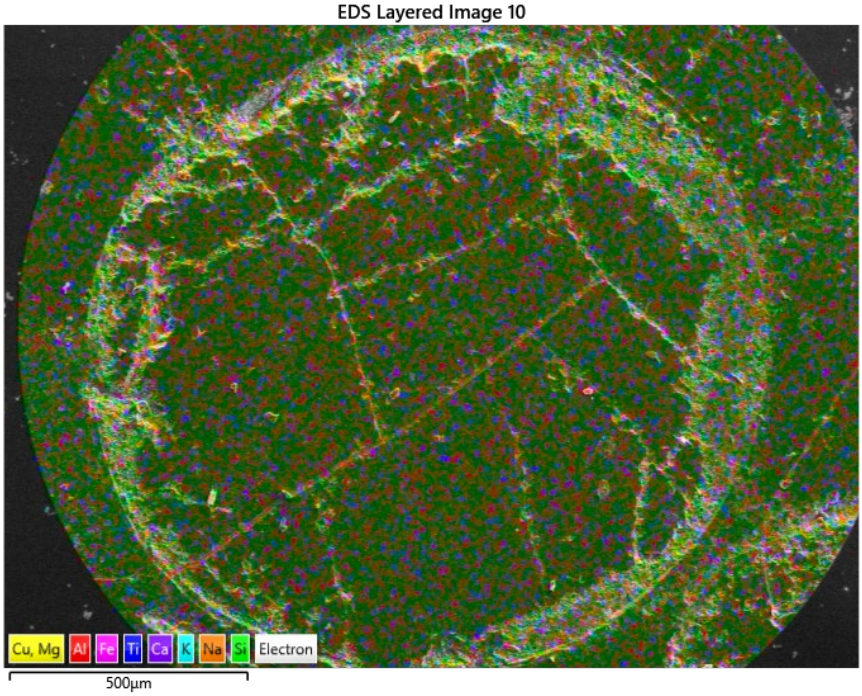

Na Kα1,2

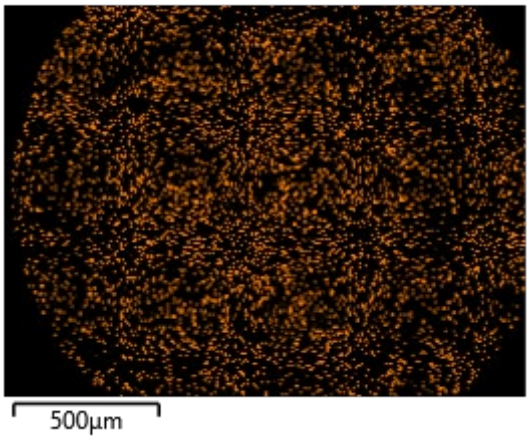

Mg Kα1,2

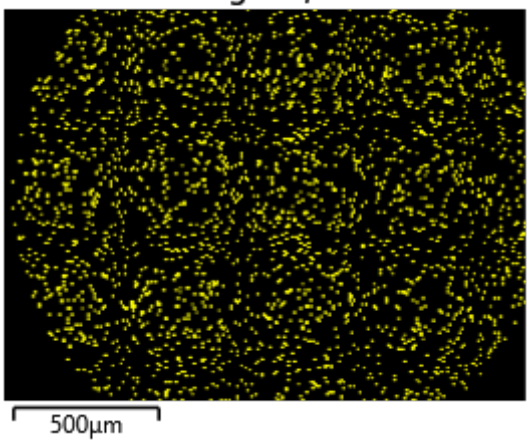

Al Kα1

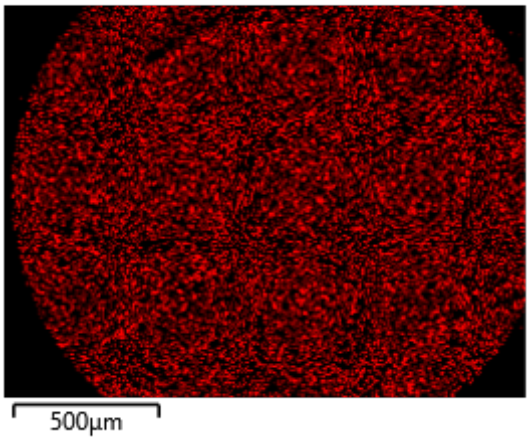

Si Kα1

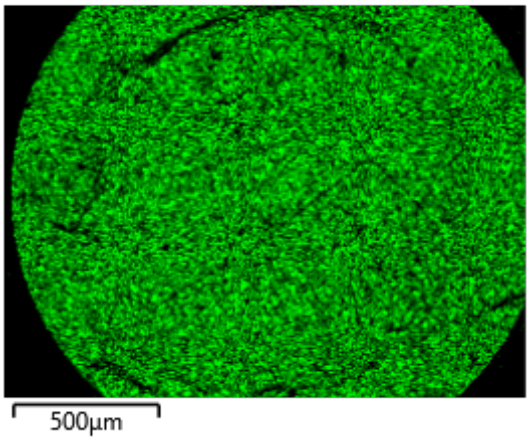

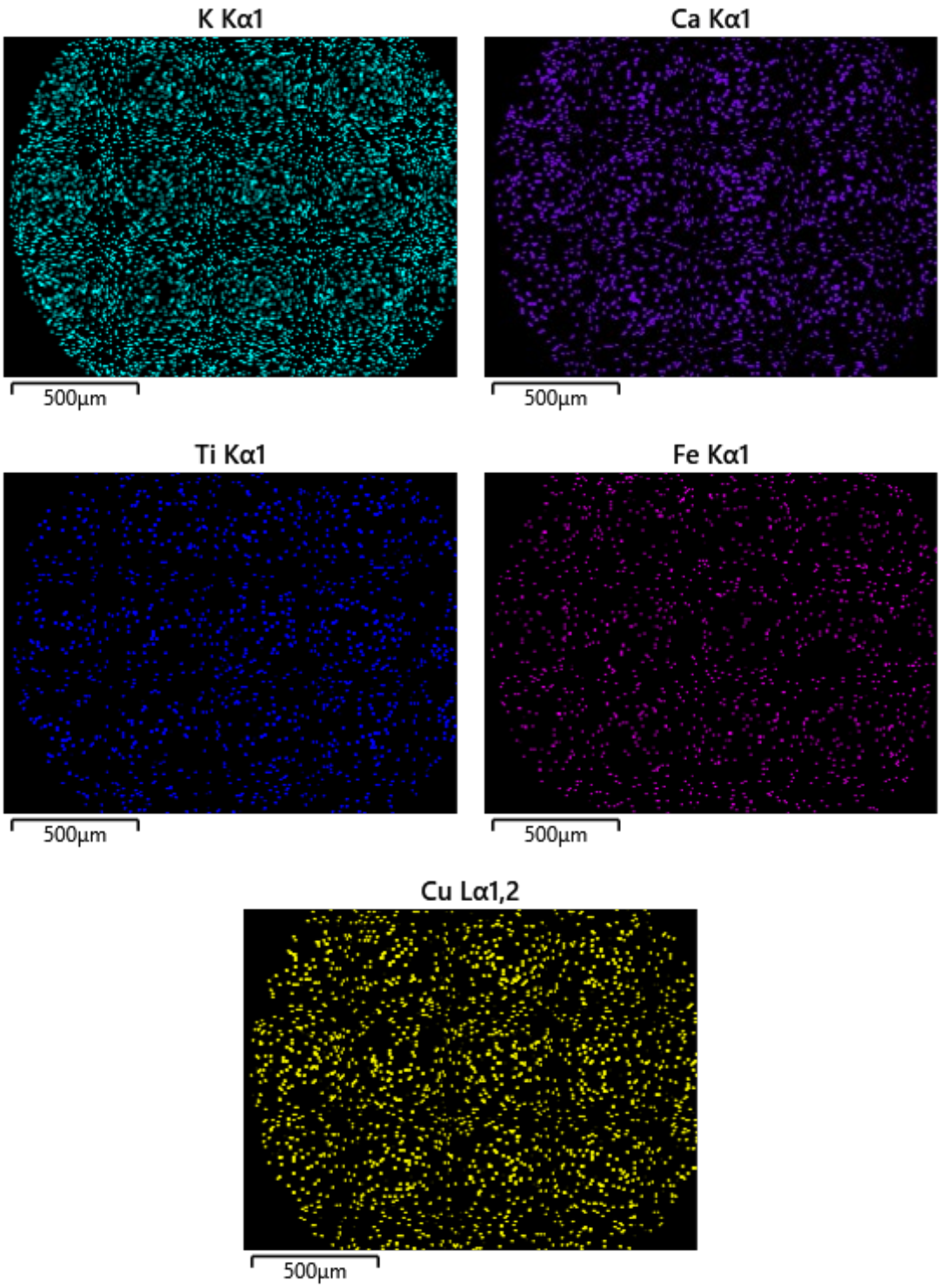
K Kα1
500µm
Ca Kα1
500µm
Ti Kα1
500µm
Fe Kα1
500µm
Cu Lα1,2
500µm

EDS Layered Image 12

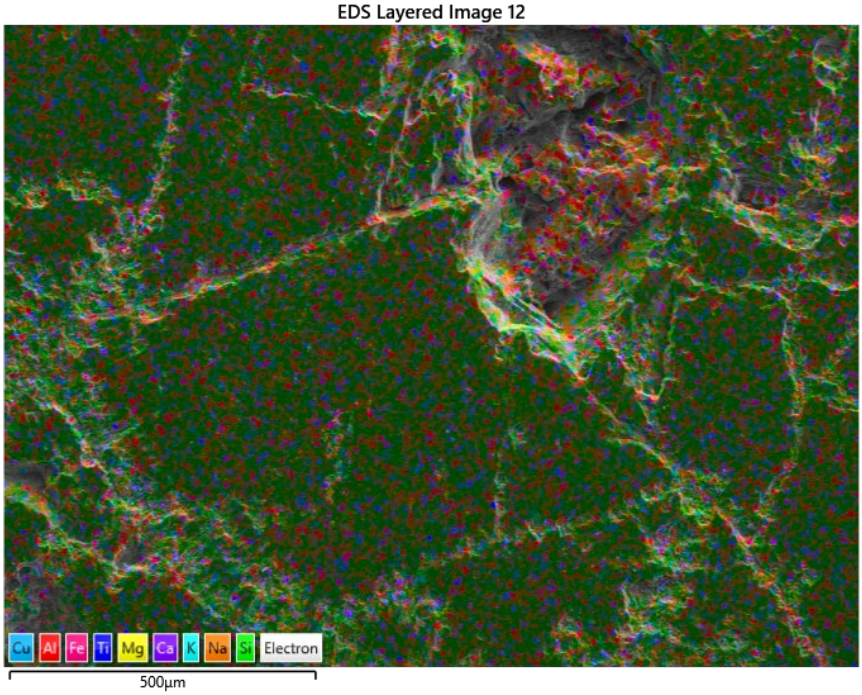

Na Kα1,2

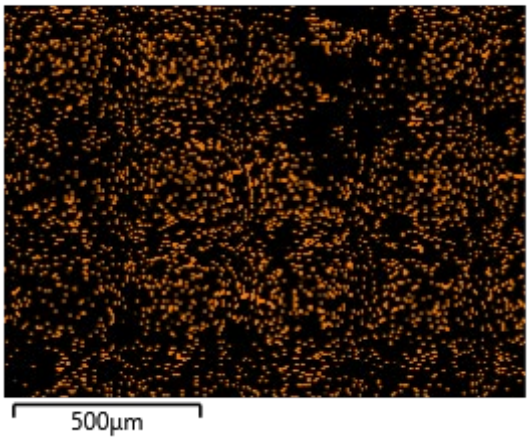

Mg Kα1,2

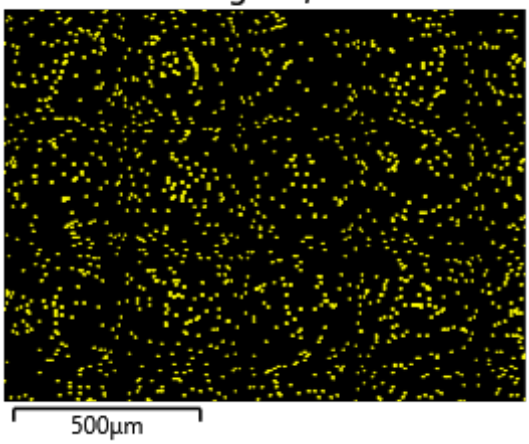

Al Kα1

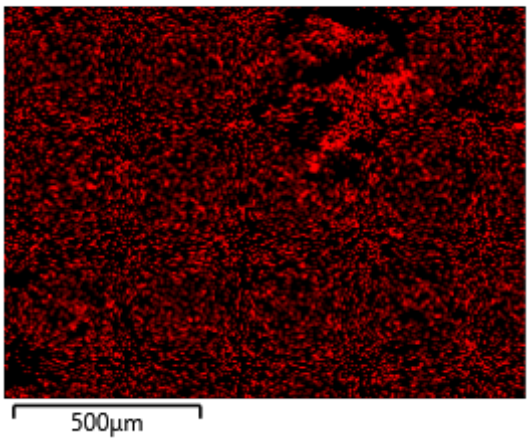

Si Kα1

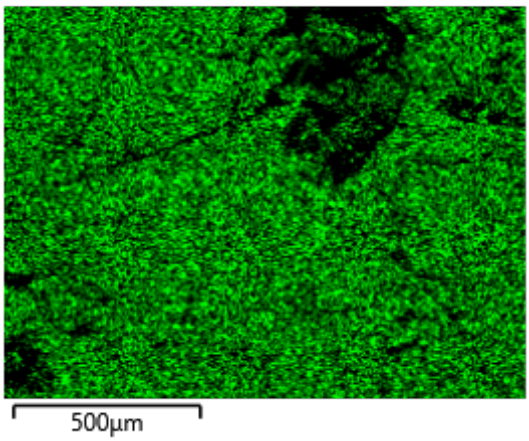

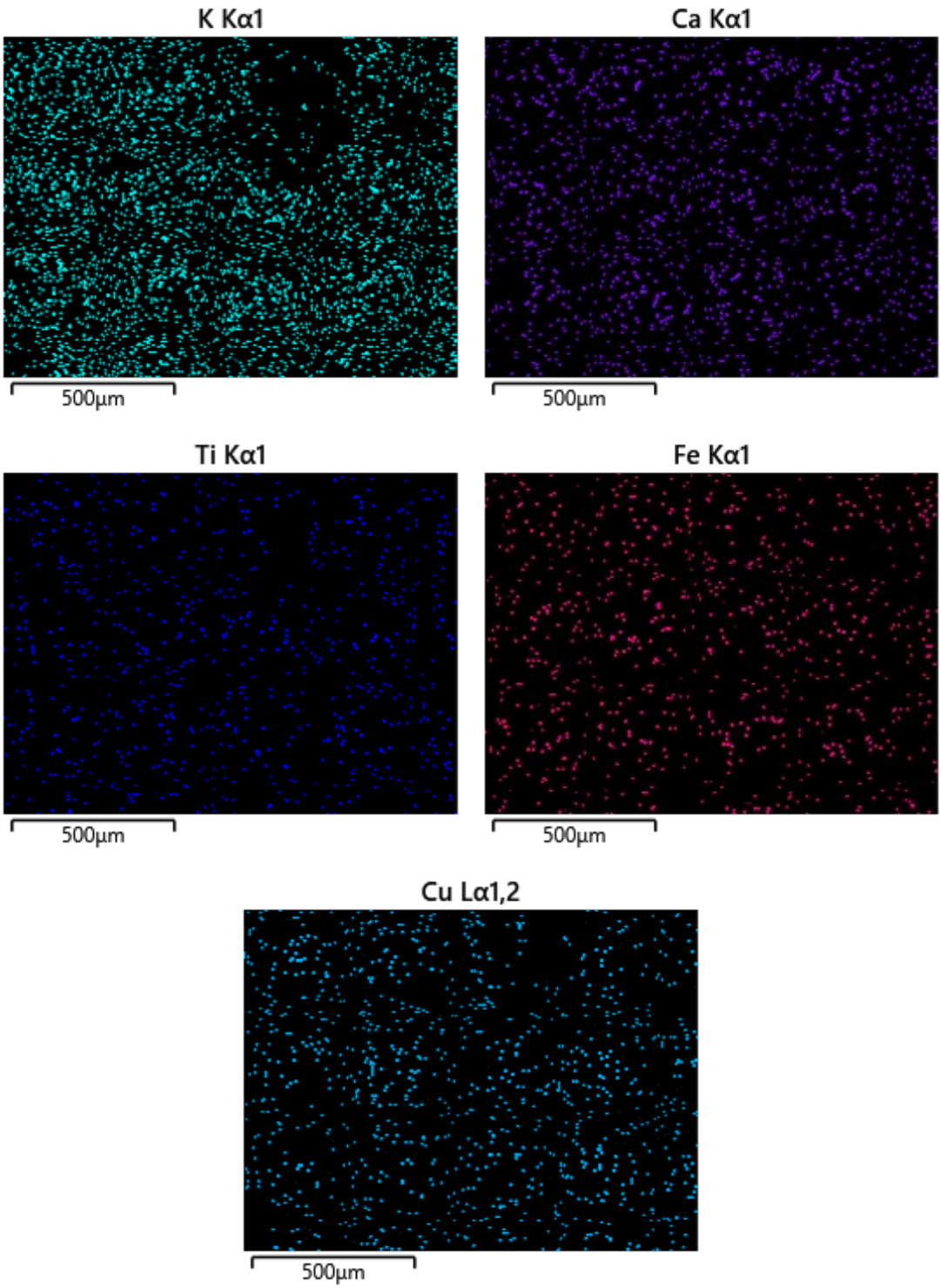
K Kα1
500µm
Ca Kα1
500µm
Ti Kα1
500µm
Fe Kα1
500µm
Cu Lα1,2
500µm

MC13

EDS Layered Image 9

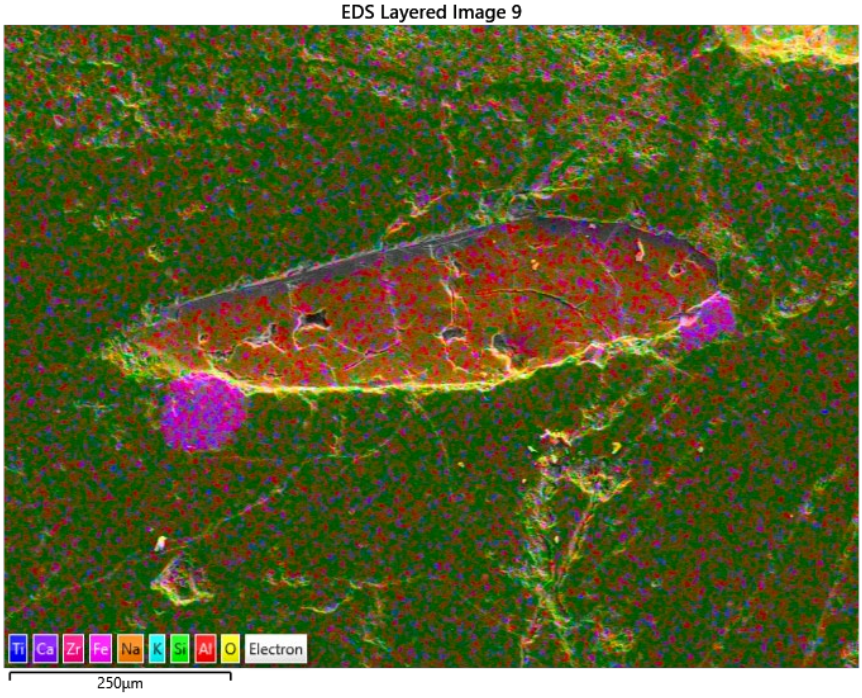

Na Kα1,2

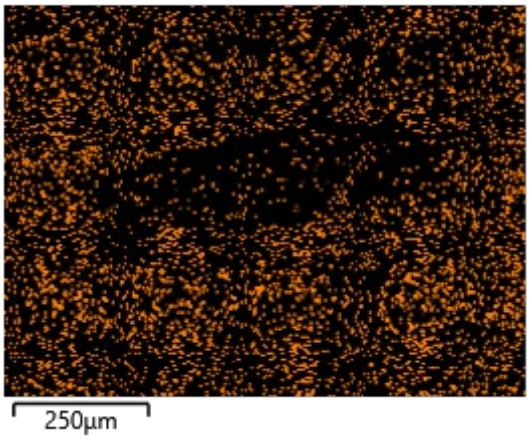

Al Kα1

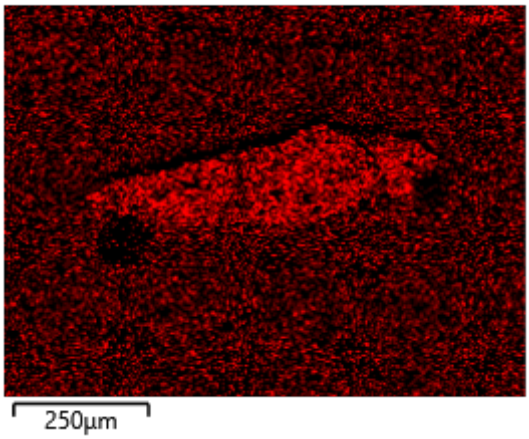

Si Kα1

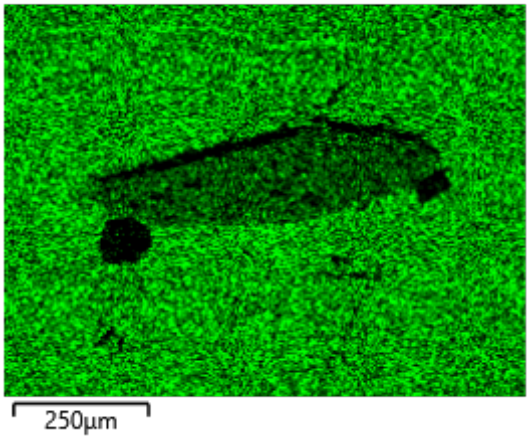

K Kα1

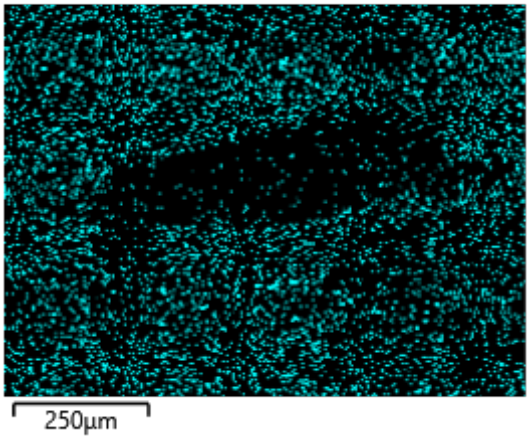

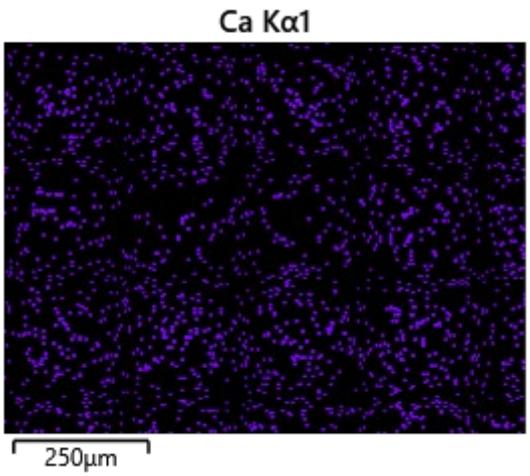

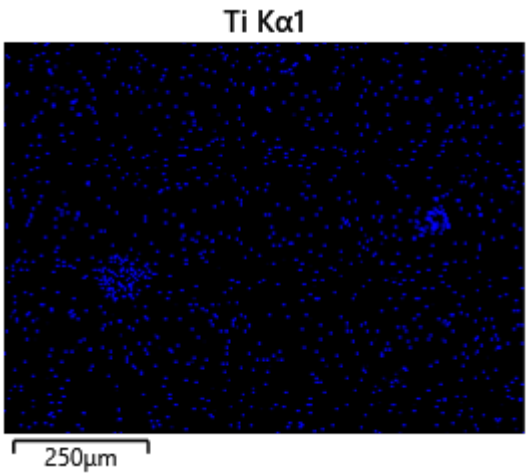

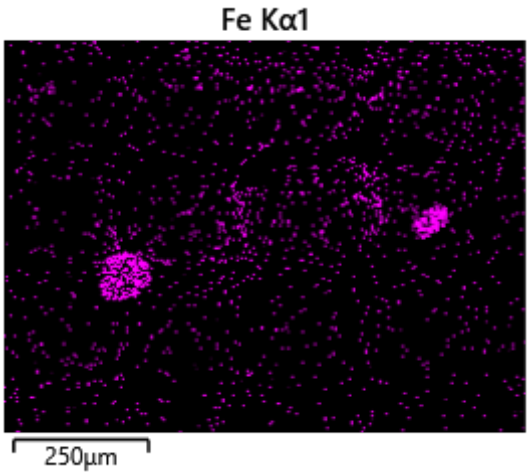

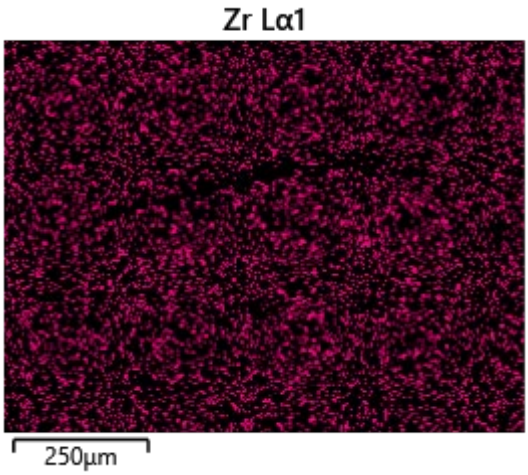

EDS Layered Image 8

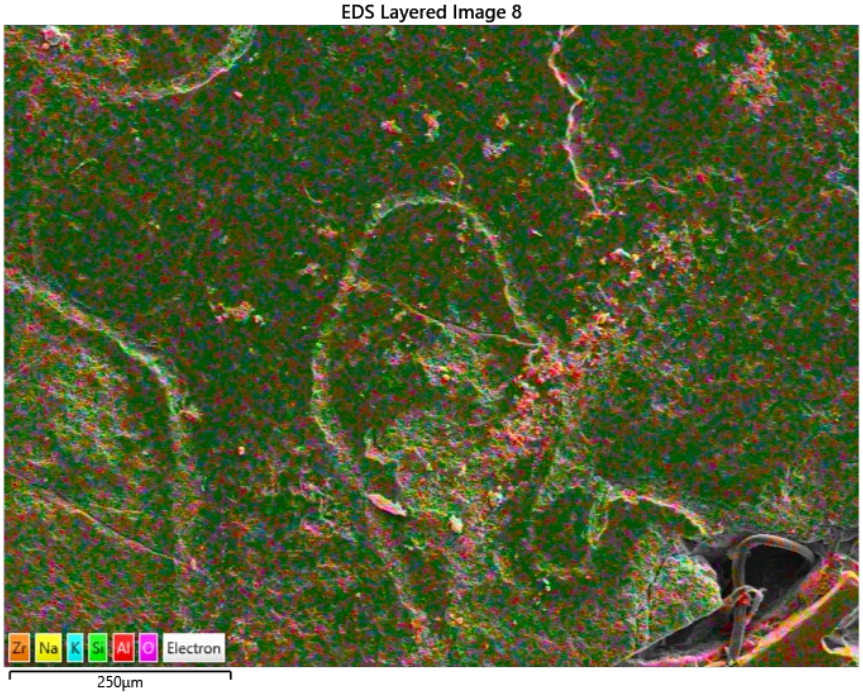

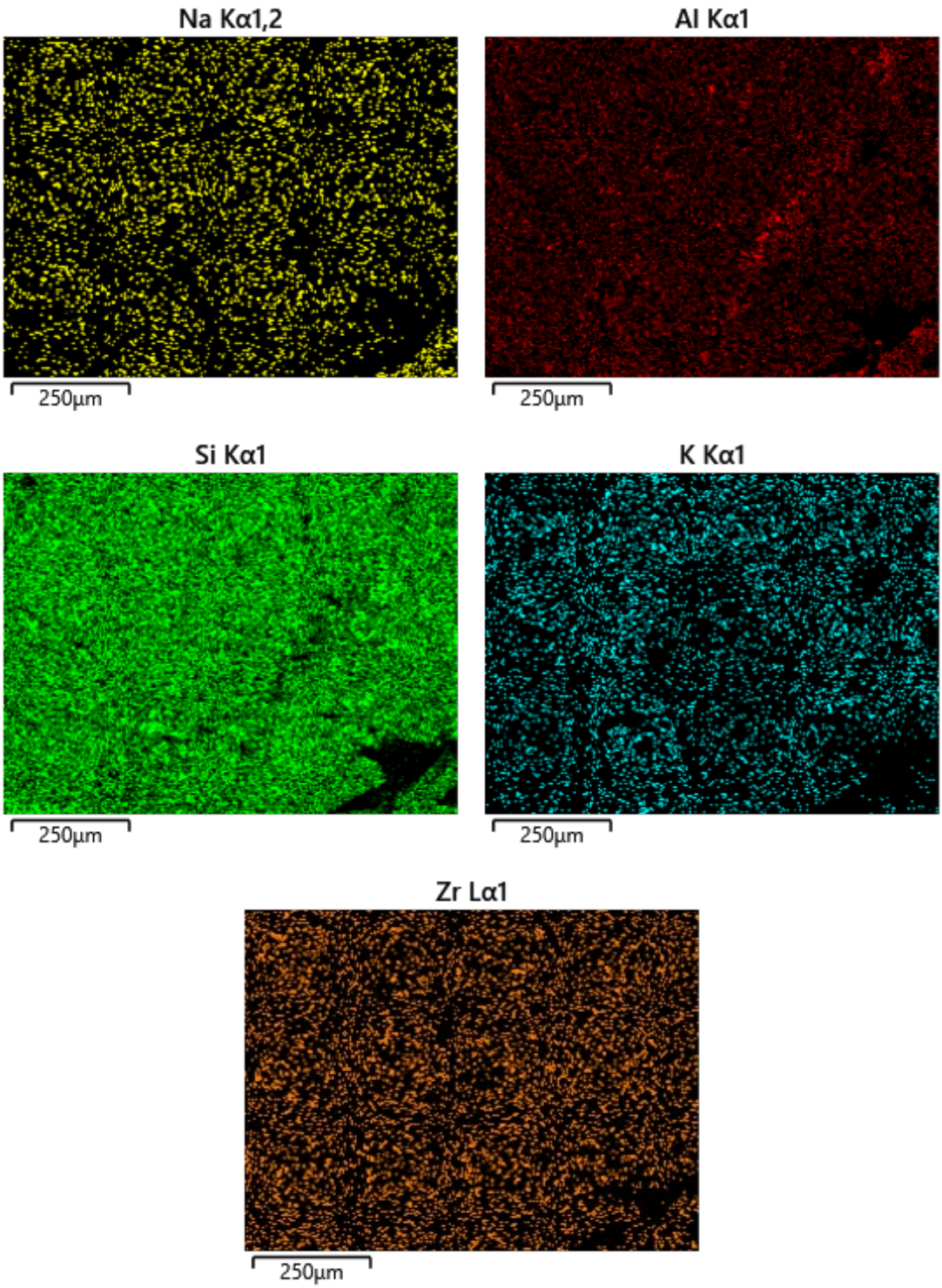
Na Kα1,2
250µm
Al Kα1
250µm
Si Kα1
250µm
K Kα1
250µm
Zr Lα1
250µm